Measurements of Flow and Combustion in a Strongly Charged Spark Ignition Engine

Wankang Zhang
MEng

Submitted in accordance with the requirements for the degree of
Doctor of Philosophy

The University of Leeds

School of Mechanical Engineering

December 2018

Intellectual Property and Publication Statements

The candidate confirms that the work submitted is his/her own and that appropriate credit has been given where reference has been made to the work of others.

Acknowledgements

Firstly, I would like to thank my supervisors Alexey Burluka, Malcolm Lawes and Junfeng Yang. They provide valuable guidance and suggestions for my research.

I would like to thank the technical staff in the ITF lab: Mark Batchelor, Brian Leach and Paul Banks for their sufficient technical helps on running experiments.

I would like to thank my parents: Xueli Zhang and Junying Sang. They provide financial support for my studies at the University of Leeds.

At last, I would like to thank my wife Xingyi Fu, for her love and support.

Abstract

The spark ignition engine is one of the most widely used power sources for vehicles. Due to the global warming, the fuel economy is encouraged to contribute in designing spark ignition engines. Therefore, one promising design is a strongly boosted downsized spark ignition engine. The present work aims to investigate combustion from two perspectives, namely, bio-derived fuels performed as additives in a strongly charged engine, and flame propagation at high pressure.

N-butanol and 2,5-dimethylfuran performed as additives in a strongly charged engine were investigated across a range of spark timings at an engine speed of 750 RPM under stoichiometric conditions. Knock characteristics of those fuels were studied, and reverse thermodynamic analysis was applied to derive the in-cylinder charge state and flame speed. The results show that 2,5-dimethylfuran preformed as additive for current unleaded gasoline and its toluene reference fuel provides good anti-knock performance in strongly charged engine. N-butanol have great improvement as an additive on anti-knock performance for toluene reference fuel.

Turbulent flow in the engine was studied by using two dimensional particle image velocimetry. Meanwhile, the effects of thermal expansion on turbulent flow which is located in front of the flame was also investigated. Burning velocity and flame speed of commercial unleaded gasoline and iso-octane under turbulent intensity of 0.75 m/s and 1.20 m/s were investigated at temperature of 650 K, pressure of 30 bar. The results suggest that several burning velocity correlations for predicting turbulent burning velocity not match the experimental outcomes. Furthermore, the thermal expansion may alter the turbulent intensity which is located in front of the flame. Flame shape and wrinkles were studied based on the captured laser tomographic images. The power spectral density of the wrinkles shows that the flame wrinkling is possibly related to the turbulent energy cascade. However, due to the limited camera resolutions, the effect of flame instability on wrinkling spectrum can not be observed clearly.

Contents

List of Figures

List of Tables

Nomenclature

Roman and Greek Symbols

A	Area
$\mathbf{A}$	Zimont turbulent flame speed closure model constant
α	Thermal diffusivity
Da	Damköhler number
δ_l	Laminar flame thickness
η	Turbulent Kolmogorov length scale
η_{Otto}	Otto cycle efficiency
ϵ	The rate of dissipation of the kinetic energy
γ	Specific heat ratio
K	Kalghatgi octane index correction factor
Ka	Karlovitz number
k	Turbulent kinetic energy
κ	Wave number
L	Turbulent integral length scale
L_λ	Turbulent Taylor length scale
Lr'	Flame wrinkle integral length scale

l	Total contour length
ν	Kinematic viscosity
m	Mass
P	Pressure
Pe	Perimeter
Q	Energy change
ϕ	Equivalence Ratio
R	Flame radius
Re	Reynolds number
Re_λ	Taylor scale Reynolds number
R_k	Correlation coefficient
r	distance
r'	Wrinkling amplitude
r_v	Compression ratio
r'	Root mean square of flame wrinkling altitude
r_p	Wrinkling altitude
ρ	Density
S	Energy spectrum
S_t	Turbulent flame speed
s'	Contour length
σ	Standard deviation
T	Temperature

t	time
Θ	Angle in polar coordinate system
τ_c	Characteristic time for chemical reaction
τ_t	Characteristic time for turbulent integral scale
τ_η	Characteristic time for turbulent Kolmogorov scale
θ	Crank angle
u	Fresh gas velocity along x-axis
u'	Turbulent root mean square velocity
u'_k	Effective turbulent root mean square velocity
u_l	Laminar burning velocity
u_t	Turbulent burning velocity
u_r	Fresh gas radial velocity
u'_r	Fresh gas radial root mean square velocity
v	Fresh gas velocity along y-axis
v_r	Fresh gas tangential velocity
v'_r	Fresh gas tangential root mean square velocity
ξ	Separation distance

Subscripts

abs	Absolute
b	Burned
bb	Blow-by
com	Combustion
$comp15$	At 15 bar during compression stroke
cyl	Cylinder
dyn	Dynamic
ht	Heat transfer
i	Sector index
pm	Piston motion
u	Unburned

Abbreviations

2,5-DMF	2,5-Dimethylfuran
aTDC	After top dead centre
BDC	Bottom dead centre
bTDC	Before top dead centre
CA	Crank angle
COV	Coefficient of variation
EGR	Exhaust gas recirculation
ER	Equivalence ratio
FFT	Fast Fourier transform
FPS	Frame per second
HCCI	Homogeneous charge compression ignition
IMEP	Indicated mean effective pressure
LUPOE2-D	Leeds university potted optical engine MK-2 disc chamber
LUSIEDA	Leeds University Spark Ignition Engine Data Analysis
MAPO	Maximum pressure oscillations
MON	Motor octane number
OI	Octane index
PIV	Particle image velocimetry
PSD	Power spectral density
RMS	Root mean square
ROI	Region of interest

RON	Research octane number
RPM	Revolutions per minute
SI	Spark ignition
TDC	Top dead centre
TRF	Toluene Reference Fuel
TRFB	Toluene Reference Fuel - n-butanol mixture
TRFD	Toluene Reference Fuel - 2,5-Dimethylfuran mixture
ULG	Unleaded gasoline
ULGB	Unleaded gasoline - n-butanol mixture
ULGD	Unleaded gasoline - 2,5-Dimethylfuran mixture
ZFSK	Zeldovich, Semenov and Frank-Kamenetskii

Chapter 1

Introduction

1.1 Motivation

The internal combustion (IC) Engine has been used as a power source for more than hundred years. In order to reduce the influences of the global warming and air pollution, fuel economy has became an inevitable option in designing IC engines. To improve the vehicle fuel economy, reducing the swept volume of the engine is one of the promising solutions (Clenci et al. 2007). However, reducing the swept volume will result in reducing the engine torque and power. The solution is to make the engine scavenge more air, so that the torque and power loss will be compensated from the reducing swept volume. As a result, implementing a strongly charged characteristic for a spark ignition (SI) engine is the trend in engine development.

The strongly charged or boosted characteristic for SI engines means an increase of the in-cylinder pressure during operation. Furthermore, an increase of intake pressure is also accompanied with a high intake temperature. Therefore, there is an increased risk of abnormal combustion occurring in strongly charged spark ignition engine, such as knock and pre-ignition. To avoid knock in the spark ignition engine, improving both engine parameter and anti-knock property of fuel could be applied. The engine parameter which needs to be improved consists of advance spark timing, lower intake temperature and equivalence ratio (Attard et al. 2010, Hanabusa et al. 2013).

Since the fossil fuel is a non-renewable energy resource, either the engine operation with lean charge for improving the engine efficiency (Hanabusa et al. 2013) or replacing the fossil with a renewable energy resource (such as, bio-derived fuels) will make great contributions for saving the non-renewable energy resource.

Since the strongly charged engines have high initial pressure and initial temperature, the flame instability tends to be involved in the flame propagation. The most obvious benefit from the flame instability is the enhanced turbulent burning velocity (Bradley et al. 2013). Furthermore, the flame propagation history has great impact on the engine performance and efficiency, however, combustion at high pressure is poorly understood. Therefore, a study of flame propagation under high pressure and temperature will provide an in-depth understanding of the high pressure combustion and potentially improve the efficiency of strongly charged SI engines.

1.2 Current Research Scope

This study aims to investigate combustion in a strongly charged engine. To achieve this goal, the experimental work has been performed by using a LUPOE2-D engine to determine the flame characteristics, such as, flame speed profile, and abnormal combustion. The following objectives have been completed:

- 'Preparation work': the LUPOE2-D is fitted with optical head and PIV system used to determine the flow field in the engine at the engine speed of 750 and 1500 RPM. Consequently, the result could provide the parameter of turbulence, such as, integral length scale, turbulent RMS velocity, and turbulence intensity profile in the engine for the following experiments.

- 'Metal head work': the LUPOE2-D is fitted with metal head so it can survive under robust operation conditions, such as, knock and high pressure. The experiments will be conducted at the intake pressure of 1.65 bar with temperature of 323 K at engine speed of 750 RPM. By manipulating the spark timing, the peak in-cylinder pressure could reach up to 150 bar. Two bio-derived fuels: n-butanol and 2,5-dimethylfuran (2,5-DMF) are partially replaced the ULG and TRF as potential fossil fuel successors. In the present study, the flame speed which is derived by LUSIEDA, and the anti-knock property of the mixtures have been investigated. In addition, the effects of spark timing on those combustion characteristics in strongly charged engine have been analysed, such as, flame speed, initial flame duration, pressure, knock onset and knock pressure oscillation. Therefore, the present study has provided evidence for bio-fuel which functions as the alternative energy to power the high efficiency IC engine.

- 'Optical head work': the LUPOE2-D is fitted with an optical head so that it can observe the cross-section of the flames directly. In this study, the engine has been treated as a small cylindrical bomb through setting the spark timing that achieves a relatively constant in-cylinder pressure and temperature during the flame radius from 12 to 19 mm. The flame speed has been measured to validate the 'metal head work'. The particular attention has been paid on the flame propagation during the fully developed stage, this includes the flame surface wrinkling at the engine speed of 750 and 1500 RPM with equivalence ratio of 0.8 and 1.0. By introducing the unburned flow velocities for the unburned gas from PIV measurement, turbulent burning velocity and flame surface turbulence have been derived at the fully developed flame

stage. The turbulent burning velocity derived from PIV method has been compared with burning velocity correlations. Therefore, this study provides an insight into the turbulent combustion under high pressure.

The 'metal head work' provides an insight into the anti-knock performance in engine which takes the unburned gas temperature history into consideration. A study of cycle-to-cycle variation is conducted by investigating the duration of three flame propagation stages.

The 'optical head work' is worked by regarding the engine as a small cylindrical bomb, so that high temperature and pressure can be achieved by compression stroke. A steady environment during flame propagation can be achieved by setting an appropriate spark timing. High flame speed can be achieved in low turbulence, so the interaction of flame propagation and flame front turbulence can be observed.

1.3 Thesis Outline

- Chapter 2 introduces the fundamental concepts of combustion, namely, engine cycle, turbulent premixed flame and its structure, particle image velocimetry.

- Chapter 3 describes the experimental installation. Specifically, the detailed specification of the experimental engine will be provided first. Then it is followed by the detailed description of the subsystems, for example, air-fuel systems, control and data acquisition systems. In the end, the particle image velocimetry system will be introduced.

- Chapter 4 provides the methodology for data analysis. For the 'metal head work', the data analysis is based on the pressure trace from combustion. In other words, it is an alternative method to derive the combustion characteristics, such as, auto-ignition onset, flame size, flame speed. As for the 'optical head work', flame measurement and turbulent flow characteristics analysis method will be also provided in this chapter.

- Chapter 5 introduces the results of the 'preparation work', which are turbulent flow root mean square velocity and integral length scale of motoring cycles at engine speed of 750 RPM and 1500 RPM. This chapter also provides motoring cycle turbulent characteristics for the following experiments and data analyses in chapter 7.

- Chapter 6 introduces the results of the 'metal head work', namely, combustion characteristics, cycle-to-cycle variation, and anti-knock performance.

- Chapter 7 provides the results of the 'optical head work'. The first part of this chapter is consist of temperature and pressure history for flame radius of 12 - 19 mm. Analyses of the flame propagation and flame wrinkling in a steady environment are reported in the following part. Then, the interaction of flame propagation and flame front turbulence will be investigated. At last, turbulent burning velocity under different conditions will be investigated, moreover, several correlations will be compared with the burning velocity derived from present study.

- Chapter 8 provides the conclusion of the present study and recommendations for future studies will also be provided.

Chapter 2

Background

2.1 Engine Cycle

2.1.1 Thermodynamic Principle of Otto Cycle

The Otto cycle is a thermodynamic cycle used to describe the functioning of a spark ignition engine. According to Stone (1999), the Otto cycle consists of four processes, see Figure 2.1. Process 1 – 2 is an adiabatic compression of the gas, the piston moves from bottom dead centre (BDC) v_1 to top dead centre (TDC) v_2. Process 2 – 3 heat is added to the constant volume due to combustion. Process 3 - 4 is an adiabatic expansion, also called power stroke. In process 4 – 1, the heat and combustion products are rejected from the system. Therefore, the efficiency of Otto cycle is defined as:

$$\eta_{Otto} = \frac{Q_{23} - Q_{41}}{Q_{23}} \tag{2.1}$$

where Q_{23} and Q_{41} are the energy changed in the system. Considering the temperature change in the process due to heat transfer and the ideal gas law, the Otto cycle efficiency can be re-formulated and depend on the compression ratio r_v (= v_2/v_1):

$$\eta_{Otto} = 1 - r_v^{1-\gamma} \tag{2.2}$$

where γ is the specific heat ratio, typically, 1.4 for air. From the above equation, it can be seen, the Otto cycle efficiency is proportional to the compression ratio r_v.

In the real engine, the overall engine efficiency could not always proportional to the compression ratio. The mechanical efficiency drops by the increasing of compression ratio due to high pressure load (Stone 1999), such as heat loss and

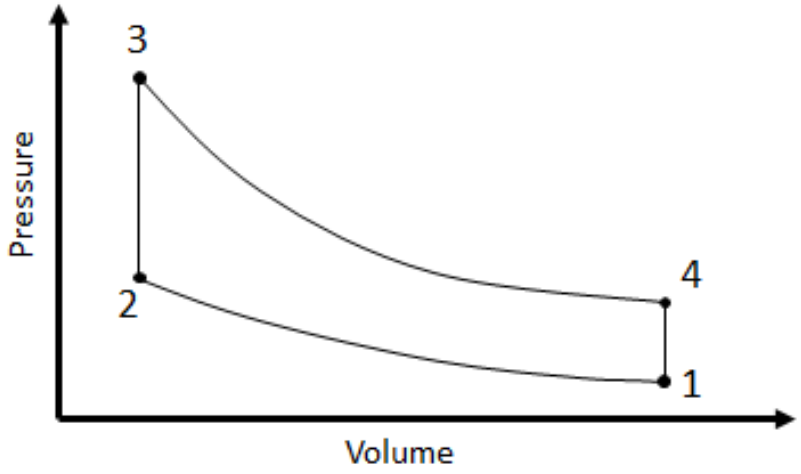

Figure 2.1: Pressure - volume diagram of ideal Otto cycle

pump loss. Evidences (Caris & Nelson 1959) are shown that optimum compression ratios for maximum efficiency and power: 16 and 17. However, those numbers are not applied to all SI engines due to some uncertain factors such as engine speed, engines geometry and different fuels (Stone 1999). Considering the intake temperature and pressure of a strongly charged engine is usually higher than a natural aspirated engine, abnormal combustion is more likely to occur in the engine, Hence, the aforementioned optimum compression ratio is not achievable for current boosted SI engines in the market.

2.1.2 Pressure in Spark Ignition Engine

For a normal combustion cycle: when the piston is about its end of compression stroke, spark is released and create a flame kernel. During the propagation of the flame, heat release causes thermal expansion and creates pressure rise. Figure 2.2 shows crank-resolved pressure in spark ignition engine. According to Stone (1999), the time interval between the spark releases at the point A and the starting point of pressure rise due to combustion at the point B called delay period, it is typically about 0.5 ms. The second stage of combustion starts from the point B and end with the point C, where the point C is located shortly after the peak pressure.

For an abnormal combustion cycle in SI engines, the mixtures are either ignited before the spark released or auto-ignition onset during the flame propagation. The compression ratio and fuel are also other factors hindering the engine to achieve its maximum efficiency and power due to the knocks induced by the high compression ratio. Knock occurs when the pressure and temperature of the unburned mixtures

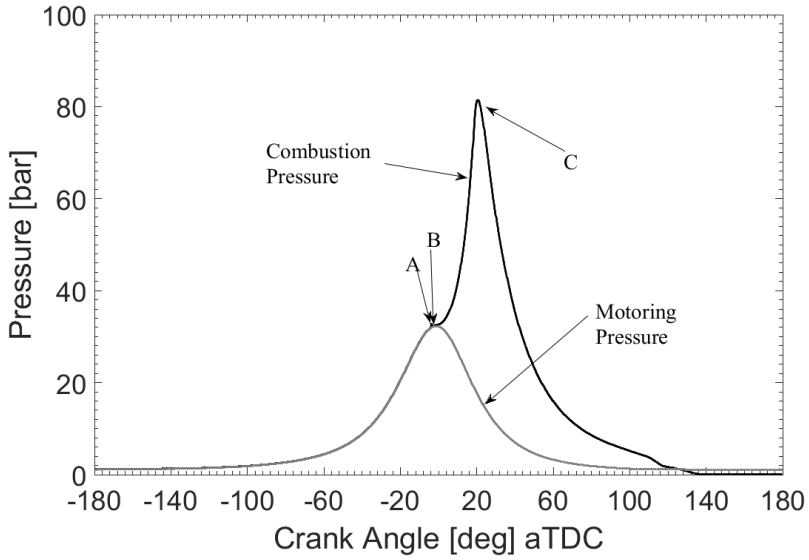

Figure 2.2: Example of crank-resolved pressures in spark ignition engine.

rise and trigger their auto-ignition during combustion. The auto-ignition usually in a point or area in somewhere close to the flame front instead of all along the flame surface due to inhomogeneous of pressure and temperature (Lumley 1999). Consequently, auto-ignition is divided into homogeneous and pinpoint type. Some of the researchers, such as, Pan & Sheppard (1994) reported that the knock is due to single or multiple pinpoints auto-ignition rather than the homogeneous auto-ignition type. The auto-ignition creates a huge heat releases and massive of pressure waves simultaneously in the cylinder. According to Ling et al. (2014), the knocking cycle pressure trace has two main characters could separate a knocking cycle from normal combustion cycles: the pressure oscillations rapidly rising rather than gently reaching to peak; another character is oscillations magnitude usually much higher than the peak oscillations from noise and vibration. Ling (2014) reported that the frequency of the pressure oscillations may be related to engine chamber geometry. The maximum velocity of auto-ignition flame observed in LUPOE2-D is approximately 60 m/s, it suggested that auto-ignition would not result in a detonation.

2.2 Premixed Flames

2.2.1 Premixed Flame Structure

The structure of a non-turbulent laminar flame is divided into three parts: preheat zone, reaction zone and recombination zone. As shown in Figure 2.3, in the preheat zone, there is no significant chemistry happening where the temperature comes from reaction zone. HO_2 radicals are mainly produced in the low temperature regime. Afterwards, HO_2 leads to the formation of H_2O_2 and this product does not dissociate under low temperature preheat zone. Consequently, H_2O_2 is convected into high temperature reaction zone to form OH radicals. Because of the large concentration of OH radicals in the prevailing reaction zone; OH causes fuel decay by attacking the fuel molecule chain. The rest of intermediate fuel molecules are consumed in latter part of reaction zone, the CO takes majority of responsibility for heat release. As a result, the location of peak heat release is somewhere near the maximum temperature. The recombination zone is filled with burned gas and the low concentrations of the radicals, the reactions do not influence the overall flame system (Glassman & Yetter 2008).

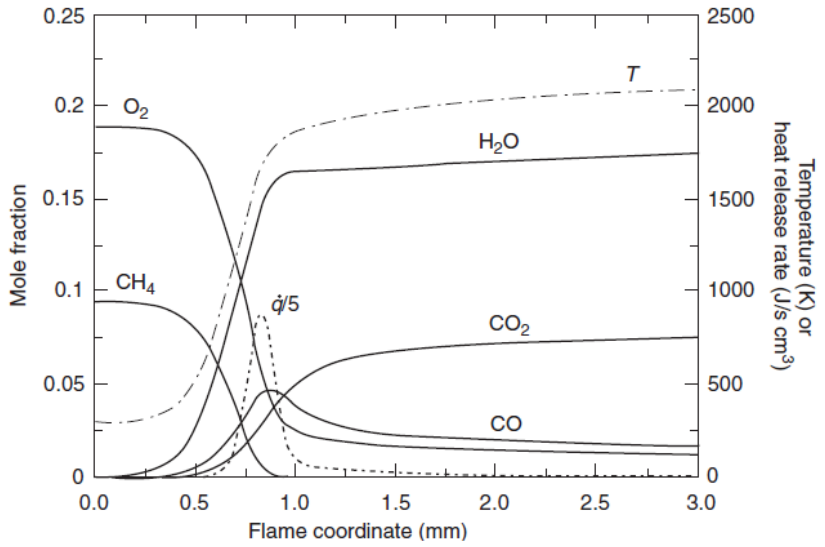

(a) Composition distribution profiles.

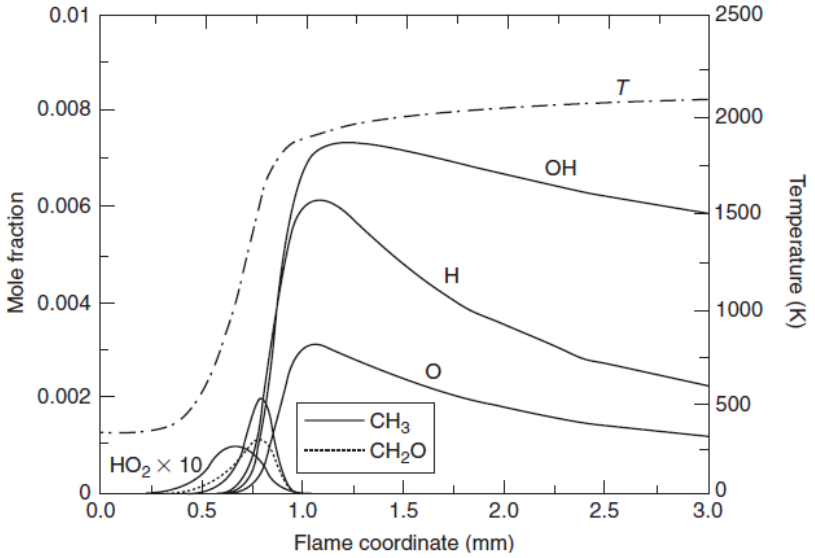

(b) Radical distribution profiles.

Figure 2.3: Composition distribution and Radical distribution profiles premixed Methane-air laminar flame at 1 atm, 293 K (Glassman & Yetter 2008).

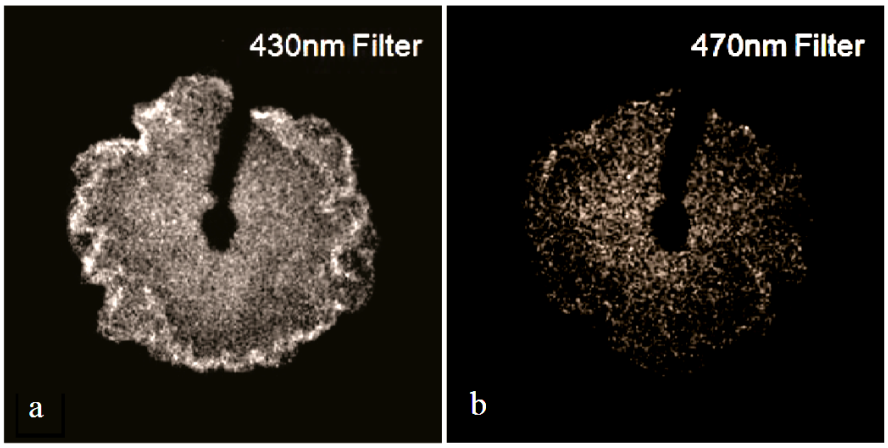

Figure 2.4: Iso-octane flame images filmed by applying different filter (Ling 2014). (a) refers the chemiluminescence from CH species, (b) refers the chemiluminescence C_2 species.

2.2.2 Flame Chemiluminescence

Flame chemiluminescence is an important phenomenon which has been expoited for flame diagnostics. The principle of the diagnostics is that light with different wavelengths are emitted from radicals and excited molecules due to the electron jump from high energy orbit to lower energy orbit (Gaydon 1974). The flame chemiluminescence has been applied to measure the combustion characteristics of hydrocarbon fuels, such as equivalence ratio and heat release by analysing chemiluminescence intensities and intensity ratios from the radicals: OH, CH and C_2 (Nau et al. 2012).

In a typical hydrocarbon flame, the spectrum of electronically excited $OH*$ radical emits from flame has intensity peaks at invisible light 281.13 nm and 302.13 nm. Formation of OH is followed by reaction (Gaydon 1974):

$$CH + O_2 = CO + OH* \tag{2.3}$$

The spectrum of electronically excited $CH*$ radical emits from flame has intensity peaks from invisible light: 314.4nm, 387.14nm to visible light: 431.42 nm, as shown in Figure 2.4(a). The formation of $CH*$ is strongly dependent on C_2 (Gaydon 1974):

$$C_2 + OH = CO + CH* \tag{2.4}$$

The spectrum of C_2 emitted from flame has intensity peaks from invisible light: 385.22nm to visible light: 410.23nm, 473.71nm, 516.52nm, etc. Figure 2.4(b)

shows the 470 nm light emits from combustion. The formation of electronically excited C_2* is followed by reactions (Gaydon 1974):

$$C + CH = H + C_2* \tag{2.5}$$

$$CH_2 + C = H_2 + C_2* \tag{2.6}$$

However, in auto-ignition and rich mixture flames, the CH species occurs without C_2. The spectrum of entire flame is also affected by many factors, such as temperature, pressure, flame shape (Gaydon 1974).

Laser-induced fluorescence (LIF) has been recently developed for flame diagnostic by imaging the OH fluorescence, such as, Kortschik et al. (2004) and Buschmann et al. (1996). The species OH and HCO are excited by a laser and emit light which wavelength longer than the laser. As a result, the distribution of OH radicals are used to locate the flame front and reaction zone. Applying simultaneous particle image velocimetry (PIV) and OH LIF measurement could enhance the understanding of the interaction between flame and turbulence and a study can be found in Boxx et al. (2015).

2.2.3 Laminar Flame Burning Velocity

The laminar flame speed is an important property of premixed combustion. In order to predict turbulent flame burning velocity, the laminar flame burning velocity is a key parameter for modelling turbulent combustion.

The thermal theories of predicting laminar burning velocity were postulated by Mallard & Le Chatelier (1883). In these theories, the flame is divided into preheat zone and reaction zone, they assumed that the reaction zone begins at a point where the temperature reaches a certain value needed for ignition but the ignition temperature is unknown in their assumption. Later, Russian investigators Zeldovich, Semenov and Frank-Kamenetskii (ZSFK) postulated an extension of Mallard-Le Chatelier approach. In ZSFK approach the notion of ignition temperature is eliminated by matching the temperature profile in the preheat and reaction zones. Furthermore, energy transported by diffusion of species is introduced. According to ZSFK, the u_l is (Glassman & Yetter 2008):

$$u_l = \left[2 \left(\frac{\lambda}{\rho C_p} \right) \frac{I}{T_f - T_0} \right]^{0.5} \tag{2.7}$$

where λ is thermal conductivity, T_f and T_0 refer the flame temperature and ini-

tial temperature. I is a function of integration of reaction rate with respect to temperature:

$$I = \frac{1}{a_0} \int_{T_i}^{T_f} \dot{\omega} dT \tag{2.8}$$

where a_0 is the mass of reactant in a unit volume, T_i is ignition temperature. I is also can be expressed as:

$$I = \frac{Z'}{a_0} \frac{RT_f^2}{E} e^{-E/RT_f} \tag{2.9}$$

where Z' is pre-exponential term in the Arrhenius expression, E is activation energy for the reaction, R is the universal gas constant. Therefore, the ZFKS approach is able to show varieties of factors affecting the flame speed such as pressure, temperature, ignition energy, etc.

The laminar burning velocity is not only predicted mathematically but also from empirical expression based on experiments. Metghalchi & Keck (1982) performed a massive of measurements of laminar burning velocity in constant volume bomb under wide ranges of pressure 0.4 - 50 atm, temperature 298 - 700 K, equivalence ratio 0.8 - 1.5 and diluent mass fractions 0 - 0.2. The developed function follows:

$$u_l = u_{l,0} \left(\frac{T_u}{298} \right)^{\alpha} P^{\beta} (1 - 2.1f) \tag{2.10}$$

where T_u is unburned gas temperature, P is unburned mixture pressure and f is diluent mass fraction. $u_{l,0}$, α, β follow equation:

$$u_{l,0} = B_m + B_2(\phi - \phi_m)^2 \tag{2.11}$$

$$\alpha = 2.18 - 0.8(\phi - 1) \tag{2.12}$$

$$\beta = -0.16 + 0.22(\phi - 1) \tag{2.13}$$

where ϕ is equivalence ratio, and for iso-octane air mixture, $\phi_m = 1.13$, $B_m = 26.32$, B = -78.34.

Bradley et al. (1998) took the stretch rate into consideration and predicted the unstretched laminar burning velocity based on experiments with conditions of: pressure 1 - 10 bar, temperature 358 - 450 K, equivalence ratio 0.8 and 1.0 for iso-octane:

$$u_l = 0.48 \left(\frac{T_u}{T_0} \right)^{1.01} P^{-0.282} \tag{2.14}$$

where u_l is for $\phi = 1.0$, T_0 is 358 K.

$$u_l = 0.4 \left(\frac{T_u}{T_0} \right)^{1.07} P^{-0.348} \tag{2.15}$$

where u_l is for $\phi = 0.8$.

2.2.4 Methods of Observing the Flame Front

It is vital to understand flame front structure thoroughly, so that the flame speed can be determined. As discussed earlier in Chapter 2.2.1 and 2.2.2, the premixed flame reaction zone is divided into two parts: the earlier part and the latter part. The earlier part is approximately coincident with the luminous zone (Fristrom & Westenberg 1961) and the secondary luminous zone located at latter zone by oxidation of CO (Fristrom & Westenberg n.d.).

There are several methods for observing the flame front. One of them is the direct photography that has been frequently used in observing flame front, owing to a high intensity of the light emission from hydrocarbon mixtures flames, see Figure 2.5 (a). However, in some cases, the luminous zone may not represent the flame front accurately. It can be found in a burner flame, the distance between preheat front and luminous zone front varies from 1 mm at 1 atm to 10 mm at 0.05 atm (Rallis & Garforth 1980).

Another approach of observing the flame front is schlieren photography methods see Figure 2.5 (b). The principle of this approach is: light passes through the objective such as flame causes irregular deflection of the light. As a result, the simple schlieren system is consisted by a point light source, an objective being studied on a screen. The method gives a better location of flame front. On the other hand, this method requires optical access through engine head and piston, mechanical vibration would bring errors to the vibrations. Furthermore, the schlieren method is too sensitive for the density changes, the shade of the schlieren image may not only create by combustion, e.g. a compressed air flow.

Owing to the development of the laser technology, laser tomographic method could be applied to visualise the flame front. Boyer (1980) proposed a method for visualising a sliced cross-section flame using laser tomographic method. The principle of laser tomographic approach is achieved by adding oil aerosol to the unburned mixture, the sheet laser is scattered by the oil particles in the unburned region. Therefore, there is high contrast between unburned region and burned region. The vaporization time and size of the particle are critical for defining the flame front. Figure 2.5 (c) shows the image filmed from laser tomographic

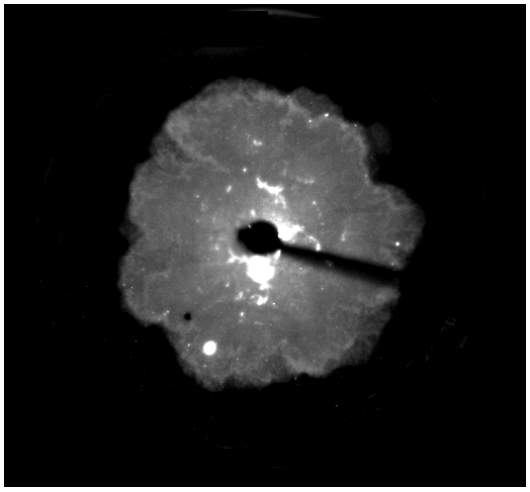

(a) Iso-octane flame images filmed from natural light.

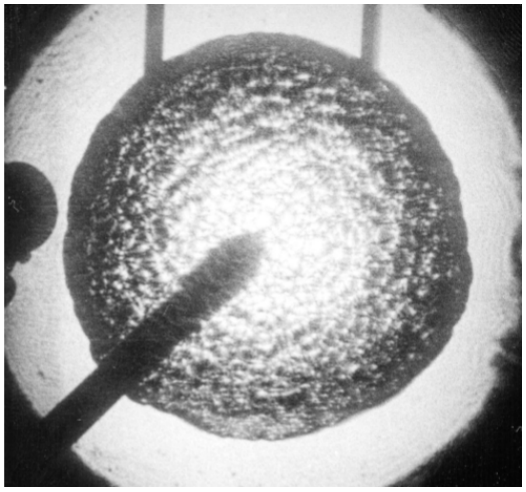

(b) Iso-octane flame image filmed from schlieren method (Gillespie et al. 2000).

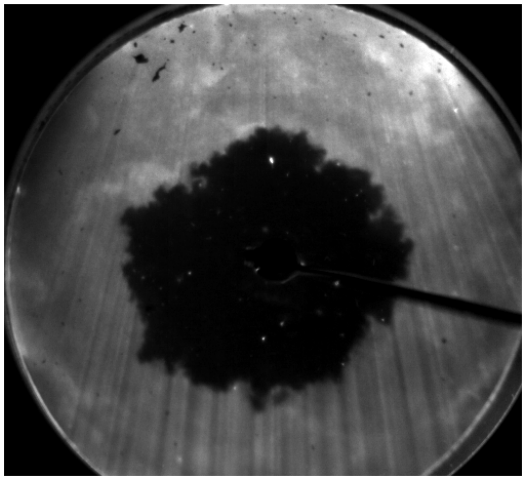

(c) Iso-octane flame image filmed from laser tomographic method.

Figure 2.5: Different methods of flame observation.

method. By tracking the particles used for the laser tomographic approach, the flow field around the flame can be observed. Therefore, this method was employed for measuring flame speed and burning velocity in this study.

2.3 Turbulent Premixed Flame

2.3.1 Turbulence

In turbulent flow, the velocities for the volume elements show random. Figure 2.6 shows the velocity with respect to time of the volume element in turbulent flow. The instantaneous velocity of volume element $u(t_0)$ is divided into two terms known as Reynolds decomposition:

$$u(t_0) = \bar{u} + u'(t_0) \tag{2.16}$$

The mean velocity $\bar{u}$ is defined as the averaged flow velocity for a large time interval Δt. The mean velocity follows the equation:

$$\bar{u} = \frac{1}{\Delta t}\int_t^{t+\Delta t} u dt \tag{2.17}$$

The turbulence intensity u_{rms} or u' is also called root-mean-square (RMS) velocity and defined as:

$$u_{rms} = \left[\frac{1}{\Delta t}\int_t^{t+\Delta t} (u-\bar{u})^2 dt\right]^{1/2} \tag{2.18}$$

For non-isotropic condition, the turbulent kinetic energy k is defined as:

$$k = \frac{1}{2}(u'^2_x + u'^2_y + u'^2_z) \tag{2.19}$$

As defined by Kolmogorov hypothesis, the flux of turbulent energy transfers from large scale eddies to create smaller eddies. Therefore, the largest eddies contain most of the kinetic energy. The kinetic energy from the large scale is conserved and transported to smaller scales, the transfer of energy is called energy cascade (Lipatnikov 2012). For the very smallest eddies, when time required for energy transfer is longer than the dissipative time, the kinetic energy could not generate even smaller eddies, due to the kinetic energy dissipate viscous heating. The size of the smallest eddies in turbulence is known as the Kolmogorov length scale. Since a large eddy could generate a range of smaller size eddies, and the kinetic energy is a function of eddy sizes. Therefore, the energy could be analysed using Fourier transform. The Fourier transform decomposes a function of kinetic energy into the wave number κ (inverse of eddy size) that make it up. Therefore the outcome of Fourier transform represents how much energy contained in a unit of wave number. The relation between turbulent energy k contained and energy

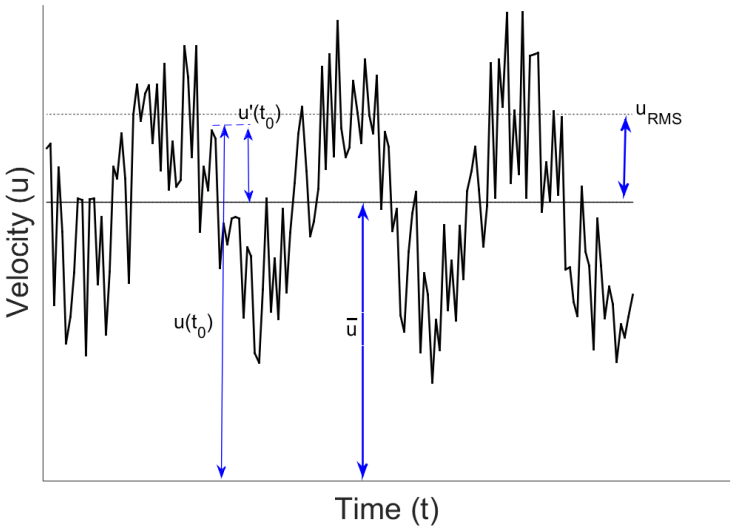

Figure 2.6: Reynolds decomposition for time-dependent flow.

spectrum $S(\kappa)$ within a wavenumber range κ_A to κ_B as follows:

$$k = \int_{\kappa_A}^{\kappa_B} S(\kappa) d\kappa \tag{2.20}$$

Scott (1992) provided a dimensionless power spectrum as a function of Kolmogorov length scales. A homogeneous isotropic turbulence energy spectrum follows:

$$S(\kappa_\eta) = \frac{0.01668 Re_\lambda^{2.5} + 3.74 Re_\lambda^{0.9} - 70 Re_\lambda^{-0.1}}{1 + (0.127 Re_\lambda^{1.5} \kappa_\eta)^{5/3} + (1.15 Re_\lambda^{0.622} \kappa_\eta)^4 + (1.27 Re_\lambda^{0.357} \kappa_\eta)^7} \tag{2.21}$$

Therefore, the turbulent energy spectrum at $Re_\lambda = 100$ and 200 is shown in Figure 2.7. In the inertial sub-range, where it is shown in Figure 2.7 spectrum with a slope of -5/3. The turbulence kinetic energy transfers from the large scales to the small scales without viscous effects in this stage. For the slope -7, the kinetic energy is transferred to heat due to viscous effects.

For the turbulence energy spectrum, Abdel-Gayed et al. (1987) proposed an effective turbulent RMS velocity u'_k. For turbulent combustion, the large eddies have little effect on the wrinkling of the initial flame kernel, only small eddies could wrinkle the flame front. Therefore the small size flame only experiences partial spectrum of turbulence which the energy is equivalent to the kinetic energy of u'_k. With the flame expansion, the flame is large enough so that experiences the whole spectrum of turbulence.

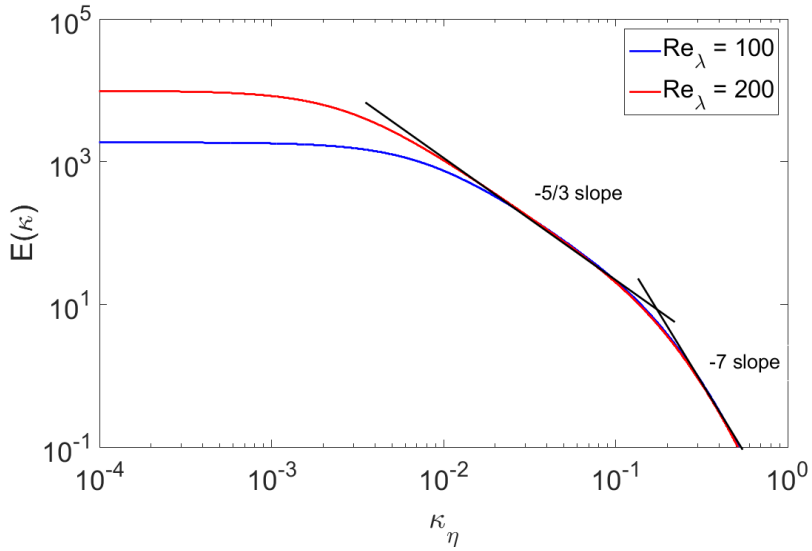

Figure 2.7: Energy spectrum as a function of wavenumber at $Re_\lambda = 100$ and 200.

The length scales are used to characterize the size of turbulence in turbulent flow. There are three scales are commonly used, which are characteristic width of integral scale L for the energy-containing eddies; Taylor microscale L_λ for the inertial subrange eddies; Kolmogorov microscale η for the dissipation range eddies (Lipatnikov 2012). The integral scale Reynolds number Re is followed by equation:

$$Re = \frac{u'L}{\nu} \tag{2.22}$$

where u' is turbulent RMS velocity, L is integral length scale of turbulent flow and ν is kinematic viscosity of the fluid. The integral length scale is defined as the mean size for the energy-containing eddies. It can be measured as integral of correlation coefficient of the fluctuation velocities at two points in the flow as a function of distance r between these two points (Glassman & Yetter 2008):

$$L = \int_0^\infty R(r)dr \tag{2.23}$$

where $R(r)$ is correlation coefficient of fluctuating velocity between two points:

$$R(r) = \frac{\overline{u'(r_0)u'(r_0+r)}}{u'_{RMS}(r_0)u'_{RMS}(r_0+r)} \tag{2.24}$$

where u' is fluctuation component velocity, r is the distance between two points.

Therefore, the corresponding integral time scale τ_t is simply calculated as:

$$\tau_t = \frac{L}{u'_{RMS}} \tag{2.25}$$

Kolmogorov microscale η, is the smallest length scale used for describing turbulent flow. According to Tennekes et al. (1972), the Kolmogorov microscale η is so small that viscosity has significant effects on it and the motion is dependent on the energy supplied by large scale motion. The rate of energy supplied by mean flow is equal to the viscous dissipation rate of the turbulence energy. Kolmogorov microscale η can be written as:

$$\eta = \left(\frac{\nu^3}{\epsilon}\right)^{1/4} \tag{2.26}$$

where ϵ is mean dissipation rate, ν is kinematic viscosity. The time scale of Kolmogorov microscale is written as:

$$\tau_\eta = \left(\frac{\nu}{\epsilon}\right)^{1/2} \tag{2.27}$$

Since the kinematic viscosity ν and dissipation rate ϵ are proportional to u'^3/L, the relationship between η and L follows:

$$\frac{L}{\eta} = Re^{3/4} \tag{2.28}$$

Also the Taylor microscale is related to integral scale L:

$$\frac{L}{L_\lambda} = Re^{1/2} \tag{2.29}$$

2.3.2 Flow in Spark Ignition Engine

In order to study combustion in an engine, an understanding of turbulence in engine cylinder is necessary. The turbulent flow inside cylinder affects the flame propagation and heat release, therefore a distribution of the individual cylinder pressure histories around the phase averaged mean appears. The distributed pressure histories are called cycle to cycle variation. It is mostly responsible for the scattered pressure curves in the same condition from the Large-Eddy Simulation (LES) (Vermorel et al. 2009). Figure 2.8 shows an example of turbulence leading to cyclic variations of initial flame. According to Kyriakides & Glover (1989),

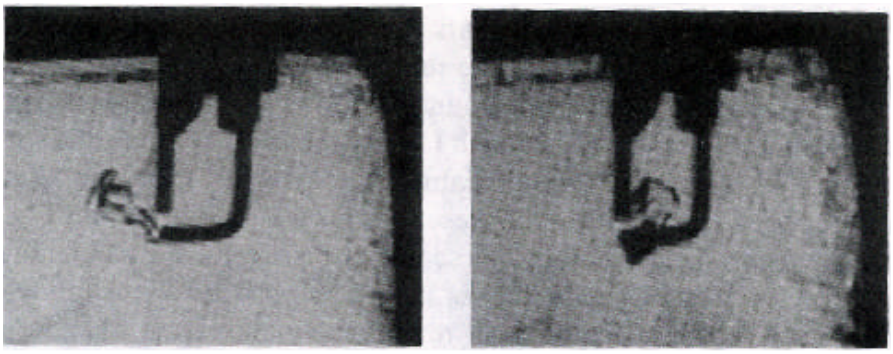

Figure 2.8: Effect of turbulence on the initial flame kernel (Stone 1999).

there is linear relationship that the ignition delay decreases with the increasing of turbulence intensity. The instantaneous turbulent fluctuating velocity in cylinder is a function of crank angle θ in particular cycle i:

$$u'(\theta, i) = u(\theta, i) - \bar{u}(\theta, i) \tag{2.30}$$

In a four stroke spark ignition engine, the intake jet-like flow creates a turbulence flow. Since the flow field is periodic, the ensemble averaging method can be performed at the same point in the engine cycle for many engine revolutions. Figure 2.9 shows the history of turbulence intensity within one of the engine cycles.

The turbulent flow in a engine consists of two forms of rotating flow, namely, swirl and tumble, see Figure 2.10. According to Inoue et al. (1980), the swirl flow could shorten the combustion duration in a constant volume combustion chamber. Later on, Witze & Vilchis (1981) performed an investigation on swirl effect under different equivalence ratios, and the result shows that the combustion duration of lean mixture is strongly reduced by increasing the swirl speed. However, the swirl has little effect on the combustion duration of rich mixtures. Hadded & Denbratt (1991) suggested that the tumble motion could significantly reduce the combustion duration which includes the initial delay time (less than 10% mass burned) and the main combustion durations (10 - 90% mass burned).

2.3.3 Premixed Turbulent Flame

According to Abdel-Gayed et al. (1989), there are four regimes to describe flame characteristics under turbulence. The regimes can be classified as: wrinkled flame, wrinkled flame with pockets, thickened wrinkled flame, and thick flame regime, see Figure 2.11. A dimensionless parameter called Damköhler number Da is used for determining whether diffusion rates or reaction rates are more 'effective' on

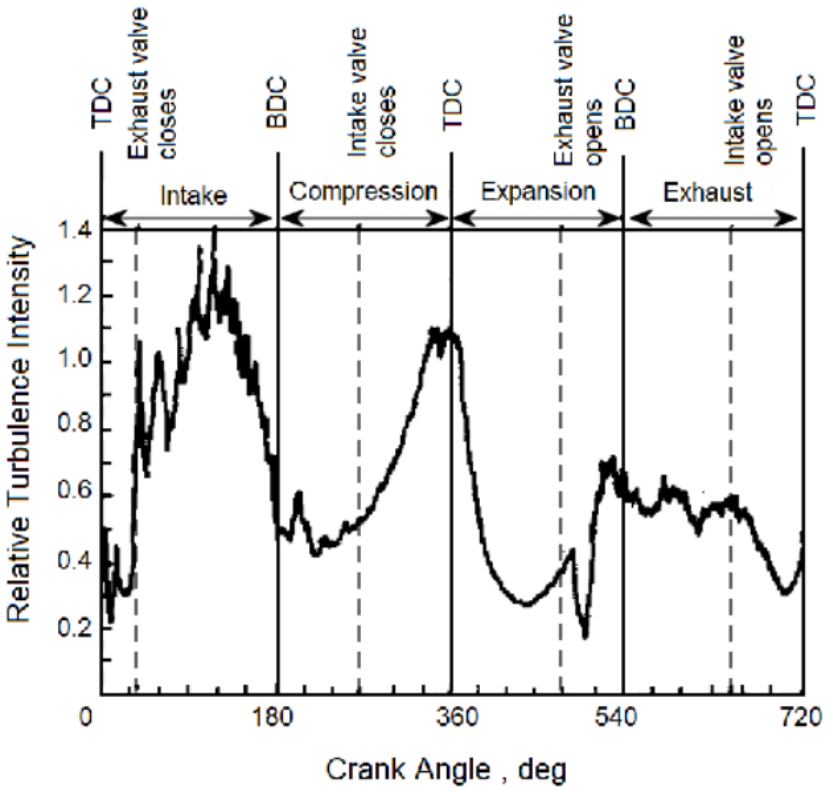

Figure 2.9: Relative turbulence intensity, $u_{RMS}/\bar{u}$ versus crank angle, reproduced from Tabaczynski (1979).

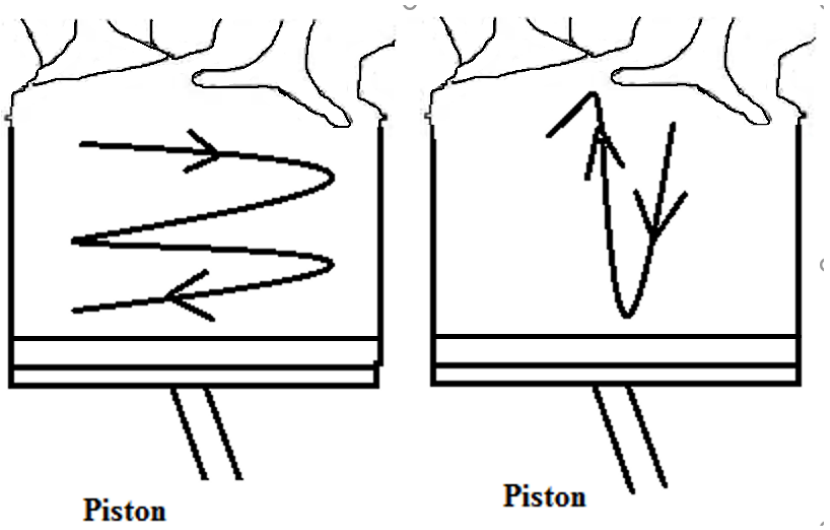

Figure 2.10: Rotating flow in engine.

the steady state chemical distribution. It describes the ratio of mixing time and characteristic chemical time (Veynante & Vervisch 2002):

$$Da = \frac{\tau_t}{\tau_c} = \frac{L u_l}{\delta_l u_{RMS}} \tag{2.31}$$

where the τ_c is characteristic time for chemical reaction, the τ_t characteristic turbulent time or transport time. In terms of the Karlovitz number Ka, it describes ratio of chemical time scale τ_c over smallest turbulent time scale τ_η:

$$Ka = \frac{\tau_c}{\tau_\eta} = \frac{\delta_l u_\eta}{u_l \eta} \tag{2.32}$$

where δ_l is laminar flame thickness, u_η is velocity of Kolmogorov scale and the follow:

$$\delta_l = \tau_c u_l \tag{2.33}$$

$$u_\eta = (\nu\epsilon)^{1/4} \tag{2.34}$$

Since the integral length scale is related to dissipation rate ϵ:

$$L = \frac{u_{RMS}^3}{\epsilon} \tag{2.35}$$

Ka can be rearranges as:

$$Ka = \left(\frac{u_{RMS}}{u_l}\right)^{3/2} \left(\frac{L}{\delta_l}\right)^{-1/2} \tag{2.36}$$

For Schmidt number 1, the mass diffusivity equals kinematic viscosity, Ka can be considered as a function of the flame thickness over Kolmogorov scale,

$$Ka = \frac{{\delta_l}^2}{\eta^2} = \frac{{u_\eta}^2}{u_l^2} \tag{2.37}$$

According to Peters (1999), for Ka <1 which both turbulence transport time τ_t and the micro-eddy time scale are larger than chemical reaction time τ_c. The reaction will reach an equilibrium before the turbulence mixing. When $u_{RMS} < u_l$, the flame reaction zone structure is not affected by the turbulence motion. In another case, when $u_{RMS} > u_l$,the large scale eddies dominate the flamelet speed so that the flamelet formed into pocket shape in the flame, see Figure 2.12(a). However, the flame thickness is larger than the smallest eddies. Therefore, the flame front is still intact.

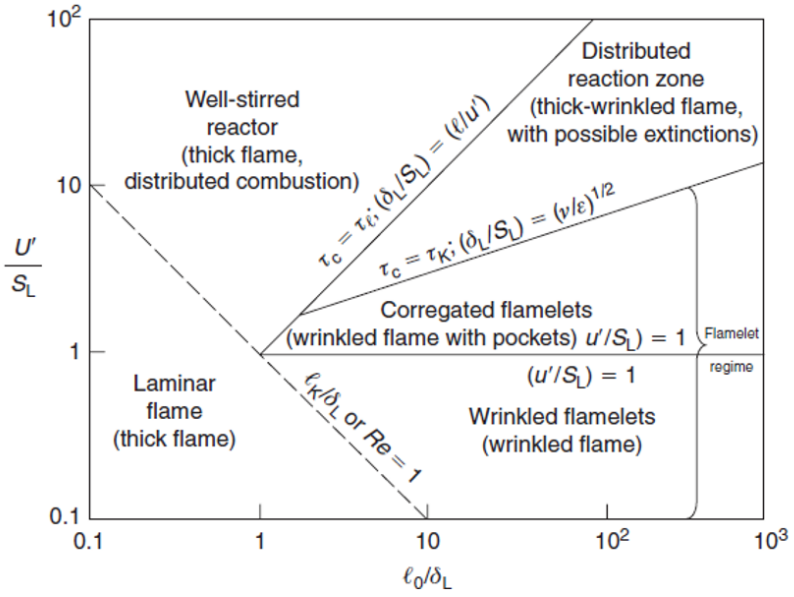

Figure 2.11: Turbulent combustion regimes (Abdel-Gayed et al. 1989).

For $1< Ka \leqslant 100$, the small scale eddy is small enough to affect and thicken the flame preheat zone. However, the mixing rate of small scale eddy is not sufficient to penetrate the reaction zone. As a result, the turbulent flow are not able to affect the reaction zone but preheat zone, see Figure 2.12(b).

For $Ka >100$, as shown in 2.12(c), the size of the small eddy is smaller than the thickness of the reaction zone and the eddies bring the burned gas into the reaction zone due to that the mixing rate of the small eddy is higher than the reaction rate. Therefore the turbulence mixing rates τ_t and τ_η dominate combustion.

2.3.4 Turbulent Premixed Flame Burning Velocity

As discussed earlier about the turbulent flame regimes in Chapter 2.3.3, the flame front is influenced by the turbulence. Considering the wrinkled turbulent flame shown in Figure 2.13, the small element of flame front dA is still acting as unwrinkled laminar flame. Therefore, the burning rate can be written as $\rho_u u_l dA$. For the wrinkled flame front with area A replaced by a planar mean flame front with area A_t. Since the planar mean flame front and the wrinkled flame front are describing the same mass burned in a unit time, burning rate $\rho_u u_l A$ is equivalent to $\rho_u u_t A_t$. As a result, the turbulent burning velocity will be (Lipatnikov 2012):

$$u_t = u_l \frac{A}{A_t} > u_l \tag{2.38}$$

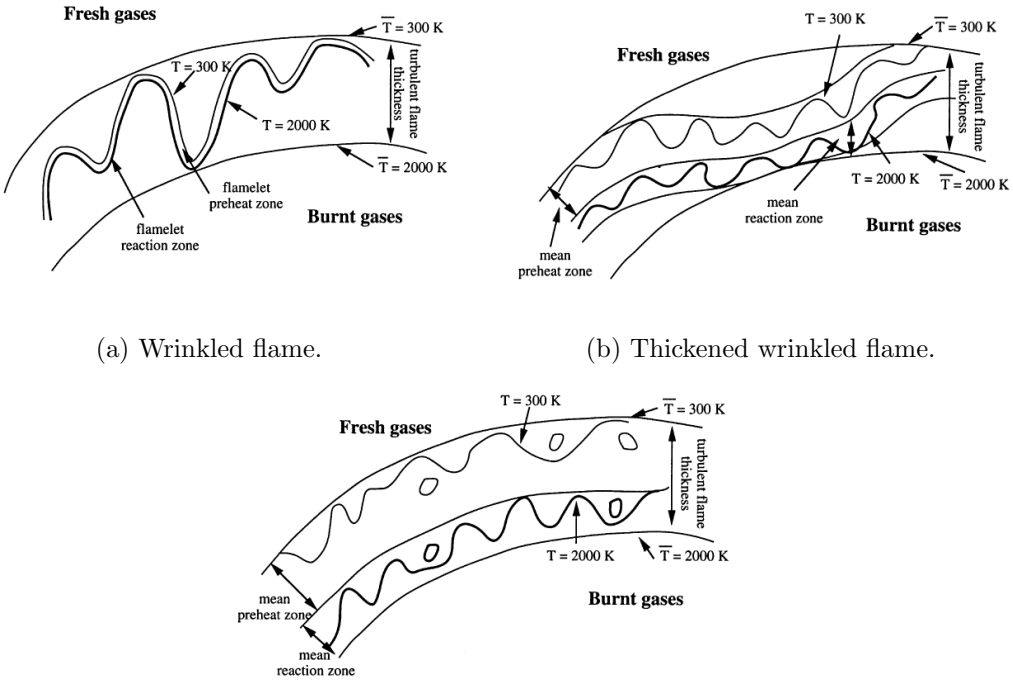

(a) Wrinkled flame.

(b) Thickened wrinkled flame.

(c) Thick flame, distributed combustion.

Figure 2.12: Turbulent premixed flame structures under different flame regimes (Veynante & Vervisch 2002)

Damköhler (1947) assumed the flame front area is proportional to the turbulent flow velocity and proposed the relationship between laminar and turbulent flame speed:

$$u_t/u_l = A/A_t = 1 + u'/u_l \tag{2.39}$$

Zimont (1979) provided turbulent flame burning velocity correlation:

$$u_t = const.u'Da^{0.25} \tag{2.40}$$

In practical turbulent premixed flame, the relationship between the u_l and u_t may be affected by not only the turbulent flow (Abdel-Gayed et al. 1985, Kobayashi et al. 1998). Turbulent burning velocity may increase due to hydrodynamic instability at high pressure. The increase of pressure has a positive effect on ratio of u_t on u_l due to the decrease of Lewis number, see Figure 2.14. According to Kobayashi et al. (2005), a measurement of turbulent flame speed for methane-air mixture at equivalence ratio 0.9, the correlation provides below:

$$u_t/u_L = 5.04[(P/P_0)(u'/S_L)]^{0.38} \tag{2.41}$$

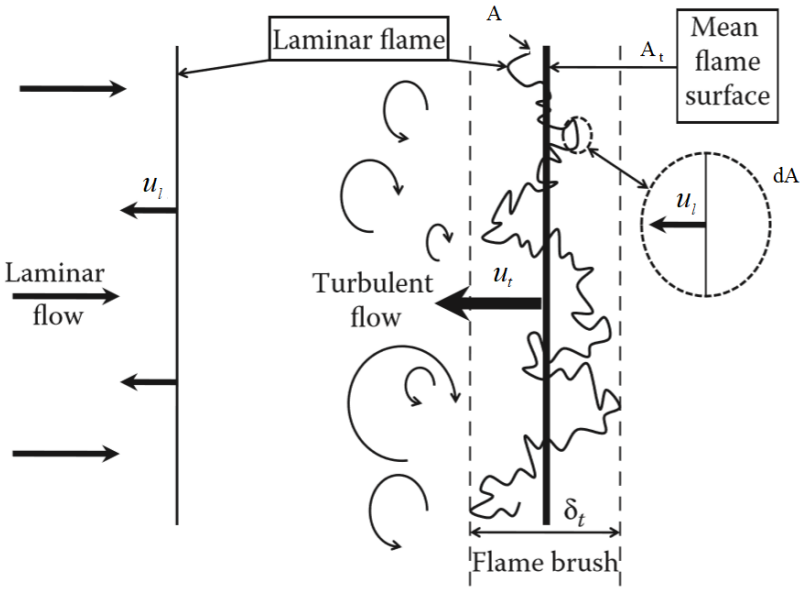

Figure 2.13: Laminar premixed flame (left) and turbulent premixed flame (right) flame front (Lipatnikov 2012).

The experiment also investigated the temperature effects on turbulent flame speed at conditions of 300 K and 573 K. The result shows pressure is the predominant parameter on the ratio of u_t on u_l.

Instead of providing the effects of pressure and temperature on the turbulent burning velocity, the thermal-diffusive instability and the stretch factor are introduced as dimensionless parameters for a more generalized expression. Figure 2.15 shows u_t/u_l as a function of u'/u_l at different stretch rate under Reynolds number effects.

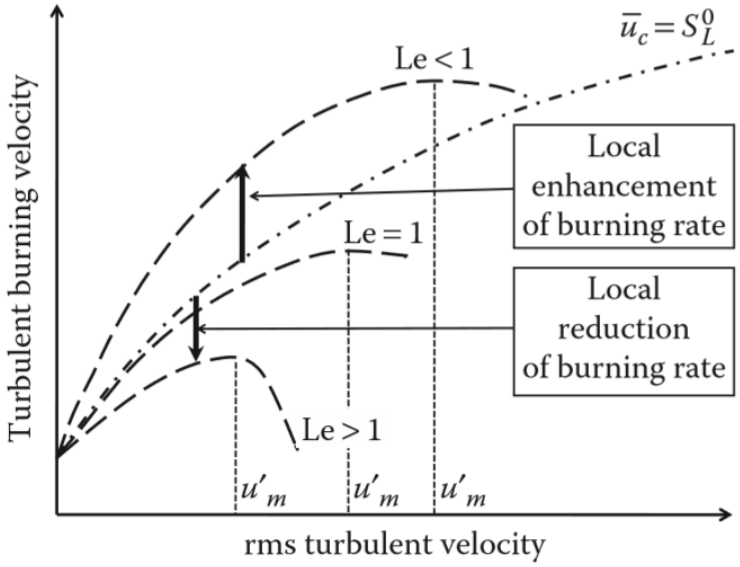

Figure 2.14: The effect of Lewis Number on turbulent burning velocity over turbulent RMS velocity (Lipatnikov 2012).

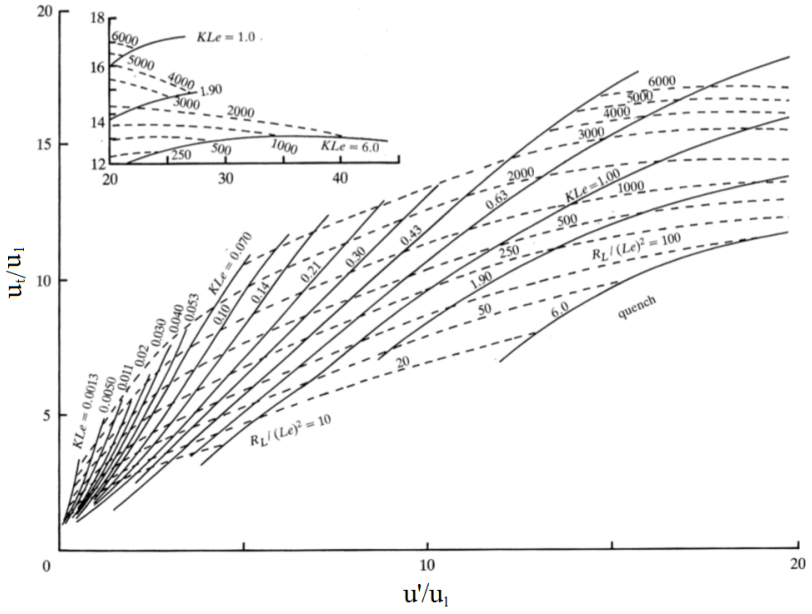

Figure 2.15: u_t/u_l as a function of u'/u_l at different stretch rate under Reynolds number effects (Bradley et al. 1992).

2.3.5 Turbulent Flame Development in Premixed Spark Ignition Engine

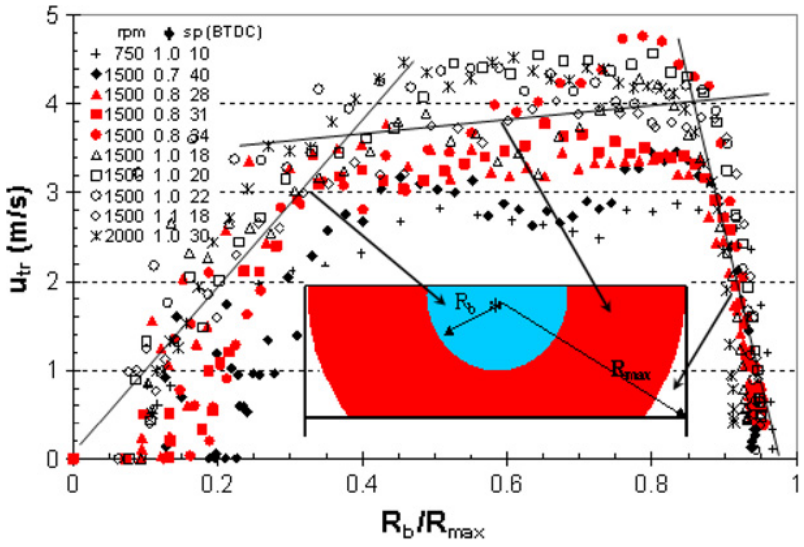

Figure 2.16: Flame profile under different engine operating conditions (Liu et al. 2013).

According to Liu et al. (2013), who performed a series of experiments on research engine LUPOE1-D (leeds university potted optical engine MK-1 disc chamber). The turbulent flame development could be classified in three stages: the initial acceleration stage, fully developed stage and finial deceleration stage, see Figure 2.16. The first stage corresponds the flame radius less than 30% of the cylinder radius which the mass burned fraction is only less than 3%. Later, during the fully developed stage, the flame grows from 30% to 85 % of the cylinder radius, the flame propagates with a nearly constant speed until two third of mixture burned. Finally, the deceleration stage involves flame-wall interactions. For the initial acceleration stage, the flame is so small the surface is not able to interact with turbulent flow, it is roughly in spherical shape and the growth is dominated by diffusion. For the fully developed stage, the constant flame speed is due to acceleration is counter-balanced deceleration caused by the flame approaching the walls (Liu et al. 2013). Another possible reason may be due to the turbulent energy spectrum. With the flame expansion, the eddies start to wrinkle the flame front and increase the surface area. As mentioned the turbulent energy spectrum corresponds eddies size earlier in Chapter 2.3.1, once the flame is under whole spectrum of the turbulent energy, the effective RMS velocity towards a constant. Therefore, the fully developed turbulent flame speed become a constant.

During the end stage of flame propagating in the cylinder, flame-wall interactions (FWI) become inevitable. The flame temperature of hydrocarbon fuel usually over 2000 K and the temperature of cylinder wall is far below this temper-

ature. The FWI result in the reduction of flame speed and incomplete combustion. The incomplete combustion will directly affect the environment because of the high level of HC and CO generated. The quench is divided into head-on quench (HOQ) and side wall quench (SWQ). HOQ refers to the flame propagating towards the wall that velocity is perpendicular to the wall. SWQ happens while the flame is propagating along the wall.

In a premixed spark ignition engine, because the flame propagates in a spherical shape, as a result, HQQ is always followed by SWQ (Dreizler & Böhm 2015). As the piston travels downwards, there is an increasing area of cold wall surface exposed to the flame resulting more heat loss through the FWI. For the laminar flame quenching distance, the pressure is inversely proportional to both SWQ and HOQ distances (Bellenoue et al. 2003). The quenching distance under turbulence increases with increasing of turbulence intensity (Ballal & Lefebvre 1975).

2.4 Lean Combustion

Backing to the compression ratio mentioned, the thermal efficiency of premixed is proportional to the compression ratio. However, there are barriers to increasing the compression ratio, for instance, knock becomes the direct result of high compression ratio. On the other hand, the compression ratio for non-knock regime extends with reducing equivalence ratio, see Figure 2.17. Modern spark ignition engines have a compression ratio around 10 and the optimum compression ratio for 500 cm^3 chamber is around 15 (Stone 1999). Therefore, the improvement of engine efficiency from increase compression ratio can be achieved by running lean combustion. According to Figure 2.18, the fuel-conversion efficiency rates to equivalence ratio under different compression ratios, there are great improvements of efficiency up to compression ratio of 16. The main benefit from lean combustion is low NO_x and CO emissions due to combustion in low temperature (Heywood et al. 1988). On one hand, the compression ratio is increased for climbing thermal efficiency. On the other hand, Schwarz (1979) reported that the lean condition $\lambda = 1.4$ under sufficient spark energy would bring down 10% of specific fuel consumption comparing with stoichiometric condition.

There is also an argument about better options between exhaust gas recirculation (EGR) and lean combustion. According to Lumsden et al. (1997), air as a diluant compared with EGR has a lower specific fuel consumption in varieties of operating conditions. The benefit may come from higher thermal efficiency by reducing the combustion duration for air dilution. However, Ayala and Heywood reported that the lean mixtures have large combustion durations variability both in initial stage (0-10% mass burned) and fully developed stage (10-90% mass burned) comparing with the stoichiometric condition. When the mixture strength approaches the lean limit, there is a significantly deterioration in drivability and engine efficiency (Ayala & Heywood 2007).

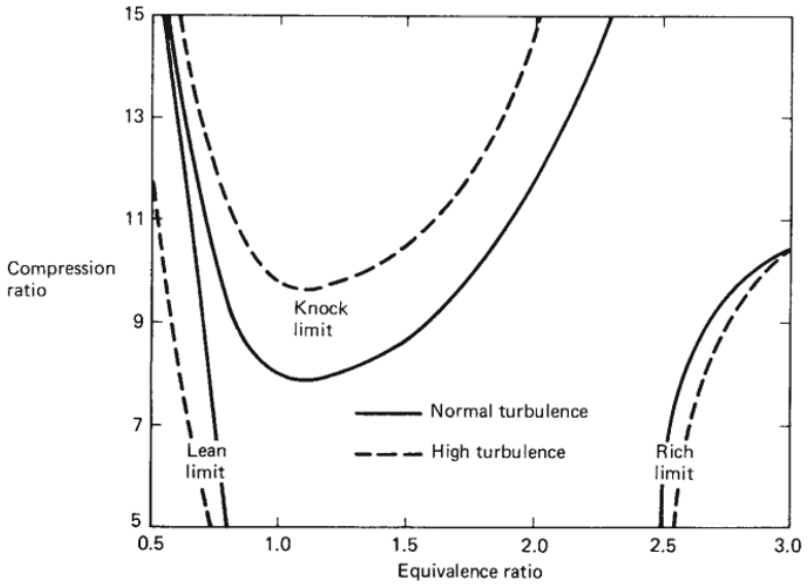

Figure 2.17: Spark ignition engine operating regime based on compression ratio and equivalence ratio (Stone 1999).

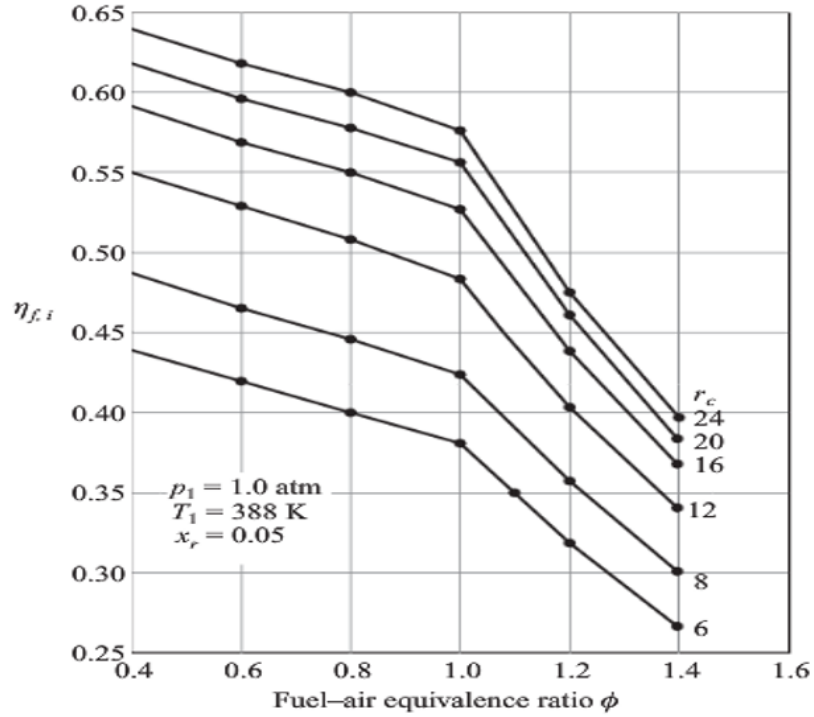

Figure 2.18: Effect of spark ignition engine efficiency on equivalence ratio under different compression ratios (Heywood et al. 1988).

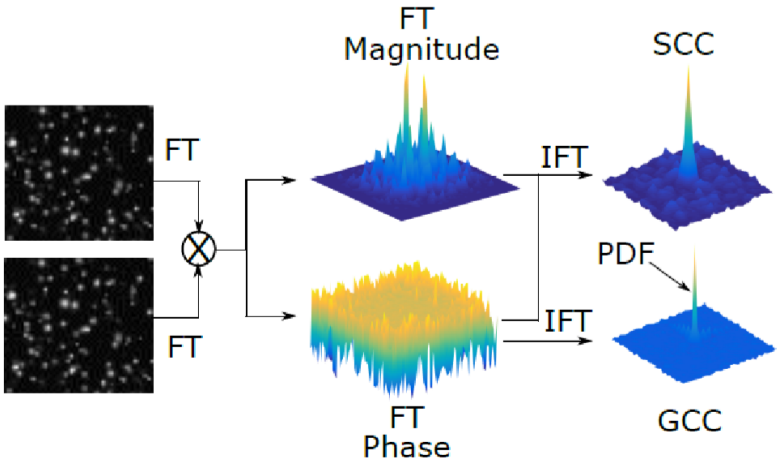

Figure 2.19: The determination of the small area of image displacement in a time interal Δt (Bhattacharya et al. 2018).

2.5 Particle Image Velocimetry

In order to study or diagnostic a turbulent flow, the visualization of the flow is essential. The flow visualization can be achieved by marking a small region of fluid and observing the locations of the markers at two or more times. Therefore, the velocity of the small regions of fluid can be observed (Adrian 1991). For the Particle Image Velocimetry (PIV) method, the concentration of the markers is high. Instead of tracking a individual marker, location of a small area of image is tracked.

The determination of the small area of image displacement is shown in Figure 2.19. In the particle PIV analysis, the small area of image is called interrogation window. For the optimal size of the interrogation windows, it is suggested greater than 4 times of the flow in-plane motion. In order to increases the detection probability and the valid detection probability of displacement peak, the numbers of the markers in a interrogation window is suggested to be no less than 15 (Keane & Adrian 1990).

Considering the flow displacement peak derived from cross correlation technique, the displacement of two interrogation window is integer in units of pixel. For some cases the 'real' displacement may locate between the pixels, see Figure 2.20. It is sufficient to use the peak PSD value and the values next to the peak, totally three data points to fit a Gaussian function to improve the sub-pixel accuracy for a 1-D displacement. In a 2-D displacement case, for an optimal accuracy, totally nine points (a peak and the adjacent value) to fit a two-dimensional Gaus-

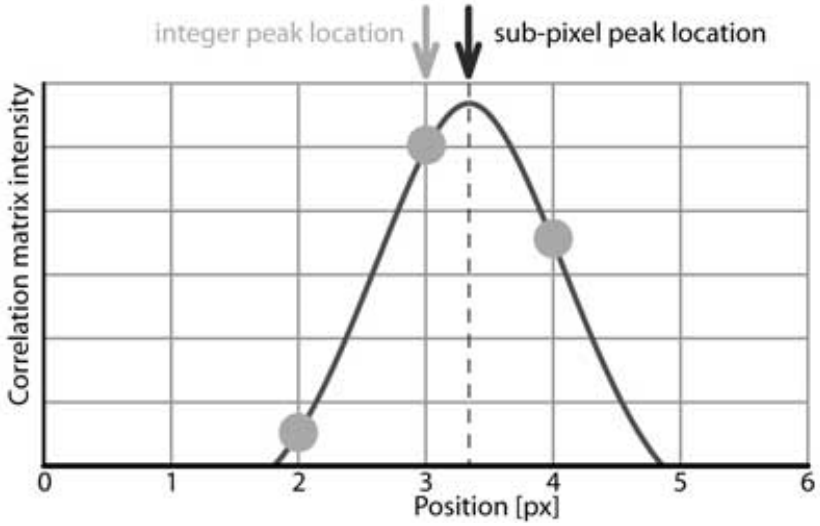

Figure 2.20: One-dimensional Gaussian function for sub-pixel accuracy, the fitting based on the integer displacement of the probability density function (Thielicke & Stamhuis 2014).

sian function (Nobach & Honkanen 2005). The other interpolation method and their performance can be found in Lourenco & Krothapalli (1995), Rösgen (2003) for finding the sub-pixel peak location. Nevertheless, the Gaussian function shows a good performance for the sub-pixel accuracy.

There are different seeding particles which may be used as markers for gas flow visualization. In order to prevent liquid seed particles from evaporating quickly and solid seed particles from agglomerating, the seeding time should neither too short nor too long. The seeds need to be homogeneous distribution without disturbing the flow. Table 2.1 shows particle materials are suggested for gas flow visualization (Raffel et al. n.d.):

Table 2.1: Seeding materials for gas flow visualization.

Seeds type	Material	Mean diameter [μm]
Solid	Polystyrene	0.5-10
	Aluminum	2-7
	Magnesium	2-5
	Glass micro-balloons	30-100
	Granules for synthetic coatings	10-50
	Dioctylphathalate	1-10
Smoke		<1
Liquid	Different oils	0.5-10

Chapter 3

Experimental Installation

In the past few decades, a number of premixed combustion experiments have been performed by Leeds combustion research group using bombs and engines to investigate the combustion process of various fuels (Bradley et al. 1992, 1998, Liu et al. 2013). However, the bomb and naturally aspirated engine could not reach very high pressures compared with modern strongly charged engines. Ling (2014) modified the naturally aspirated LUPOE2-D so that the peak motoring pressure could reach over 30 bar to simulate the in-cylinder condition of super- and turbo-charged engines. The modified LUPOE2-D is capable of running various liquid fuels such as gasoline, iso-octane and any other fuels that are volatile enough to achieve homogeneous mixture in the intake. The engine is also able to run in a direct injection mode by mounting the fuel injector in the engine head and modifying the fuel supply system. Similarly, diesel fuel could be used in this engine with a high compression ratio liner and direct injection mode. The engine could run stably from 400 RPM to 2000 RPM, typically within -15 to 35 RPM variation from 750 RPM and -30 to 50 RPM variation from 1500 RPM. This chapter will provide the details of specifications, air-fuel system of LUPOE2-D engine and the control and data acquisition system.

3.1 LUPOE2-D Research Engine

LUPOE2-D was derived from a two stroke single cylinder engine. It is now fitted with the boosting system developed by Ling (2014). LUPOE2-D installation consists of engine itself, dynamometer drive, air and fuel supply, data acquisition and control system. Figure 3.1 shows the overview of LUPOE2-D.

The engine is driven by an electric motor and a dynamometer to achieve desired operating speeds. The engine has a flywheel storing high angular momentum to keep engine running smoothly during compression and expansion stroke. A shaft encoder is employed to give reference timing signals at TDC and at fixed difference of crank angle to the control unit.

LUPOE2-D is a ported engine, there is no valves on the engine head and the engine head has been modified in order to achieve the full-bore optical access. The optical head features a top window, two side windows, spark plug and dynamic pressure transducer, shown in Figure 3.2, The top window provides full top view of combustion process and a custom-built spark plug sits in the centre of the bore with electrodes is about 3 mm below the lower surface of the top window. The side windows allow laser sheet to pass through the bore for PIV measurement. In some experiments, such as study of high pressure combustion and knock, instead of using an optical head, a more robust metal head is employed to avoid damages to the optical window.

In order to achieve a featureless flow in engine, the piston crown is flat and two identical rectangular intake ports are placed opposite to each other with 20^o inclination to eliminate swirl and tumble. This arrangement allows to isolate effects of turbulence from those induced by those large scale flows. Two rows of 10 mm diameter exhaust holes form the exhaust port. This port gives into the void between liner and cylinder barrel, directly leading to exhausts pipe. Ports opening and closure timing is controlled by the piston motion. The engine parameters are shown in Table 3.1.

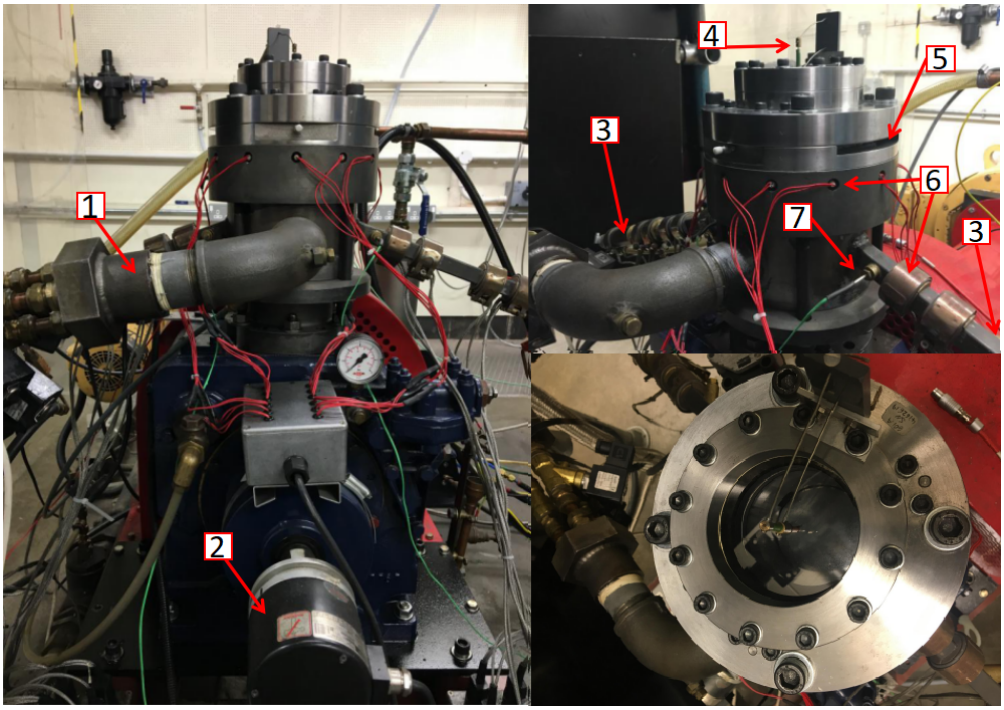

1 - exhaust pipe 2 - shaft encoder 3 - intake pipe 4 - spark plug
5 - side window 6 - heater 7 - thermocouple

Figure 3.1: An overview of LUPOE2-D.

Table 3.1: LUPOE2-D specifications

Engine Head	Disc
Bore [mm]	80
Stroke [mm]	110
Connect Rod Length [mm]	232
Clearance Height [mm]	7.5
Compression Ration	11.38
Numbers of Exhaust Holes	30
Inlet Ports Opening/Closure CA [deg]	107.8
Exhaust Ports Opening/Closure CA [deg]	127.6
Available Engine Speed [RPM]	400 - 2000

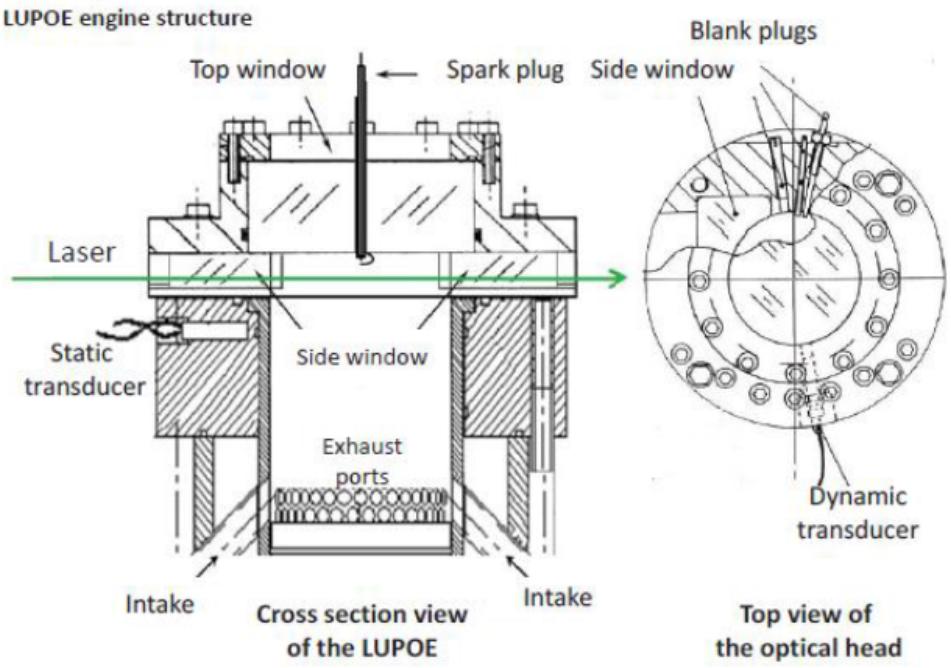

Figure 3.2: Cross section view and top view of LUPOE2-D cylinder(Ling 2014).

3.2 Breathing and Fuel Supply Arrangements

LUPOE2-D is designed to study combustion under high pressure conditions. The air fed to engine is supplied from a laboratory compressor and transported through a pipe. The system supplies 7 bar compressed air to a filtered regulator which reduces pressure to about 4 bar. During passage from the compressor, the temperature of the compressed air drops to room temperature owing to the long distance from the laboratory compressor. The air is then reheated to the desired temperature in the engine intake pipe. As shown in Figure 3.3, the regulated air is split into two lines, and passes through a Bronkhorst EL-FLOW thermal mass flow meter with each maximum flow rate of 32.3 g/s. In order to minimise air flow oscillations, there is a 5 L surge tank between the thermal flow meter and the intake pipe. A feedback system is employed to achieve precisely the air fuel ratio required. The pressure in the cylinder at the port closure is influenced by engine speed, exhaust valves timing and air flow rate. According to Ling's design (Ling 2014) for the boosting system, the initial cylinder pressure has been boosted by accumulating the flow in cylinder. Theoretically, the initial in-cylinder pressure could reach a maximum regulated value 4 bar if the engine speed is slow enough or the flow rate is large enough. Since the engine is running at relatively high speed with moderate air flow rate, a moderate mass has been accumulated into the cylinder that creates an initial pressure allowing engine to withstand during the firing cycle. Since different engine speeds are required in this study, the initial cylinder pressure was controlled by adjusting the air flow rate to maintain the same initial cylinder pressure. Comparing with the previous LUPOE2-D (Ling 2014) exhaust pipe and liner configurations, the present experimental setup needs more skip firing cycles (cycles without spark) to purge the residual gases inside the cylinder and scavenge the fresh charge to guarantee the expected mixture strength for the incoming firing cycle.

The fuel mass flow rate for the desired equivalence ratio of each intake pipe is controlled by Bronkhorst CORI-FLOW Coriolis mass flow meter with the maximum of 1.2 g/s of liquid. As shown in Figure 3.3, the fuel supply is driven by a 12 V pump with a 3 bar pressure relief valve to protect the system from damage and maintain constant fuel pressure. A needle valve is situated at the upstream of the venturi carburetor fuel orifice to control the fuel timing.

The intake air temperature is controlled on each intake pipe, with one 200 W and five 175 W band heaters, those theoretically, could achieve an incremental temperature of 33 K for the intake air temperature with the maximum air flow

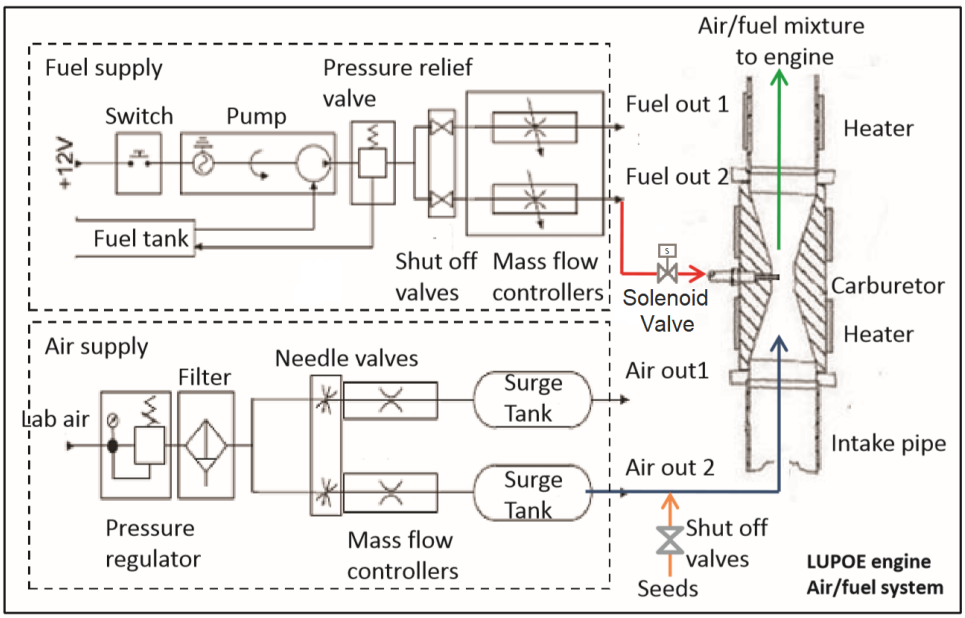

Figure 3.3: Schematic diagrams of engine air fuel systems, sketch is modified from Ling (2014)

rate of 32.3 g/s with 100% heat transfer efficiency. A K-type thermocouple is located at the end of the intake pipe next to the intake port to give feedback to the temperature control unit. The venturi carburetor is about 350 mm upstream of the intake port to ensure fuel is fully vaporised before the cylinder. The engine cylinder barrel has twelve 50 W cartridge heaters surrounding the middle of the barrel, a thermocouple giving feedback for temperature control. The temperature control unit is supplying power to barrel heaters and intake pipe heaters on each side until the feedback readings meet the desired value, and then cuts off the power supply, see Figure 3.4. As an illustration of the accuracy of the temperature control, at barrel and intake temperature of 323 K, with 5.2 g/s air flow rate for each intake, there are: about +1 K accuracy of barrel temperature and about +8 K accuracy of intake temperature. Comparing with air and intake pipe, the barrel has very large thermal inertia, which allows absorbing the excessive heat without raising temperature rapidly. For the stoichiometric iso-octane/air mixture, the accuracy of intake temperature is usually within a range of $\pm$ 5K. Due to the lack of cooling system, the engine might be over-heated during the operating. To minimize the impact of hot cylinder wall, the engine needs sufficient time before and after each run to settle down the temperature.

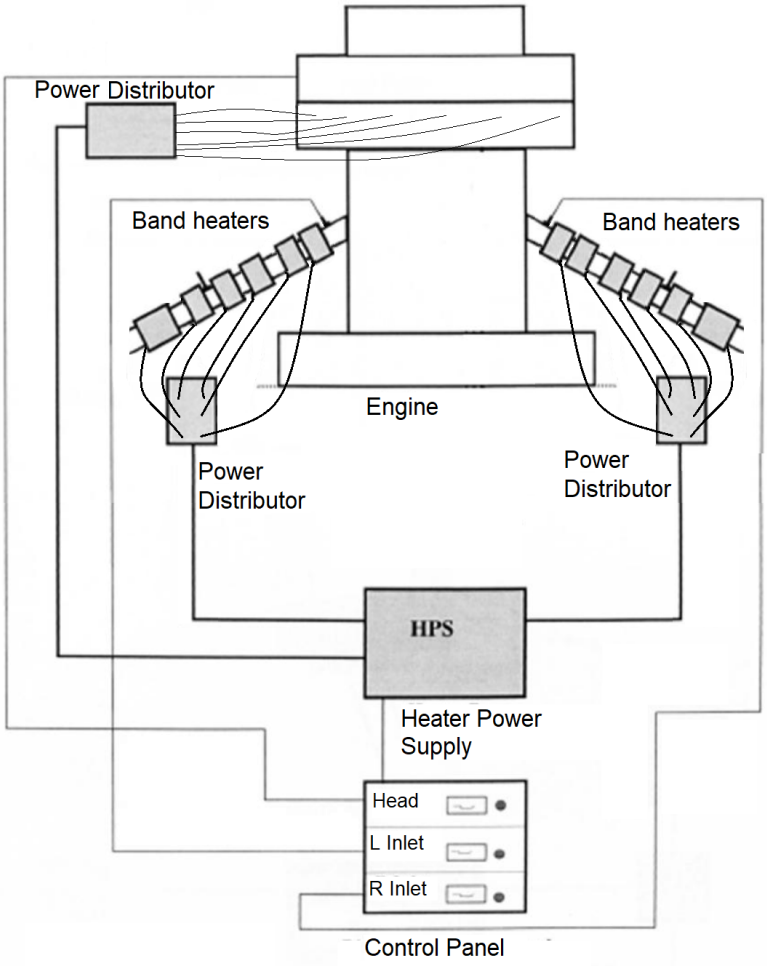

Figure 3.4: LUPOE2-D heating unit. The sketch is modified from EBRAHIM (2003)

3.3 Engine Control and Data Acquisition Systems

3.3.1 Control System and Engine Cycle Sequence

The engine control system was redesigned by Ling (2014). The engine spark timing, spark intensity, fuel/exhaust valve timing and data record timing are controlled by DsPIC 6140A micro-controller, see Figure 3.5. The controller is pre-programmed by software MPLAB ICD 3 based on C language for desired timing settings. The programme runs a series of logical judgement, see Figure 3.6, depending on a feedback signal generated by a Hohner 3202 shaft encoder. The shaft encoder generates 5 TTL pulses per crank angle i.e. 1800 pulses per revolution and a separate TTL pulse at TDC to trigger the programme recounting the encoder pulses. The calibration of the piston position employs a capacity proximity sensor to ensure that the TDC signal is at the accurate piston position. An artificial BDC signal pulse will be generated when the encoder pulse count is satisfied. And this artificial BDC signal in controller will assist the later programming and processing.

When the engine is in operation, a trigger signal is given to the micro-controller to start collecting signals from the engine. Specifically, for a firing cycle, the controller awaits the pre-set fuelling cycle count. Once the counted cycle matches the pre-set values, the controller will send signal to the inlet fuel valve and count fuelling cycle. If the fuelling cycle count is satisfied, the controller will cut off the inlet fuel valve signal. Similarly, in firing cycles, if the crank angle count reaches the pre-set spark timing, signals will be sent to start to charge capacitor for the spark and release spark. Typically, the programme is running following sequence: fuelling cycles – stop fuelling – charge spark – release spark – purging cycles – fuelling cycles, such intervals to obtain accurate combustion data at desired conditions without suffering influences from previous explosion, see Figure 3.7. Due to the different heat capacity ratio, γ, between air-fuel mixtures and air (γ of air is higher) the pressure trace in Figure 3.8 has been used to approximate to obtain approximately when purging/fuelling cycles are completed. Owing to the engine low volumetric efficiency, in 750 RPM case, the engine usually take up to 9 cycles to purge or 6 cycles to charge. As a result, in this study, 24 skip firing cycles including 16 fuelling cycles could totally avoid the influence from EGR and pre-ignition due to combustion residuals.

In order to run experiment safely, the controller is programmed to terminate

the intervals and cut off fuel once the total cycle count exceeds the desired value. In addition, the trigger is self-return switch button to ensure terminating the interval timely.

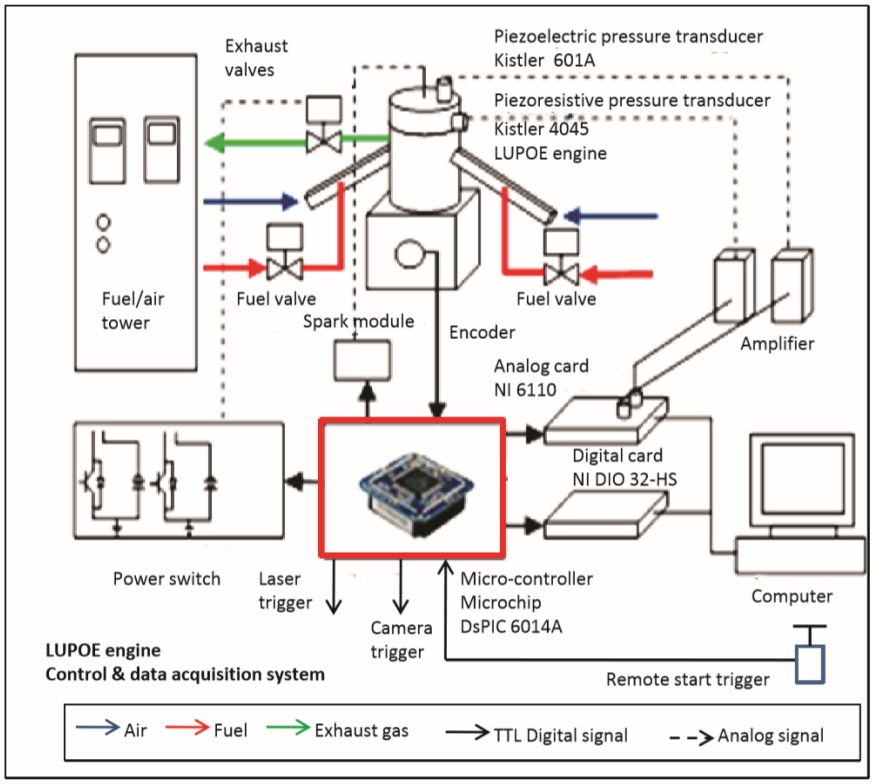

Figure 3.5: Schematic diagram of LUPOE2-D control and acquisition systems (Ling 2014)

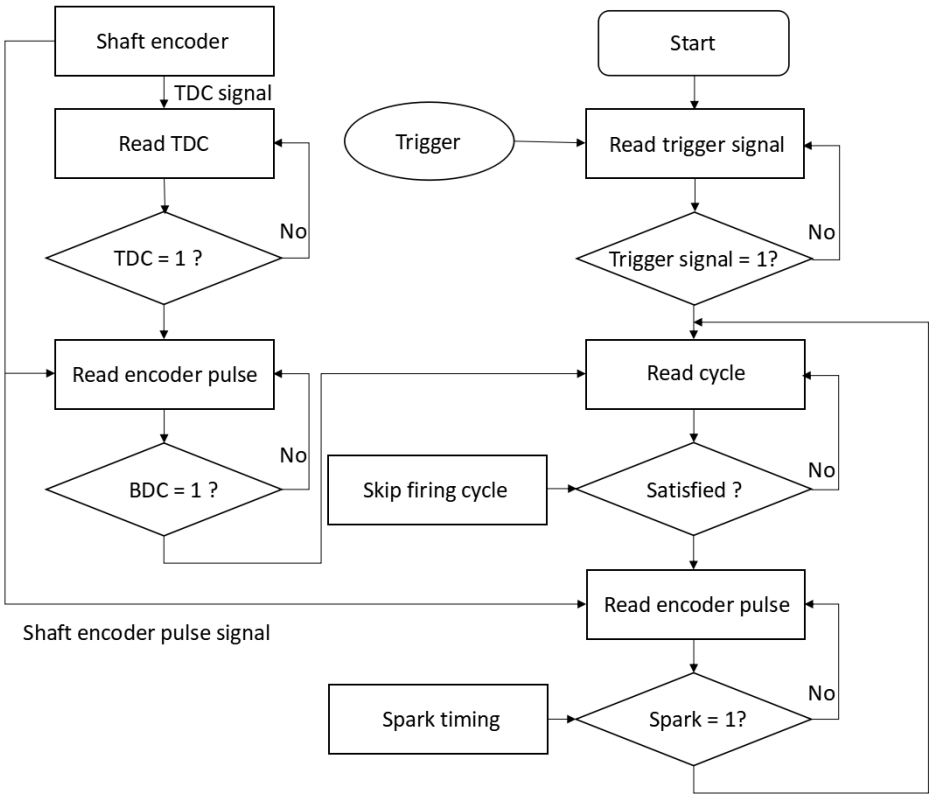

Figure 3.6: Flow chart of micro-controller control sequence

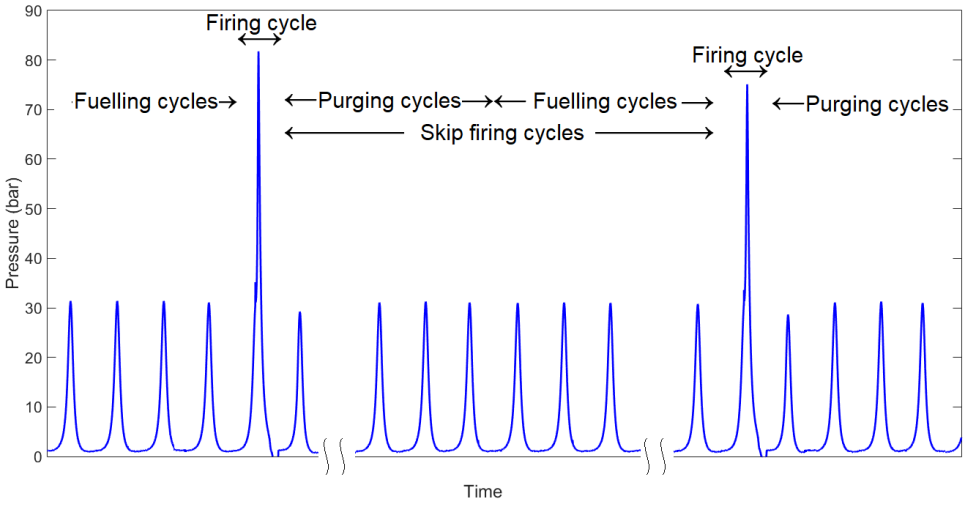

Figure 3.7: Engine operating sequence

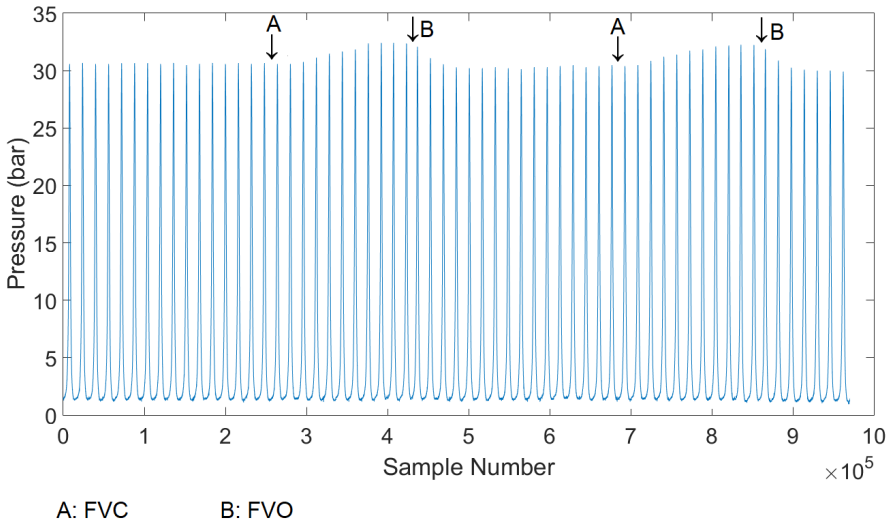

Figure 3.8: LUPOE2-D motoring cycle at 750 RPM, point A refers fuel valve closed, point B refers fuel valve open.

3.3.2 Data Acquisition Systems

In order to obtain instantaneous pressure inside the cylinder for further analysis, the engine employs a Kistler 601A dynamic transducer with a measurement range of 0 - 250 bar to measure the rapid pressure variation inside cylinder during combustion taking its advantage of the high response rate. The transducer is located at the engine head to monitor the pressure for entire cycle. The transducer signal goes through a Kislter type 5007 charge amplifier with output range 0 - 10 V. Since the cylinder pressure measurement needs a "reference level" for dynamic pressure, a static pressure transducer Kistler 4045A20 is applied with measurement range of 0 - 20 bar mounted at piston position 58.6^o bTDC. The signal from the transducer is fed into a Kistler Series 4601A amplifier with voltage output of 0 - 10 V. Both transducers were calibrated using a dead weight tester. Because of the absolute pressure transducer is mounted at lower position on cylinder, the absolute pressure can not be measured when the piston position is between 58.6^o bTDC and 58.6^o aTDC. As a result, a reference point, 60^o bTDC was used in this study to calculate the pressure difference between absolute pressure and dynamic pressure. Figure 3.9 shows the absolute pressure, dynamic pressure and the cylinder pressure in a motoring cycle. The cylinder pressure is calculated based on the combination of dynamic pressure and the pressure difference as:

$$P_{cyl} = P_{dyn} + (P_{abs(\theta=60)} - P_{dyn(\theta=60)}) \tag{3.1}$$

where P_{cyl}, P_{dyn} and P_{abs} are cylinder pressure, dynamics pressure, absolute pressure, respectively. In order to minimise noise influence on "reference level", multiple pressure data points were sampled within a narrow interval at 60^o bTDC to obtain the average pressure for the reference point. Both amplified dynamic and absolute pressure signals are acquired by a National Instruments 6110 analogue PCI card.

The digital (TTL) signals are collected by a National Instruments DIO 32-HS Digital card. In order to analysis firing and abnormal combustion cycles, the digital card collects all the signals from micro-controller which includes TDC and BDC signals, shaft encoder signal, spark charging and release signals, valve and record trigger signals, see Figure 3.10. A pre-built Labview programme is employed to coordinate the National Instruments cards and computer. In this study, sampling rate of 200 KHz was set in this programme in order to capture the pulses generated from shaft encoder even at higher engine speeds. Additionally, for knocking cycles, the high sampling rate is required to capture any pressure

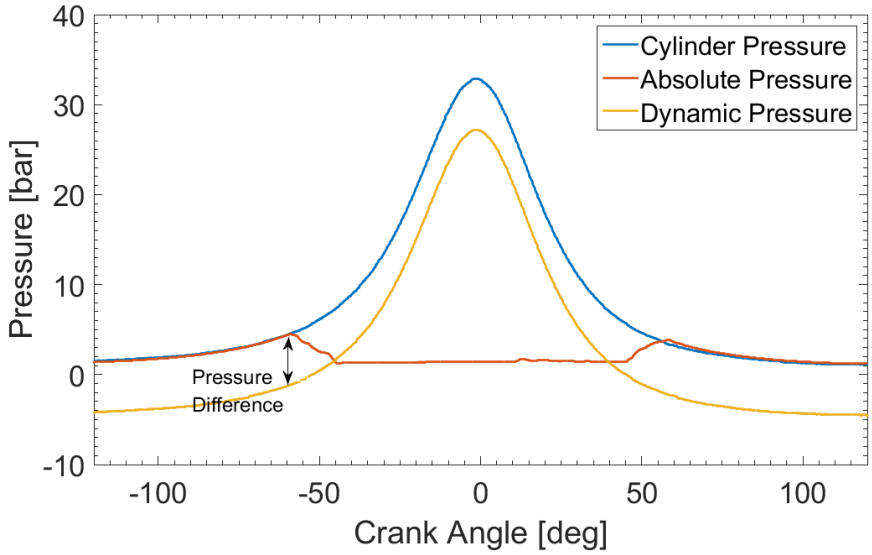

Figure 3.9: Pressures in engine

oscillations generated from abnormal combustion. At a high sampling rate, large number of non-firing cycles take significant computer memory space. A series of signal are generated to trigger the digital card to record until the numbers of samples reaches a pre-set value. In this study, the record trigger was sent when starting of last fuelling cycle before the firing cycle, then recorded one 63000 samples at 750 RPM and half of the value at 1500 RPM after each trigger signal, see Figure 3.11. As a result, there will be enough informations to identify abnormal combustion in a non-firing cycle to assure the reliability of the firing cycle data.

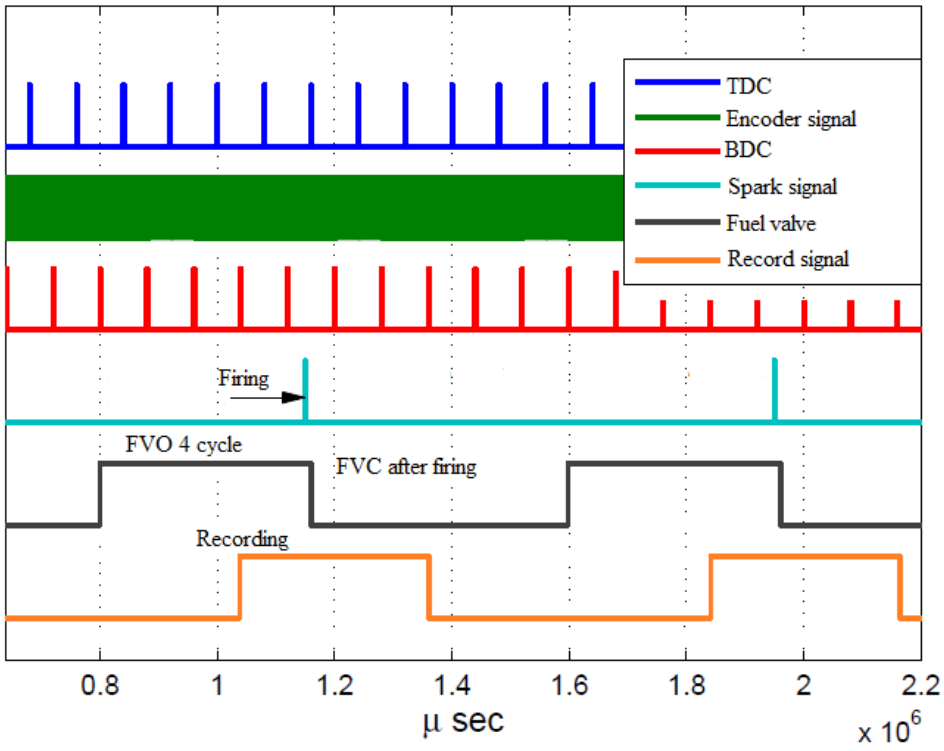

Figure 3.10: Digital signals at engine speed 750 RPM with 9 skip firing cycles, 4 fuelling cycles

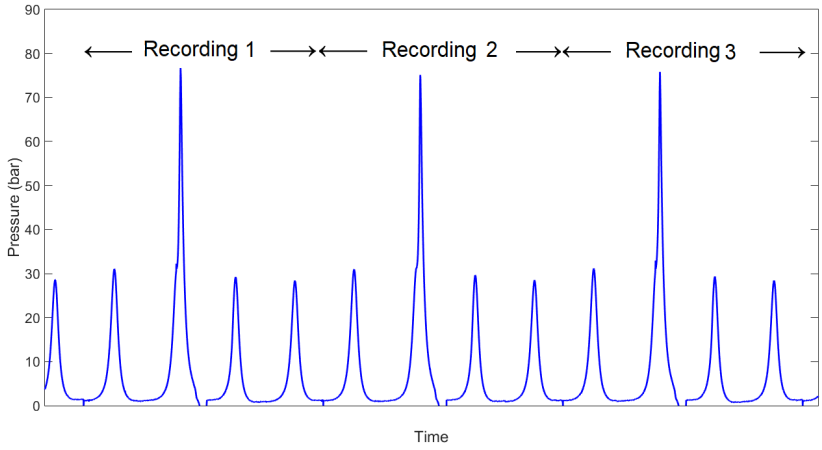

Figure 3.11: Recorded data for multiple acquisition trigger

3.4 Particle image velocimetry system

In order to diagnostic fresh gas flow, particle image velocimetry (PIV) was introduced in this study, see Figure 3.12. The PIV system is consisted by three parts: a single cavity copper vapour laser, the tracer particles generator, a high speed camera.

For the single cavity copper vapour laser was used as light source in this study, it produces laser contains wave length 511 nm (green) and 578 nm (yellow) with a pulse energy about 1 mJ at repetition rate of 10 KHz. Due to its short pulse duration 5 to 60 ns, the beam energy density is higher enough to provide enough light for the high speed camera running at frame speed of 10 KHz. The width of the laser beam is approximately 25 mm diameter, it passes a series of lenses to form a laser sheet, see Figure 3.13. The position of the spherical convex lens with focal distance -150 mm is adjustable, therefore, the position of the thin sheet can be controlled by moving this lens. In order to control the thickness of the laser sheet in the engine chamber, the laser sheet focus position is optimised (usually in the middle of the chamber) to ensure the particles captured are in the same plane rather than a surrounding volume. A paper painted in black was used for laser sheet calibration. The laser sheet will burn a mark on the paper to make sure the sheet is being well positioned. Figure 3.14 shows the burned mark at the laser sheet focused point. it shows the thinnest laser sheet could reach 0.5 mm approximately. The thickest part of the laser sheet in engine chamber is 1 mm approximately. Therefore, the relatively thin laser sheet could proved a good measurement of the in-cylinder flow field and tomography image with clear flame edge.

Considering the solid tracer particles will potentially damage the engine, such as the piston ring and the engine chamber. Refined olive oil was used as tracer particles in this study due to its cheap and relatively high smoking point. A thermal mass flow meter was positioned at the upstream of the seeds generator to ensure an accurate control of the fuel required. As shown in Figure 3.3 in earlier section, the tracer particles were supplied at the downstream of the surge tank and formed a uniform distribution before feeding the engine. The size of the tracer particle is typically less than 5 μm, the lag fluid flow calculated by Ling (2014) shows it is negligible for measuring the turbulence in the experiment. In this study, there were only small amount of the olive oil supplied to the engine, the consumption rate of the olive oil was so small so that the influence of the olive oil on combustion is negligible.

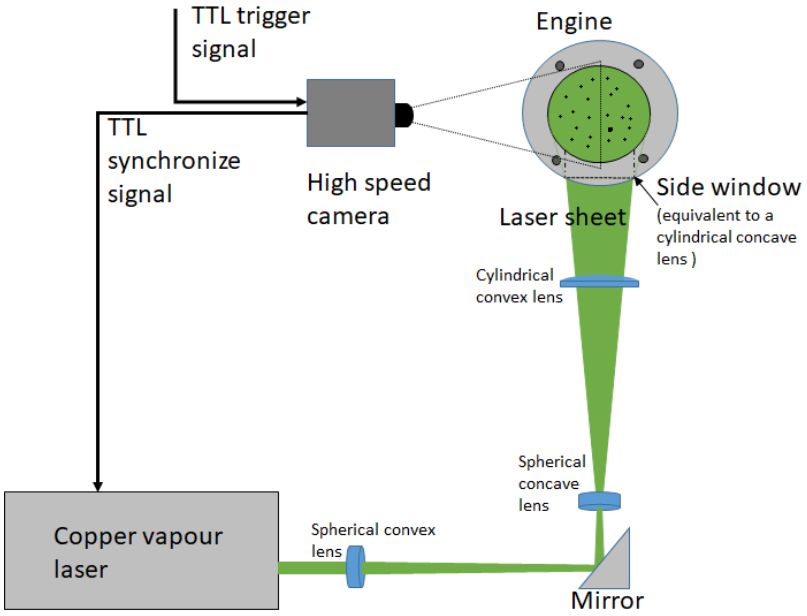

Figure 3.12: A schematic diagram of PIV setup in this study.

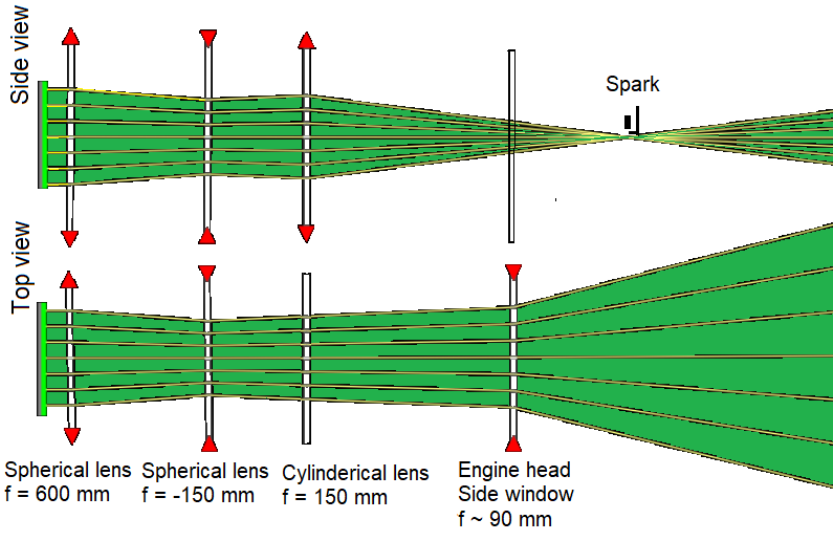

Figure 3.13: lenses setup for laser sheet generation.

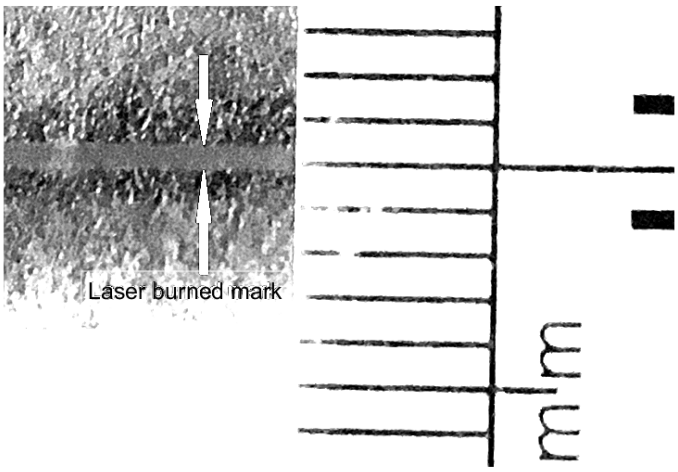

Figure 3.14: Leaser sheet thickness.

The tracer particles movement and the flame tomographic images were captured by a high speed camera 'Photron AR-X' operating at frame speed of 10KHz with a resolution of 512 x 512. For the full bore view, the pixel size in this study is about 0.162 mm. For a zoomed in flame study, the pixel size is approximately 0.064 mm from calibration. The illumination is provided by the synchronized single cavity copper vapour laser. The camera shutter time is about 4 μs to eliminate influence from the light emitted from chemical reaction to form a great contrast between unburned and burned region.

The images were processed by a time-resolved PIV tool 'PIVlab' to obtain the flow field. For the PIV interrogation window shifting, a multi-pass approach was applied, starting with the interrogation window size of 32 x 32 pixels and 50% of overlap, the velocity result will be the guide for the smaller interrogation windows. Therefore, the influence of PIV processing from in-plane pair loss in this study is negligible. For the sub-pixel accuracy, the Gaussian 2 x 3-point fit was applied to avoid the peak locking problems. In the final post processing, 5 times standard derivation was applied to reject the abnormal vectors. The summary of PIV settings shown in Table 3.2.

Table 3.2: General PIV settings

Camera	Photron APX RS
Resolution [Pixel]	512 x 512
Filming Speed [KHz]	10
Exposure Time [s]	1/253000
Interrogation Window [Pixel]	32 x 32
Interrogation Window (zoomed-in) [Pixel]	64 x 64
Overlap	50%

Chapter 4

Data Processing

4.1 Pressure Data Precessing

The raw analogue and digital signals recorded by computer are based on real time; the shaft encoder signal and BDC signal are employed to obtain the crank angle reference. Since the raw data contains large amount of samples, a Matlab programme was used to undertake the pressure processing. As shown in Figure 4.1, the instantaneous engine speed is varying approximately 5% from the setting value during the engine operation. The timing and number of samples in each cycle are not constant. Therefore, the accurate piston position is recorded using a shaft encoder signal. The structure of data processing module is shown in Figure 4.2. The programme starts a cycle by a BDC signal. Then, inside each cycle, the crank angle will be extracted from the shaft encoder signal. Since there are 1800 pulses per revolution from the encoder, the crank angle resolution obtained in such a manner is 0.2 degree.

Due to the variation of combustion phasing, peak cylinder pressure P_{max} may differ from cycle by cycle. The peak pressure is a useful proxy measure of the burning rate. In order to characterise the cycle to cycle variations, the coefficient of variation of peak pressure COV is defined as:

$$COV = \frac{\sigma_{P_{max}}}{\overline{P_{max}}} \tag{4.1}$$

where $\sigma_{P_{max}}$ is standard deviation of peak pressures, $\overline{P_{max}}$ is averaged peak pressures. Similarly, the coefficient of variation of the timing from ignition to peak

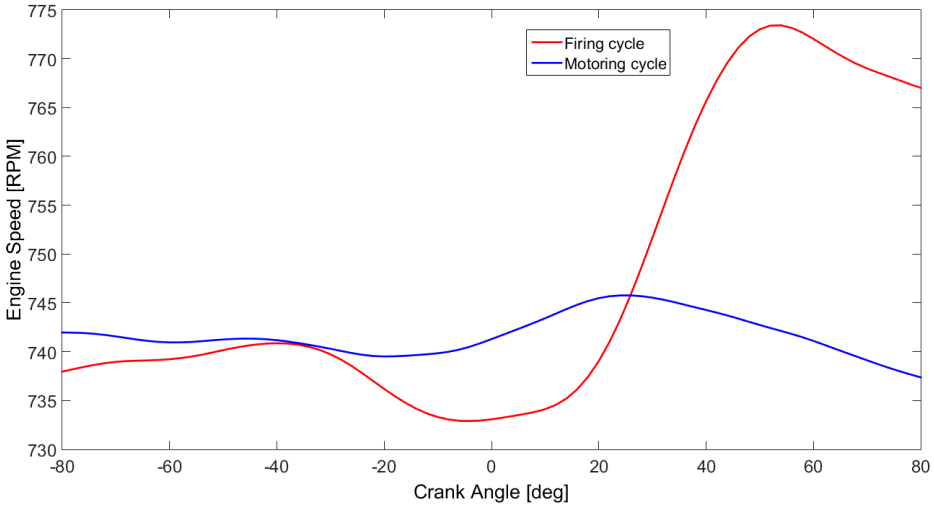

Figure 4.1: Variation of engine speed in a typical firing and motoring cycles from -80 CA to 80 CA

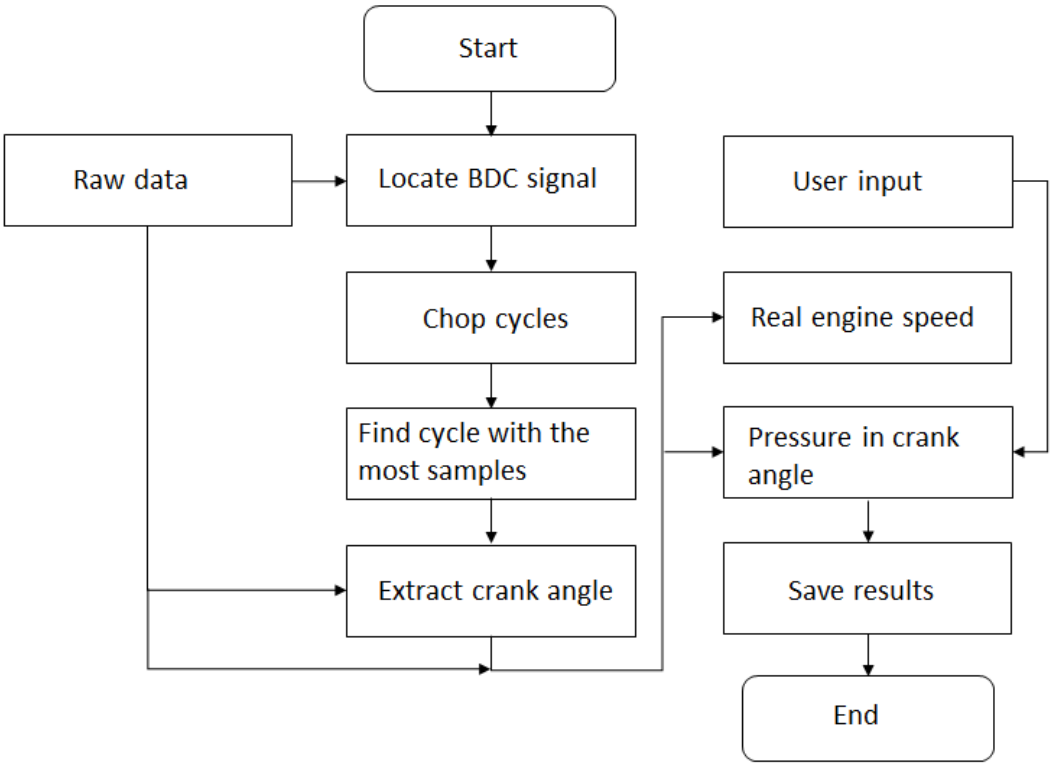

Figure 4.2: Flow chart of pressure signal processing code in Matlab

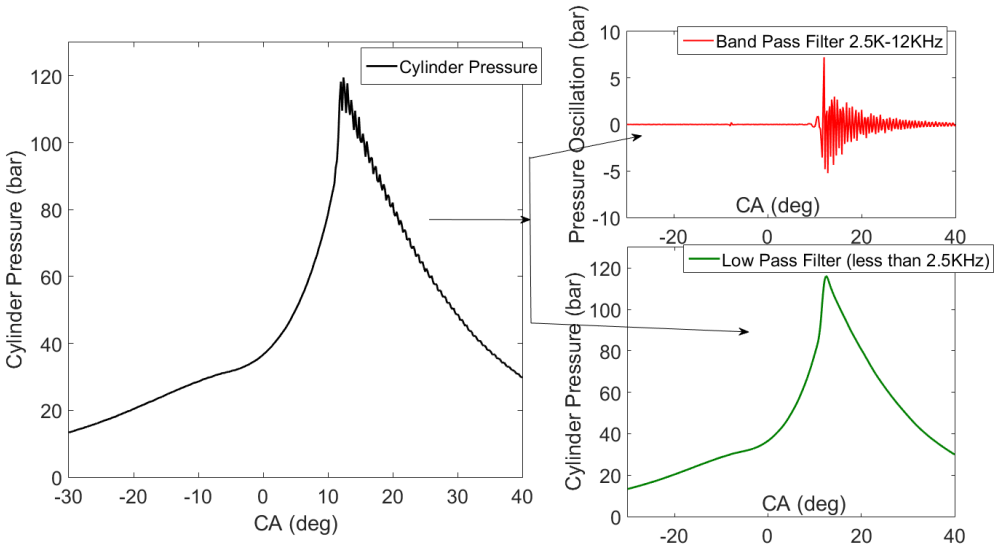

Figure 4.3: Example of typical knocking cycle unfiltered cylinder pressure (left), pressure oscillations (top right) and cylinder isolated from pressure oscillations (bottom right).

pressure in crank angle, COV_{CA} is introduced as:

$$COV_{CA} = \frac{\sigma_{CA_{max}}}{\overline{CA_{max}}} \tag{4.2}$$

where $\sigma_{CA_{max}}$ is standard deviation of time in crank angle from ignition to peak pressure, and the $\overline{CA_{max}}$ is the averaged crank angle duration from the ignition to the peak pressure. According to the scatter plot of maximum pressures, the combustion cycles are classified as fast, middle or slow cycle, in which the highest one third of total number of cycles are fast cycle and the lowest one third of total number of cycles are slow cycle. The remaining one third of cycles are middle cycle.

In a typical knocking cycle, the fuel-air mixture auto-ignited locally ahead of the advancing flame front. The auto-ignition with strong energy release generates shock that wave is reflecting in the cylinder and causes pressure oscillations. In order to separate this oscillations from the pressure trace, a band-pass filter with passing frequency 2.5 - 12 KHz should be employed (Ling 2014). Figure 4.3, shows a typical knocking cycle in which the P_{max} and CA_{max} are clearly obtained using a low pass filter with passing frequency less than 2.5 KHz. In order to define the knock strength, maximum pressure oscillations (MAPO) was introduced in this study, which is the maximum pressure obtained from the band-pass filter. In some cases, signal noise, vibration due to high cylinder pressure and high engine speed

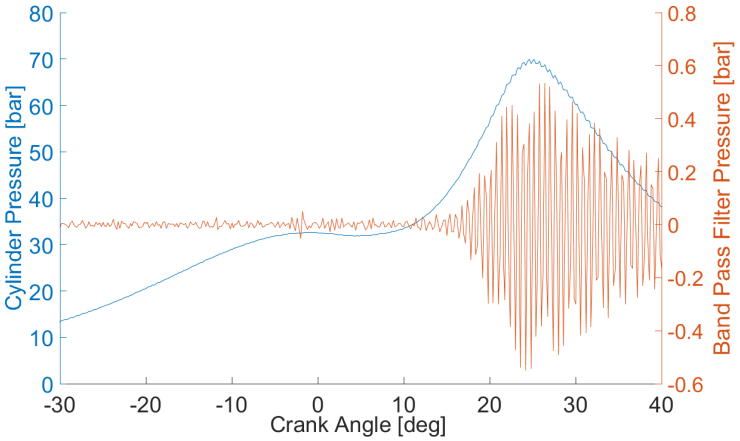

(a) Knocking free cycle.

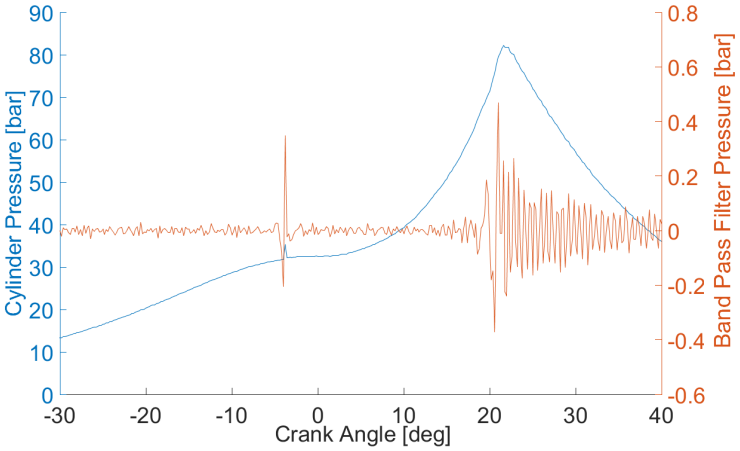

(b) Knocking cycle

Figure 4.4: Comparison of pressure oscillations in a knocking cycle and a normal cycle.

may cause pressure oscillations. For instance, Figure 4.4(a). Figure 4.4(a) shows a typical non-knock firing cycle but with a high band pass filter pressure where the MAPO is about 0.5 bar; While, Figure 4.4(b) shows a typical mild knocking cycle, the MAPO from the band-pass filter is about 0.5 bar. Despite the same level of MAPO in both normal and knocking cycle, the distinction between two cycles with the filtered pressure traces is the sharp raise of oscillation wave peak in the knocking cycle. In Figure 4.4(a), the wave peaks are increasing gradually, and the MAPO is located at or after the peak cylinder pressure location. On the other hand, in a knocking cycle, the MAPO is usually ahead of the peak combustion pressure. As a result, the knocking cycle defined by Matlab programme must satisfy two features simultaneously: MAPO should be greater than 0.4 bar; the band pass filter pressure wave should raising rapidly. In other words, the wave local peak altitude should be less than 30% of the next following wave peak.

4.2 LUSIEDA Analysis

Further analysis of the pressure trace is performed using Leeds University Spark Ignition Engine Data Analysis (LUSIEDA). This code has been developed by the combustion group since 1980s (Desoky 1981, Hynes 1986, Abdi Aghdam 2003, Hattrell 2007). The programme is fed with experimental data of cylinder pressure and corresponding crank angle to obtain mass burning rate, flame temperature, unburned gas temperature, flame speed and other combustion parameters.

LUSIEDA employs a zero-dimensional combustion model, in which the fluid in cylinder is consisted by two zones, a burned zone and an unburned zone. Each zone has its own thermodynamic system. Assumptions are applied for this two zone model:

1. The burned and unburned zones are ideal gases of different properties.
2. Pressure is uniform in the cylinder.
3. Temperature in each zone are uniform and no heat, mass transfer between each other.
4. Burned zone is spherical and the flame is a deflagration combustion wave.

The calculations start with an initial guess of Δm_b to evaluate pressure change due to combustion ΔP_{com}. The final Δm_b is confirmed until the calculated ΔP_{com} matches the value from the measurement with a limited error. The sub-models influencing the pressure have been taken account into the LUSIEDA: piston motion ΔP_{pm}, heat transfer ΔP_{ht}, blow-by and pressure equalising ΔP_{bb}. As a result, the total pressure change due to combustion ΔP_{com} is followed by equation,

$$\Delta P_{com} = \Delta P_{cyl} - (\Delta P_{pm} + \Delta P_{ht} + \Delta P_{bb}) \tag{4.3}$$

4.3 Flame Boundary Detection

In this study, PIV system was also providing laser sheet flame images for deriving flame contours. The burned and unburned gas zones have been discriminated by color gradients using a Matlab code, see Figure 4.5. Since the flow seeding in the fresh gas creates the bright region in the image, the brightness of burned mixture is much lower than the unburned region. In some cases, the uniform light intensity and engine oil droplet reflections are forming speckles or shades in captured raw images. For the Otsu's method (Otsu 1979), a global threshold has failed to distinguish unburned and burned regions correctly. For instance, the shades in Figure 4.5(a) bottom will be classified as burned region. In the engine cylinder, the incoming laser sheet produces a higher intensity compared to the side shaded by the flame, see Figure 4.6(a) and (b). In order to detect the flame boundary accurately, an adaptive threshold was applied for image binarisation. For the adaptive threshold, a Gaussian lowpass filter is applied to forming a threshold map, see Figure 4.6(c). So that every individual pixel has its own threshold. As a result, the threshold for individual pixel is able to decide based on the light intensity around the pixel. A Wiener filter is applied to the binarised image to eliminate the noise such as the intensity spike in the middle of the image in 4.6(b). The filtered image will be in a grey scale image again. But the noise pixel intensity will be similar to its surrounding pixels. After a second time of binarisation, the binary image is formed for the definition of the contour, see Figure 4.6(d).

From the experiment, the burned region shape was in average of a circular shape, and the burned region region centroid remained at the position of the spark kernel. As a result, flame can be treated as a symmetric object and the spark location can be regarded as centroid of the geometry. In order to eliminate influence from spark stem or other rare unexpected faulty contours defined in dark region for burned region measurement, half of the burned region with the best contrast was used for calculation, in which the half burned region is located at the laser incoming side. The main reason to use half flame at laser incoming side is to avoid later on faulty measurement of unburned gas velocity by PIV system at the laser outgoing side. Figure 4.7 demonstrates the flame speed observation in this study.

The burned region has been divided into equal sectors with an angle of 10 degree. Thus, area $A_i(t)$ of sector i (i = 1, 2, ...18) at time t, can be obtained by the programme. According to the sector area equation, radius $R_i(t)$ of sector i at

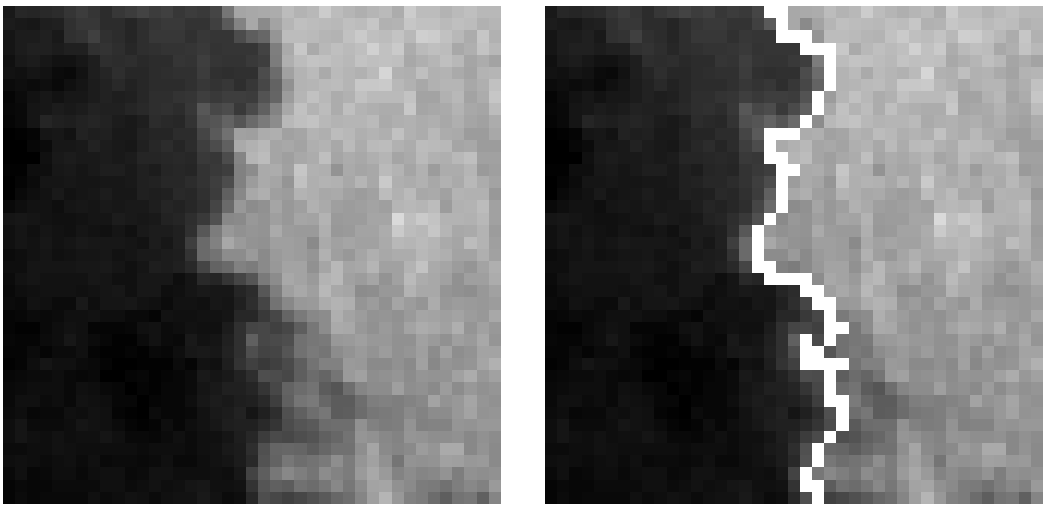

(a) Raw image (b) Flame contour defined by the programme

Figure 4.5: Detailed flame in engine cylinder, dark region refers burned mixture and bright region refers unburned mixture.

time t, follows:

$$R_i(t) = \sqrt{\frac{360A_i(t)}{10\pi}} \tag{4.4}$$

Local flame speed $S_i(t)$ at time t in the sector i follows:

$$S_i(t) = \frac{dR_i(t)}{dt} \approx [R_i(t) - R_i(t - \Delta t)]/\Delta t \tag{4.5}$$

Overall flame speed $S(t)$ is obtained by taking an arithmetic average of the 18 local sector flame speed $S_i(t)$,

$$S(t) = \frac{1}{18}\Sigma S_i(t) \tag{4.6}$$

From the contour detection, flame contour coordinates were obtained. The contour coordinates are sorted to make sure that the coordinates are listed in a clockwise direction around the contour, see Figure 4.8. The distance, r_n, from the n^{th} contour pixel to the centroid(C_x,C_y) can be calculated. Since the length between two neighbouring pixels differs, e.g. two-adjacent pixels in horizontal or vertical will be 1 unit of pixel length; in diagonal will be $\sqrt{2}$ units of pixel length. Therefore, the r_n based on integer pixel number is re-sampled along the contour length based on $r(s')$. Thus, the fluctuation $r_p(s')$ which is the amplitude of flame

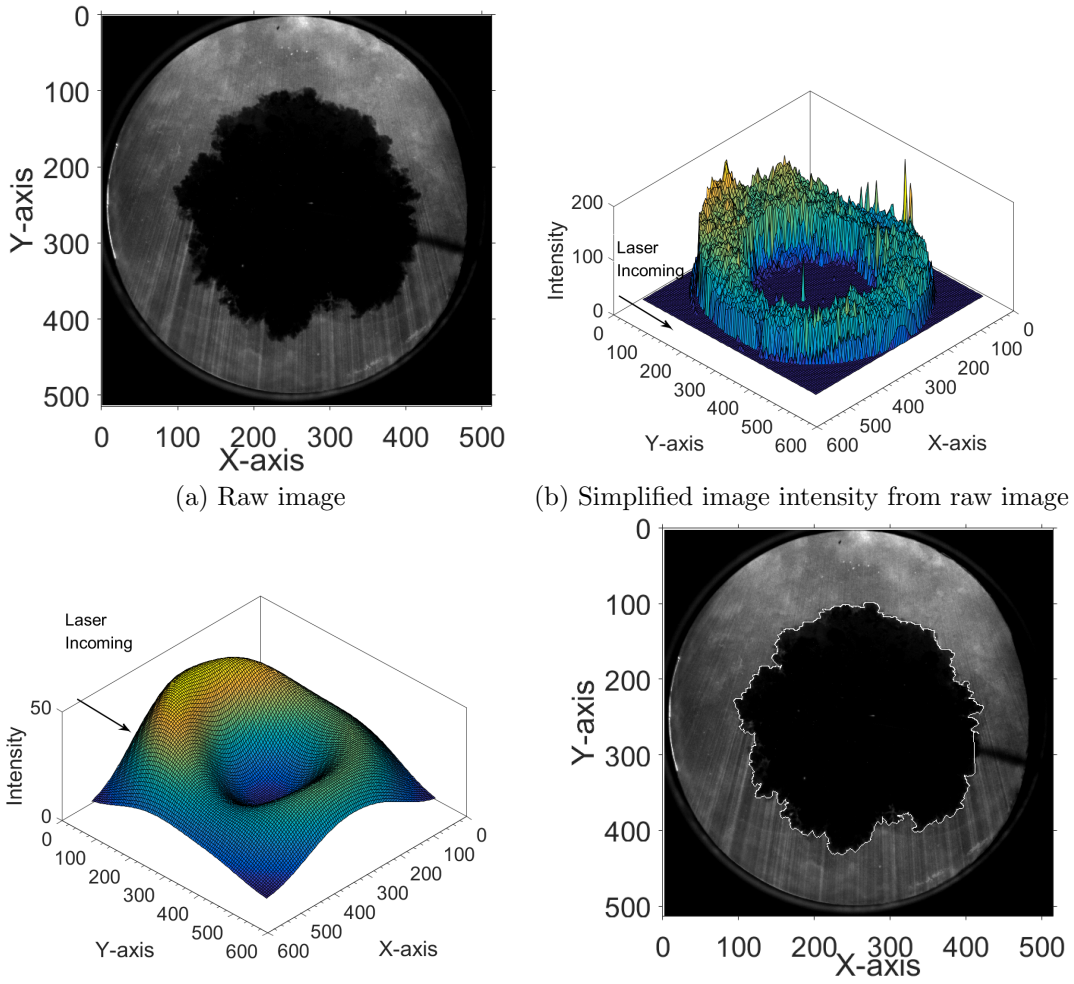

(a) Raw image

(b) Simplified image intensity from raw image

(c) Simplified threshold map for binarization

(d) Final contour detected by the programme

Figure 4.6: Illustration of adaptive threshold for flame contour detection, axis unit [pixel].

wrinkling at contour length s' follows:

$$r_p(s') = r(s') - R \tag{4.7}$$

where R is averaged flame radius from all sectors. The RMS amplitude of flame wrinkling r_{rms} is derived from the contour pixels:

$$r_{rms} = \sqrt{\frac{1}{l}\int_0^l [r'(s')]^2 ds'} \tag{4.8}$$

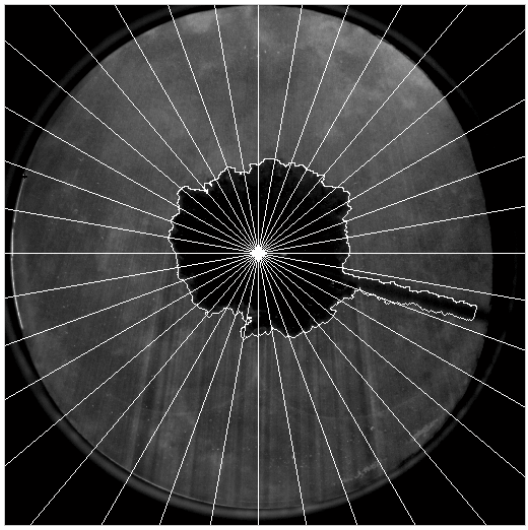

(a) Boundary detection at t

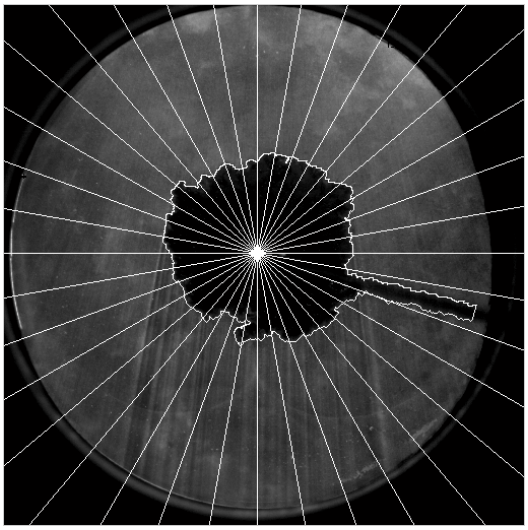

(b) Boundary detection at t+Δt

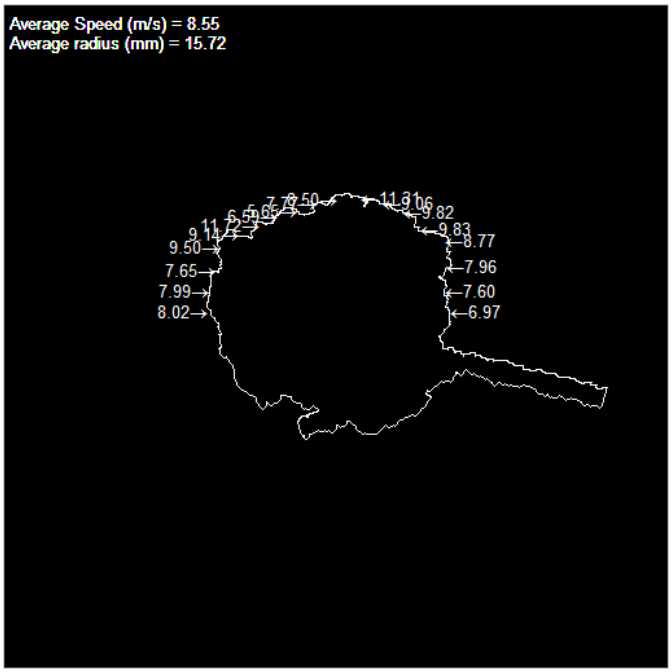

(c) Flame speed derived from (a) and (b), where the number with arrow refers the local sector flame speed

Figure 4.7: Illustration of flame speed observation based on sector radial flame velocity.

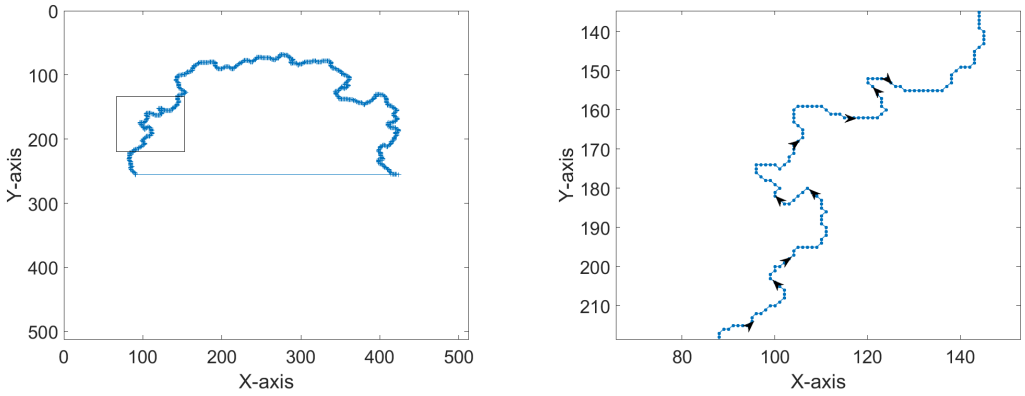

(a) Flame contour formed by sorted contour coordinates

(b) A detailed Flame contour coordinates tracking from selected area in (a)

Figure 4.8: Clockwise direction of contour tracing, axis units [pixel].

where l is total length of the flame contour. From the amplitude of flame wrinkling, an integral scale of flame wrinkling Lr' is obtained by autocorrelation function:

$$Lr' = \int_0^l R_k(\xi) d\xi \tag{4.9}$$

$$R_k(\xi) = \frac{2}{l} \int_0^{\frac{l}{2}} r'(s') r'(s' + \xi) ds' \tag{4.10}$$

where $R_k(\xi)$ is spatial length correlation of fluctuating component between ξ separation distance.

4.4 Unburned Gas Velocity Measurement

PIV results are stored in a Cartesian coordinate system in which each point has its velocity along x and y direction, where u is velocity along x-axis and v is velocity along y-axis. However, to describe the gas velocity in a polar coordinate system is more convenient for deriving burning velocity in the engine cylinder, hence was adopted herein. In order to unify coordinate systems, a global coordinate system centre (C_x, C_y) was introduced where (C_x, C_y) indicates the spark position. The unburned gas radial velocity at point (x,y) can be represented in polar coordinate system by radius $R(x, y)$, angle $\Theta(x, y)$ and radial velocity $u_r(x, y)$,

$$R(x,y) = \sqrt{(x - C_x)^2 + (y - C_y)^2} \tag{4.11}$$

$$\Theta(x,y) = \arctan\left(\frac{y - C_y}{x - C_x}\right) \tag{4.12}$$

$$u_r(x,y) = -u(x,y)\cos(\Theta(x,y)) - v(x,y)\sin(\Theta(x,y)) \tag{4.13}$$

where positive $u_r(x, y)$ means the outward direction. Similarly, the tangential velocity is,

$$v_r(x,y) = u(x,y)\sin(\Theta(x,y)) - v(x,y)\cos(\Theta(x,y)) \tag{4.14}$$

where positive $v_r(x, y)$ means the velocity normal to radial velocity and towards right direction.

To avoid the moving shadows caused by engine oil droplets and other substances absorbing or reflecting laser, see Figure 4.9, PIV processing only took the top half of the image on the incident laser sheet side.

Another limitation of PIV is the accuracy of fresh gas velocity next to the flame front. There are some discussions about the unburned gas velocity profiles ahead of flame reported by Balusamy et al. (2011). Figure 4.10(a) presents an image of PIV result at moment of motoring cycle. In firing cycle, the unburned region will be involved in interrogation window inevitably no matter how reshape or re-orient the PIV interrogation window. In order to show the effect of burned dark region on PIV result, an artificial black region was added to Figure 4.10(a) to simulate the unburned dark region, see 4.10(b). According to Figure 4.10(c) and (d), there is clear velocity magnitude reduction around the artificial annulus. Figure 4.11 shows the fresh gas velocity magnitude with respect to distance from the artificial black region. The fresh gas velocity in the original image was compared to those in the modified image at the same location. It is clearly that the velocity magnitude just ahead of the artificial dark region is reduced comparing with the original one.

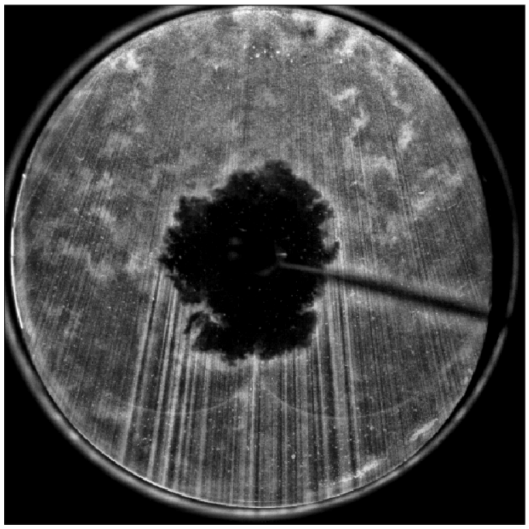

(a) PIV image A

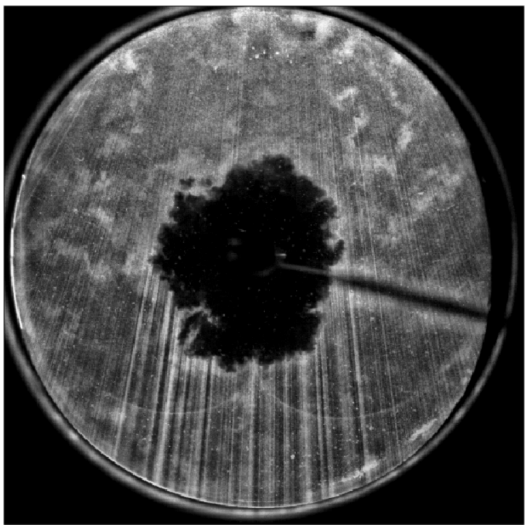

(b) PIV image B

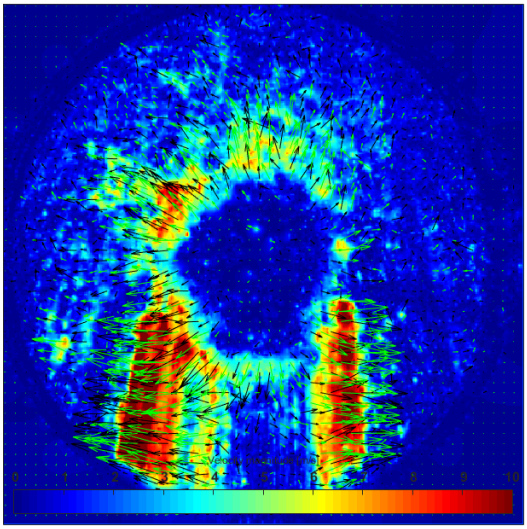

(c) Simplified PIV result from PIV image A and B with flow direction and altitude

Figure 4.9: Illustration of the effect of shadows induced by the flame on the flow velocity derived from PIV.

The measurements restore the same magnitude until several pixels further from the black region edge. Reducing the interrogation widow size could bring the accurate measurement closer to the dark region but the accuracy in the black region affected area will be reduced. In a firing cycle, while the flame is propagating, the peak unburned gas velocity magnitude is expected to reach the maximum value just next to the flame contour. However, for the unburned flow, PIV only is able to give the accurate velocity several pixels away from the flame contour. As a

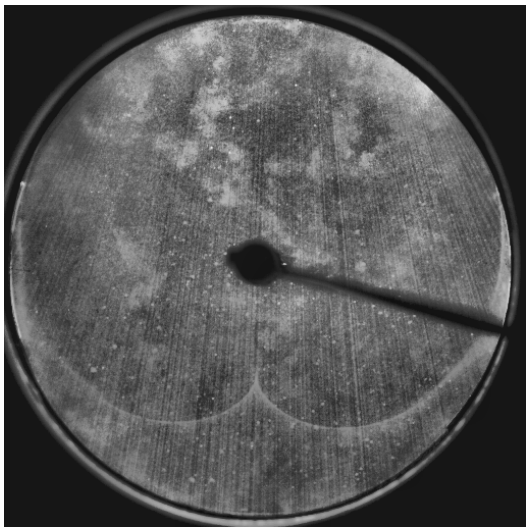

(a) Image from motoring cycle

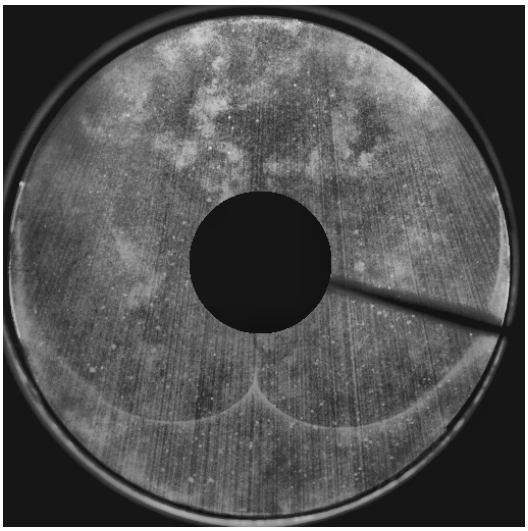

(b) Artificial dark region added to (a)

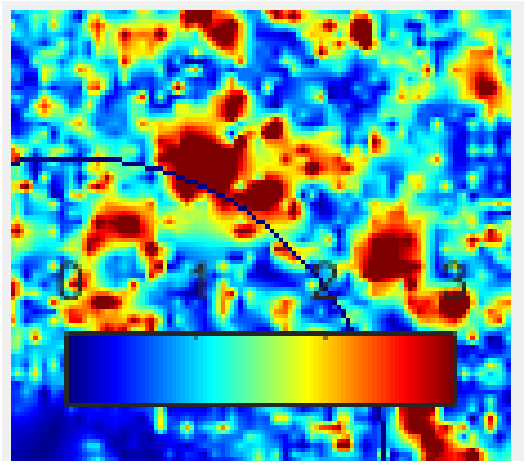

(c) Unburned velocity magnitude without artificial dark region

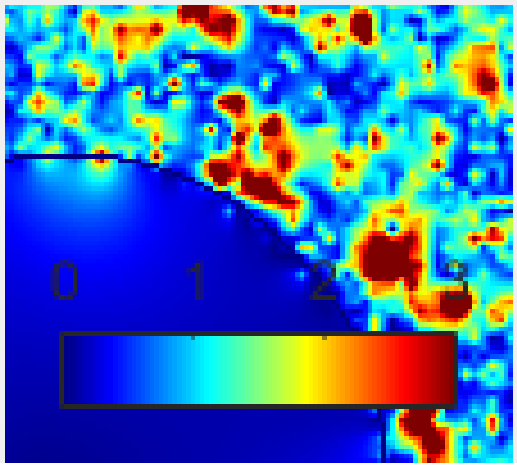

(d) Unburned velocity magnitude near the edge of artificial dark region

Figure 4.10: Motoring cycle PIV results from original image and modified image, the dark line refers the contour of artificial dark region.

result, the continuity equation is employed to extrapolate the unburned gas radial velocity at flame front u_r. The continuity equitation is written in differential form:

$$\frac{\delta\rho}{\delta t} + \frac{1}{r}\frac{\delta}{\delta r}\rho r u_r = 0 \tag{4.15}$$

where density ρ does not depend on radius considering r $\geq R_i$ for unburned gas. Integrating equation above, one gets:

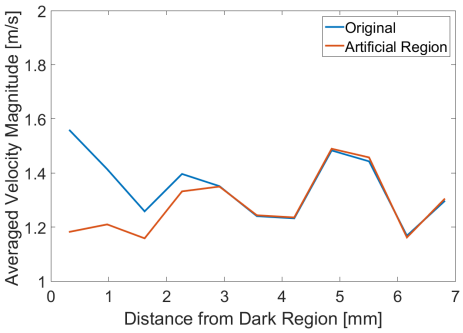

(a) Fresh gas velocity altitude for original and artificial image with PIV interrogation widow size of 32 pixels.

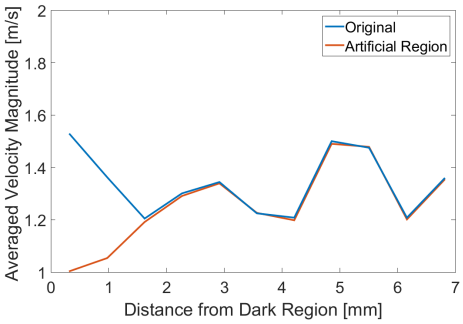

(b) Fresh gas velocity altitude for original and artificial image PIV interrogation widow size of 16 pixels.

Figure 4.11: Fresh gas velocity magnitude from image and modified image.

$$(\rho u_r r)\,|_{R_i}^{r} + \left(\frac{r^2}{2}\frac{d\rho}{dt}\right)|_{R_i}^{r} = 0 \tag{4.16}$$

$$\rho r u_r(r) - \rho R_i u_r(R_i) - \frac{r^2}{2}\frac{d\rho}{dt} + \frac{R_i^2}{2}\frac{d\rho}{dt} = 0 \tag{4.17}$$

$$u_r(r) = \frac{R_i u_r(R_i)}{r} - \frac{r}{2\rho}\frac{d\rho}{dt} + \frac{R_i^2}{2\rho r}\frac{d\rho}{dt} \tag{4.18}$$

$$u_r(r) = Ar + \frac{B}{r} \tag{4.19}$$

where A and B are functions of time only but do not depend on r.

As a result, unburned gas radial velocity $u_r(r)$ is a function of r, where r is the distance from centroid to the measured point. In order to form a representative unburned gas radial velocity $u_{r_i}(r)$ in local sector, a certain amount of velocity samples $u_r(r)$ in the local sector are needed for averaging. In this case, the unburned region in local sector is divided into segment with width of 10 pixel (1.6mm) shown in Figure 4.12. The unburned gas velocity in the segment will be averaged to form a sample point for extrapolating unburned gas radial velocity at flame contour $u_{r_i}(R_i)$. Finally, the turbulent burning velocity in i^{th} local sector u_{t_i} follows the equation:

$$u_{t_i} = S_{ti} - u_{r_i} \tag{4.20}$$

where S_i is local sector flame speed. Similarly, the overall turbulent burning

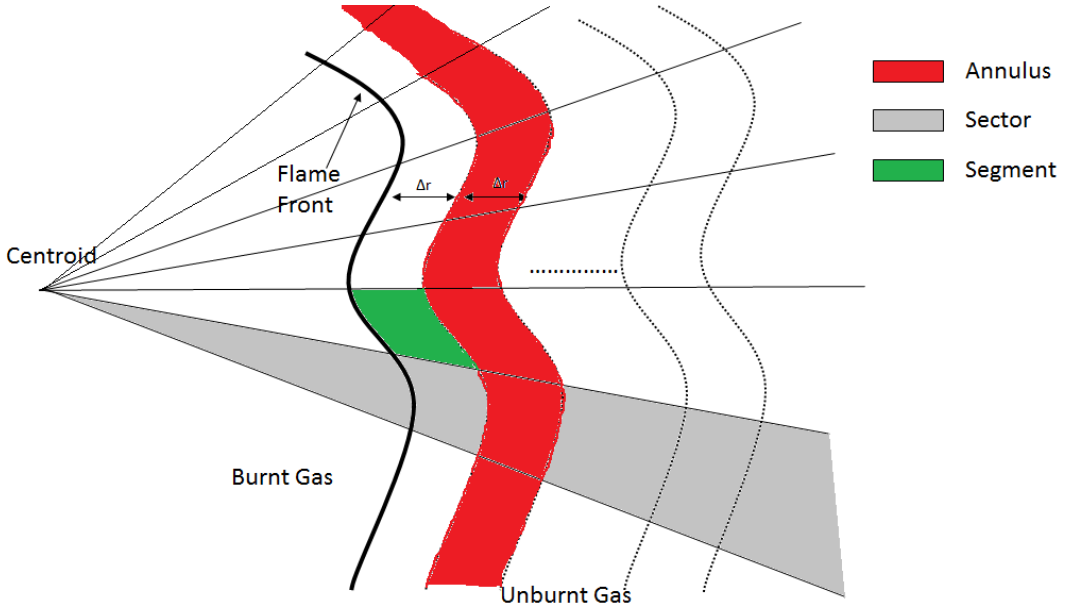

Figure 4.12: Definitions of annulus, sector and segment used in dividing the cylinder space.

velocity will be the value u_{t_i} averaged from all the sectors:

$$u_t = \frac{1}{n}\Sigma u_{t_i} \tag{4.21}$$

where n is the numbers of sectors.

In the considered flow, there are four integral length scales of turbulence: integral length scale from longitudinal correlations of velocity components u and v, $L_u x$ and $L_v y$; integral length scale from transversal correlation direction of turbulent flow velocity components u and v, denoted as $L_u y$ and $L_v x$. The longitudinal correlation function of velocity u, $R_{ux}(r)$, with respect to correlation distance r follows:

$$R_{ux}(x,y,r) = \frac{\frac{1}{N-1}\sum_{i=1}^{N}(u(x,y,i))(u(x+r,y,i))}{u'(x,y)u'(x+r,y)} \tag{4.22}$$

where i is the cycle number and x, y are the spatial co-ordinates, N is total number of cycles. Similarly, the transversal correlation function of velocity u, $R_u y(r)$, with

respect to correlation distance r follows:

$$R_{uy}(x,y,r) = \frac{\frac{1}{N-1}\sum_{i=1}^{N}(u(x,y,i))(u(x,y+r,i))}{u'(x,y)u'(x,y+r)} \tag{4.23}$$

Thus, longitudinal and transversal integral length scale follow equation,

$$L_{ul} = \int_{0}^{r1^*} R_{ux}(x,y,r)dr \tag{4.24}$$

$$L_{ut} = \int_{0}^{r2^*} R_{uy}(x,y,r)dr \tag{4.25}$$

where $r1^*$ and $r2^*$ are the first r value in auto-correlation function that make $R_{ux}(x,y,r1^*)$ and $R_{uy}(x,y,r2^*)$ equal to zero. In the correlation function, the velocity fluctuation $u(x,y,i)$ is obtained as:

$$u(x,y,i) = U(x,y,i) - \bar{U}(x,y) \tag{4.26}$$

where $U(x,y,i)$ is the instantaneous velocity in the current cycle i, $\bar{U}(x,y)$ is the ensemble averaged velocity from N cycles. RMS velocity $u'(x,y)$ is obtained from $u(x,y,i)$:

$$u'(x,y) = \sqrt{\frac{1}{N}\sum_{i=1}^{N} u(x,y,i)^2} \tag{4.27}$$

Chapter 5

Turbulence in Motoring Cycle

This chapter presents the outcomes of investigation of flow field details, in order to quantify the effects of turbulence on combustion under strongly charged engine conditions. The turbulent flows in motoring cycle were measured from -10 to 44^oCA at 750 RPM and from -20 to 34^oCA at 1500 RPM. Because of combustion is occurring within those period. The laser sheet plane for studying motoring cycle turbulence will be the same plane for studying the turbulent flame propagation. The measurement plane is 3.5 mm from the piston crow, when piston is at TDC. The investigation has been curried by using PIV in the LUPOE2-D fitted with optical head, the details which is presented earlier chapter. The derivation of velocity field from raw PIV images was done by PIVlab. This investigation has been performed in the cold flow with stoichiometric iso-octane/air mixture thus enabling measurement over the most of field of view parallel to the piston crown. However, there is no attempt has been made to measure velocities in the tumble plane aligned with the axis of the piston motion.

5.1 Flow Field in Individual Cycle

Figure 5.1 shows a snapshot of turbulence flow field and flow velocity magnitude at TDC for the engine speed 750 RPM. As shown by the vectors, the size of swirl motion in cylinder flow field is negligible. The statistics of the velocity components for Figure 5.1 is shown in Figure 5.2, although there is a small mean velocity in y-axis direction, the overall flow in cylinder has no preferential direction, and the averaged radial velocity component is -0.0625 m/s which is negligible in flame propagation. Furthermore, the distributions of velocity components are relatively symmetric and follows a normal distribution. Therefore, the in-cylinder flow at 750 RPM can be treated as characterless flow.

Figure 5.3 shows the flow field and the magnitude at the engine speed 1500 RPM. Like 750 RPM motoring cycles, velocity vectors do not present there is a preferential direction. Since the increasing of engine speed from 750 RPM to 1500 RPM, the averaged velocity components are shifting away from zero, which the mean flow velocity is larger than it is at 750 RPM. This may because of there is an increase of uncertainty with increasing of the engine speed. Considering these average velocity components are relatively small compare with the u' and flame speed in engine obtained by LUSIEDA at 750 and 1500 RPM, the influence from mean flow direction on flame drifting is limited. And the spark location is still regarded as the flame centroid for later flame processing.

As mentioned in Chapter 4.4, there is also a noticeable observation in Figure 5.1 and 5.3 that the flow field magnitude in bottom half cylinder is clearly lower than the top half cylinder. It is highly possible due to reflections from the cylinder wall and engine oil droplets that create an non-uniform brightness in bottom half cylinder. Furthermore, a series of straight line which was formed by large velocity flows, especially at 1500 RPM, due to relative large size and quantity engine oil droplets creating noticeable shadows in bottom half cylinder. However, since these faulty measurements are only taking a small amount of data samples, the influences on calculation can be neglected.

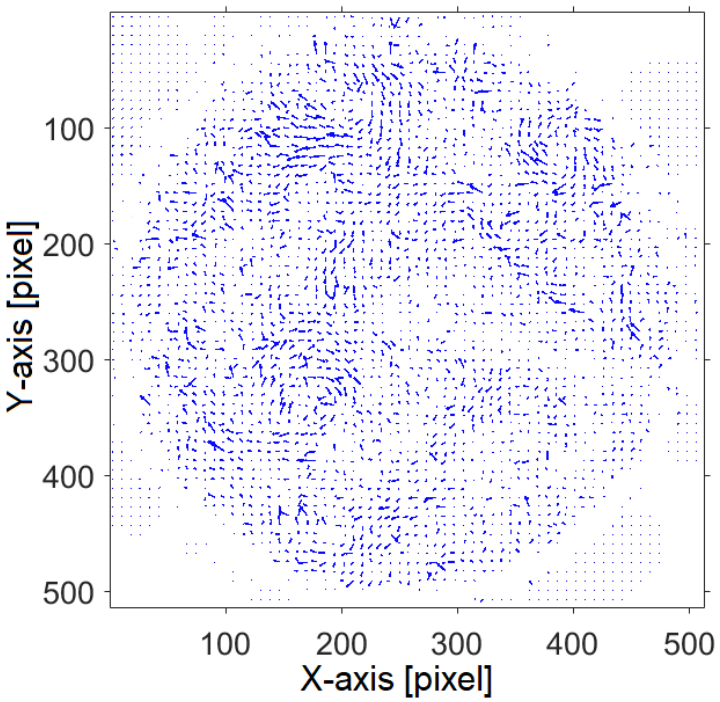

(a) Turbulence flow field

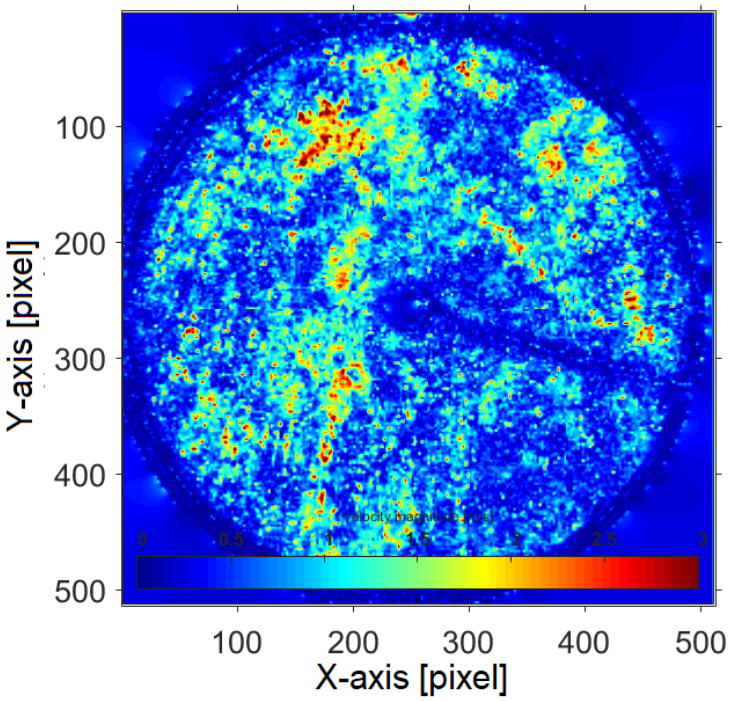

(b) Flow field velocity magnitude at TDC, color bar blue to red refers 0 to 3 m/s

Figure 5.1: A snapshot of simplified turbulence flow field and flow velocity altitude captured by PIV near TDC at engine speed of 750 RPM

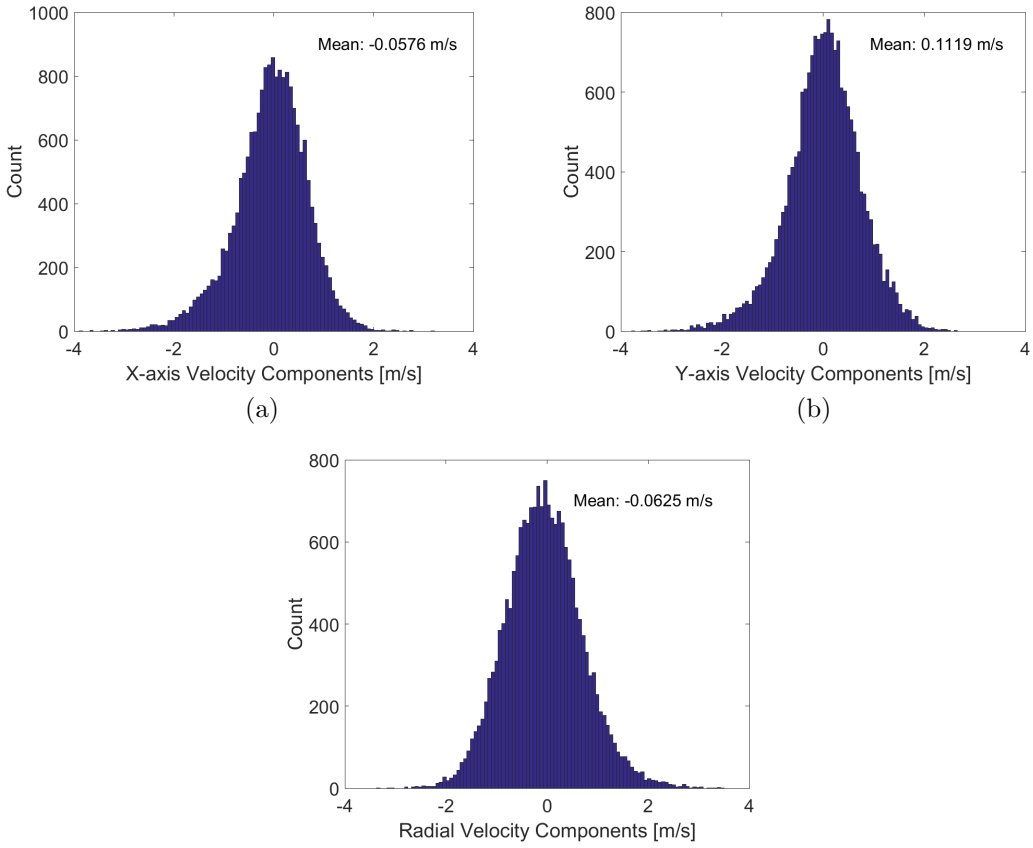

Figure 5.2: Distribution of velocity components for Figure 5.1

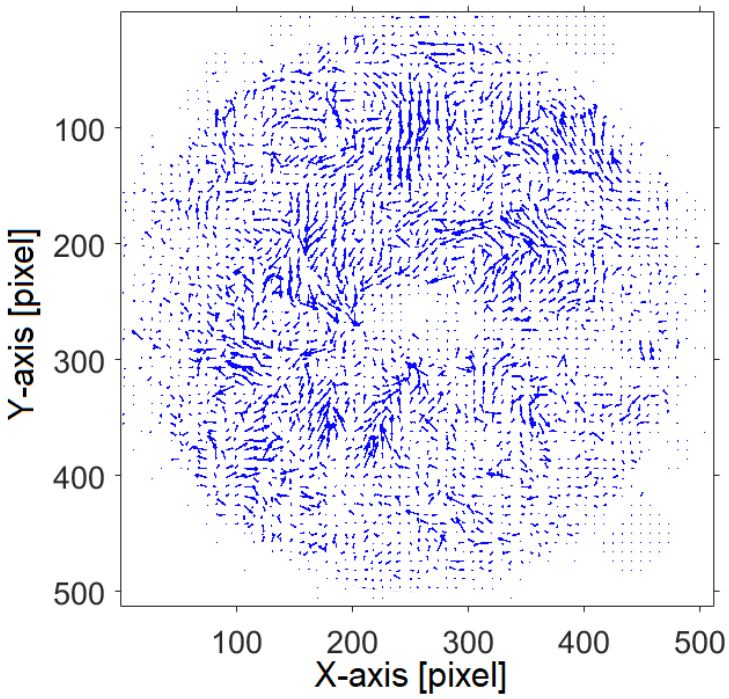

(a) Turbulence flow field

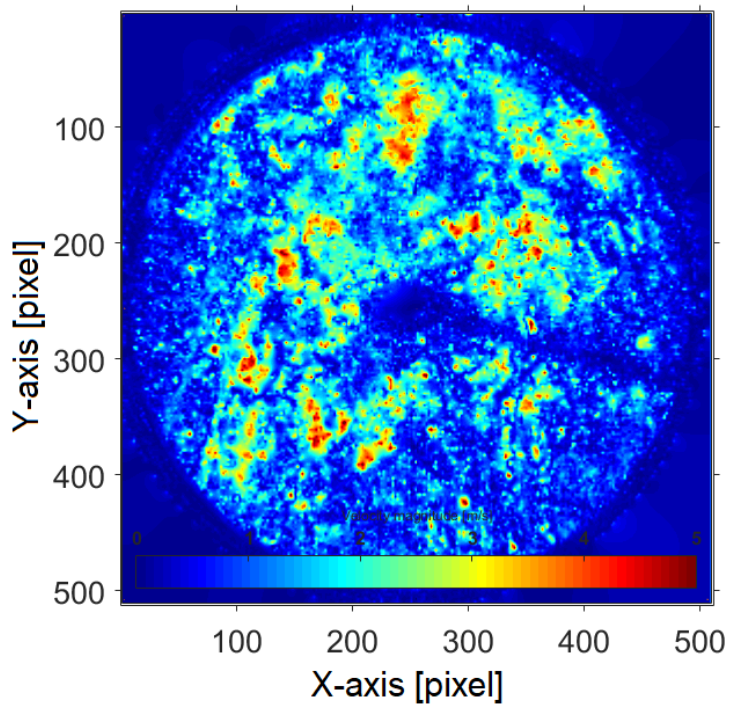

(b) Flow field velocity altitude, color bar blue to red refers 0 m/s to 5 m/s

Figure 5.3: A snapshot of turbulence flow field and flow velocity altitude captured by PIV near TDC at engine speed of 1500 RPM

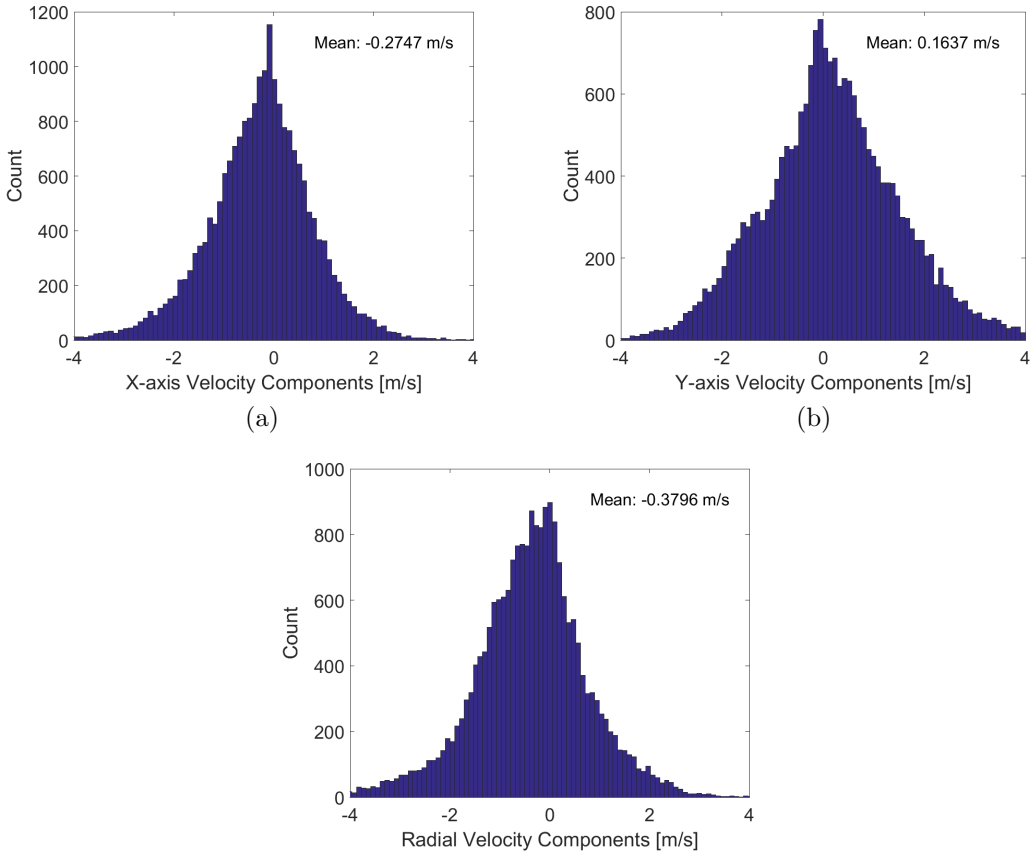

Figure 5.4: Distribution of velocity components for Figure 5.3

5.2 Turbulence Parameter for Motoring Cycle

The turbulent RMS velocity u' was measured from 50 motoring cycles based on both ensemble and spatial averaging. To eliminate the effect of spark plug and cylinder wall on turbulent flow, the region of interest was taking an annulus region with inner radius of 5 mm and and outer radius of 36 mm in this study, see Figure 5.5. Figure 5.6 shows the measured u' as a function of crank angle at engine speed 750 RPM. There is highly identical RMS velocity either derived from spatial averaging and ensemble averaging. The radial and tangential RMS velocities u_r and v_r are highly comparable before 30 CA aTDC. There is a disagreement between the RMS velocities after 30 CA aTDC. It is highly possible that the relatively large piston moving down speed induces the tumble or other flow motions to the cylinder turbulent flow. Considering the major combustion process has been completed before 30 CA aTDC (see Chapter 6.2). Therefore, the disagreement between the RMS velocities would not be a problem. The crank angle within the two parallel solid lines refers the averaged flame radius at stoichiometric condition from 10 to 25 mm in the Chapter 6 studies. The dash line is the crank angle range for $\phi =$ 0.8. Therefore, the averaged u' is almost constant as 0.75 m/s during the period of time for flame propagation studies in Chapter 6. The constant u' from -10 to 20 CA indicate the turbulence decay is compensated by the turbulence induced by the piston movement. However, the balance breaks after 20 CA, because the acceleration of piston speed. The fast movement of the piston induces turbulence where the u' of the motoring cycles are showing rapid rising.

In the case of 1500 RPM, see Figure 5.7, u' starts to increase from -10 CA. The u' at TDC for 1500 RPM is about 50% higher than that at 750 RPM. During the 3 to 18 CA aTDC, the u' derived from spatial averaging increases from 1.1 to 1.3 m/s and it give u' 1.2 m/s in average across this duration. Similar to the 750 RPM, the u' can be treated as constant 1.2 m/s at averaged flame radius 10 - 25 mm in the Chapter 6 studies.

In order to obtain the u' profile across the radial direction, the cross-section of cylinder region of interest in Figure 5.5 was divided into 15 annulus with a width of 2 mm approximately. The annulus index was sorted from 1 to 15 corresponding from inner annulus to outer annulus see Figure 5.8. Figure 5.9 shows that the u_r in local annulus is varying from 0.7 m/s to 0.8 m/s approximately at 10 CA aTDC at 750 RPM. The u_r across radial direction is relatively stable, due to the homogeneous turbulence. Overall, the value of averaged u'_r in local annulus is around 0.75 m/s that highly matches the averaged u'_r for the whole region of

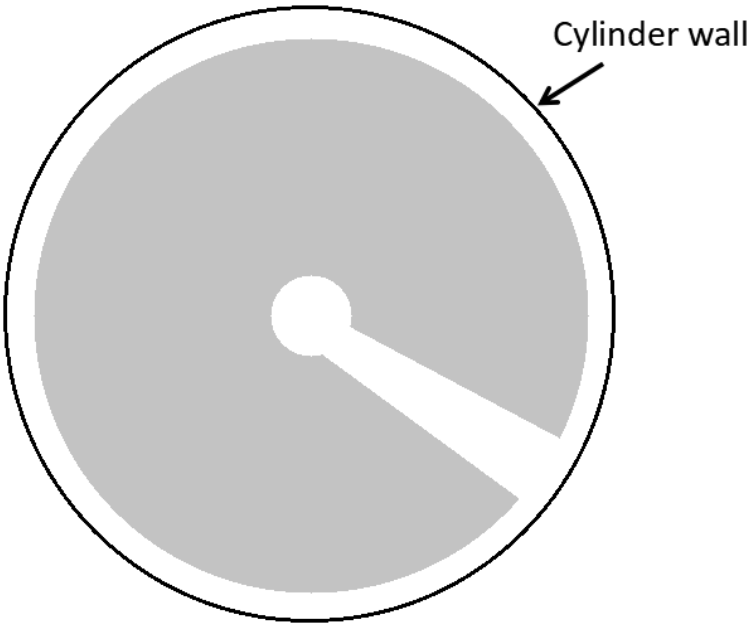

Figure 5.5: Region of interest in gray color has been selected to calculate the turbulent characters in motoring cycles.

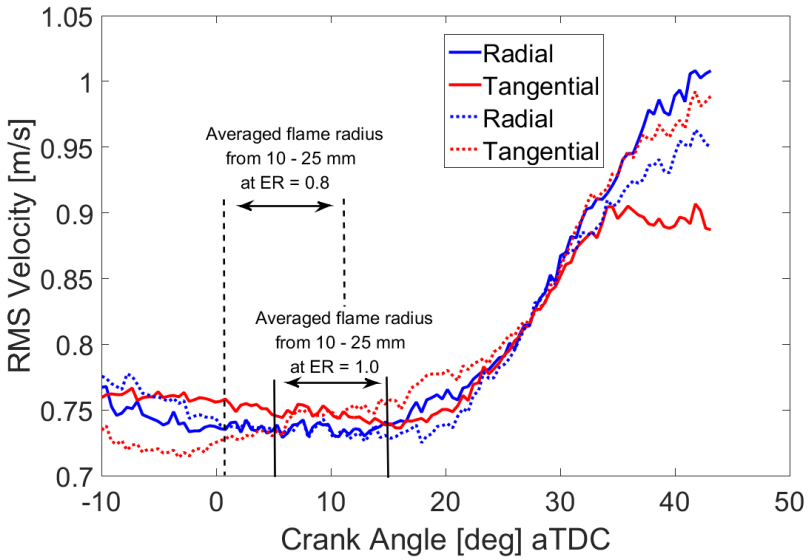

Figure 5.6: RMS velocity as a function of crank angle at 750 RPM based on 50 Motoring cycles based on spatial averaging (solid line) and ensemble averaging (dash line).

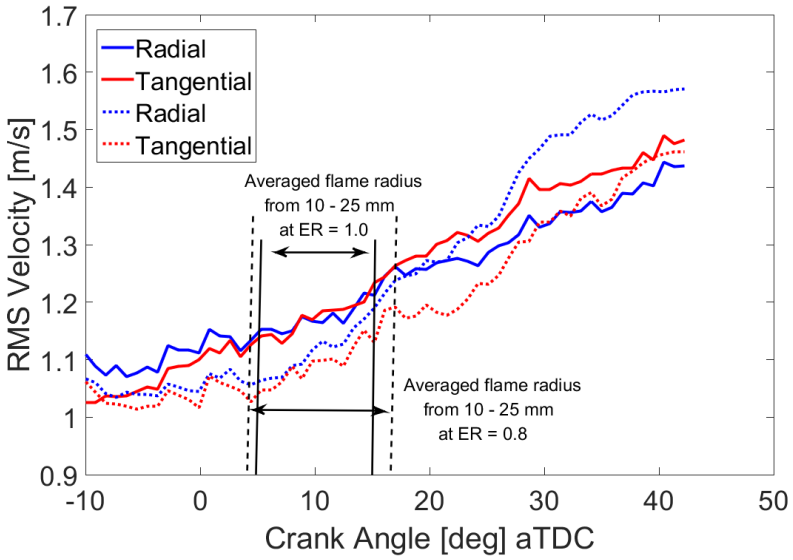

Figure 5.7: RMS velocity as a function of crank angle at 750 RPM based on 50 Motoring cycles based on spatial averaging (solid line) and ensemble averaging (dash line).

interest. This averaged value of u'_r highlights that the turbulence distribution is nearly homogeneous in LUPOE2-D. In 1500 RPM case, the u'_r at in local annulus is around 1.16 m/s at 10 CA aTDC, see Figure 5.10. Similar with 750 RPM, turbulence distributes nearly homogeneous at 1500 RPM. Therefore, in Chapter 6 studies, cold flow turbulent u'_r can be treated as constant in any position in the studied plane.

Figure 5.11 shows the longitudinal integral length scale along X-axis L_{xx} and Y-axis L_{yy} in a sample window size 100 x 100 where the bottom of the window located at 10 mm above the centre. there is no clear observations that the longitudinal integral length scale is affected by the engine speed. Between 750 and 1500 RPM, the integral length scale is about the same value. For the transversal integral length scales, the value is about half of its longitudinal integral length scale. Because of there are only 30 cycles were used in deriving the integral length scale. The ratio of the longitudinal integral length over transversal integral length is not always about 2 and the L_{xx} and Y-axis L_{yy} are not always same. From the integral length scale result, it is highly possible that the in-cylinder turbulence is homogeneous. From the longitudinal integral length scale trace across the studied period, there is a trend shows the integral length scale increases with the increasing of crank angle through the whole recorded period. Overall, the turbulent integral length scales L is about 3.5 mm at 10 CA aTDC and this value will be used for later

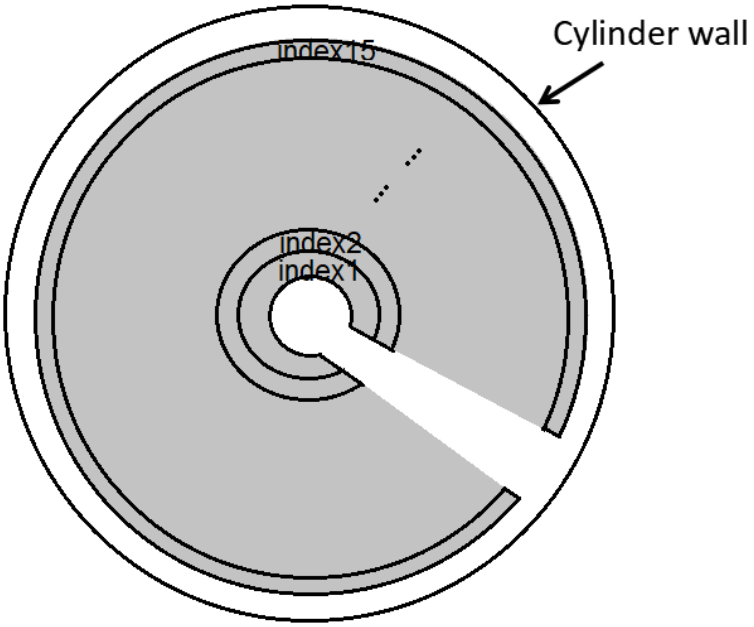

Figure 5.8: The partition of ROI

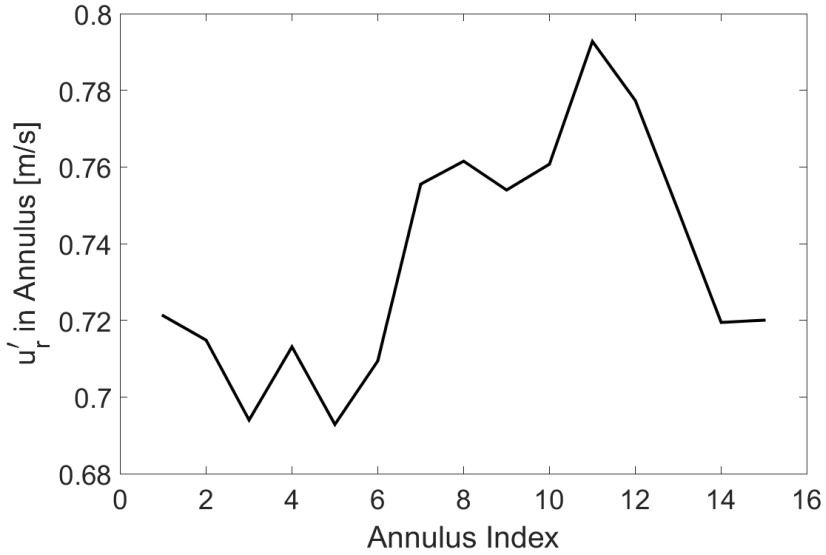

Figure 5.9: The u_r' derived from spatial averaging at local annulus at 10 CA aTDC based on 50 motoring cycles at 750 RPM.

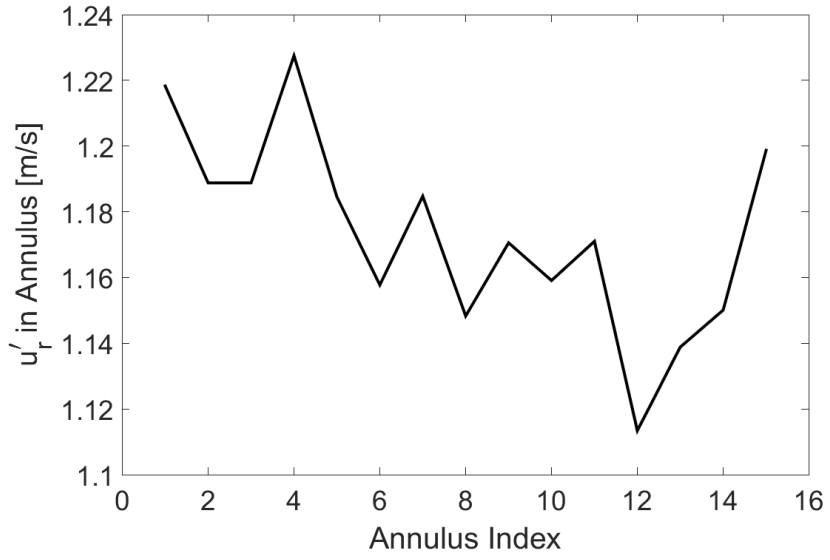

Figure 5.10: The u'_r derived from spatial averaging at local annulus at 10 CA aTDC based on 50 motoring cycles at 1500 RPM.

flame propagation studies in Chapter 6.

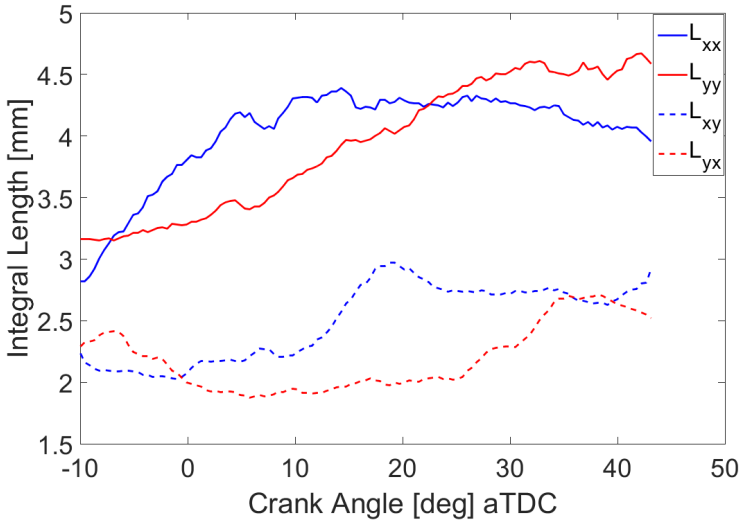

(a) 750 RPM

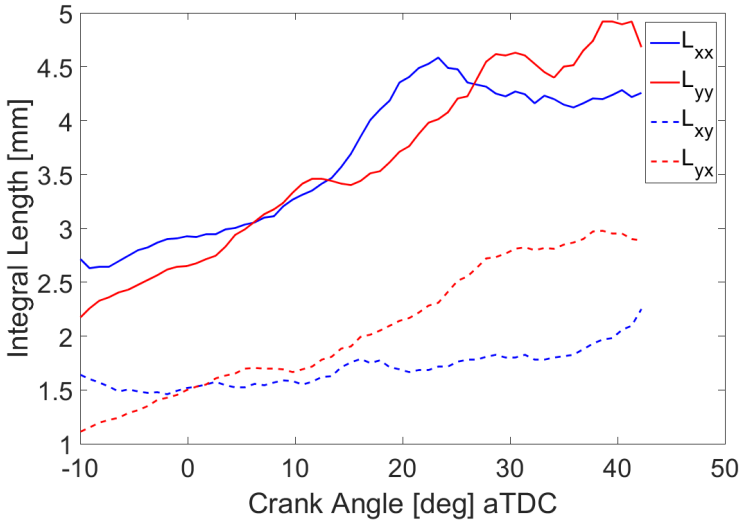

(b) 1500 RPM

Figure 5.11: Cold flow integral length scales as a function of crank angle at 750 and 1500 RPM.

Chapter 6

Characterisation of Combustion

6.1 Fuels and Initial Condition

LUPOE2-D engine can be considered as a reciprocating combustion rig. Since it has spark ignition features, the engine can be used for testing fuel combustion in strongly boosted engine. The combustion pressure, flame speed and anti-knock characteristics were obtained for varieties of fuels, i.e. knock boundary, knock onset, knock intensity after the knock boundary. This Chapter focus on the combustion performance of bio-derived fuel blends in strongly charged engine. The fuels include a reference commercial unleaded gasoline (ULG) with RON (Research Octane Number) of 95, and a toluene reference fuel that matches the RON and the hydrogen/carbon ratio. A series of fuel blends were also employed, such as ULGB20 (20:80 volumetric n-butanol:ULG), ULGD20 (20:80 volumetric 2,5-dimethylfuran:ULG), TRFB20 (20:80 volumetric n-butanol:TRF) and TRFD20 (20:80 volumetric 2,5-dimethylfuran:TRF). The property of the bio-derived fuel (Cooney et al. 2009, Rothamer & Jennings 2012) and the fuel blends are listed in Table 6.1 and Table 6.2. The tests were conducted under, an engine speed of 750 RPM and a constant intake air flow rate of 10.2 gs^{-1} producing 1.65 bar of the initial pressure i.e. pressure in the cylinder at the moment of ports closure. Combustion routinely produced knock and high combustion pressure, hence a metal head was employed. Because of this, LUSIEDA was used to derive the combustion process from the measured pressure trace.

The averaged pressures from 50 motoring cycles for the stoichiometric air-fuel mixtures is shown in Figure 6.1. Due to blow-by and heat losses occurred for the present engine, the in-cylinder pressures for all mixtures reach the peak value at 1.2 CA bTDC with a similar value 32 bar. Due to the lack of knowledge

Table 6.1: Properties of the bio-derived fuel used in current study

Fuel Name	LCV [MJ/kg]	RON	MON	Air/Fuel at ER = 1
n-butanol	33.1	96	78	11.2
2,5-DMF	33.3	101	88	10.8

Table 6.2: Properties of the fuels used in current study

Fuel Name	% vol. Blend	LCV [MJ/kg]	RON†	MON†	Air/Fuel at ER = 1
ULG	–	42.34	95.0	86.6	14.2
TRF	65.63 iso-octane, 11.40 n-heptane, 22.97 Toluene	42.83	95.0	89.8	14.5
ULGB20	80 ULG, 20 n-butanol	40.13	95.3‡	84.2‡	13.6
TRFB20	80 TRF, 20 n-butanol	40.60	95.3	86.5	13.8
ULGD20	80 ULG, 20 n-butanol	40.35	96.5‡	87.0‡	13.4
TRFD20	80 TRF, 20 2,5-dimethylfuran	41.00	96.5	89.4	13.6

†basd mole fraction mixing rule (Pera & Knop 2012).

‡basd on TRF mole fraction in the mixture.

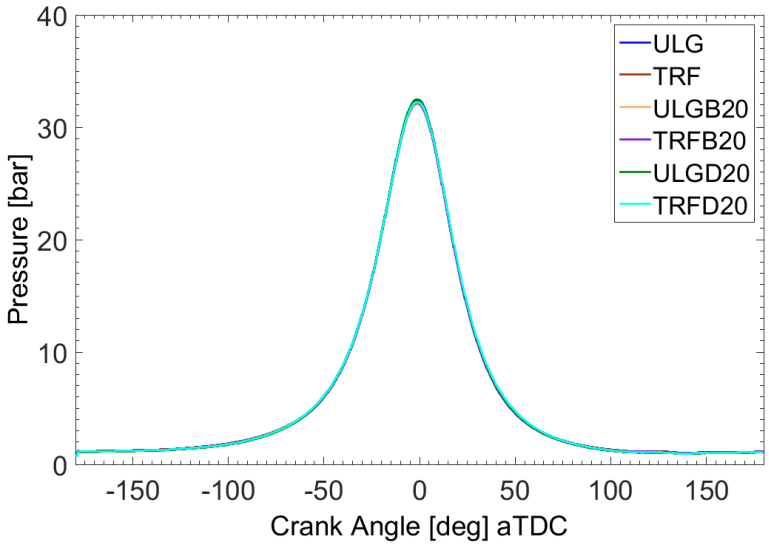

Figure 6.1: Averaged motoring pressure of stoichiometric air fuel mixtures at engine speed 750 RPM from 30 cycles

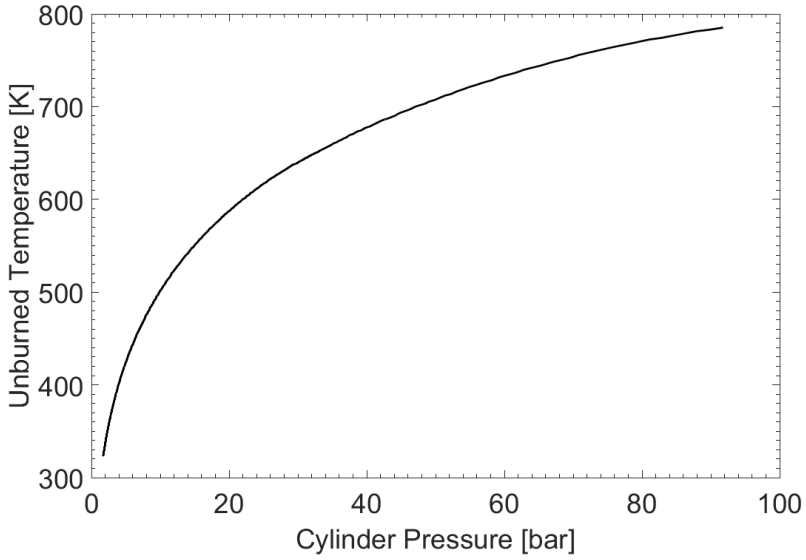

Figure 6.2: The typical unburned temperature of stoichiometric iso-octane/air mixture as a function of in-cylinder pressure at engine speed 750 RPM.

on the temperature dependence of heat capacity ratio γ for the mixed fuels, the polynomial function based on iso-octane was applied by LUSIEDA for calculating the γ value of fuels and air-fuel mixtures. A typical temperature curve as a function of pressure was plotted for stoichiometric ULG-air mixture see Figure 6.2. The temperature reads 640 K at 30 bar, and 648 K at 32 bar.

6.2 Pressure and Flame Speed in The Normal Combustion Event

All the tests were run at a constant spark timing the optimum timing for max power like conventional engines. Because of this, the combustion pressures of all the fuels were sampled at engine speed of 750 RPM with spark timing of 2^o bTDC to avoid any knocking cycles, see Figure 6.3. The pressure traces have been sampled for 50 runs for all the fuels, and the averaged pressure from these 50 runs were compared and presented in Figure 6.4. According to Figure 6.4, adding 20% by volume of n-butanol has little influence on the peak pressure. The ULG and TRF blends are all sharing the same pressure trace as their n-butanol blends. For the 2,5-DMF blends, the peak pressure of TRFD20 is lower than that of the pure TRF, which the blends about 9% of peak pressure drop. On the contrary, there is little difference on mean pressure between ULGD20 and ULG. Table 6.3 summaries the pressure characteristics from Figures 6.3 and 6.4. As shown in table, COV and COV_{CA} highly agree with each other for all fuels. A retarded peak pressure was observed for TRFD20, which indicates a larger cylinder volume. Meanwhile, the in-cylinder pressure of TRFD20 is higher than other fuels during the expansion stroke after 30 CA aTDC. As a result, the IMEP indicating overall pressure work for TRFD20 is almost identify with other fuels.

Flame speed derived by LUSIEDA is shown in Figure 6.5. As can be seen, the flame propagation can be classified as three stages refer to Liu et al. (2013): initial acceleration, fully developed and deceleration stage when the flame radius grows from 0 - 12 mm, 12 - 32 mm and 32 - 40 mm, respectively. Flame radius from 0 - 12 mm, the burned mass is usually within 3% of total mass, see Figure 6.6. At small initial fraction of burned mass, it is difficult to derive the accurate flame

Table 6.3: Summaries for Figure 6.3 and 6.4

Fuel Name	Mean Peak Pressure [bar]	Mean Peak Pressure at Crank Angle [deg] aTDC	COV	COV_{CA}	IMEP [bar]
ULG	73.03	23.86	0.0747	0.0631	10.78
TRF	67.66	25.91	0.1156	0.0923	10.30
ULGB20	72.47	23.48	0.0732	0.0724	10.48
TRFB20	65.94	25.81	0.0681	0.0693	10.39
ULGD20	72.28	24.31	0.0605	0.0554	10.93
TRFD20	61.06	28.80	0.0884	0.0748	10.67

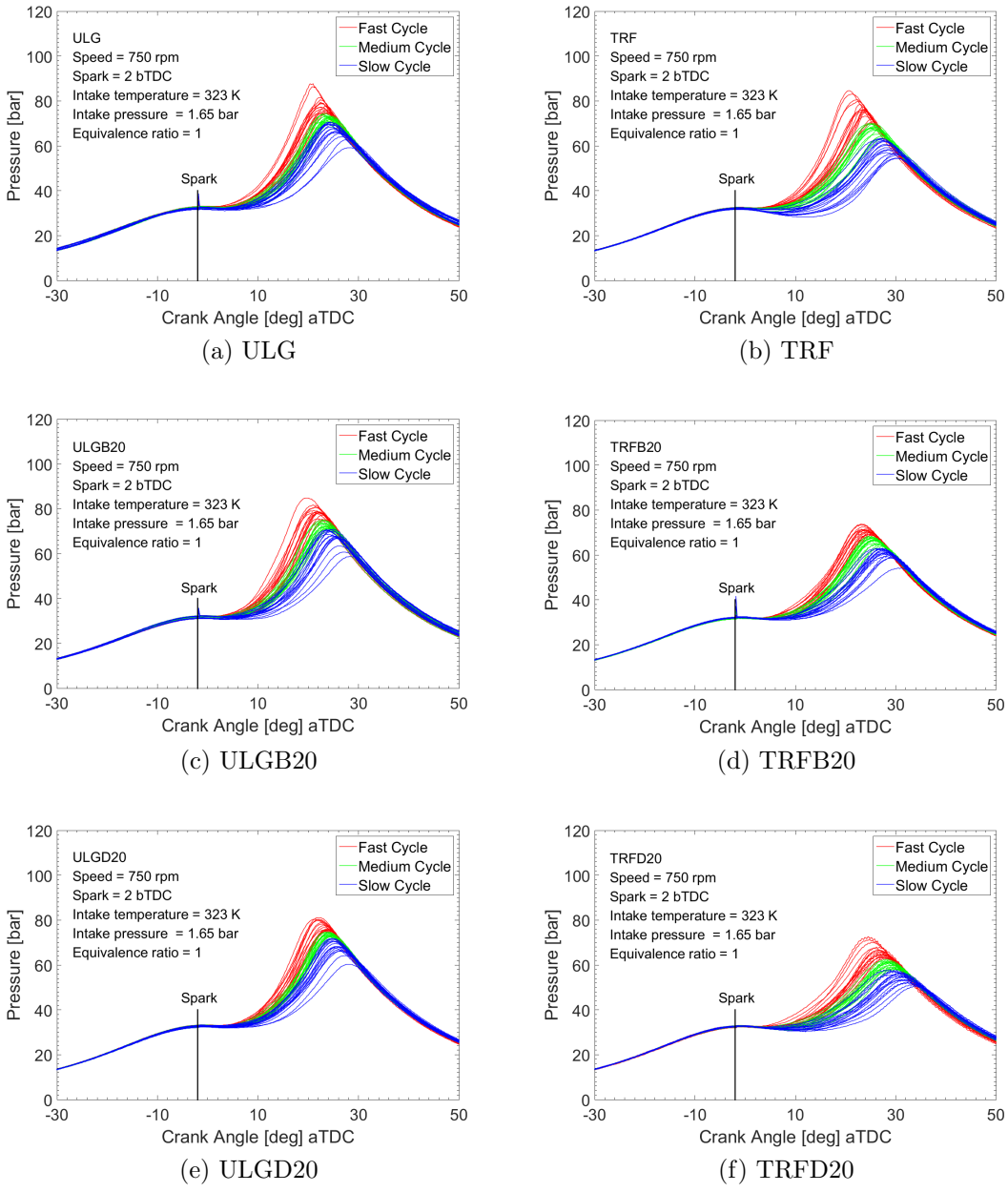

Figure 6.3: Pressure traces collected from LUPOE2-D 50 explosions for the fuels at spark timing of 2 CA bTDC. (a) ULG (b) TRF (c) ULGB20 (d) TRFB20 (e) ULGD20 (f) TRFD20.

radius from the pressure trace because of pressure signal noise is strongly affect on deriving flame speed. Therefore, the present work focus on the flame propagation duration instead of flame speed for the initial stage. The fully developed stage is taken at flame radius from 12 - 32 mm, because the flame stops accelerating during

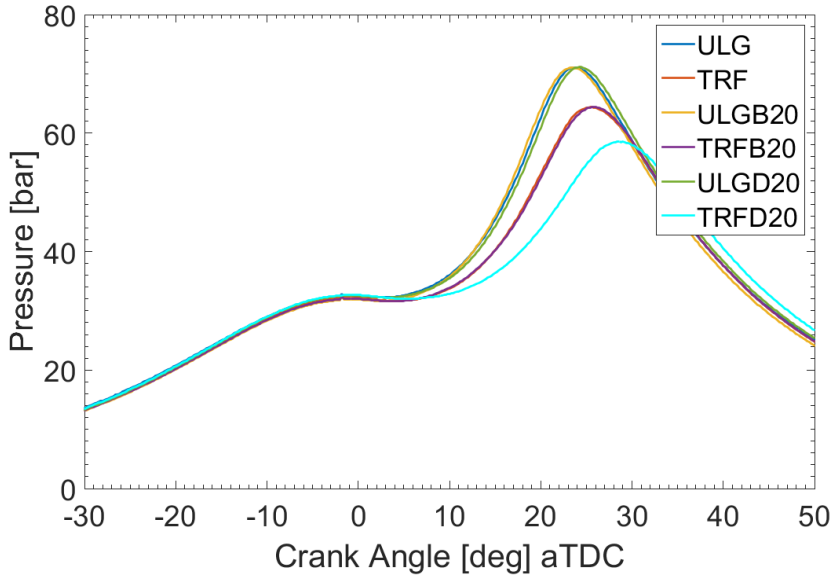

Figure 6.4: Mean pressure of the fuels at speak timing of 2 CA bTDC.

this stage and maintain nearly a constant flame speed before the deceleration happens due to the FWI. During this stage, up to 30% of mass is burned. The final deceleration stage occurs for the flame radius 32 - 40 mm. In this stage, the majority of mass fraction is burned and it is responsible for major pressure rise.

The classification of cyclic variation of combustion in this study was determined by peak combustion pressures. According to Figure 6.3, the fast cycles in most of the cases reach their peak pressure much earlier comparing with other cycles. A clear distinguish of fast cycles from the rest of the cycles is possible from 5 CA after spark released. However, a 5 CA duration for flame propagation is short considering ULG takes average of 7.82 CA to reach flame radius of 12 mm and more than 25 CA for all three flame propagation stages. According to Figure 6.6, although the most of the pressure rise due to the consumption of a large amount of mixtures occurs from flame radius 30 mm to 40 mm, and less than 3% of mixture was burned during the initial combustion period, the cycle-to-cycle variation could be foreseen after a 5 CA duration after spark released. Figure 6.5 shows clearly that the flame speed races start to vary cyclically since flame radius about 8 mm. Furthermore, the flame speed of fast cycle is staying at a relative higher level compared with the medium and slow cycles shortly after the latter period of the initial stage. A few number of fast cycles have relatively slower flame propagation speed at the end of the initial stage, and their flame speeds elevated during the later propagation stage. It seems that the variation of flame

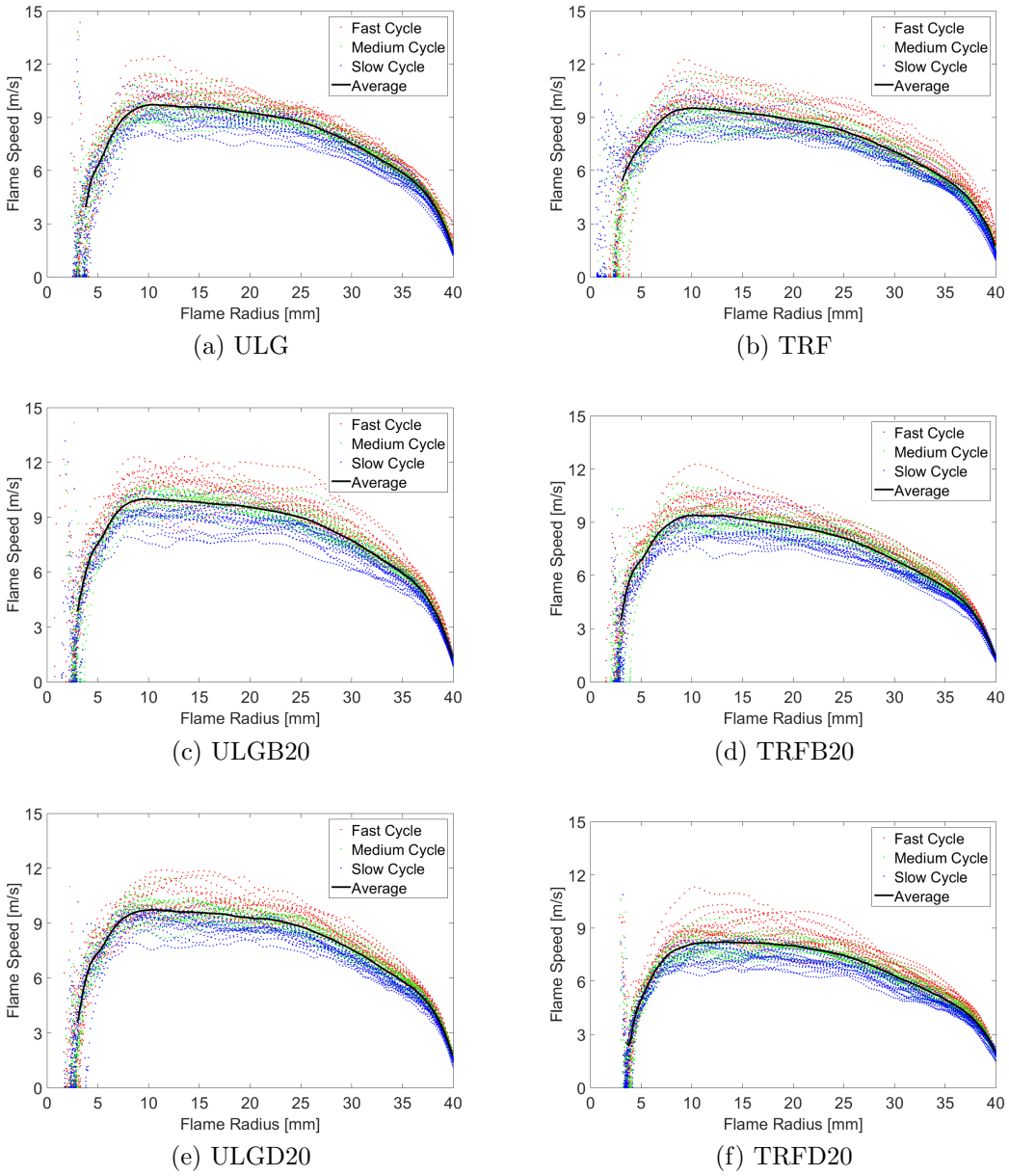

(a) ULG (b) TRF

(c) ULGB20 (d) TRFB20

(e) ULGD20 (f) TRFD20

Figure 6.5: LUSIEDA derived flame speed from Figure 6.3. (a) ULG (b) TRF (c) ULGB20 (d) TRFB20 (e) TRFD20; data samples for fast cycles are in red color, medium cycles in green, slow cycles in blue

speed is not the major source of the cycle-to-cycle variations. The result shows the cycle-to-cycle variations potentially arises from the flame initial stage. There are several potential sources of cycle-to-cycle variations. Bardin et al. (2014) listed a number of potential sources that could be eliminated or minimized by particular equipment proved that the variations were coming from the initial stage.

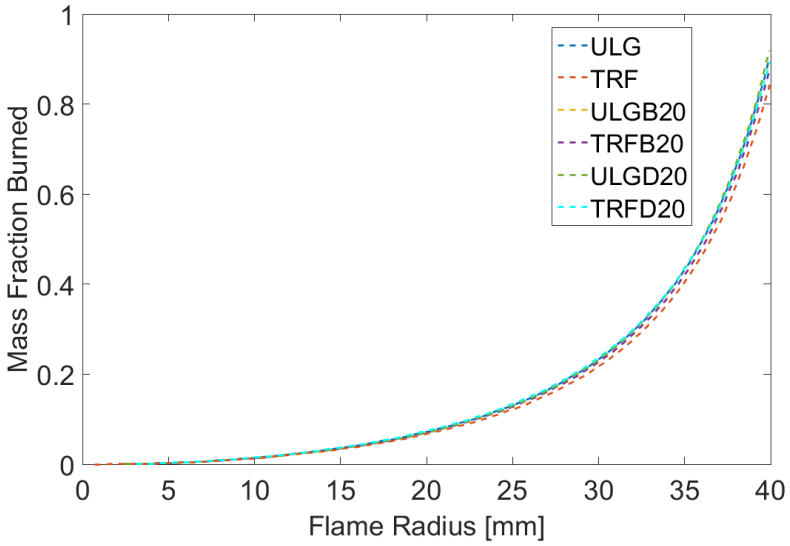

Figure 6.6: Burned gas mass fraction with respect to flame radius derived from LUSIEDA.

According to the Table 6.4, adding 20% by volume of n-butanol to ULG improves the flame speed slightly. However, for TRFB20, n-butanol lowers the flame speed slightly. Overall, the results show that n-butanol has little influence on the combustion duration and the fully developed flame speed. The ULG has a comparable flame speed with ULGD20 except a slight increase at the initial stage. On the contrary, TRFD20 reduces the flame speed more than 10% as compared with TRF. The final deceleration stage of all six fuels is taken upto one third of the total combustion duration. Furthermore, there is no major difference in final deceleration duration. The TRFD20 was expected to have a longer combustion duration due to its longest initial and fully developed stage duration among all six fuels. However, the results show the flame speed in fully developed stage has little effect on final stage duration. Overall, the TRF and ULG have comparable fully developed flame speeds. TRF flame speed is slightly, about 5%, lower than that of ULG, since iso-octane is occupying nearly two third of total TRF volume and its flame speed is lower than ULG at the condition of $\phi = 1$, 750 RPM (shown in Chapter 7.2.2). However, TRF is showing 13.4% longer initial combustion duration than ULG. There is a small extension of initial combustion duration by adding 2,5-DMF to both ULG and TRF.

From Table 6.5, the COVs for the fully developed flame stage duration of all six fuels present some disagreement with COVs of peak pressures listed in Table 6.3: the TRF fully developed flame stage duration has little variation comparing

Table 6.4: Combustion stage and flame speed derived by LUSIEDA.

Fuel Name	Initial Stage Duration [deg]	Fully Developed Stage Duration [deg]	Average Flame Speed at Fully Developed Stage [m/s]	Final Deceleration Duration [deg]
ULG	7.82	10.30	8.82	7.92
TRF	8.64	10.85	8.41	8.34
ULGB20	7.80	10.06	9.06	8.30
TRFB20	8.56	11.01	8.30	8.87
ULGD20	8.12	10.32	8.86	8.10
TRFD20	9.07	12.16	7.52	8.70

with its largest COV_{CA} among the fuels. In addition, according to Figure 6.7, the variations of averaged flame speed in this combustion stage for all six fuels do not show explicit links with variations of peak pressures. As a result, it seems that the effect of fully developed flame speed variations on cycle-to-cycle variations is limited. Figure 6.7 shows the COV of duration of each fuel has a good agreement with the peak pressure variations during the initial combustion stage. Although the COV of final stage duration shows similar result, the final stage duration is not the main reason for total combustion length since there is only small difference in the final stage duration, and the difference is less than 1 CA among all six fuels. Furthermore, in final combustion stage, the temperature and pressure of unburned mixtures are influenced by the previous combustion stages. As a result, the cycle-to-cycle variation may mainly come from the initial combustion period. Figure 6.8 shows the peak pressure with respect to the initial stage duration. The

Table 6.5: COVs of three combustion stages for the fuels

Fuel Name	COV of Initial Stage Duration	COV of Fully Developed Stage Duration	COV of Flame Speed in Fully Developed Stage	COV of Final Deceleration Duration
ULG	0.0786	0.0639	0.0611	0.0745
TRF	0.1542	0.0769	0.0806	0.1050
ULGB20	0.0819	0.0843	0.0822	0.0845
TRFB20	0.0769	0.0739	0.0725	0.0550
ULGD20	0.0583	0.0654	0.0681	0.0669
TRFD20	0.0887	0.0806	0.0842	0.0752

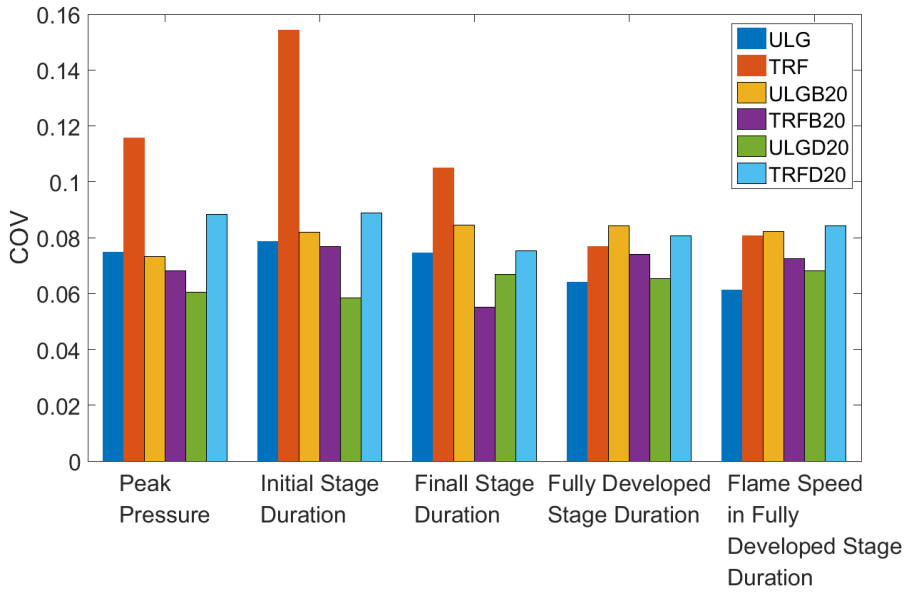

Figure 6.7: Variation of: peak pressure, each flame propagation stage duration and flame speed fully developed stage.

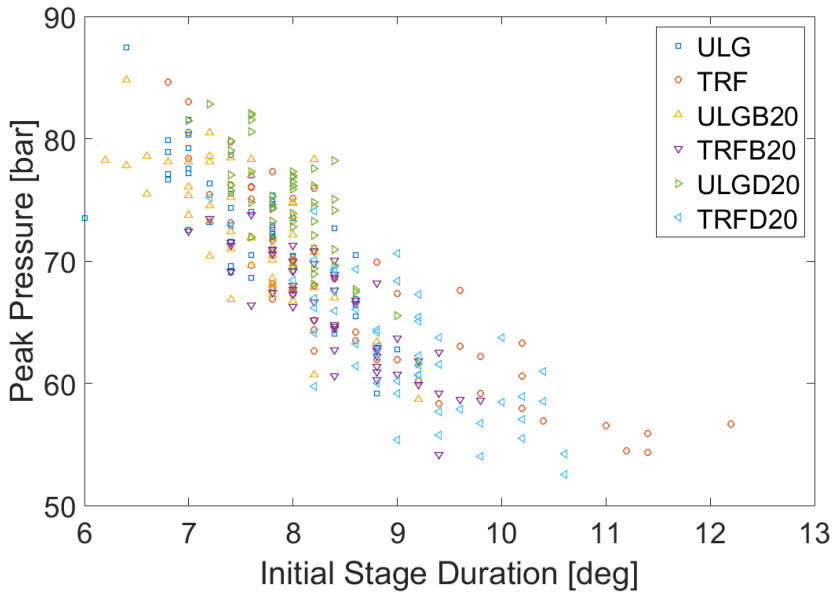

Figure 6.8: Peak pressure with respect to the initial stage duration

initial stage duration has a noticeable impact on the peak pressure: the shorter the initial stage duration, the higher the peak pressure.

6.3 Effect of Spark Timing on Combustion

6.3.1 Combustion Duration

Results upon the combustion pressure for a wide range of spark timing are reported and discussed in this section. Figure 6.9 shows the impact of sparking timing on the averaged combustion pressure inside the LUPOE2-D engine. There is little difference in averaged peak pressures among the ULG and ULG blends until the spark timing reaches 5 CA bTDC. For the retarded ignition timing behind 5 CA bTDC, the peak pressures start to deviate among the ULG and its blends due to the appearance of the knocking cycles involved in averaging peak pressure. ULG and ULGB20 share the most common trace. However, the average peak pressure of ULGD20 is close to the TRF and TRFB20 at a very advanced spark timing. TRF and TRFB20 share a similar averaged peak pressure trace despite a narrow range of speak timing settings cause disagreement of the pressures. Since the knock occurs over half of the combustion cycles, hence raises the averaged pressure. There is no strong knock observed across all spark timing for TRFB20. And its pressure trace is slightly lower than TRF after spark timing 4 CA bTDC. TRFD20 shows the lowest averaged peak pressure. Advancing the spark timing for TRFD20 provides a similar amount of growth in averaged peak pressure compared with TRFB20 and TRF.

Advancing spark timing may result in knocks in the combustion chamber that causes a sudden rise of flame speed as predicted by LUSIEDA, see Figure 6.10. Considering the knock may potentially show up during the fully developed flame and deceleration stage, and interfere the flame radius derived by LUSIEDA in the fully developed flame and deceleration stage, this study will focus on the initial stage of combustion phase. Figure 6.12 shows initial combustion durations of different fuels gradually decrease by using advanced spark timing.

ULGB20 and TRF exhibit a little fluctuation on initial stage duration. Adding 20% by volume of n-butanol is not affecting the initial combustion durations of ULGB20, but reduces that of TRFB20 at sparking timing 4 CA and 6CA bTDC. This may come from the experiment errors, since the derived flame radius is very sensitive to the pressure. However, the unusual initial stage duration of TRF is also shown in mean peak pressure in Figure 6.9. Adding 20% by volume of 2,5-DMF to TRF prolongs the initial combustion duration for about 0.5 CA or 0.1 ms compared to the base fuel. For ULG as base fuel, adding 20% by volume of 2,5-DMF result in a slight increase in initial stage duration.

Overall, advancing the spark timing from 2 CA bTDC to 10 CA bTDC, the

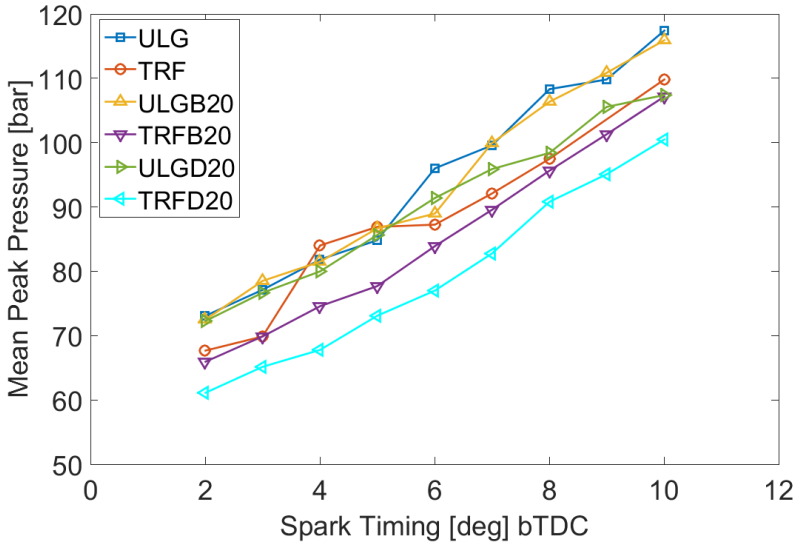

Figure 6.9: Spark timing influence upon the filtered peak combustion pressures.

averaged initial temperature drops from 649 K to 637 K, and the averaged pressure drops from 32.8 bar to 29.1 bar. Considering the whole flame propagation history, the temperature and the effect of pressure on flame speed at the moment when spark engaged is negligible. Figure 6.11 shows the effect of spark timing on fresh gas temperature at end of the initial acceleration stage. At the end of initial combustion stage of ULG, the averaged unburned temperature for spark timing of 2 CA bTDC and 10 CA bTDC is 644 K and 664 K, respectively. Similarly, other fuels also show a temperature increased around 20 K at the ending point of initial combustion stage when advancing the sparking timing from 2 CA bTDC to 10 CA bTDC. However, the tendency of initial stage duration for different spark timing does not follow the same relationships. Furthermore, it is clearly showing that the temperatures of fresh gas at end of initial stage are similar at spark the timing 8 and 10 CA bTDC. But there is still a wide spread of the initial stage durations. It seems that the temperature is not the only driving force causing the decrease of initial combustion period with an advanced spark timing.

The difference of initial combustion duration results in different combustion temperatures at fully developed stage. In Figure 6.5, the fully developed flame speeds derived from LUSIEDA for these fuels were based on different unburned temperature, since they were under different cylinder pressure. Instead of comparing the flame speed for the same spark timing, the comparison is taken at the same fresh gas temperature. Because the unburned temperature directly links to the pressure, the identified unburned temperature can derived from the same in-

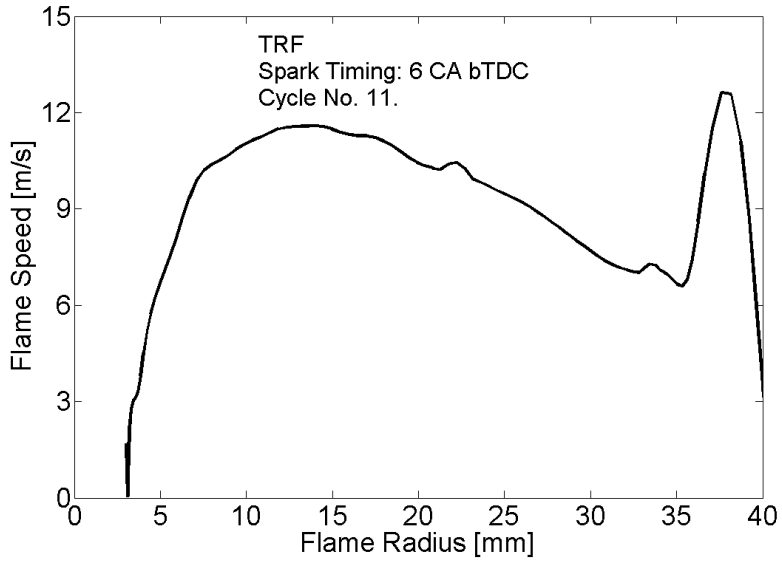

Figure 6.10: Typical knocking cycle flame speed derived by LUSIEDA, the knock happens on average flame radius of 35 mm where a sudden rise of the flame speed.

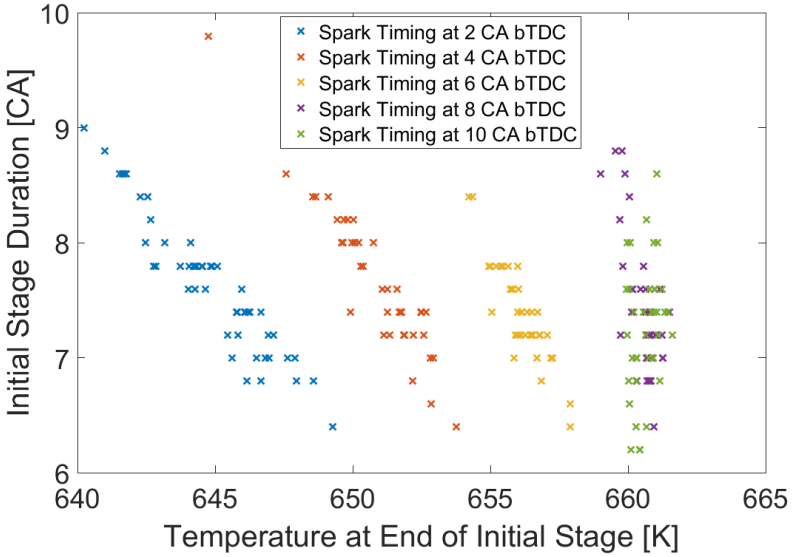

Figure 6.11: ULG fresh gas temperature at the end of the initial acceleration stage for different spark timing.

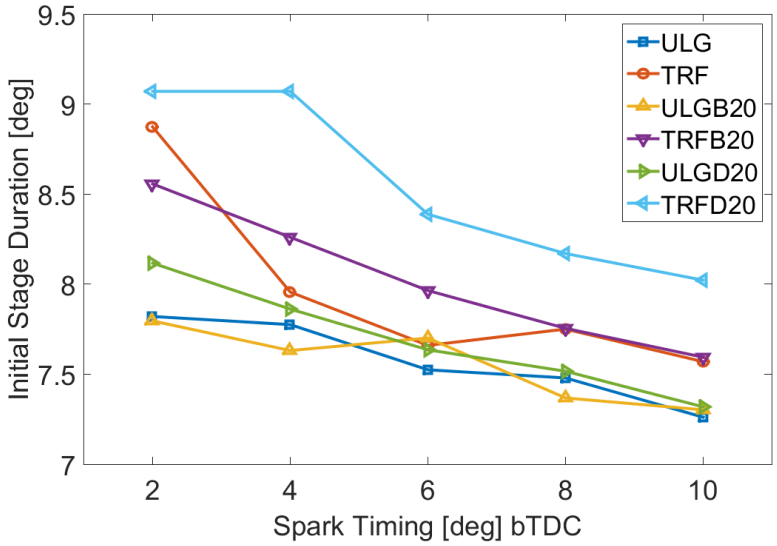

Figure 6.12: Averaged initial combustion duration for the fuels under different spark timing.

cylinder pressure. As a result, fully developed flame speeds for these fuels could be compared under the similar temperature and pressure. Figure 6.13 demonstrates the flame speed with respect to fresh gas temperature at the moment when flame radius at about 20 mm. Flame speeds of ULG and TRF at lower unburned temperature e.g. at 650 K, is very close to each other. For the unburned temperature at 680 K, flame speed of ULG is about 4% faster than TRF. Furthermore, ULFB20 shows a similar flame speed as the base fuel in most of the cases. However, the flame speed of TRFB20 is slightly lower than its base fuel at low temperature region (¡670 K). At the high temperature region, the flame speed of TRFB20 tends to be faster than its base fuel. For ULGD20, the flame speed reduces slightly by about 0.24 m/s compared to ULG, at temperature of 670 K. Compared to TRF and TRFD20 at 670K, 20% by volume of 2,5-DMF cases about 0.72 m/s of flame speed reduction, around 7.3% slower. There is agreement between ULG and TRF that adding 2,5-DMF will result in a reduction of flame speed. And TRFD20 shows the lowest pressure comparing with other five fuels.

Overall, from unburned temperature 650 K to 680 K (pressure from 33 bar to 40 bar), the flame speed increases for ULG, TRF, ULGB20, TRFB20, ULGD20, TRFD20 are 17.7%, 14.6%, 14.2%, 20.1%, 18.2%, 20.2%, respectively. There is an approximately 5% increase in fresh gas temperature. According to Metghalchi & Keck (1982), the temperature result in 10% increase of the laminar burning velocity in this case. However, the turbulent flame speed increases more than

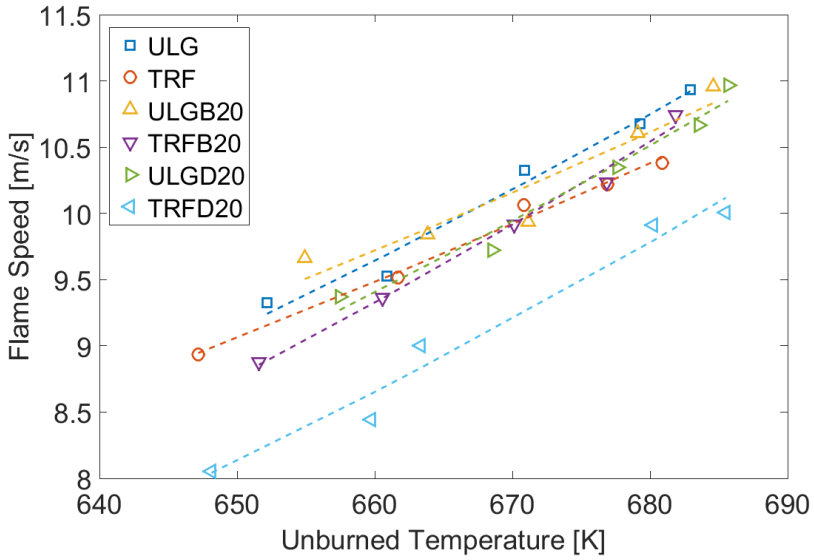

Figure 6.13: Averaged flame speed at flame radius of 20 mm under different spark timing with respect to unburned temperature for these six fuels.

10%. The turbulence and its length scale measured in motoring cycle are nearly constant during this stage. This indicates that temperature and pressure may play significant roles on the flame propagation speed. However, the effect of temperature seems strong approximately $S_t \sim T^3$ and Zimont approximation (Zimont et al. 1998) that estimated about $S_t \sim T$ could not match the change of flame speed that varies linearly with the temperature.

6.3.2 Knock Boundary and Pressure Oscillation

The knock boundary in this study is defined as the spark timing which produced knock in 30% of all cycles. The knock boundaries observed from pressure traces for ULG, TRF, ULGB20, TRFB20, ULGD20, TRFD20 are 6 CA bTDC, 4 CA bTDC, 7 CA bTDC, 9 CA bTDC, 10 CA bTDC, 10 CA bTDC, respectively. According to Figure 6.9, the maximum value of averaged peak pressure that ULG, TRF, ULGB20, TRFB20, TRFD20 can reach before the knock boundary are 84.8 bar, 69.8 bar, 89.0 bar, 95.1 bar, 105.5 bar, and 95.6 bar respectively. At this point, adding n-butanol or 2,5-DMF will enable the strongly charged engine to achieve higher peak pressure before knock appearing in the combustion phase. Especially those TRF-based fuel blends, there is an over 30 bar elevation on the averaged maximum pressure for the knock boundary after blending with butanol or 2,5-DMF.

In addition, for those knocking cycles MAPO greater than 1 bar are observed for ULG, TRF and ULGB20 at their knock boundary. For TRFB20, TRFD20 and ULGD20, current spark timing of 10 bTDC, could not observe any knocking cycle that MAPO reaches 1 bar. In order to investigate n-butanol and 2,5-DMF as additive for improving TRF anti-knock properties, a further advanced spark timing was employed to enable comparisons between these bio-fuels. A spark timing of 14 CA bTDC was applied on TRFB20 to achieve an averaged peak pressure of 122.93 bar and 1.61 bar of averaged MAPO for knocking cycles. A spark timing of 16 CA bTDC was applied on TRFD20 to achieve an averaged peak pressure of 122.69 bar and 1.39 bar of averaged MAPO for knocking cycles.

In Figure 6.14, TRF not only shows the earliest knock boundary but also strong knock after knock boundary comparing with the rest of fuels. Especially at spark timing of 6 CA bTDC, the knocking cycles are very aggressive that pushing average MAPO over 2 bar higher than any other fuels. Although TRF matches RON with ULG and it has higher MON, TRF shows relatively poor anti-knock property which the knock boundary and non-knock peak pressure are the lowest among these fuels. If the blending rule follows volumetric basis, the RON and MON will be 93.2 and 89.4. Still, the poor anti-knock property of TRF was unexpected considering its high MON. ULG at spark timing 10 CA bTDC also exhibits such aggressive raising of averaged MAPO.

For the condition in the present work, the fresh gas temperature at 15 bar T_{comp15} during compression stroke is 552 K. According to Kalghatgi (2005):

$$K = (T_{comp15}0.0056) - 4.68 \tag{6.1}$$

$$OI = (1 - K)RON + KMON \tag{6.2}$$

the Kalghatgi factor K for the operating condition is -1.59. Table 6.6 shows the subsequent octane index (OI) for the operation condition of all six fuels. Because of the negative Kalghatgi factor and the relatively lower MON than RON for all fuels, all six fuels have OI greater than their RON. Since the TRF has a large MON, it results in the smallest OI among the six fuels. And this makes sense that TRF has relatively poor anti-knock performance in a strongly charge engine compared with other five fuels. Although the ULGB20 and ULGD20 show a similar OI, ULGD20 is not showing any traces of strong knock in the spark timing range from 2 - 10 CA bTDC. Similarly, TRFD20 is also showing a mild knock at an advanced spark timing considering the fuels with a similar OI such as ULG, TRFB20.

Table 6.6: Octane index for the six fuels

ULG	TRF	ULGB20	TRFB20	ULGD20	TRFD20
108.3	103.3	112.9	109.3	111.6	107.8

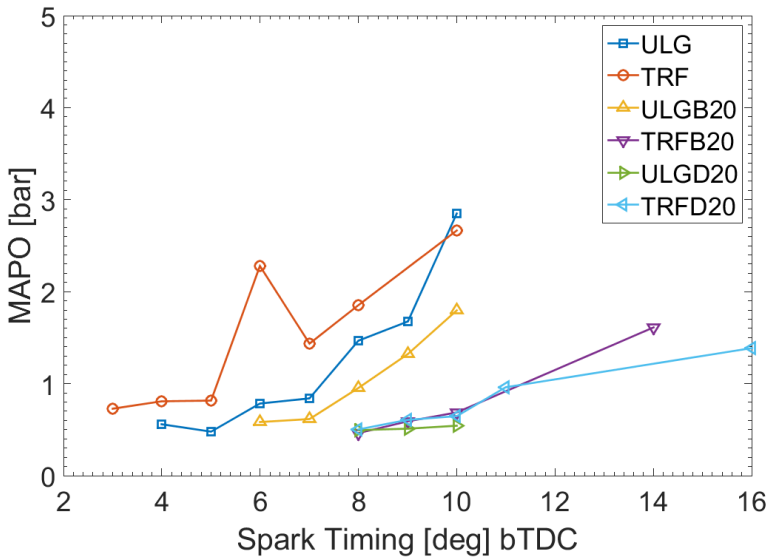

Figure 6.14: Averaged MAPO for knocking cycles with respect to spark timing for these five fuels

The blends TRFB20 and TRFD20 show great improvement on the knock boundary, despite a relatively small MAPO growth rate with advancing spark timing comparing with the rest of fuels. Considering that n-butanol has similar RON and lower MON comparing with TRF which improves the OI of TRFB20, 20% of n-butanol in TRFB20 improved the anti-knock property dramatically by more than 7 OI, both on knock boundary and after the knock boundary. However, the effectiveness of n-butanol in ULGB20 is not as same as it is in TRFB20, there is only 1 CA improvement of knock boundary. After the knock boundary, the MAPO of ULGB20 at spark timing 7 CA to 10 CA bTDC shows the same growth rate that ULG was performed at spark timing from 6 CA to 9 CA bTDC. On the opposite, for ULGD20, there is huge difference comparing with ULGB20, not only knock boundary, but also knock intensity growth after the knock boundary. Instead of performing like ULGB20, the anti-knock property of ULGD20 is like TRF with n-butanol and 2,5-DMF blends.

6.3.3 Knock Onset

The observations of Knock onset is shown in Figure 6.15(a). The auto-ignition kernels are observed at image No.19, in which the flame arising from auto-ignition takes less than 1 ms to takeover whole combustion chamber. Once the auto-ignition occurs, the flames arising from auto-ignition will consume the unburned mixture immediately. From Figure 6.15(b), a huge increase of pressure growth rate straight after the auto-ignition onset was spotted in image No.19. In this study, after identifying a combustion cycle as knocking cycle, knock onset was defined at the crank angle where the one before last crank angle resolved bandpass filter pressure simple is smaller than 0.1 bar. From 6.15(c), the time that the band pass filter pressure reaches a threshold 43.35 ms, about 15.4 CA aTDC. Because the resolution of crank angle is 0.2 CA, the knock onset was defined in this knocking cycle is 15.0 CA, about 0.4 CA (0.09 ms) before the band pass filter pressure reaches the threshold. According the Figure 6.15(a), the image No.19 is located at 43.25 ms, which matches 0.4 CA before the threshold.

Figure 6.16 shows MAPO versus mass fraction burned and cylinder pressure at knock onset for the TRF based on 30 knocking cycles at spark timing of 6 CA bTDC. According to Figure 6.16(a), the intensity of knock decreases with the mass fraction burned at the moment of knock onset. Since the flame radius corresponding to a burned mass fraction 0.7 is usually more than 35 mm, the autoignition is unlikely to occur because of heat losses from cylinder wall and lack of developing space. In some rare cases, knock onset at flame radius around 35 mm. However, the auto-ignition usually result in a mild knock due to lack of space for propagation. Similarly, for a heavy knock, because of low mass fraction burned at auto-ignition occurs, the flame arising from auto-ignition will consume the remaining fresh charge and generate strong pressure waves. Since the mass fraction burned is proportional to pressure rise, Figure 6.16(b) is similar to Figure 6.16(a); it shows MAPO is inversely proportional to the pressure at knock onset. Knock onset at high cylinder pressure results in mild knock and strong knock can be obtained at relatively low cylinder pressure.

Figure 6.17 illustrates the effect of spark timing on knock onset for the TRF. The effect of spark timing on MAPO versus mass fraction at knock onset is mixed within those of the mass fraction burned, see Figure 6.17(a). Due to cycle-to-cycle variations, at same mass fraction burned, the corresponding pressure may different, see Figure 6.17(b). Furthermore, a large quantity of mild knock occurs at the mass fraction burned of 0.5 to 0.7. However, there is no trace showing that any auto-ignition could happen when mass fraction burned is above 0.8. Ling

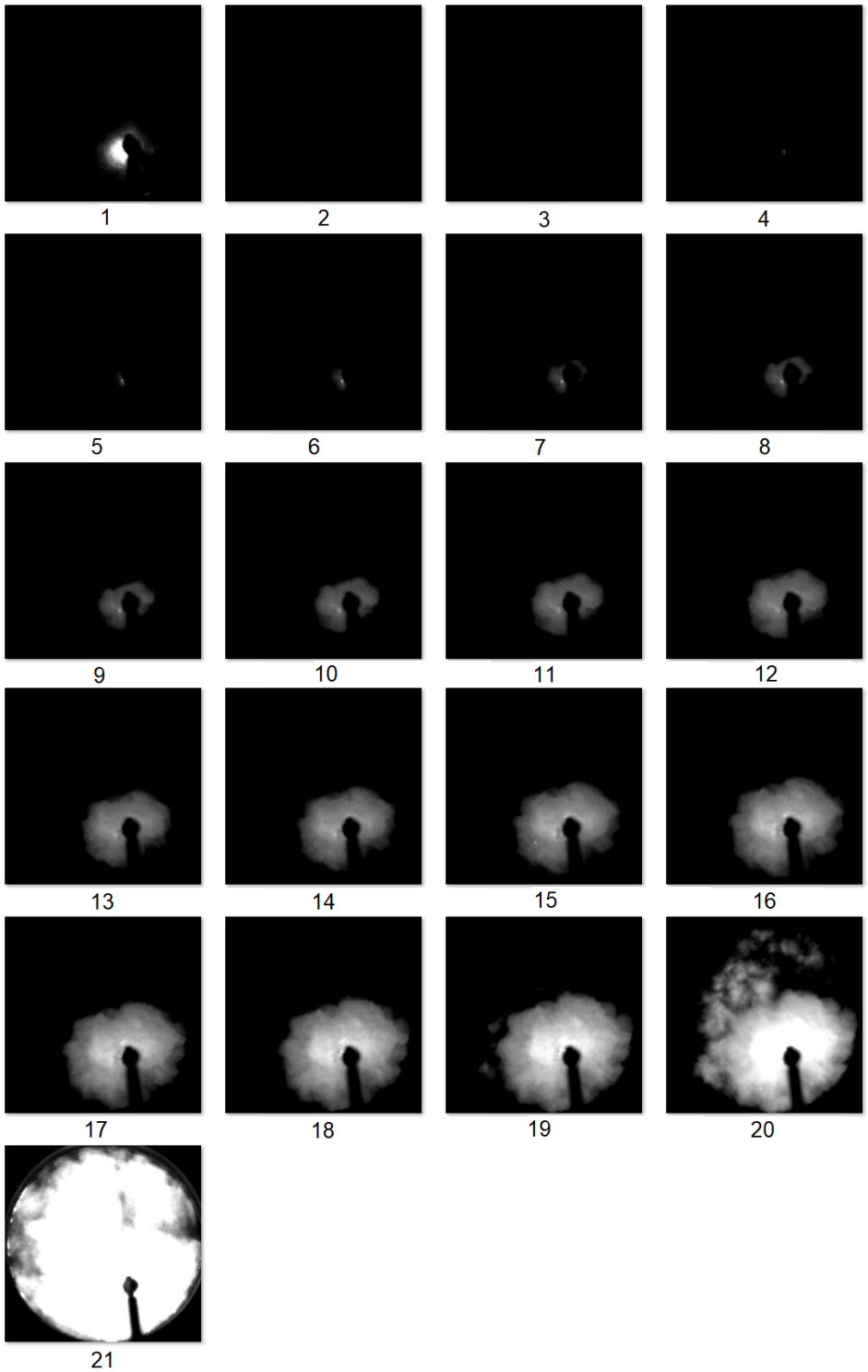

(a) Typical knocking cycle flame images with time interval 0.2 ms. Camera speed of 5000 FPS, engine speed of 750 RPM, side spark applied.

Figure 6.15: Auto-ignition observed in knocking cycle.(To be continued)

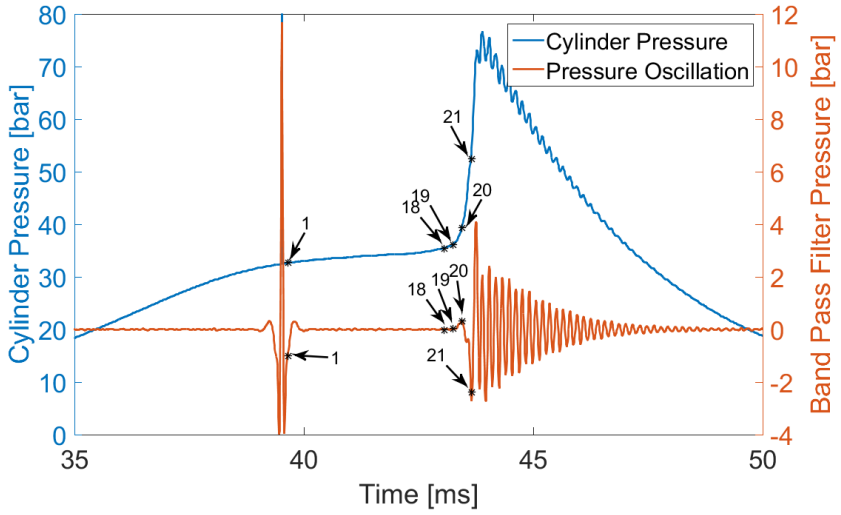

(b) Cylinder pressure collected from the knocking cycle in (a)

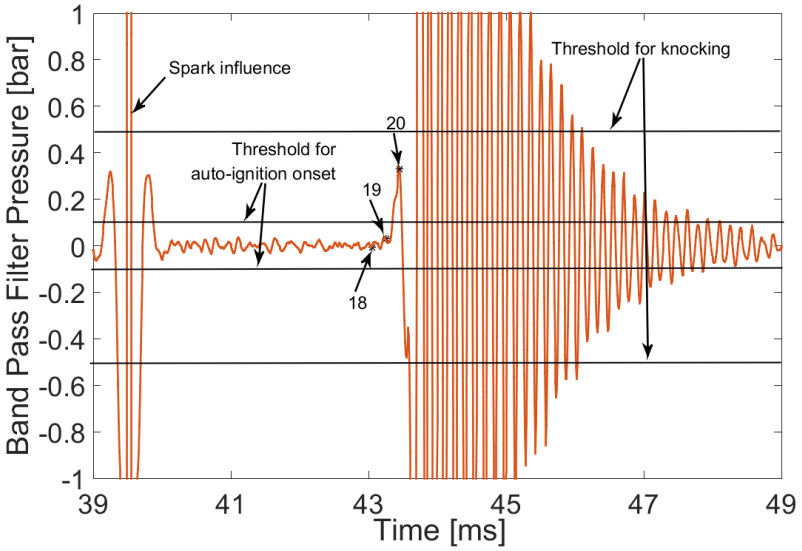

(c) The detailed band pass filter pressure in (b)

Figure 6.15: Auto-ignition observed in knocking cycle.

(2014) investigated autoignition in a boosted and a natural aspirated LUPOE2-D at same intake temperature. It is highly agreed that the amplitude of MAPO is strongly dependent on the mass fraction burned upon knock onset. For the natural aspirated LUPOE2-D with atmosphere intake pressure, the auto-ignition can be observed when mass fraction burned is above 0.8. For 2.1 bar intake pressure, there is no auto-ignition onset when mass fraction burned is above 0.6; for 1.65 bar intake pressure in this study, the maximum mass fraction burned value for

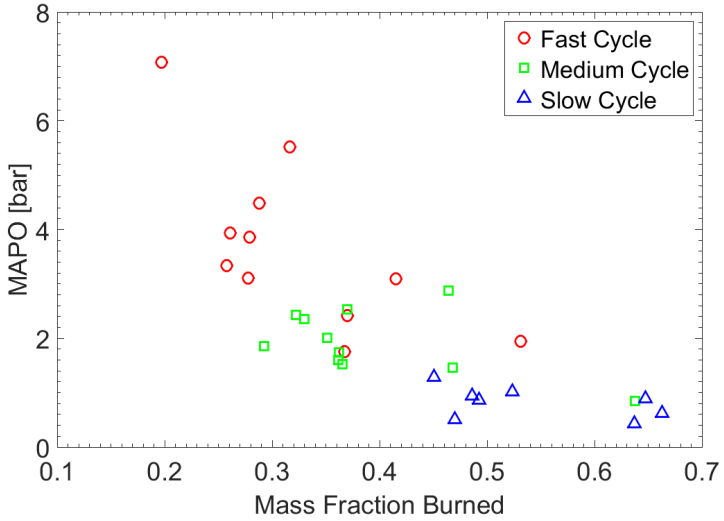

(a) MAPO versus mass fraction burned at knock onset.

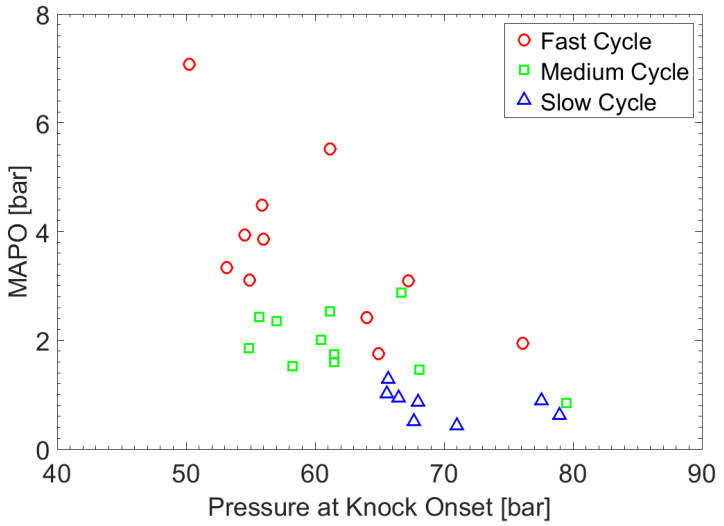

(b) MAPO versus cylinder pressure at the knock onset.

Figure 6.16: MAPO of TRF for spark timing 6 CA bTDC at engine speed 750 RPM

auto-ignition onset is about 0.8. As a result, the upper limit of mass fraction burned for the auto-ignition onset is strongly dependent on intake pressure.

Similarly, Figure 6.18 demonstrates the ULG knocking cycle MAPO with respect to mass fraction burned at knock onset. Comparing with TRF result Figure 6.17(a), ULG and TRF show highly agreement on the upper limit of mass fraction burned that auto-ignition could occur. Once the mass fraction burned was about 0.5, the knock was likely to be mild. Comparing with TRF, ULG seems have

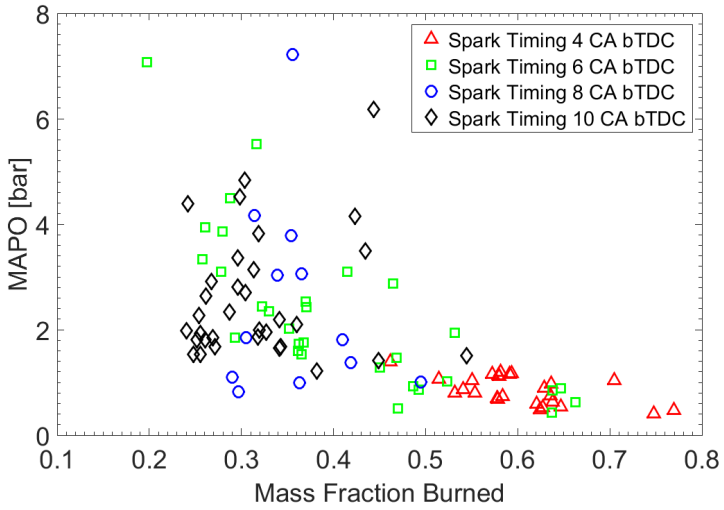

(a) MAPO versus mass fraction burned at the knock onset.

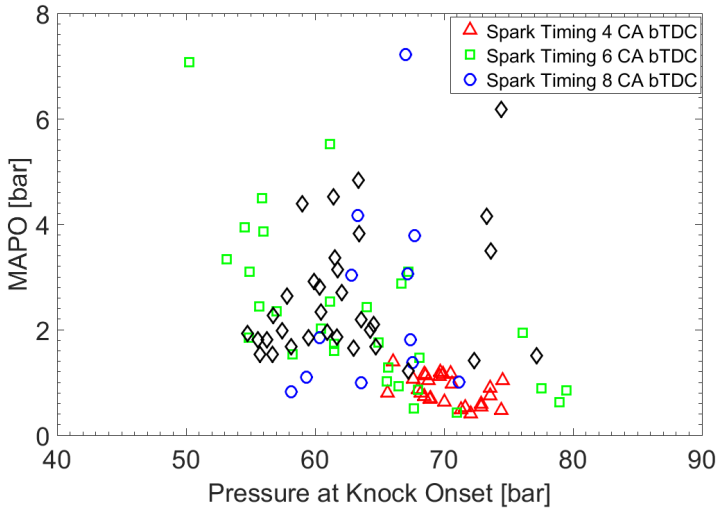

(b) MAPO versus cylinder pressure at the knock onset.

Figure 6.17: MAPO of TRF for spark timing 4 CA bTDC (triangle), 6 CA bTDC (squire), 8 CA bTDC (circle) and 10 CA bTDC (diamond) at engine speed 750 RPM

stronger knock at lower mass fraction burned. However, this may due to other reason according to Ling (2014), the interaction between autoignition sites and autoignition onset position may have a significant impact on the knock intensity.

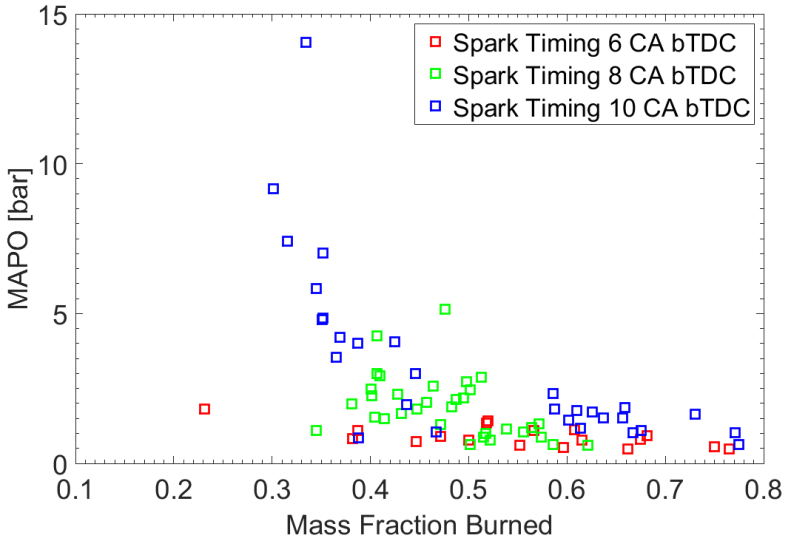

Figure 6.18: MAPO of ULG for spark timing 6 CA bTDC (red), 8 CA bTDC (green) and 10 CA bTDC (blue) at engine speed 750 RPM

Since advancing spark timing results in slightly enhanced flame speeds, the pressure curve growth rate of advanced spark timing usually higher than the retarded spark timing, see Figure 6.19. Because the unburned charge temperature history has a strong dependency on flame speed; and the flame speed can be affected by spark timing. As a result, auto-ignition delay time may be affected by unburned gas temperature history before knock onset due to different spark timing. Therefore, the comparisons of the anti-knock performance among the six fuels should not only focus on the knock boundary, but also the auto-ignition delay time under similar temperature.

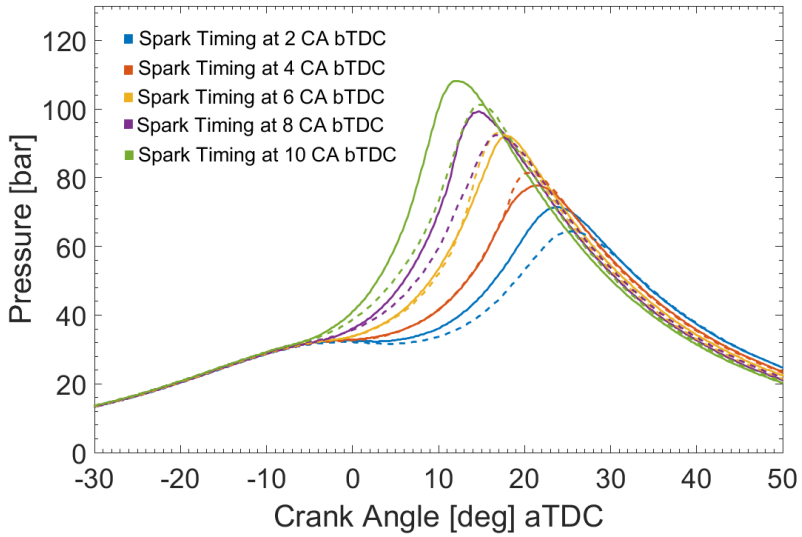

Figure 6.19: Mean pressure trace from ULG (solid) and TRF (dash) at various of spark timing settings at engine speed 750 RPM

In this study, the relative ignition delay is defined as: the time was taken from unburned charge temperature at 600 K to knock onset. Because 600 K as a starting point could avoid the influence of spark timing on unburned charge temperature trace before the starting point. Based on LUSIEDA derived unburned charge temperature shown in Figure 6.20, it is clear showing that with the advancing of spark timing result in high rate of unburned charge temperature rising. On the other hand, the rapid rising of unburned temperature leads to short relative ignition delay. Figure 6.22 demonstrates the averaged relative ignition delay at same spark setting. TRF shows shorter relative ignition delay at spark timing of 6 CA bTDC. However, for spark timing of 8 CA and 10 CA bTDC, TRF shows longer relative ignition delay than ULG and ULGB20. The ignition delay was investigated by Leeds RCM for the same fuels at pressure of 20 bar, according

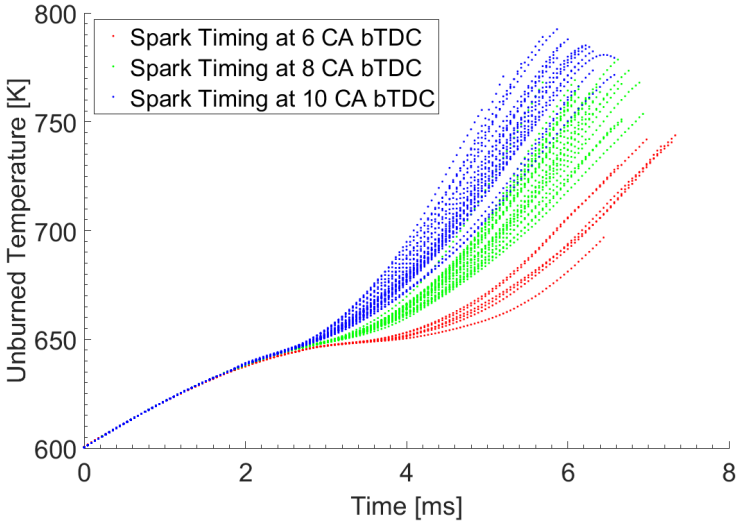

(a) ULG unburned temperature history at different spark timing, 6 CA bTDC (red), 8 CA bTDC (green), 10 CA bTDC (blue).

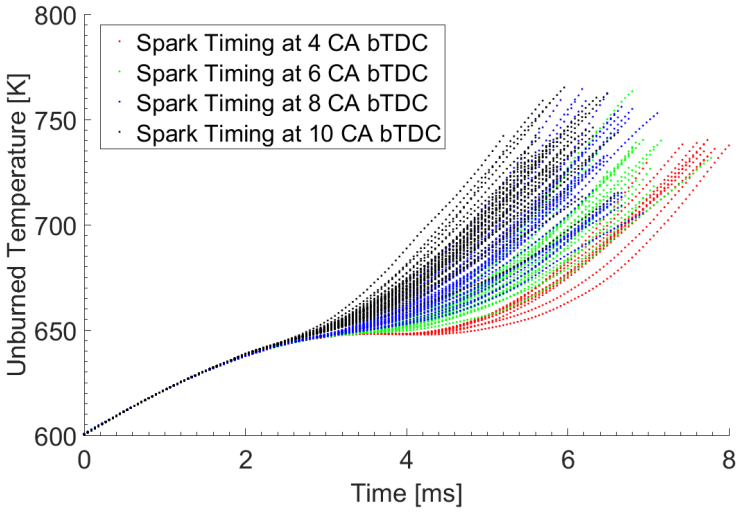

(b) TRF unburned temperature history at different spark timing, 4 CA bTDC (red), 6 CA bTDC (green), 8 CA bTDC (blue), 10 CA bTDC (black).

Figure 6.20: Unburned temperature history start from 600 K until knock onset for ULG and TRF those knocking cycles which MAPO are greater than 1 bar.

to Agbro et al. (2017), the ignition delay of TRF at temperature 679 K shows approximately 23 ms and ULG takes about 5 ms more than TRF. At temperature of 729 K, the ignition delay of TRF is about 12 ms. And the difference of ignition delay between TRF and ULG is less than 2 ms. Considering the unburned charge temperature at a low temperature level (less than 660 K) for spark timing 4 CA bTDC has longer duration than the advanced spark timing, such as 8 CA and 10 CA bTDC, it is reasonable that the knock boundary of TRF is very different from ULG.

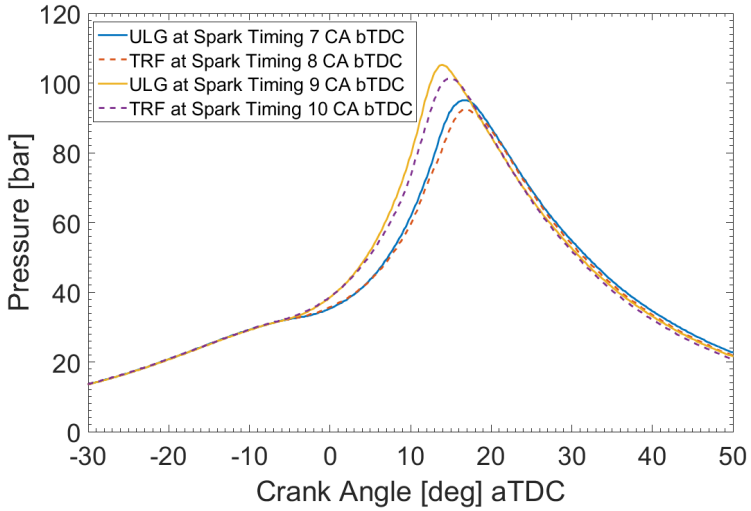

Figure 6.21: Mean pressure trace from ULG and TRF at an advancd spark timing at engine speed 750 RPM.

For the purpose of comparison, the anti-knock property assessment of ULG and TRF were compared at similar temperature history instead of same spark timing. Because the unburned charge temperature is derived from the pressure trace, the similar temperature history of ULG and TRF can be matched by their pressure traces. According to Figure 6.19 and Figure 6.20, TRF and ULG have similar temperature history traces at spark timing of 4 and 6 CA bTDC; and Figure 6.21 shows TRF mean pressure trace at spark timing 8 CA and 10 bTDC are comparable to ULG at 7 CA and 9 CA bTDC, respectively. Comparing the relative ignition delay at similar mean pressure trace between ULG and TRF, the relative ignition delay for TRF is always slightly shorter than ULG across all the sparking timing settings. Overall, the relative ignition delay for TRF at advanced spark timing is very comparable to ULG and it is highly agreed with the results from RCM (Agbro et al. 2017).

For ULGB20, ULG and ULGB20 share almost identical pressure trace, see

Figure 6.23, which means similar unburned charge temperature history between these two fuels. According to Figure 6.22, the relative ignition delay times of the ULG and ULGB20 are identical. Therefore, 20% of n-butanol is not giving any dramatic relative ignition delay benefit to ULGB20 at same unburned temperature history.

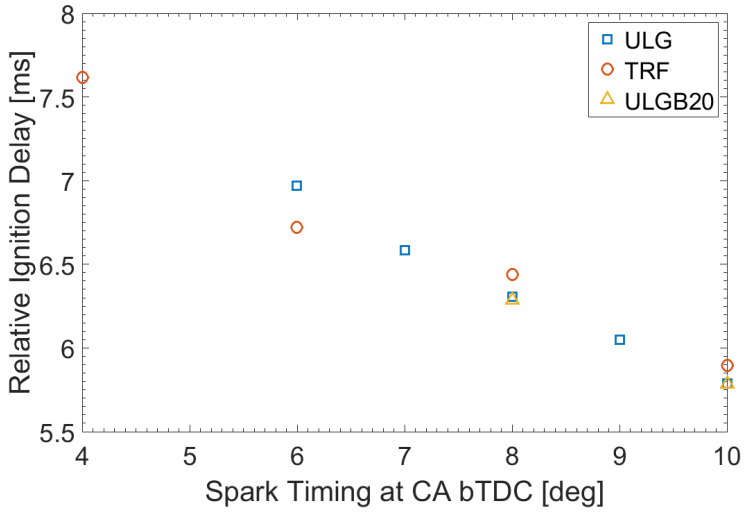

Figure 6.22: Mean relative ignition delay for ULG, TRF and ULGB20 those knocking cycles which MAPO are greater than 1 bar at different spark timing settings.

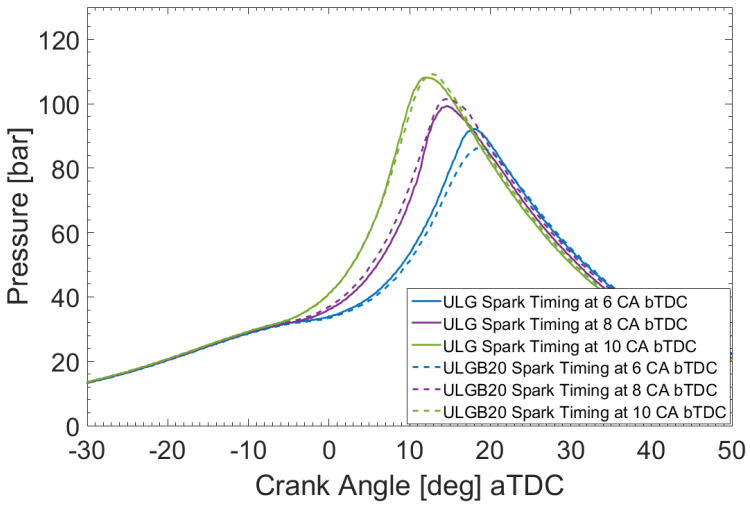

Figure 6.23: Mean pressure trace from ULG and ULGB20 at spark timing of 8 CA and 10 CA bTDC at engine speed 750 RPM.

For those fuels TRFB20, ULGD20 and TRFD20, there is no trace of knock

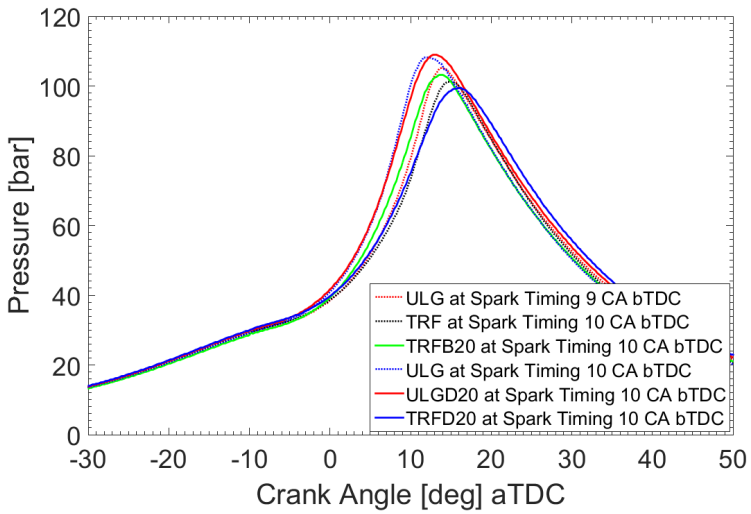

Figure 6.24: Mean pressure trace from TRFB20, ULGD20 and TRFD20 at spark timing of 10 CA bTDC at engine speed 750 RPM.

with MPAO greater than 1 bar observed at spark timing 10 CA bTDC. According to Figure 6.24, TRFB20 pressure growth rate is somewhere between ULG at spark timing 9 CA and 10 CA bTDC. Since ULG at spark timing 9 CA bTDC has MAPO much greater than TRFB20, by inference, adding 20% of n-butanol will result in great improvement of the anti-knock performance of TRF. The ignition delay time from RCM result (Agbro et al. 2017) is also showing that TRFB20 always has longer ignition delay time from 679 K to 750 K at 20 bar compared with TRF. In addition, comparing the pressure trace between TRF and TRFB20 at same spark timing 10 CA bTDC, TRFB20 has greater burning rate than TRF, as a result, flame speed is also enhanced by adding 20% of n-butanol at relatively high temperature. Figure 6.13, TRF shows that its flame speed is higher than TRFB20 at relatively low temperature, but lower than TRFB20 at high temperature region.

For ULGD20 at spark timing of 10 CA bTDC, the pressure trace has same trend comparing with ULG and ULGB20 at the same spark timing. Unlike ULGB20 at spark timing 10 CA bTDC, there is only very mild knock observed and the MAPO is less than 1 bar. Similarly with TRFB20, comparing with ULG and ULGB20, the low level of MAPO at spark timing 10 CA bTDC indicates 20% of 2,5-DMF will result in significant improvement of anti-knock performance. Furthermore, ULG as the base fuel seems to have little influence from n-butanol and 2,5-DMF on the burning rate since the pressure trace of ULGB20 and ULGB20 either at spark timing of 2 CA or 10 CA bTDC is showing highly identical.

For TRFD20, the pressure trace is highly identical with TRF at spark timing

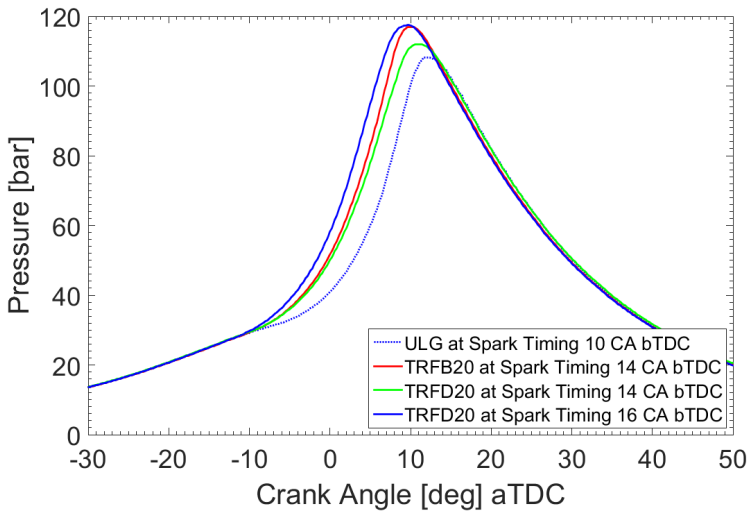

Figure 6.25: Mean pressure trace from TRFB20 and TRFD20 with advanced spark timing at engine speed 750 RPM.

10 CA bTDC. The MAPO of the knocking cycle is the same as TRFB20 that no knocking cycle with MAPO greater than 1 bar was observed, there is an great improvement of the anti-knock performance compared with TRF. As shown in Figure 6.13, the flame speed of TRFD20 is lower than TRF at low temperature, that explains pressure trace of TRFD20 does not match the base fuel at spark timing 2 CA bTDC. However, the flame speed of TRFD20 tends to catch up with TRF at high temperature.

Comparing with n-butanol and 2,5-DMF as the additive for TRF, they have very similar pressure trace at spark timing 14 CA bTDC, see Figure 6.25. The relative ignition delay for TRFB20 and TRFD20 for spark timing 14 CA bTDC are identical, 4.66 ms and 4.69 ms, respectively. In this study, it is difficult to identify which fuel has better anti-knock performance between TRFB20 and TRFD20, due to the safety pressure for the engine.

In general, TRF has a good representation of the ignition delay in high temperature region for ULG. However, in engine, temperature and pressure are not constant, different fuels may have different flame speed under different temperatures and pressures. Since the flame speed is vital to the unburned charge temperature history, as a result, the flame speed is also a key factor for anti-knock performance of a fuel in engine. For n-butanol and 2,5-DMF, they have great improvement on anti-knock performance for TRF. However, those additives has significant influence on the pressure trace. Considering ULG, those additives has little influence on the pressure trace and only 2,5-DMF acts as an octane enhancer.

Chapter 7

Turbulent Flame Propagation in an Engine

LUPOE2-D engine may be considered as a well stirred cylindrical bomb. The turbulent intensity, u', keeps constant during the flame development. Since a spherical bomb for flame study in Leeds combustion group has a large volume (Vancoillie et al. 2014, Lawes et al. 2012), the pressure change due to flame propagation is negligible until the flame radius becomes relatively large. The previous PIV results for motoring cycle in Chapter 5 shows that the turbulent flow in engine cylinder is relatively homogeneous. As a result, LUPOE2-D engine can be used for turbulent flame study under a well known and controlled turbulence condition. On the other hand, the engine cylinder is much smaller than the bomb used for turbulent conditions in study turbulent flame. Although a relatively small flame creates a noticeable pressure change in the engine, this pressure change due to thermal expansion may be counteracted by the movement of piston. In order to eliminate the pressure effects on the propagation of fully developed flame, the spark timing in the present work has been set to achieve a constant pressure when the flame radius grows from 12 - 19 mm, see Figure 7.1. A single component fuel, iso-octane, and a multi-component fuel, ULG were used for the present work. Two sets of engine speeds 750 RPM and 1500 RPM were chosen to compare different turbulence intensities. And the different mixture strengths were created by varying equivalence ratio ϕ from 0.8 to 1.

According to the lean limit of SI engine fuelled by iso-octane (Quader 1974), the LUPOE engine may theoretically run with iso-octane at a $\phi = 0.6$. However, there is a strong self-ignition in purge cycles after the firing cycle for the conditions ϕ less than 0.8. This undesirable self-ignition might potentially damage the vulnerable optical windows and induce a uncontrollable temperature in the following firing

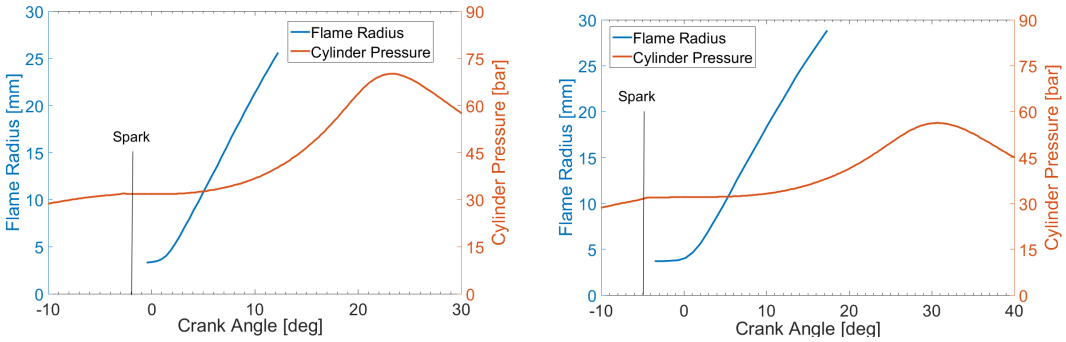

(a) 750 RPM (b) 1500 RPM

Figure 7.1: Example of measured flame radius and pressure as a function of crank angle for stoichiometric ULG mixture at 750 and 1500 RPM.

cycles. The self-ignition in the purging cycles is highly possible because of there is small quantity of fuel in the fuel line goes into the intake pipe and fuelling the engine even though the up stream valve was closed. The hot residual combustion products remaining from the previous firing cycle mix with the fresh charge and create a warm mixture that makes the following cycle running like HCCI model. For the condition of equivalence ratio greater than 0.8, it is assumed that the high portion of combustion residuals and low portion of air should hinder the self-ignition. However, this assumption needs be confirmed in the further experiment.

7.1 Combustion Pressure and Temperature

7.1.1 Pressure Traces

The optical engine combustion pressure was collected for the four different conditions, $\phi = 0.8$ and 1.0 at 750 RPM, $\phi = 0.8$ and 1.0 at 1500 RPM. Because the engine is lack of cooling system, the data collection from the experiment in each condition was only taken for the first few cycles in each run to avoid losing the control of engine temperature. Total 30 firing cycles with good image quality were selected for analysis in this study.

Since the specific heat capacity of the stoichiometric mixture is lower than the lean mixture, and the engine speed affects on the blow by, the intake temperature and intake air flow rate have been adjusted to comparable temperature and pressure conditions achieve similar temperature and pressure conditions during the desired period. For instance, the intake temperature for the lean mixture was about 5K lower than stoichiometric mixtures to compensate high temperature after compression due to the higher specific heat capacity. Figure 7.2 presents the pressure traces of the selected ULG explosions. This study focuses on the flame propagation under constant pressure, temperature and turbulence instead of the fuel performance. By retarding the spark timing, the most period of fully developed flame propagation is able to take place during the expansion stroke. The pressure increase due to the flame expansion is compensated by the pressure drop during the expansion stroke. This creates a short period of constant pressure that provide a relatively stable environment for studying the flame propagation.

Figure 7.3 shows the cylinder pressure with respect to the measured flame radius for ULG at engine speed 750 RPM. Pressure increases at 750 RPM is about 5.4% for $\phi = 0.8$, 5.7% for $\phi = 1.0$ during the fully developed stage that flame radius grows from 12 - 19 mm. At the engine speed of 1500 RPM, the pressure increases about 1.1% $\phi = 0.8$, 2.6% $\phi = 1.0$.

For iso-octane, the pressure traces of the selected 30 firing cycles are shown in Figure 7.4. The pressure near TDC is up to 2 bar lower than the ULG. This pressure change is likely because of the specific heat of iso-octane is lower than ULG mixture. Figure 7.5 demonstrates the overall pressure with respect to the flame radius. The pressure remains almost constant during flame growth from 12 - 19 mm and the pressure increase growth of pressure during this period is less than 8%.

According to the approximations (Metghalchi & Keck 1982), at 30 bar with temperature 650 K, the effect of pressure on laminar burning velocity is less than

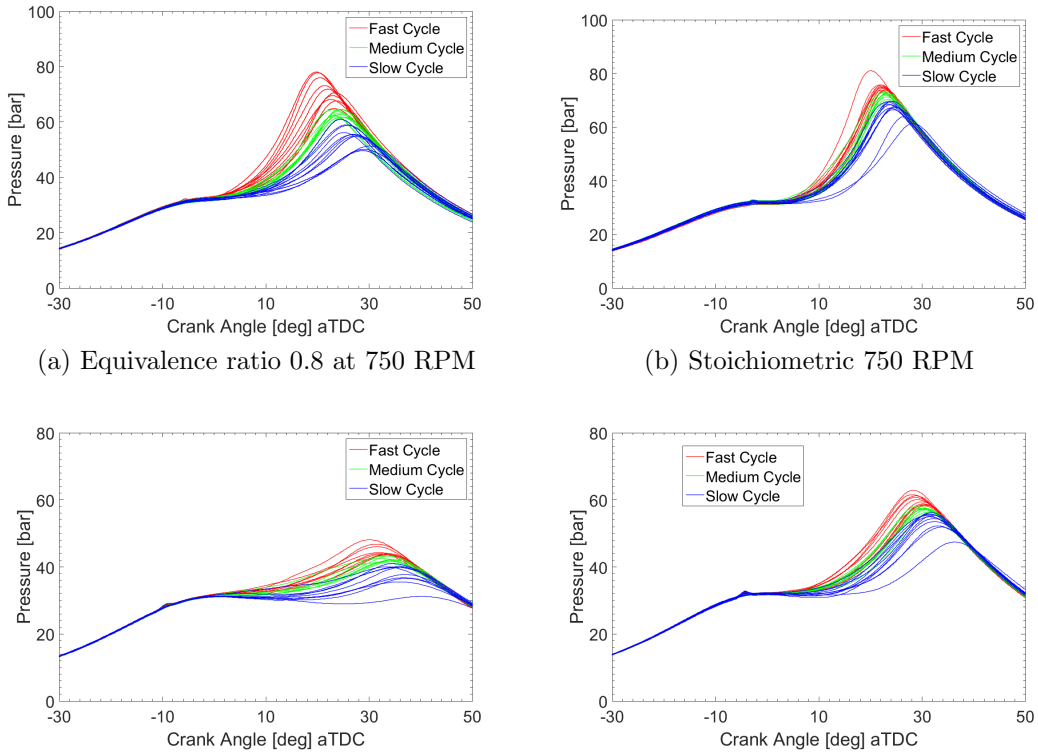

(a) Equivalence ratio 0.8 at 750 RPM

(b) Stoichiometric 750 RPM

(c) Equivalence ratio 0.8 at 1500 RPM

(d) Stoichiometric 1500 RPM

Figure 7.2: ULG pressure traces in this study

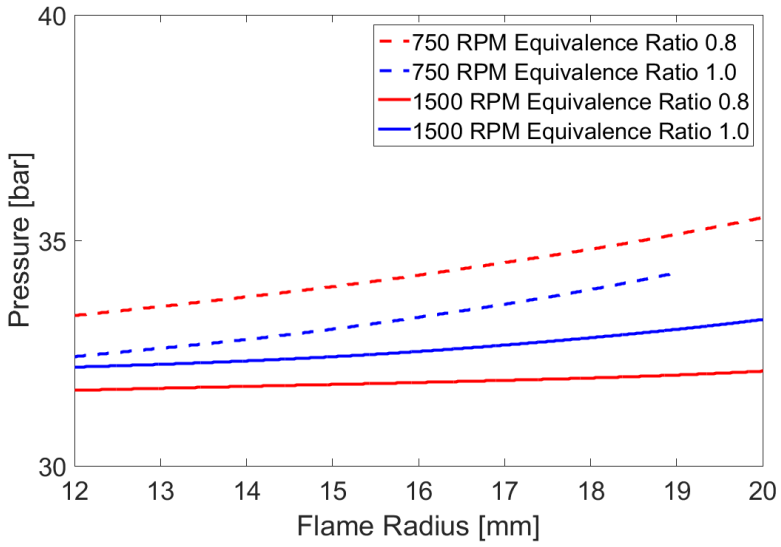

Figure 7.3: Averaged ULG pressure as a function of flame radius at 750 RPM (dash lines) and 1500 RPM (solid lines)

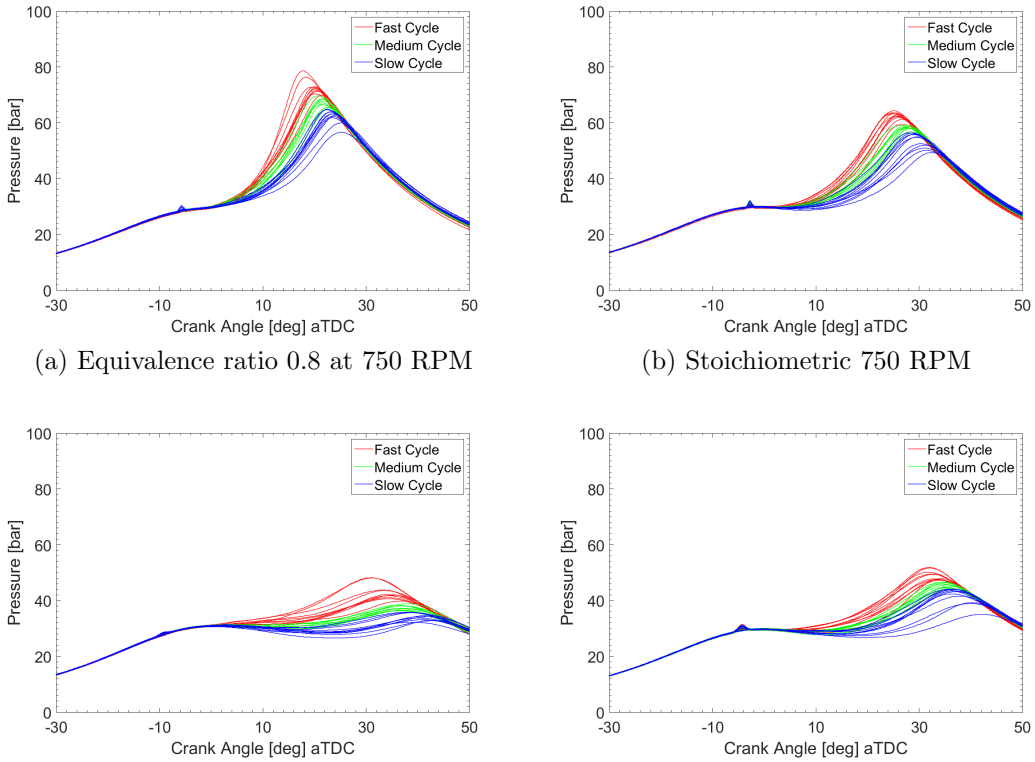

(a) Equivalence ratio 0.8 at 750 RPM

(b) Stoichiometric 750 RPM

(c) Equivalence ratio 0.8 at 1500 RPM

(d) Stoichiometric 1500 RPM

Figure 7.4: Iso-octane pressure traces in this study

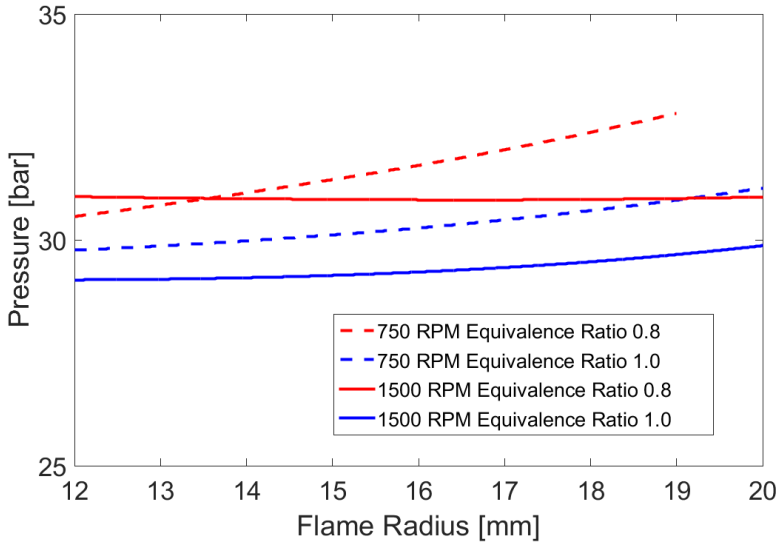

Figure 7.5: Averaged iso-octane explosion pressure as a function of flame radius at 750 RPM (dash lines) and 1500 RPM (solid lines)

2% if the pressure varies about 10% from it original value. This indicates that there should be a little pressure effect on flame propagation in this study.

7.1.2 Temperature History

Since the expansion and compression can be treated as isentropic processes, a stable cylinder pressure will results in a stable fresh gas temperature. According to Table 6.4 LUSIEDA result in Chapter 6.2, the whole fully developed flame at 750 RPM was lasting for no more than 12 CA (2.67 ms) and the period duration which flame radius grows from 12 to 19 mm takes less than 2 ms and the measured flame radius in Figure 7.1 fits within this the short duration. Since flame radius is less than 20 mm and far away from the cylinder wall, the heat loss is mainly from the piston and engine head. The overall heat dissipation from the charge among the four conditions is negligible as shown in the LUSIEDA derived unburned temperature results for the ULG, see Figure 7.6. For the iso-octane, see Figure 7.7, the temperature of unburned mixtures during flame radius from 0 mm to 20 mm varies from 640 K to 660 K. Overall, the unburned temperature in fully developed flame stage with flame radius up to 19 mm period can thus also be considered as nearly constant. The fast cycles tend to have higher fresh gas temperature at the end of initial flame acceleration stage compared with the rest of the cycles. This higher unburned temperature makes the fast cycles take the privilege of flame propagation, especially there will be an increase of diversity on unburned temperature after flame radius 20 mm. According to the laminar burning velocity approximation (Metghalchi & Keck 1982), at pressure 30 bar, the temperature change from 640 K to 660 K may potentially increase the laminar burning velocity up to 8%. The estimated iso-octane laminar burning velocity at temperature 650 K, pressure 31 in the present study is 0.57 m/s and 0.79 m/s at equivalence ratio 0.8 and 1, respectively.

The combustion regimes, Borghi diagram, of iso-octane in the aforementioned four conditions were classified based on the laminar burning velocity and motoring cycle turbulence results, see Figure 7.8. Four experimental conditions mostly locate at the corrugated flamelets region. For the engine speed 750 RPM with ϕ = 1.0, the flame has high chance to across the wrinkled flamelets region. Albeit the disagreement on laminar burning velocity from other sources and calculations (Bradley et al. 1998), it can be seen that the potential combustion region across both corrugated and wrinkled flamelets regions. The effect of turbulent flow on the flame structure will not be considered in the present study.

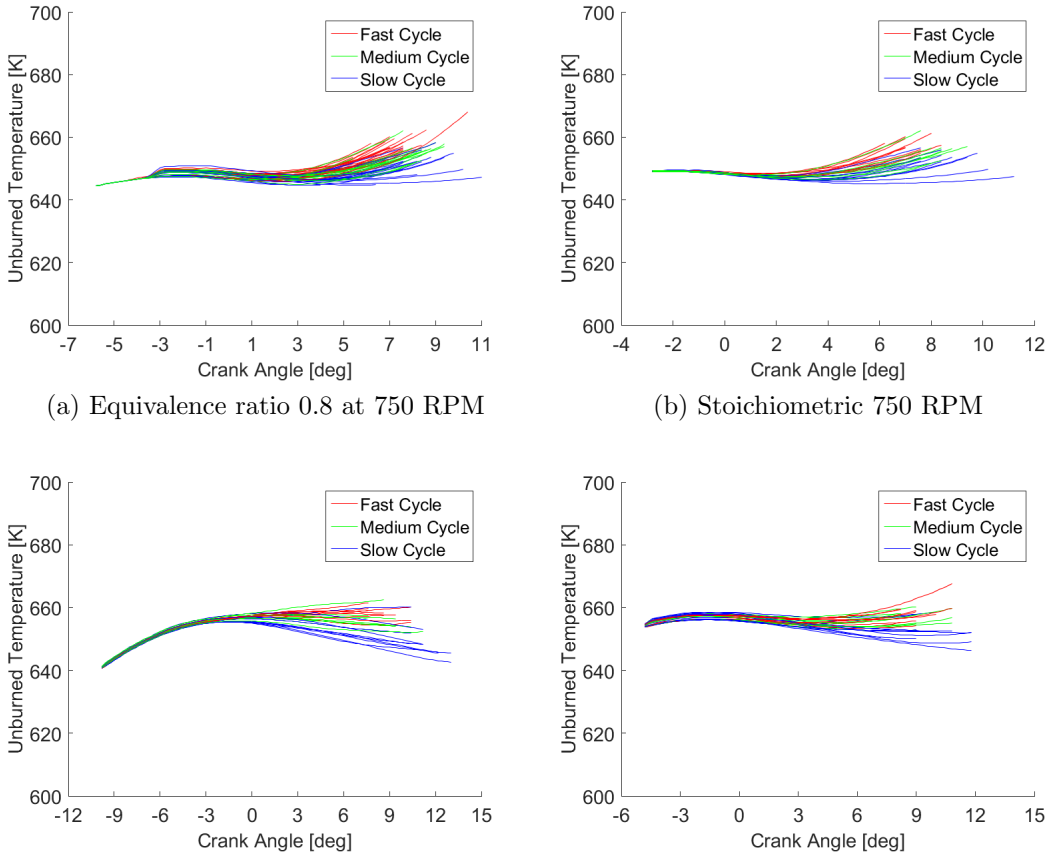

(a) Equivalence ratio 0.8 at 750 RPM

(b) Stoichiometric 750 RPM

(c) Equivalence ratio 0.8 at 1500 RPM

(d) Stoichiometric 1500 RPM

Figure 7.6: ULG unburned temperature history for flame radius from 0 mm to 20 mm in this study

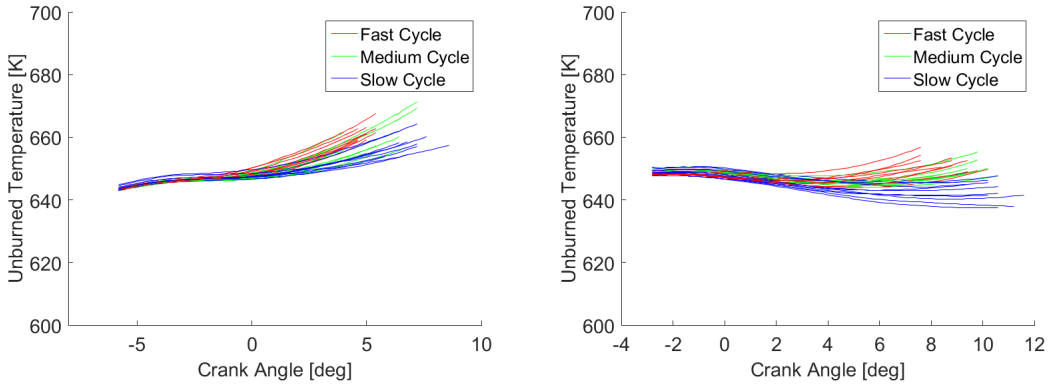

(a) Equivalence ratio 0.8 at 750 RPM

(b) Stoichiometric 750 RPM

(c) Equivalence ratio 0.8 at 1500 RPM

(d) Stoichiometric 1500 RPM

Figure 7.7: Iso-octane unburned temperature history for flame radius from 0 mm to 20 mm in this study

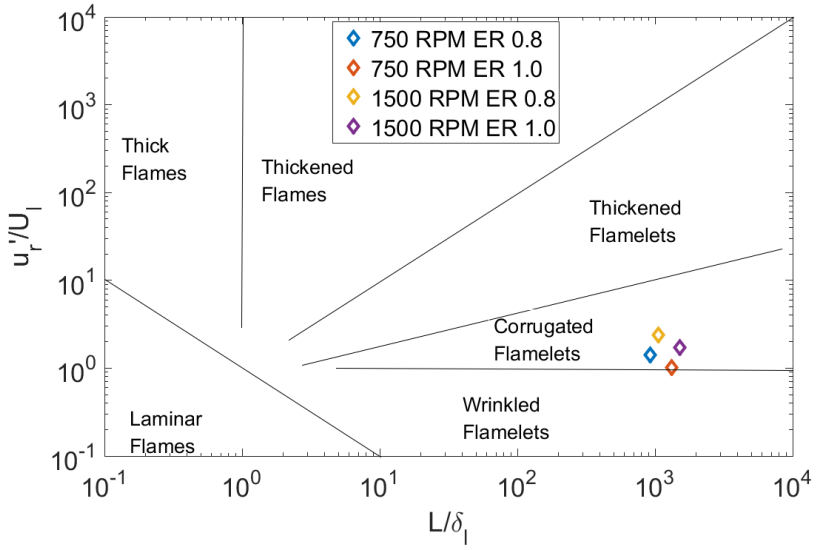

Figure 7.8: Borghi diagram for the iso-octane turbulent flames for the four experiment conditions

7.2 Observations of Turbulent Flame Propagation

7.2.1 Observations of Flame

Laser sheet method was applied in order to obtain burned gas region and the contour wrinkling in this study. In order to obtain the flame speed versus flame size, the averaged flame speeds and radius from equation and in local sectors in Chapter 4 have been employed herein. Figure 7.9 provides a general observation of the turbulent flame edge contours for the four different conditions. Since 1500 RPM with $\phi = 0.8$ has the highest turbulent RMS velocity u' over u_l ratio, It is clearly showing that the highly wrinkled flame happens at 1500 rpm with $\phi = 0.8$ due to the highest u' over u_l ratio.

Figure 7.10 and Figure 7.11 present the flame radius development versus crank angle for ULG and iso-octane, respectively. Due to the visual limits blocking of spark plug, the initial flame kernel was observed to occur from a radius of 3mm. Since it is clear showing in Figure 7.9 that the turbulent flame grows non-uniformly in different sectors, for instance, some of the local flame radii are over 5 mm but in some part of local flame radii are still smaller than 3 mm. This suggests that the smallest average flame radius that could be reliably determined is about 6 mm. As a result, the observation of initial flame kernel propagation is unachievable with current set-up. Most of flame propagation traces are agreed with the definition of fast, medium and slow cycles based pressure trace, see Figure 7.10. Considering the region of interest only half of the cylinder for flame radius study, and the flame radius is only represent a 2D flame propagation instead of 3D. As a result, there will potentially mismatch between image result and the result derived from pressure.

As shown in Figure 7.10, the ULG initial stage duration is about 2.26 ms (10.17 CA), 1.92 ms (8.64 CA), 1.74 ms (15.63 CA) and 1.24 ms (11.17 CA) at the conditions of 750 RPM $\phi = 0.8$ and 1.0, 1500 RPM $\phi = 0.8$ and 1.0, respectively. The results are clearly showing that the initial stage duration for stoichiometric mixtures is shorter than it is at $\phi =$ at 0.8. Furthermore, the higher engine speed is also helpful for reducing the initial stage duration. At the 1500 RPM, the initial stage duration decreased about 23.0% and 35.4% for $\phi = 0.8$ and 1.0, respectively, compared to those at 750 RPM. However, the initial stage duration from flame observation at engine speed of 750 RPM $\phi = 1.0$ is slightly mismatched with LUSIEDA results from metal head experiments, Figure 6.12, where the initial

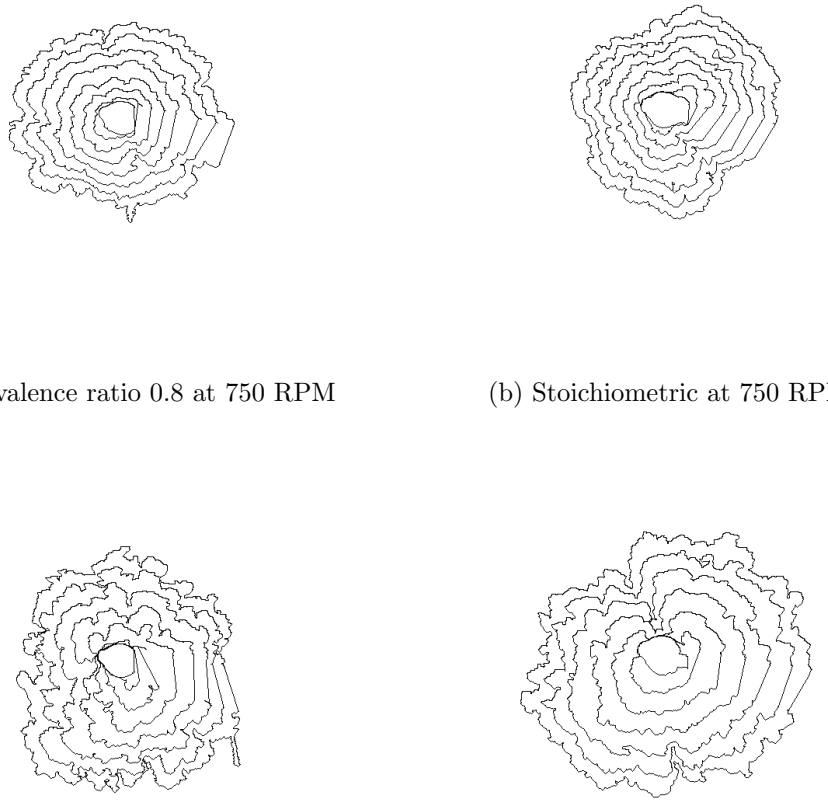

(a) Equivalence ratio 0.8 at 750 RPM

(b) Stoichiometric at 750 RPM

(c) Equivalence ratio 0.8 at 1500 RPM

(d) Stoichiometric at 1500 RPM

Figure 7.9: The turbulent flame development history with 0.3 ms time interval for iso-octane under four different conditions $\phi = 0.8$ and 1.0 at engine speed of 750 RPM and 1500 RPM

stage duration is supposed to between 1.78 ms (8.00 CA) and 1.67 ms (7.5 CA).

As shown in Figure 7.11, the initial stage duration for iso-octane at the condition of 750 RPM $\phi = 0.8$ and 1.0 is about 2.01 ms (9.06 CA), 2.12 ms (9.52 CA), respectively; at the condition of 1500 RPM $\phi = 0.8$ and 1.0 is 1.72 ms (15.47 CA) and 1.36 ms (12.26 CA), respectively. There is about 14.4% initial stage duration increase at $\phi = 0.8$ and 35.8% reduction at stoichiometric. The effect of engine speed on the initial stage duration is highly agreed for both ULG and iso-octane under stoichiometric condition. However, this agreement is less pronounced for the lean condition, e.g. $\phi = 0.8$ which the initial stage duration of iso-octane

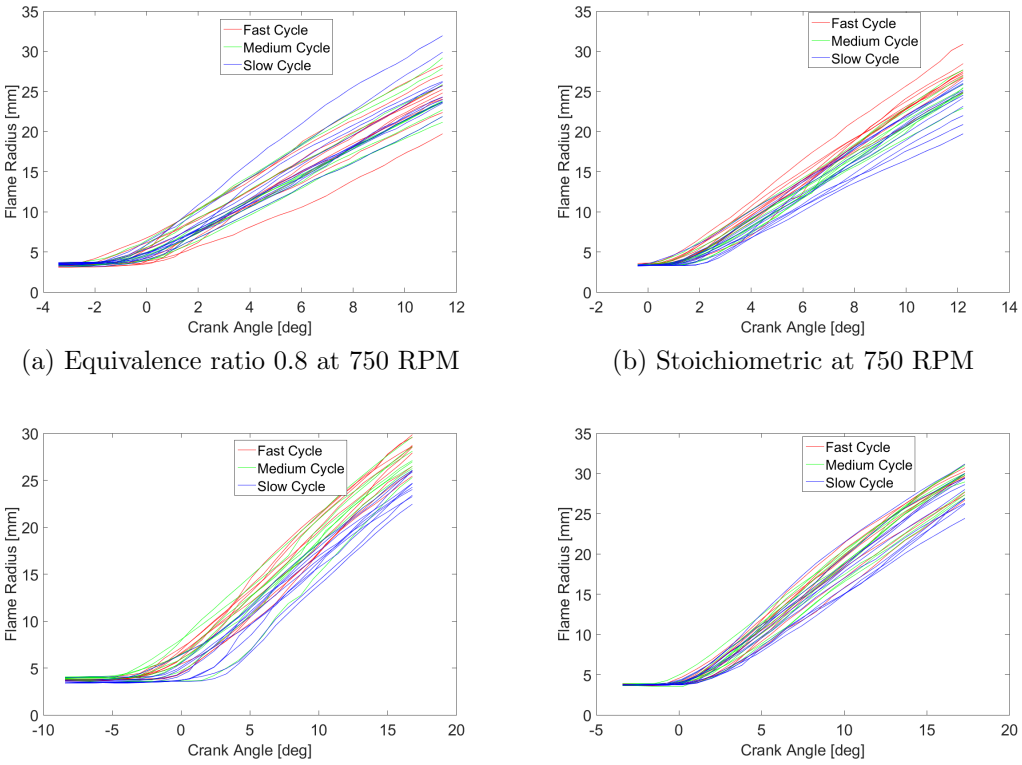

(a) Equivalence ratio 0.8 at 750 RPM

(b) Stoichiometric at 750 RPM

(c) Equivalence ratio 0.8 at 1500 RPM

(d) Stoichiometric at 1500 RPM

Figure 7.10: The flame radius development versus Crank Angle for ULG under four different conditions $\phi = 0.8$ and 1.0 at 750 RPM and 1500 RPM

at $\phi = 0.8$ 0.8 is expected to be longer. As a result, iso-octane at $\phi = 0.8$ may potentially have strongly enhanced flame speed at 750 RPM compared to that of ULG.

Figure 7.12 is showing the iso-octane flame radius derived by LUSIEDA based on the firing cycle pressure. The initial stage duration are 1.93 ms (8.69 CA), 1.97 ms (8.86 CA), 1.76 ms (15.83 CA) and 1.32 ms (11.90 CA) at the conditions of 750 RPM $\phi = 0.8$ and 1.0, 1500 RPM $\phi = 0.8$ and 1.0, respectively.

The flame radius derived by LUSIEDA are comparable with the image observation. However, a small discrepancy has been observed for 750 RPM stoichiometric condition in which the LUSIEDA e.g. at engine speed of 750 RPM $\phi = 1.0$, the LUSIEDA derived initial stage duration is 0.15 ms (0.66 CA) shorter than the optical result for iso-octane. Similar for ULG, the LUSIEDA results indicate that ULG has an initial stage duration 1.76 ms (7.90 CA) at 750 RPM $\phi = 1.0$, the LUSIEDA derived initial stage duration is 0.16 ms (0.74 CA) shorter than optical observation. This matches the results difference on iso-octane and Chapter 6.2

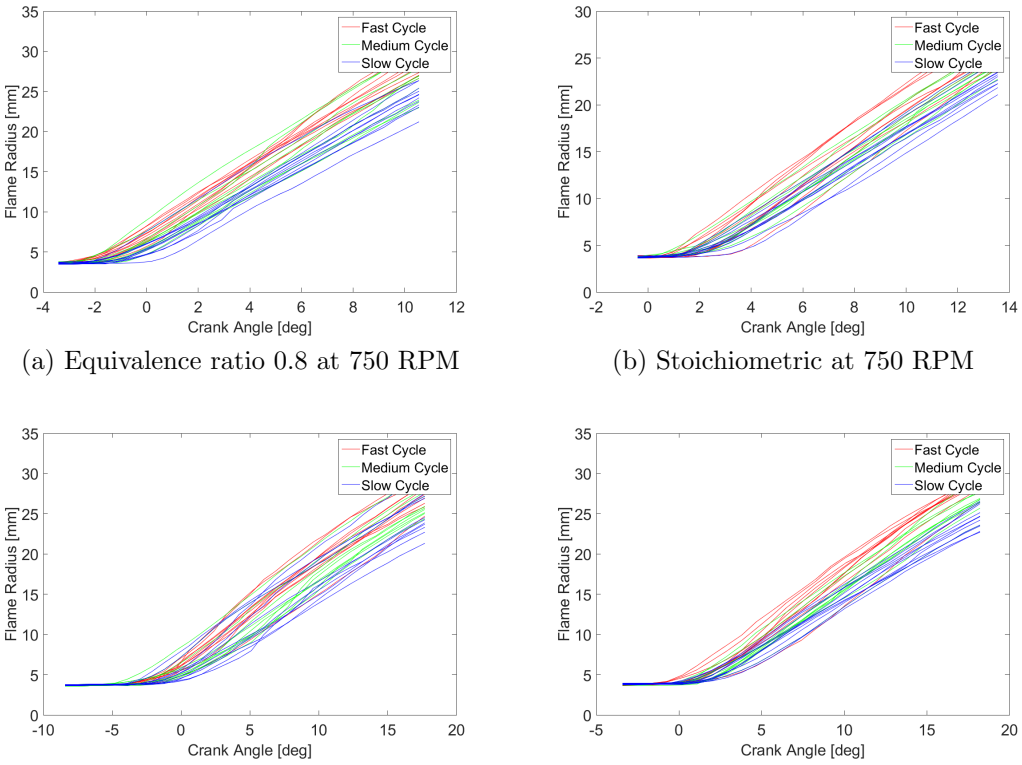

(a) Equivalence ratio 0.8 at 750 RPM

(b) Stoichiometric at 750 RPM

(c) Equivalence ratio 0.8 at 1500 RPM

(d) Stoichiometric at 1500 RPM

Figure 7.11: The flame radius development versus crank angle for iso-octane under four different conditions $\phi = 0.8$ and 1.0 at 750 RPM and 1500 RPM.

metal head result that mentioned earlier. This initial duration between optical observation and pressure derivation can be considered as offset.

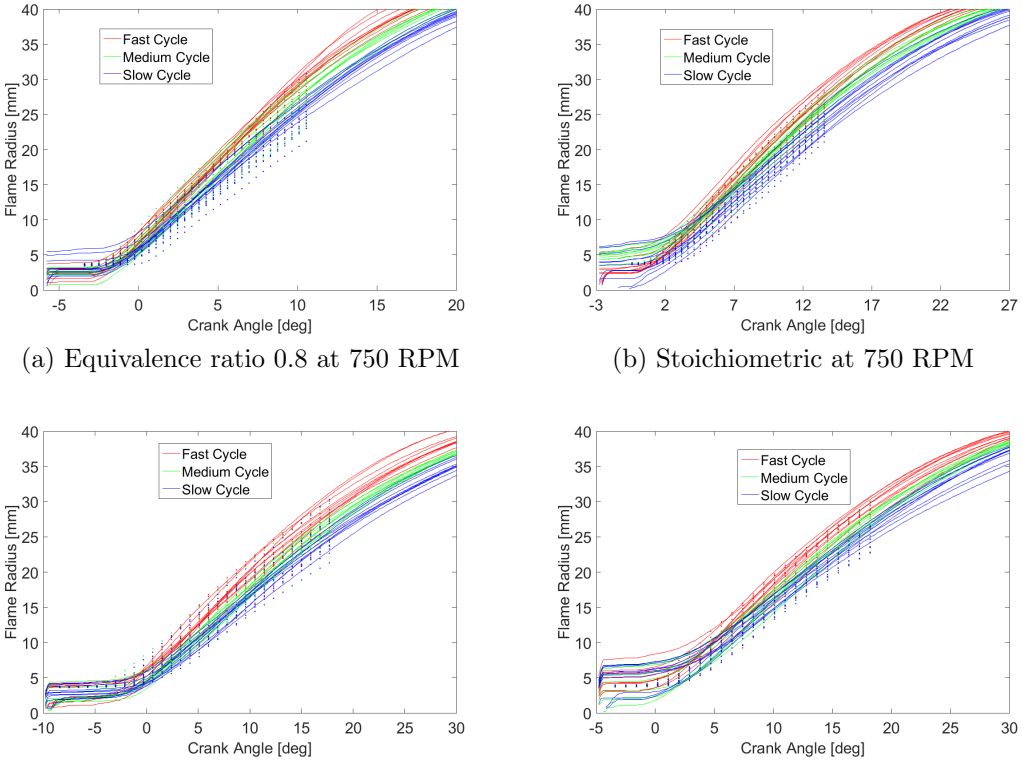

(a) Equivalence ratio 0.8 at 750 RPM

(b) Stoichiometric at 750 RPM

(c) Equivalence ratio 0.8 at 1500 RPM

(d) Stoichiometric at 1500 RPM

Figure 7.12: Comparison between LUSIEDA derived iso-octane flame radius development (line) and image observation (dot) for the four different conditions

In this study, the turbulence integral length scale in engine is less than 5 mm, where Reynolds number at engine speed 1500 RPM is estimated about 3500. As a result, the Kolmogorov length scale is about 0.01 mm. The thermal diffusivity calculated from Gaseq developed by Morley (2005) is 2.14x10^{-6} m^2/s at 650 K, 30 bar for stoichiometric iso-octane mixture. This means the laminar flame thickness in this experiment is far less than 0.01 mm and the smallest wrinkle can be found at the Kolmogorov length scale. The camera resolution for full bore view is about 0.16 mm x 0.16 mm, as a result, the pixel size is too big for the observation of the small wrinkle. In order to investigate the detailed flame propagation, the camera zoomed in on the laser sheet flame to achieve a resolution of 0.065 mm x 0.065 mm.

Figure 7.13 shows the camera zoomed in flame contour. In the experiment, one quarter of flame propagation was captured due to the limited camera performance. Furthermore, under such camera settings, the camera is still able to record the whole one quarter flame propagation even though the average flame radius is upto 25 mm. Considering the laser sheet thickness is about 0.5 to 1 mm, the resolution for non-zoomed in case, pixel size 0.16 mm, the camera will filter out some small winkles either at the middle of the laser sheet or somewhere out of the centre of the laser sheet. For the high resolution, the laser sheet image is potentially involved in high level of 'noise' which is coming from different plane inside the laser sheet. Furthermore, the brightness of the laser sheet images is not sufficient to distinguish the flame and fresh gas. As a result, there is a limitation that the resolution is not able to reach the smallest wrinkles.

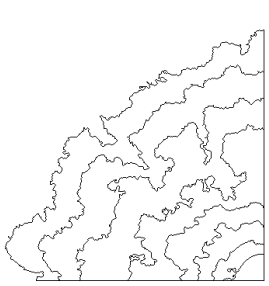

(a) Equivalence ratio 0.8 at 750 RPM

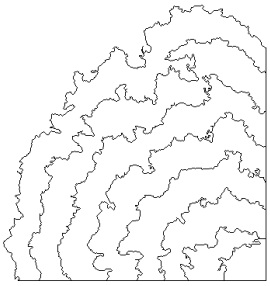

(b) Stoichiometric at 750 RPM

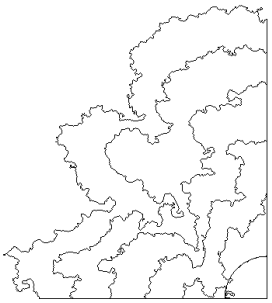

(c) Equivalence ratio 0.8 at 1500 RPM

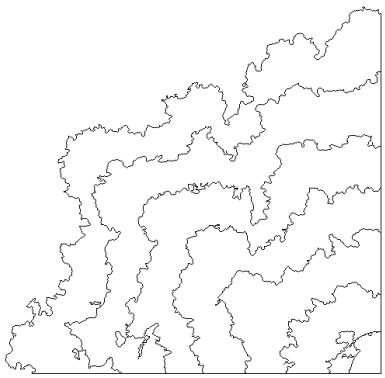

(d) Stoichiometric at 1500 RPM

Figure 7.13: The turbulent flame development history with 0.3 ms time interval for iso-octane under four different conditions: $\phi = 0.8$ and 1.0 at engine speed of 750 RPM and 1500 RPM for camera zoomed-in cases.

7.2.2 ULG and Iso-octane Flame speeds

Figure 7.14 shows the flame speed for each condition versus flame radius among 30 firing cycles. There are small number of extreme values e.g. the scattered data points that over 12 m/s at 750 RPM and over 18 m/s at 1500 RPM appearing in each condition. Usually, the extreme values come from overestimating the flame speed due to flame propagating from different plane to the laser sheet planes that increases the local flame speed. As a result, the data simply averaged will trim off some extreme values to reduce the influence from the outliers, the threshold in defining outliers is the mean value plus or minus one standard derivation. The averaged flame speeds at flame radius 12 to 19 mm is 7.95 m/s for $\phi = 0.8$ mixtures and 9.15 m/s for stoichiometric mixture at 750 RPM; 11.97 m/s for $\phi = 0.8$ mixtures and 14.18 m/s for stoichiometric mixture at 1500 RPM. The flame speeds in all conditions stay nearly constant during the flame radius from 12 to 19 mm.

For iso-octane, the flame speed of each condition measured from laser sheet image is presented in Figure 7.15. The averaged flame speeds of iso-octane have been observed: 8.58 m/s at $\phi = 0.8$ and 8.06 m/s at stoichiometric condition, at 750 RPM; For engine speed 1500 RPM, 11.22 m/s at $\phi = 0.8$ and 12.46 m/s at stoichiometric condition, at 1500 RPM.

For ULG, as the equivalence ratio shifts from stoichiometric ($\phi = 1.0$) to lean condition ($\phi = 0.8$), the flame speed decreases by 13.1% and 15.6% for 750 RPM and 1500 RPM, respectively. By cranking up the engine speed from 750 RPM to 1500 RPM, the flame speed increases by 50.6% and 55.0% for $\phi = 0.8$ and stoichiometric mixture, respectively. For Iso-octane, as the equivalence ratio shifts from $\phi = 1.0$ to $\phi = 0.8$, the flame speed increases by 6.5% and decreases by 10.0% for 750 RPM and 1500 RPM, respectively. By cranking up the engine speed from 750 RPM to 1500 RPM, the flame speed increases by 30.8% and 54.6% for $\phi = 0.8$ and stoichiometric mixture, respectively.

Considering the impact of engine speed on the flame speed of ULG and iso-octane, there is a highly agreement on flame speed change due to doubling the engine speed for stoichiometric condition. However, there is an inconsistency of flame speed between stoichiometric and $\phi = 0.8$. There is an abnormal enhancement of flame speed at $\phi = 0.8$ for iso-octane mixtures. At engine speed of 750 RPM, the flame speed of iso-octane with $\phi = 0.8$ is faster than the flame speed at stoichiometric condition. Iso-octane mixture at engine speed of 1500 RPM, the flame speed reduction due to reducing mixture strength is not as strong as ULG. All the evidences are showing that there is an enhancement of flame speed for iso-octane mixtures at $\phi = 0.8$ under low turbulence.

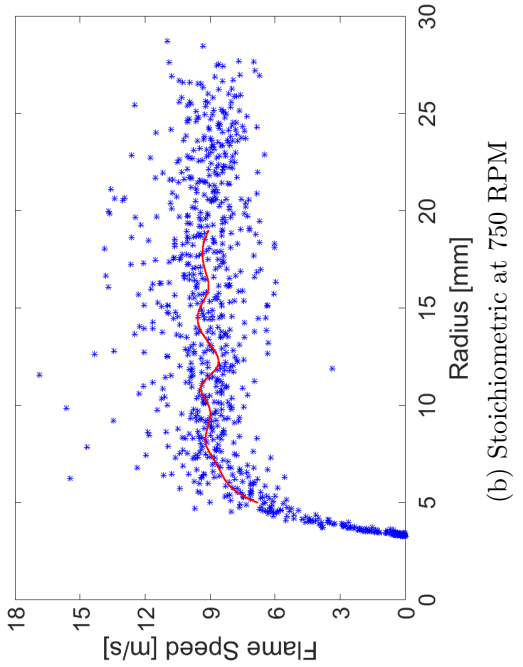

(a) Equivalence ratio 0.8 at 750 RPM

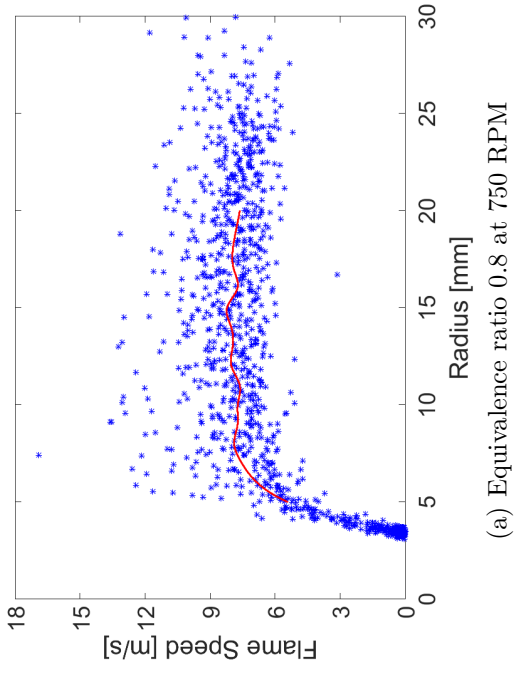

(b) Stoichiometric at 750 RPM

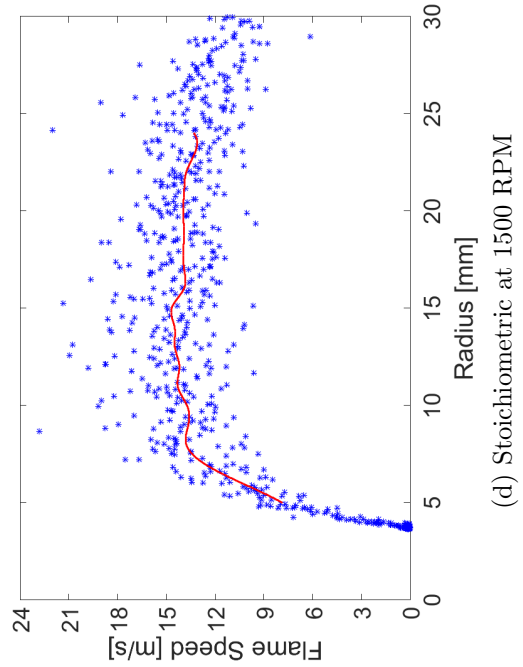

(c) Equivalence ratio 0.8 at 1500 RPM

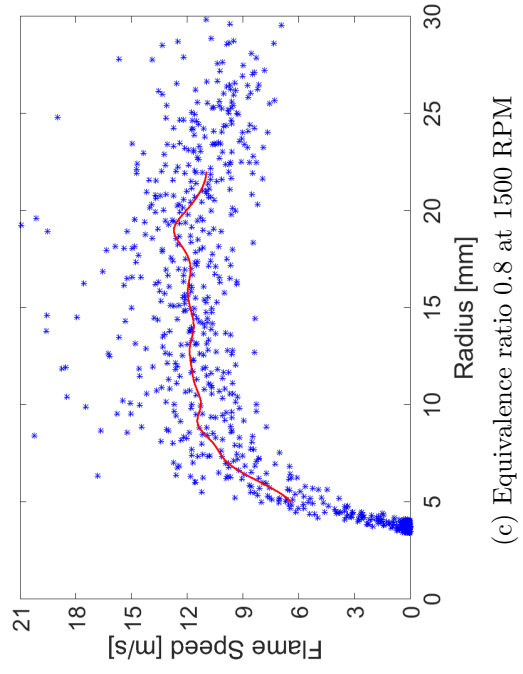

(d) Stoichiometric at 1500 RPM

Figure 7.14: ULG flame speed and averaged flame speed (red) versus flame radius based on 30 explosions.

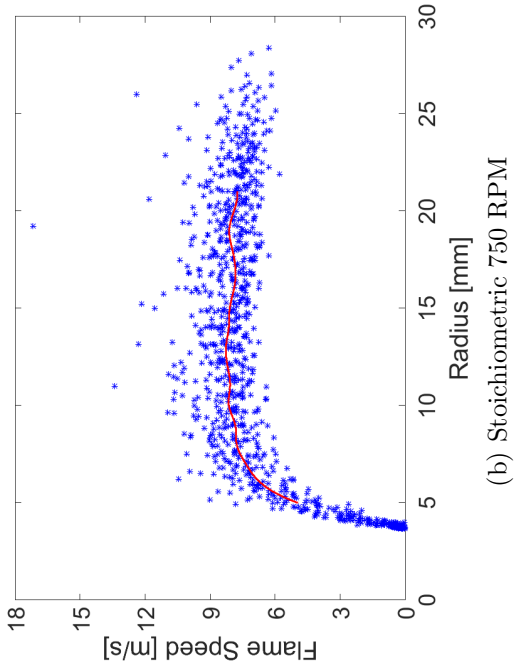

(a) Equivalence ratio 0.8 at 750 RPM

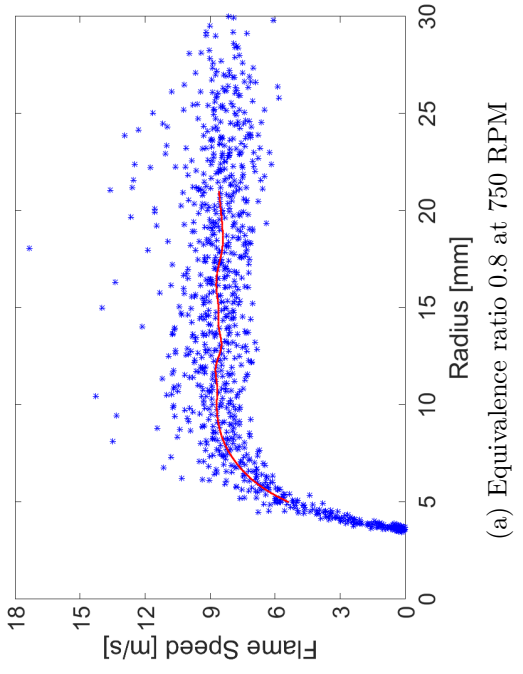

(b) Stoichiometric 750 RPM

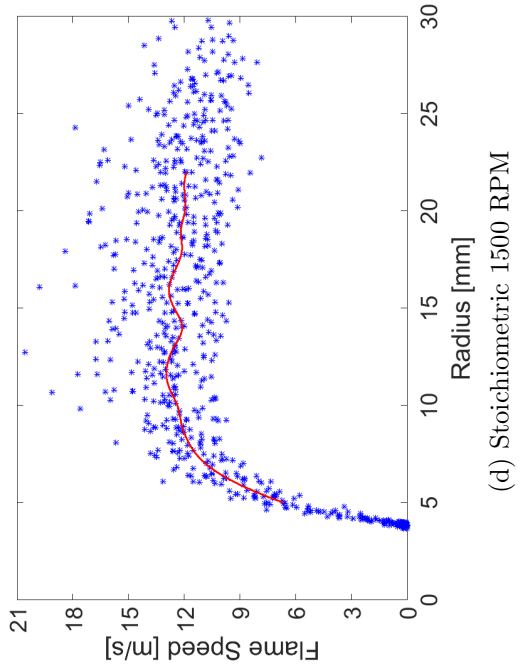

(c) Equivalence ratio 0.8 at 1500 RPM

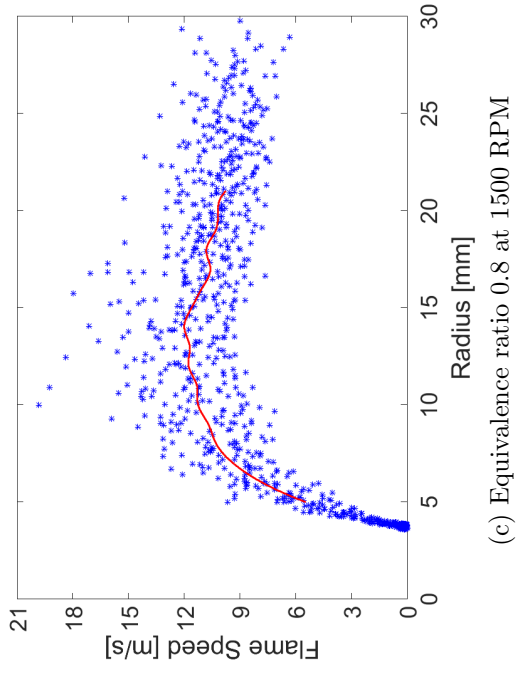

(d) Stoichiometric 1500 RPM

Figure 7.15: Iso-octane flame speed and averaged flame speed (red) versus flame radius based on 30 explosions.

According to laminar burning velocity expressions of iso-octane in this experiment condition (Metghalchi & Keck 1982), the laminar burning velocity at the temperature and pressure of 650K, 30 bar is about 0.79 m/s and 0.57 m/s at equivalence ratio 1 and 0.8, respectively. There is about 30% of reduction of laminar burning velocity. According to Zimont turbulent flame speed closure model (Zimont et al. 1998), the effect of laminar burning velocity u_l on turbulence u_t is $u_l \sim u_l^{0.5}$. As a result, the predicted turbulent burning velocity reduction is about 15.6% from equivalence ratio from 1 down to 0.8. Since the turbulent burning velocity is proportional to turbulent flame speed, the predicted result agrees quite well with the effect of equivalence ratio on measured ULG flame speed result.

For the effect of turbulence on the flame speed, there is 60% of the u' increases with increasing engine speed from 750 RPM to 1500 RPM. For the ULG and iso-octane in stoichiometric condition, the effect of u' on the flame speed is about approximately $St \sim u'$. However, at the condition of $\phi = 0.8$, the effect of u' on the flame speed seems weaker than the stoichiometric condition, especially for iso-octane, 60% of u' increase only result in 30.8% of flame speed increase.

Figure 7.16 show the flame speed of ULG and iso-octane versus the time after spark. The time evolution of flame speed of stoichiometric iso-octane is also lower than $\phi = 0.8$. The flame speed at 750 RPM is constant upon averaged flame radius 10 - 25 mm. It is highly agreed on the flame speed versus flame radius at 750 RPM shown in Figure 7.14 and 7.15. However, the flame speed at flame radius 10 - 20 mm at 1500 RPM shown by Figure 7.14 and 7.15 not agrees with what shown by Figure 7.16, the flame speed at 1500 RPM is not exactly as a constant. According to the flame speed as a function of radius, the flame speed becomes constant after flame radius 10 mm and starts to decrease after flame radius 25 mm. The flame speed is very sensitive to the flame radius. Deriving the average flame speed as a function of the flame radius could avoid averaging the speed when flame is upon inappropriate flame size. Because of flame speed and its diversity at engine speed of 1500 RPM is relatively large, i.e. when flame radius of every cycle in the range from 10 to 25 mm for iso-octane at 1500 RPM, the time evolution of flame speed is 'compacted' within 1.4 to 2.1 ms after spark. Out of this 'compacted' period, some flame speed with inappropriate flame size will be involved in averaging of the flame speed.

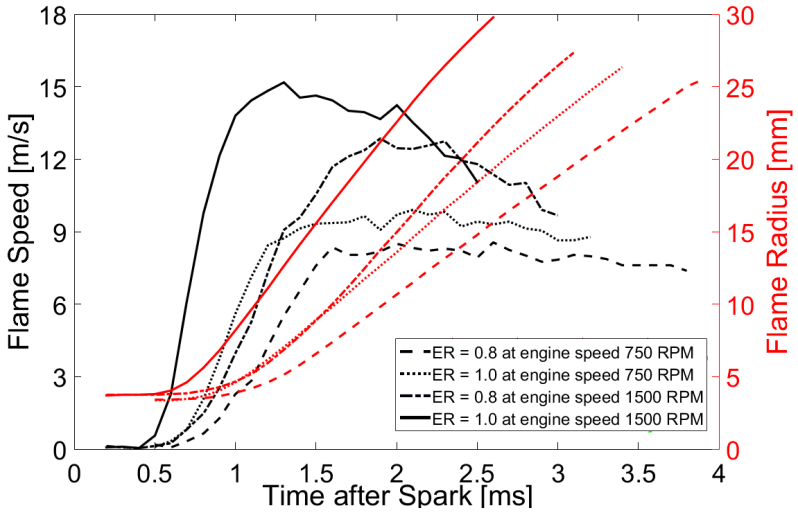

(a) ULG

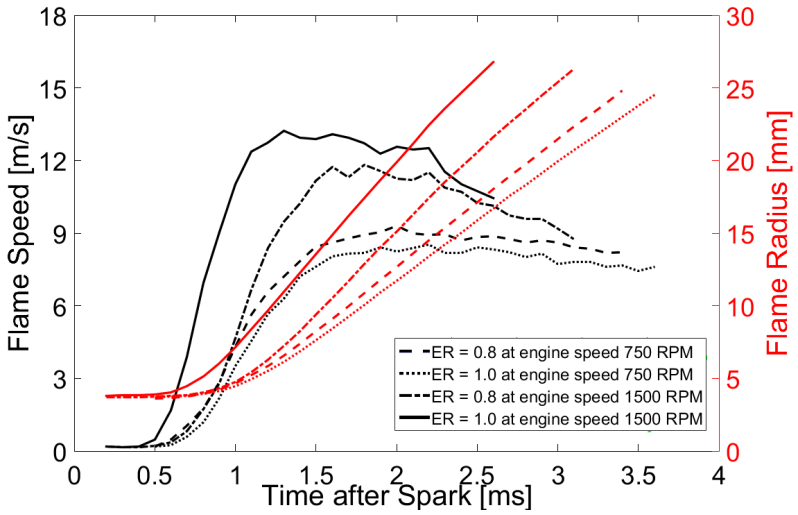

(b) Iso-octane

Figure 7.16: Averaged speed and flame radius versus the time after spark

Figure 7.17 shows iso-octane turbulent flame speed derived from the camera zoomed in images. The averaged flame speed shows constant at flame radius 12 - 19 mm. At engine speed of 750 RPM $\phi = 0.8$, stoichiometric, the flame speed is about 8.31 m/s and 8.35 m/s, respectively. For the flame speed at engine speed 1500 RPM, 12.36 m/s at $\phi =$ of 0.8, 14.15 m/s at stoichiometric condition. The result basically agreed with the flame speed derived from non-zoomed in images. Because of there is unavoidable flame propagation normal to the laser, especially at high engine speed. The flame speed derived from zoomed in images is much easer influenced by such direction flame propagation. As a result, the flame speed sample scatters have wider range of spread compared with the non-zoomed case. As observed in non-zoomed in case of iso-octane, the flame speed between stoichiometric and $\phi = 0.8$ at engine speed of 750 RPM is very close. Under high turbulence, at engine speed 1500, the flame speed difference between stoichiometric and $\phi = 0.8$ start to show up. For the zoomed in case, although there is about 69.6% of S_t increase for the 60% of u' increase at the stoichiometric condition, there is about 48.7% increase of S_t at $\phi = 0.8$. Therefore, the results are suggested that the effect of u' on the S_t may be influenced by the equivalence ratio.

Figure 7.18 shows the flame speed standard deviation for the derivation of the flame speed. There is an noticeable of high levels of standard deviation at higher engine speed indicates that the flame speeds are spread out over a wider range of values. For different equivalence ratio, the stoichiometric condition shows relatively low uncertainty compared with $\phi = 0.8$. This may relate to the effect of turbulence on flame propagation at different equivalence. Moreover, the flame propagates normal to the laser sheet due to flame surface wrinkling is potentially resulting in an increase of uncertainty. For the zoomed setup, there is a slight increase of the uncertainty compared with the non-zoomed setup. Considering the flame speed derived from a quarter of the flame by using zoomed setup, it could be a potential reason for the increased uncertainty for the zoomed in case.

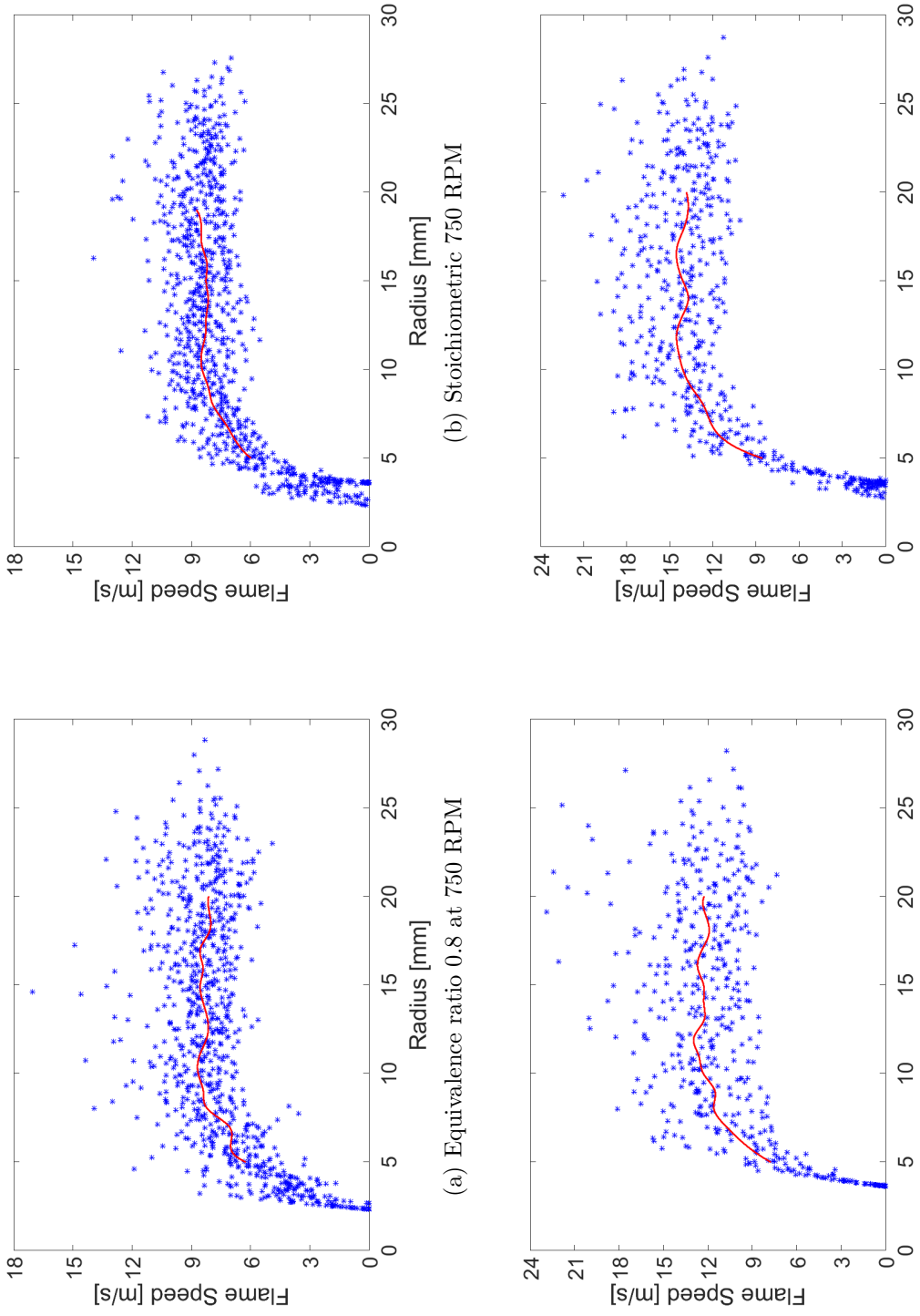

(a) Equivalence ratio 0.8 at 750 RPM

(b) Stoichiometric 750 RPM

(c) Equivalence ratio 0.8 at 1500 RPM

(d) Stoichiometric 1500 RPM based

Figure 7.17: Iso-octane flame speed and averaged flame speed (red) versus flame radius based on 30 explosions.

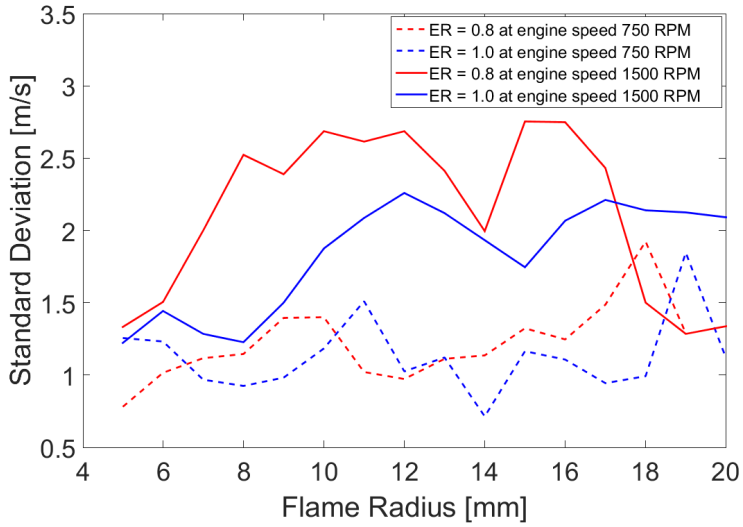

(a) Non-zoomed setup

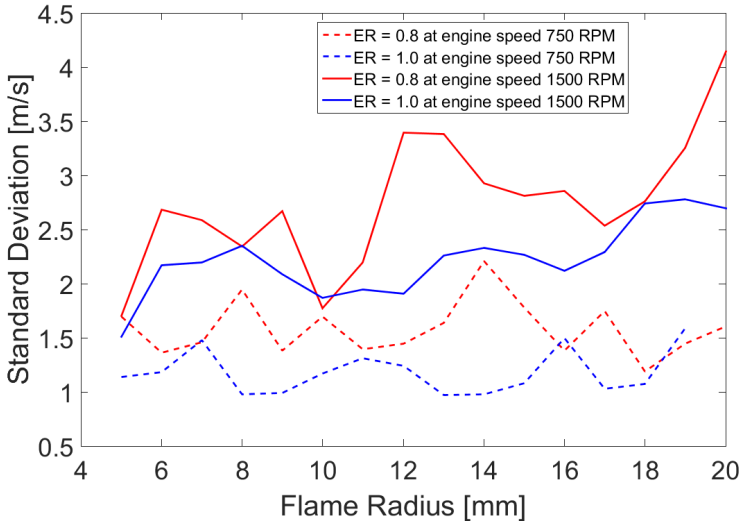

(b) Zoomed setup

Figure 7.18: Standard deviation of iso-octane flame speed for non-zoomed and zoomed setup

7.2.3 Flame Wrinkle

Since the flame images in LUPOE2-D are showing relatively symmetric and round shape, see Figure 7.9, the flame contour wrinkles can be described by a non-dimensional parameter sphericity to quantify the flame surface wrinkles. The sphericity is defined as (Russ 2016),

$$sphericity = \frac{4\pi A}{{P_e}^2} \tag{7.1}$$

where A is measured laser sheet flame area and P_e is the perimeter of the flame which is the contour length. In this study, due to top half part of the flame is validated, doubling top half part of burned gas region and the flame contour length will be the value of A and P_e and respectively. Wrinkled flame front means more flame surface area and creates a larger perimeter result of a small flame sphericity. If the sphericity equals 1 means flame is a circle without wrinkling.

Figure 7.19(a) shows ULG flame sphericity with respect to flame radius in all conditions, according to the figure, the flame sphericity decreases with an increasing of flame radius, the flame has more wrinkled surface with the expansion of the flame. Comparing the flame sphericity in each condition, engine speed increases or equivalence ratio decreases is causing reduction of flame circularity which means more winkled flame front. Furthermore, the sphericity increases during flame growth is also observed in all conditions despite the flame is in fully developed stage. Iso-octane shows mostly agree with ULG, see Figure 7.19(b). However, the sphericity of iso-octane at engine speed of 750 RPM for equivalence ratio 0.8 and stoichiometric shows similar value at the early period of fully developed stage, after flame radius of 15 mm, the sphericity of $\phi = 0.8$ has clearly lower than the stoichiometric condition.

The low value of sphericity is potentially indicate large flame surface. Although there is decrease in sphericity during flame radius from 12 - 19 mm, the flame speed seems not influenced by the sphericity. Furthermore, the sphericity of iso-octane $\phi = 0.8$ at engine speed of 750 RPM shows very close to it is at stoichiometric condition. However, the flame speed is clearly enhanced at $\phi = 0.8$ and the similar sphericity between stoichiometric and equivalence 0.8 could not provide such enhancement for flame development at $\phi = 0.8$. It seems that the sphericity is not providing a convincible evidence. However, considering the camera resolution may not capture all the detailed flame contour, part of perimeter contributed by some small wrinkles can not be counted. The further investigation will be carried on the zoomed in flame images.

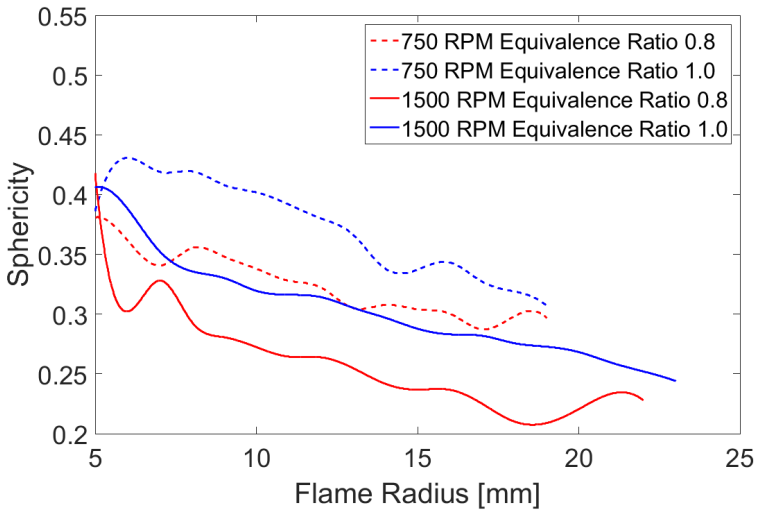

(a) ULG flame sphericity with respect to flame radius in all conditions

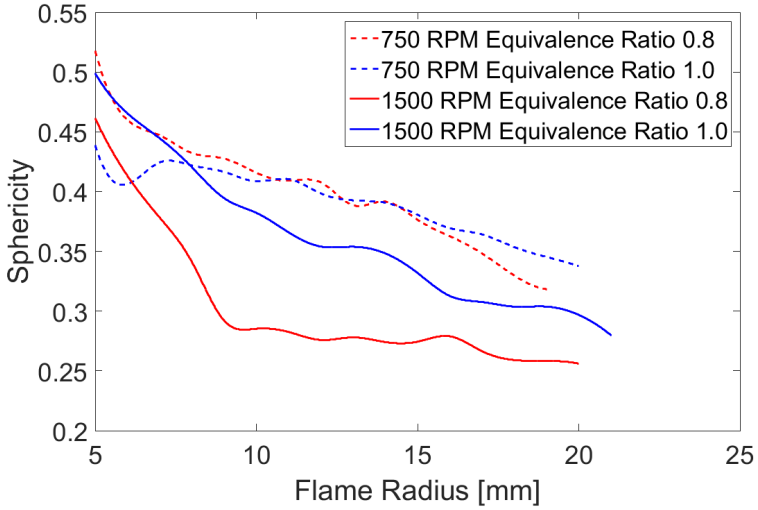

(b) Iso-octane flame sphericity with respect to flame radius in all conditions

Figure 7.19: Averaged flame sphericity with respect to flame radius based on 30 firing cycles

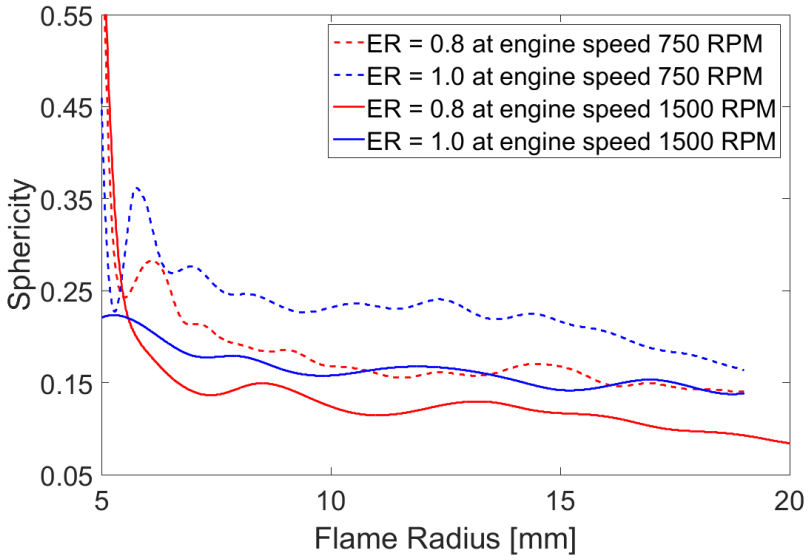

Figure 7.20: Iso-octane flame sphericity versus flame radius derived from zoomed in images for all conditions

Figure 7.20 shows the iso-octane sphericity derived from zoomed in flame. The sphericity shows more or less constant during the flame radius from 12 - 19 mm. Comparing the sphericity from Figure 7.19(b), there is clearly a decrease of sphericity at same flame radius for the zoomed in one. It is highly possible that the zoomed in flame contour perimeter takes the perimeter contributed by small wrinkles which the non-zoomed case could not capture. Because of the flame image pixel size is still much greater than predicted the smallest wrinkle size, the sphericity of the flame may potentially smaller than the actual value. Furthermore, the sphericity derived from enlarged flame is highly agreed on the influence of equivalence ratio and engine speed on the sphericity shown by Figure 7.19(a). It is not coincidence that both ULG and enlarged iso-octane sphericity at $\phi = 0.8$ engine speed 750 RPM and stoichiometric engine speed 1500 RPM have similar value. These two fuel may have similar effect on sphericity under the influence of turbulence and equivalence ratio.

Figure 7.21 shows the development of the flame contour RMS r' amplitude of flame wrinkling. Similar with the sphericity presented in this study, for both ULG and iso-octane, r' increases with growth of flame radius. Engine speed increases or equivalence ratio decreases is causing of increasing of r'. However, the r' of iso-octane at engine speed of 750 RPM with $\phi = 0.8$ shows lower than it is at stoichiometric condition. Figure 7.22 shows the r' derived from the zoomed in images. There is not big difference of r' between zoomed in and non zoomed in

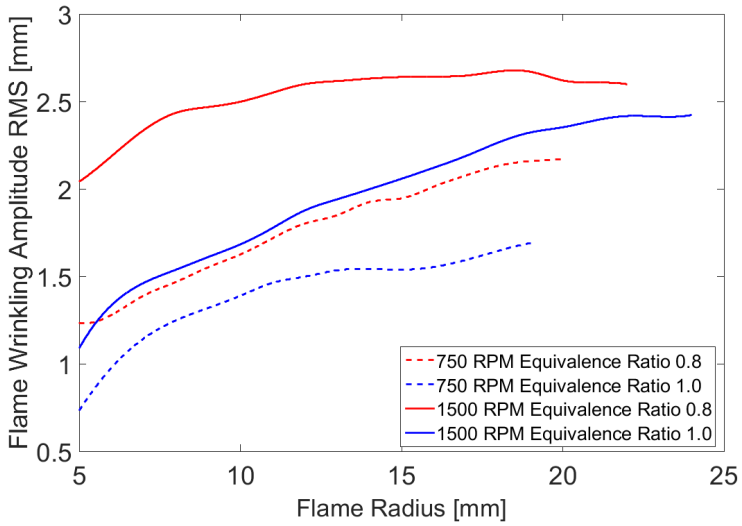

(a) ULG RMS amplitude of flame wrinkling

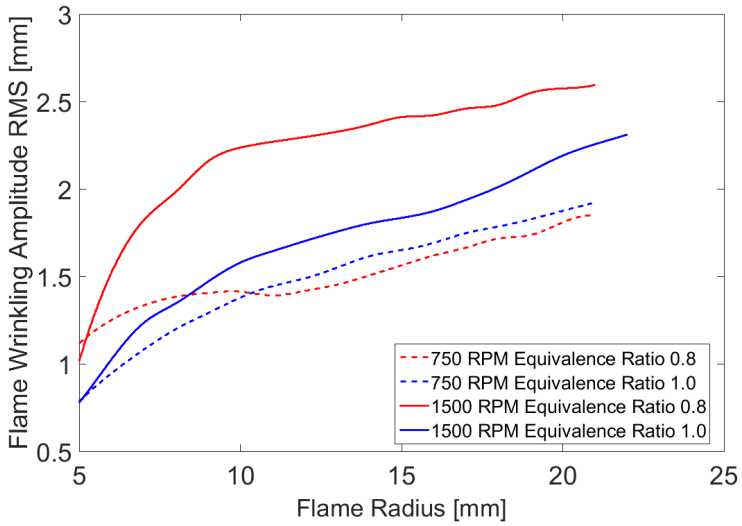

(b) Iso-octane RMS amplitude of flame wrinkling

Figure 7.21: Averaged amplitude of flame wrinkling RMS versus flame radius based on 30 explosions

case. However, in the zoomed in case, the r' at engine speed of 750 RPM with $\phi = 0.8$ shows higher than it is at stoichiometric condition, and not agreed with non-zoomed in case. Considering both ULG and iso-octane at engine speed 1500 RPM under high turbulence, there is a clear difference of r' between stoichiometric and $\phi = 0.8$. It is possible that the effect of equivalence ratio on r' is not sensitive under low turbulence; under high turbulence, the influence of equivalence ratio may be dramatic.

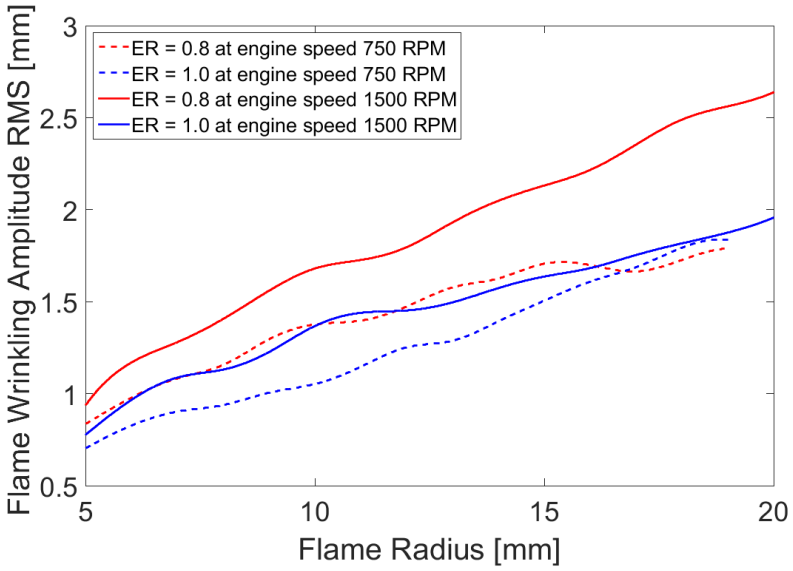

Figure 7.22: Iso-octane amplitude of flame wrinkling RMS versus flame radius derived from zoomed in images.

Unlike Figure 7.21, Figure 7.23 shows the flame contour RMS amplitude of flame wrinkling r' versus the time after spark. Both fuels show the r' at same engine speed share the same trend. From the time evolution of r', it seems that equivalence ratio have little influence on the flame wrinkling amplitude RMS. However, considering the flame radius development based on time is different in each condition, e.g. ULG under engine speed 1500 RPM at 2 ms after spark, the averaged flame radius difference is about 8 mm which compensates the r' difference brought by equivalence ratio. Under the non-zoomed in case, the r' shows its development with flame size growth. Because of the r' is not sensitive to the small wrinkles, the quantity of large wrinkles and their magnitude will make major contribution to the r' value. As a result, the r' is not a single factor to influence the flame speed. Since the r' increases with flame size, it is possible the wrinkle size increases with flame size.

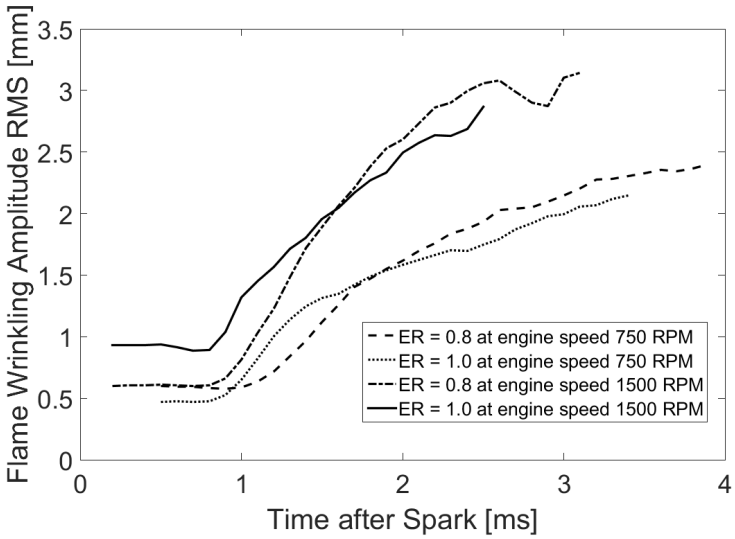

(a) ULG RMS amplitude of flame wrinkling

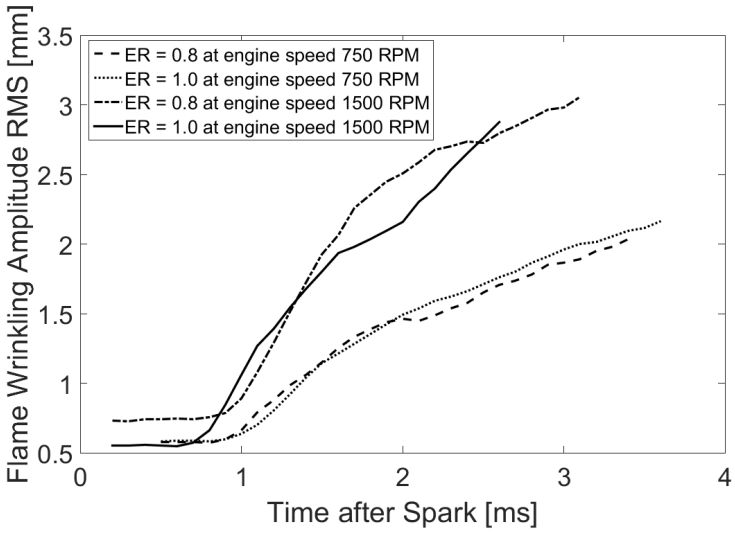

(b) Iso-octane RMS amplitude of flame wrinkling

Figure 7.23: Averaged RMS amplitude of flame wrinkling with respect to flame radius based on 30 explosions

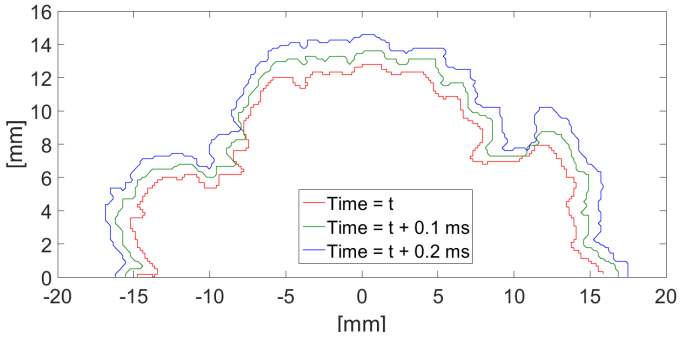

(a) Iso-octane flame sequential contours where flame centre is located at (0,0)

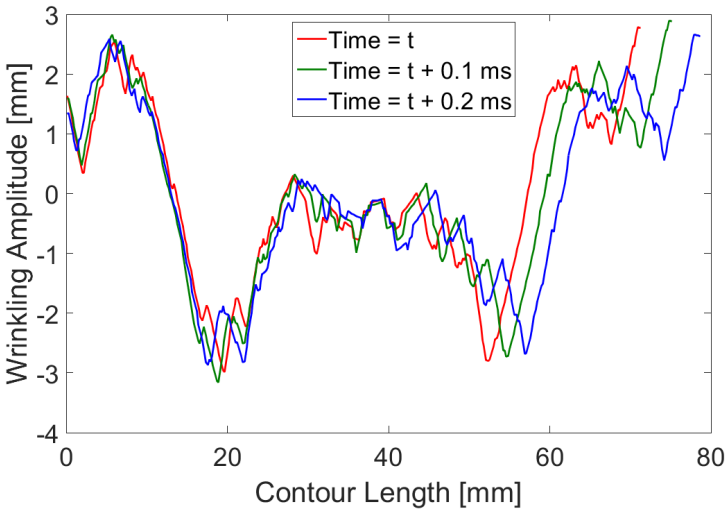

(b) Wrinkling amplitude derived from these sequential contours

Figure 7.24: Flame contours with 0.1 ms time interval of a random iso-octane explosion at 750 RPM stoichiometric condition

From a random explosion contour wrinkling amplitude with respect to contour position, see Figure 7.24, wavelengths of some of the wrinkles are stretched with the expansion of flame. In order to investigate the profile of the winkling, a characteristic size of flame wrinkles Lr' was obtained from the autocorrelation of the series which is same method for obtaining the turbulence integral length scale. Figure 7.25 shows integral length scale of flame wrinkles Lr' with respect to flame radius. It is clear that the Lr' increases as the flame grows for both fuels. There is a highly agreement on the Lr' derived from zoomed-in images shown by Figure 7.26. From the figure, a liner relationship can be observed between integral length scale of wrinkles and flame radius. It seems that the flame wrinkle will be stretched with flame expansion. The Lr' at different conditions are clearly larger than the

turbulent integral length scale after the flame radius of 10 mm. And a relative large Lr' in the large size flame contour, which means that the flame contour may have only a few very large wrinkles. Linear increase with radius suggest that those wrinkles grow without changing the flame shape much. It is also can be observed from the Figure 7.24 that only a few large scale wrinkles present on the flame contours.

Figure 7.27 demonstrates power spectral densities (PSD) for ULG and iso-octane at fully developed stage where flame radius around 12 mm, 15 mm, and 18 mm under engine speed of 750 RPM, stoichiometric mixture. Although the RMS magnitude of wrinkling and Lr' are increased as the flame growth, according to the figure, the PSD of the flame at different radii exhibit the same general trend and value after a wave number around 0.07 mm^{-1} for both fuels. For the small wave number, e.g. wave number greater than 0.07 mm^{-1}, the trend and value of PSD of the flame is almost same; and it is also observed in different equivalence ratio and different engine speed. As a result, the flame radius dose not affect energy in a wrinkle in a flame at fully developed stage. Considering the relationship between Lr' and flame size, the result suggested that the scale of the wrinkles increase with increasing of the flame flame size rather than the amplitude of the wrinkles.

Figure 7.28 demonstrates the averaged power spectral densities for ULG and iso-octane flame in fully developed stage in all conditions. For the very larger wave number, e.g. wave number greater than 2 mm^{-1}, due to resolution of the flame contour and noise from the defining unburned region by programme, the slope of the spectrum is greater than -5/3. Between wave numbers 1 mm^{-1} and 2 mm^{-1}, the slope of the spectrum is almost -5/3 which the energy cascade follows the turbulence energy spectrum in the inertial subrange. As a result, it is highly possible that the energy of wrinkles may relate to the turbulent flow in this range. Figure 7.29, shows the PSD derived from zoomed in images, the spectrum shows slope close to -5/3 when the wave number from 1 - 4 mm^{-1}. In zoomed in case, the spectrum at the wave number greater than 2 mm^{-1} shows still follows gradient -5/3 trend. Furthermore, at the end with large wave number, the spectrum derived from zoomed in images also shows the slope is flatten out. It is conformed that the slope flatten out is due to noise generated from the limited resolution.

For the large flame wrinkling, the wave number smaller than 0.3 mm^{-1}, the slope of the spectrum is close to -2.7. For both fuels at 1500 RPM with ϕ = 0.8, the ratio of u'/u_l is the largest among those conditions, the energy density is also the highest among those conditions. However, there is no clear evidence showing that the ratio of u'/u_l is turning the slope of spectrum. The slope is also

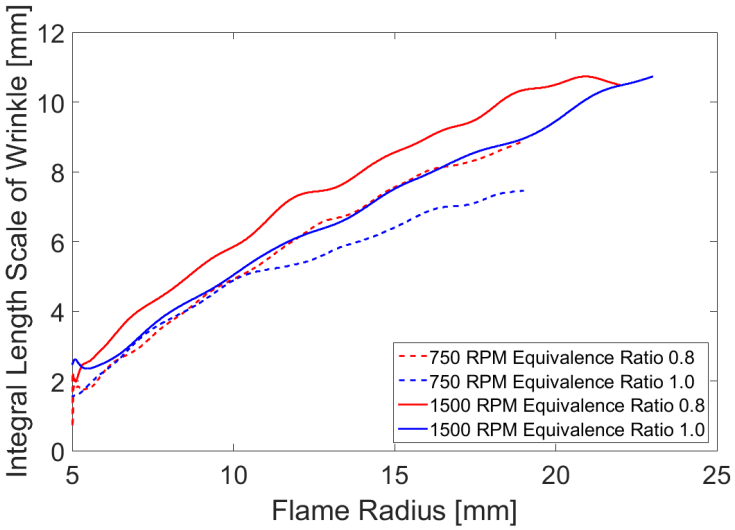

(a) ULG integral length scale of flame wrinkles

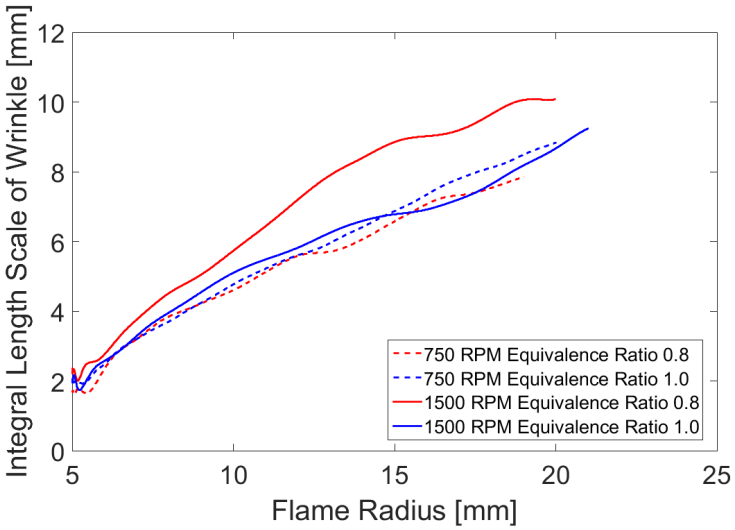

(b) Iso-octane integral length scale of flame wrinkles

Figure 7.25: Averaged integral length scale of flame wrinkles Lr' for ULG and iso-octane with respect to flame radius based on average over 30 explosions

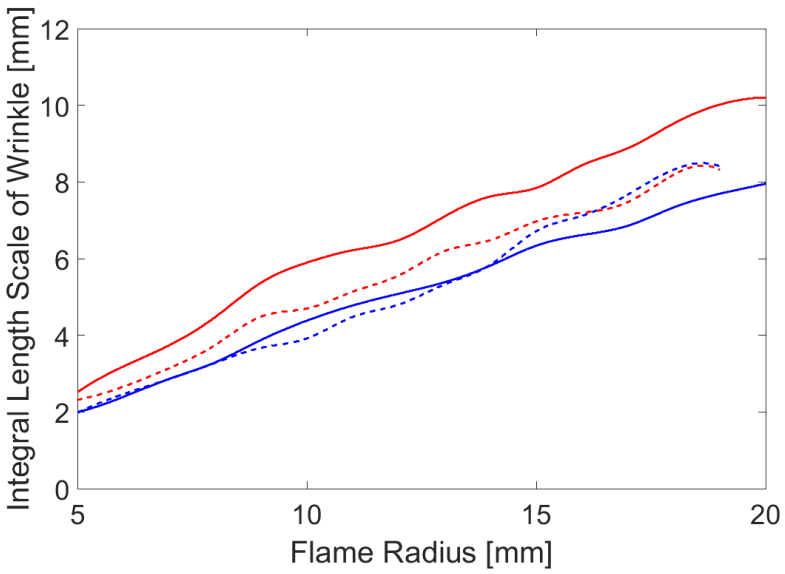

Figure 7.26: Iso-octane integral length scale of flame wrinkles derived from zoomed in images versus flame radius.

agreed with Atashkari et al. (1999) in a bomb study. Considering the experiment performed by Atashkari et al. (1999) applies different fuel, initial condition and turbulent flow compared with this study; and in this study the equivalence ratio and engine speed have no clear influence on the spectrum slope. The slope of -2.7 spectrum in shows in both experiment should confirm the flame wrinkling is under the influence of another turbulent energy cascade. The figures also show the magnitude of the spectrum for $\phi = 0.8$ at engine speed of 1500 RPM at same wave number is higher than other cases. However, there is no agreement on the effect of engine speed and equivalence ratio on magnitude of the spectrum compared with other conditions.

Considering the measured turbulent integral length scale in motoring cycles is about 3 - 4 mm during the main combustion period, the energy cascade start to show -5/3 gradient should approximately less than 3 mm (greater than 1/3 mm^{-1}). Considering the fresh gas is pushed by the burned gas towards radial direction, it is possible that the flame front fresh gas has an increasing integral length scale. Furthermore, the integral length scale of wrinkling increases with the flame radius. However, from Figure 7.27, there is no clear observation of the effect of flame radius on the starting point of the inertial subrange. This is due to limited size of the combustion chamber that could not provide a further stable propagation of the flame. Considering the contour length at flame radius 18 mm is approximately as twice as flame radius at 12 mm. If there is a stretch of fresh

gas eddies with flame propagation, it is impossible to observe the inertial subrange starting point because of the small turbulent integral length scale. And the slopes of -2.7 and -5/3 are so close that hard to find the exact point for changing gradient.

Considering the turbulent regimes according to Bradley et al. (2013), and some hydrocarbons critical radii for onset of instability (Jomaas et al. 2007). There is cellular flame presenting in the experiment condition in this study. Considering the flame wrinkles introduced by flame cellularity should influence the spectrum slope because of there is another energy source bring the energy into the to wrinkles. However, the spectrum shows the slope -2.7 and -5/3, indicating the energy source is from turbulence. As a result, there is no trace of energy from flame cellularity. It is highly possible that the wrinkles from the flame cellularity is so small that the current camera resolution could not capture.

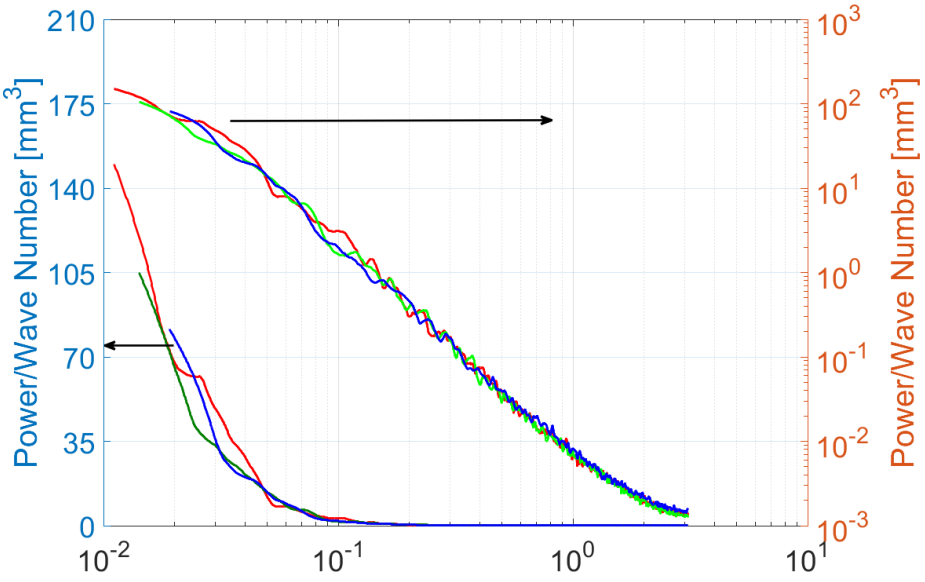

(a) PSD for ULG explosions

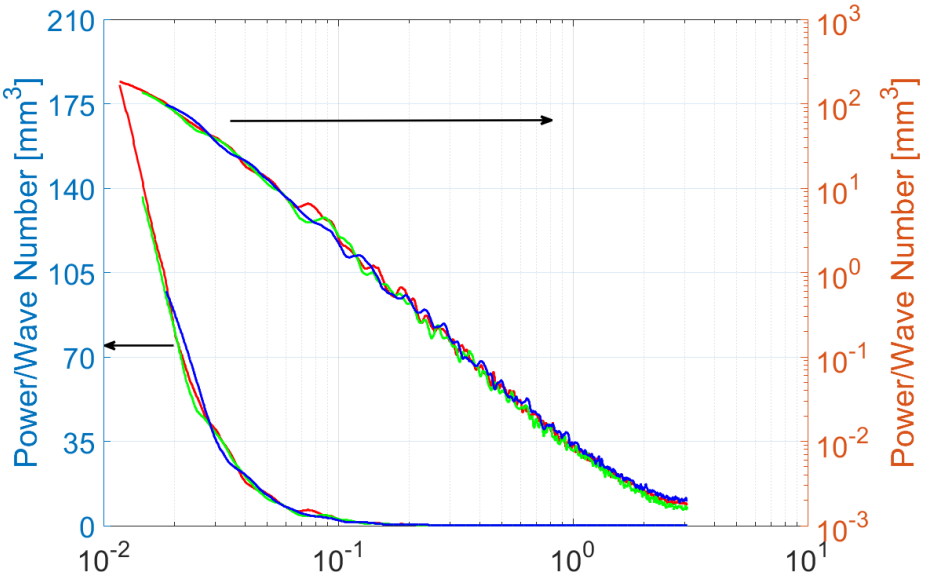

(b) PSD for iso-octane explosions

Figure 7.27: PSD for ULG and iso-octane flame contours at radius about 18 mm (red), 15 mm (green) and 12 mm (blue) based on average over 30 explosions

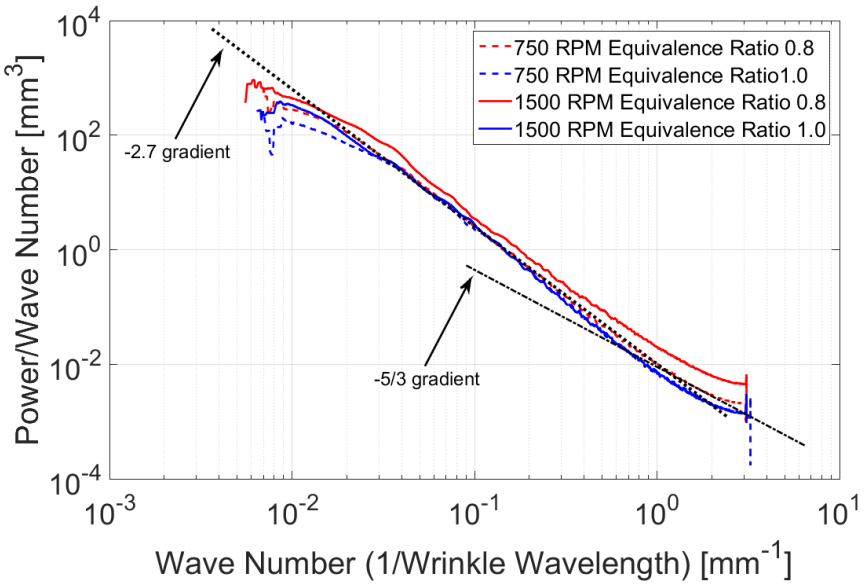

(a) PSD for ULG explosions

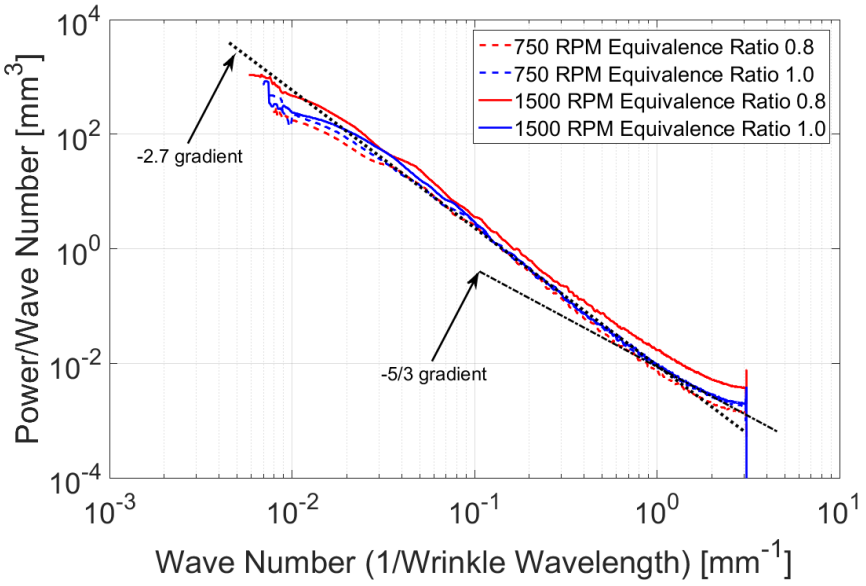

(b) PSD for iso-octane explosions

Figure 7.28: PSD for ULG and iso-octane flame contours at radius from 12 - 19 mm based on average over 30 explosions in all conditions

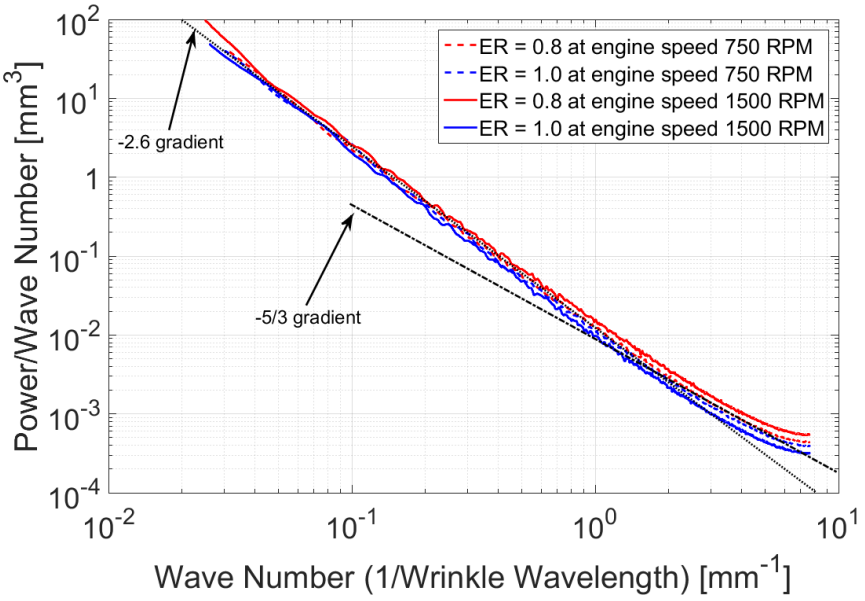

Figure 7.29: Iso-octane integral length scale of flame wrinkles derived from zoomed in images versus flame radius.

7.3 Flame Front Turbulence

7.3.1 Selection of Flame Front Unburned Annulus Width

The measurement of turbulent RMS velocity u' based on the spatial averaging ahead of the flame was based on spatial averaging in a narrow unburned gas "annulus" surrounding the flame shown in Figure 7.30. The width of annulus ranges from 0.32 mm to 1.60 mm. A study was taken to investigate the width of fresh gas annulus effects on flame front turbulence calculations. Figure 7.31 shows how the width of fresh gas annulus affect the u'_r derived over it. Figure 7.31(a) shows the annulus width has little influence on u'_r averaged over it, because of the wider annulus has more data samples, the unburned gas u'_r profile has less fluctuations. However, the wide annulus will be a filter that smooth the result. As shown in Figure 7.30 a wide annulus will fill the flame edge 'pocket' with so that smooth out detailed flame front velocity. In some cases, the wider annulus may result in the u'_r slightly lower in the annulus next to the flame front, due to u'_r decays when data samples are away from the flame front, see Figure 7.31(b). In order to minimise the influence from the u_r decay along the radial direction and keep the sufficient amount of data samples in the annulus for processing speed, the annulus width was suggested to be no more than 1.6 mm. In some cases, such as observation of unburned gas moving velocity, the annulus width will need to

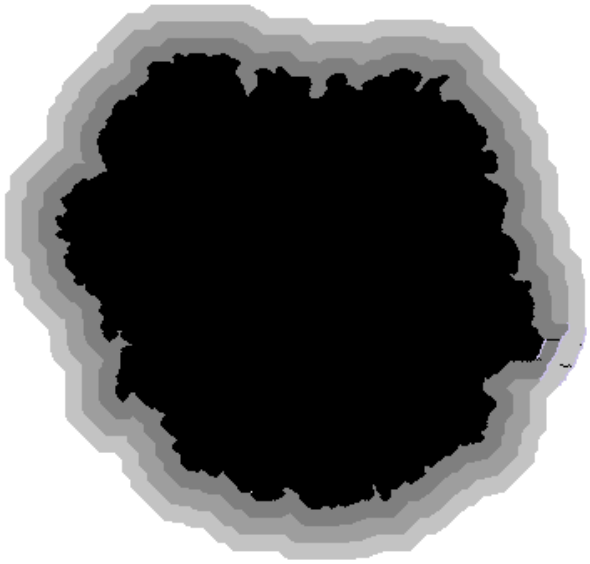

Figure 7.30: Burned gas (black) and different unburned gas annulus (gray) average flame radius = 23.16 mm and annulus width = 1.60 mm

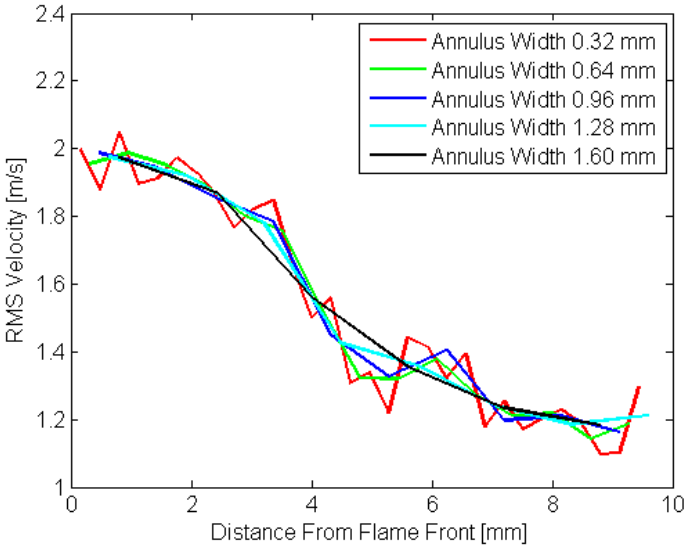

(a) Stoichiometric 750 RPM average radius = 9.65 mm

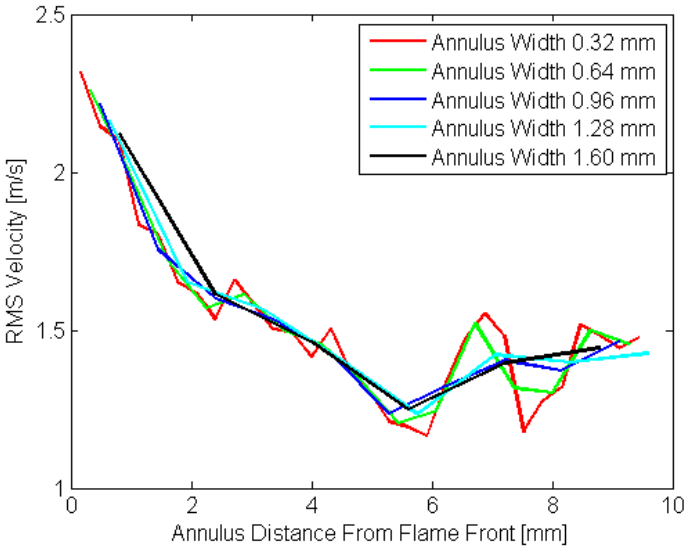

(b) Stoichiometric 750 RPM average radius = 13.05 mm

Figure 7.31: Random ULG explosion at 750 RPM of RMS velocity of fresh gas annulus as function of distance of away from flame front for different annulus width

be lower, down to 0.64 mm in this study to achieve good sensitive for the velocity change. It can be assumed that the u_r decay is making little contribution to the u'_r and u_r measured in a narrow annulus.

7.3.2 Flame Front Unburned Turbulence Profile

Figure 7.32 demonstrates the unburned gas radial RMS velocity v'_r and tangential RMS velocity v'_r respect to distance from flame front. The RMS velocity–distance profile was observed at flame radius from 5 mm to 15 mm with annulus width of 1.6 mm for ULG at four different conditions. The radial velocity of unburned mixture u_r are all positive going outwards, see Figure 7.33(a) and (c), the overall flow directions of unburned mixture are influenced by flame propagation can be last for a long distance from flame front. The u'_r–distance profiles for different flame radius are merged at somewhere around 15 - 20 mm away from flame front despite u'_r next to the flame front. As a result, for the influence of flame propagation on u'_r is limited by the distance away from flame. For the value of u'_r where the curves converge, it is very close to motoring cycle u_r components RMS velocity. For the turbulent flow in tangential direction, similarly with u'_r, there is also an increase of the v'_r of unburned gas next to the flame front in initial flame and n acceleration stage. It is also shows the flame propagation is not only having influence on the u'_r but also on the v'_r. For the tangential flow v_r, there is no clear observation on nether the distance away from the flame front nor the flame radius in initial acceleration stage has influences on the v_r.

Considering the cylinder radius is 40 mm and the flame propagation may alter the flame front turbulent flow and the effect of flame propagation on turbulent RMS velocity could last about 20 mm away from the flame. The RMS velocity-distance profile shows similar trend during flame radius from 12 to 19 mm. As a result, there is little influence from the fresh gas flow interact with the cylinder wall. However, the u'-distance profile for the large size of the flame such as flame radius of 18 and 19 mm, there is a trace to show that the fresh gas u' that far from the flame surface is influenced by the cylinder wall. This is why the flame speed is studied in the fully developed stage with a maximum of 20 mm flame to avoid the influence from the cylinder wall.

In the fully developed flame stage, it is certain that both u'_r and v'_r ahead of the flame is greater than they are measured at same region and same time in motoring cycles. The flame propagation has altered flame front turbulent RMS velocity and flame radius is not a factor dominate the turbulent flow ahead of flame during the fully developed stage. It is similar with the flame speed in fully developed stage which the flame speed is a constant. As a result, the flame front turbulent RMS velocity u'_r and v'_r are not dominated by the size of flame. At very small flame radius such as 5 and 6 mm, the flame size is small and the flame front turbulent RMS velocity u'-distance profile seems already been influenced

by the flame propagation. Considering the flame front turbulent RMS velocity increases with the increasing of the flame speed in acceleration stage. There is highly possible that the flame front turbulence is induced by the propagation of the flame and the flame speed may have direct influences. The summuary of possible mechanisms of turbulence generation at the premixed flume front can be fond in Hirano (2000).

Figure 7.34 shows the vorticity magnitude versus the distance measured from flame front. The vorticity magnitude is nearly a constant when flame at the fully developed stage. In this study, there is no evidence of the vorticity magnitude is settling down at 15 - 20 mm away from the flame front. There is a clearly observation that the vorticity magnitude trace for the large flame radius is descending faster than the smaller flame despite they have similar value at the flame surface. It seems that there is a strong influence of the cylinder wall on the vorticity magnitude compared with the turbulent RMS velocity. It is highly possible that there is no direct connection between the vorticity magnitude and the turbulent RMS velocity.

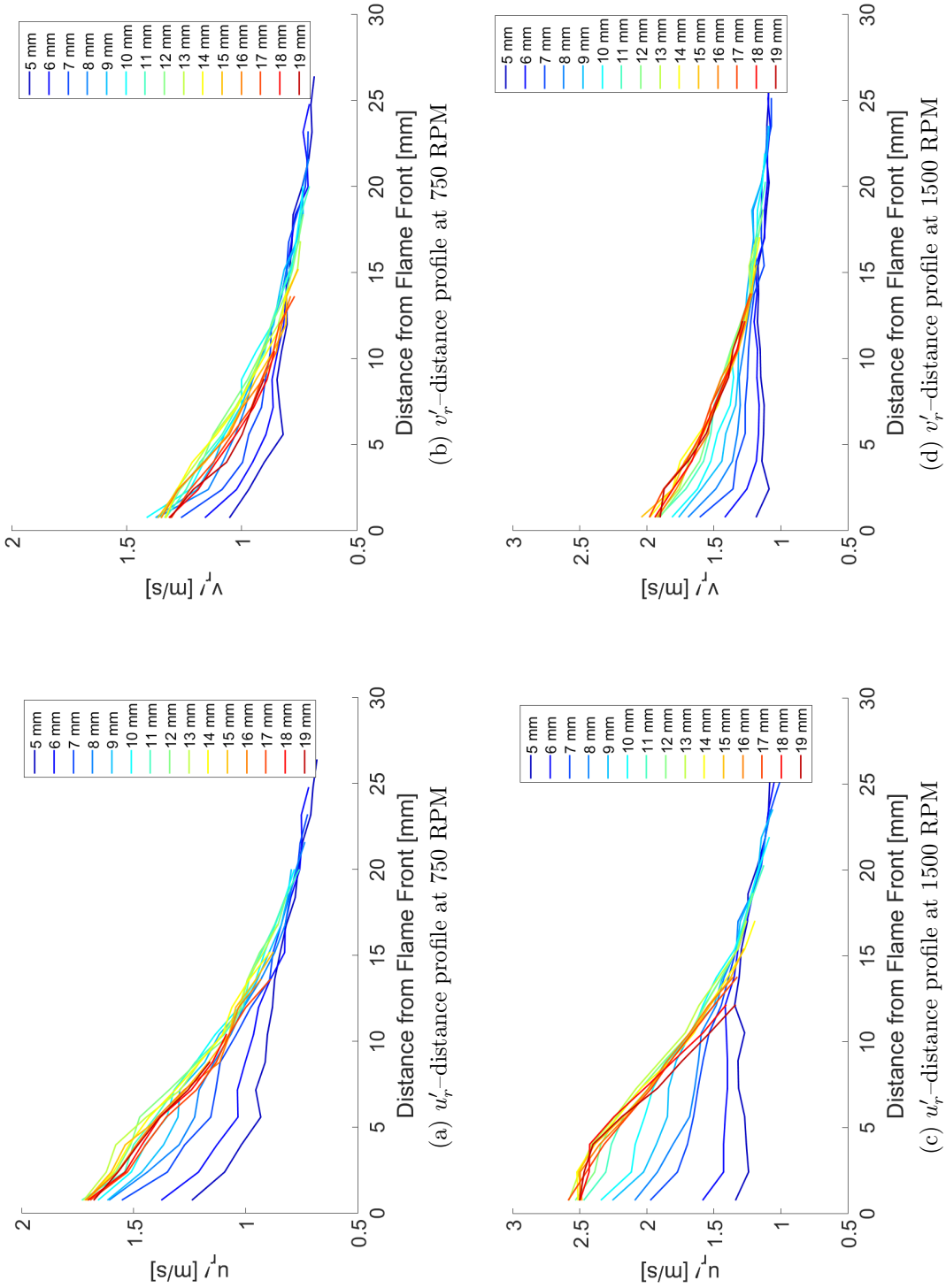

(a) u'_r–distance profile at 750 RPM

(b) v'_r–distance profile at 750 RPM

(c) u'_r–distance profile at 1500 RPM

(d) v'_r–distance profile at 1500 RPM

Figure 7.32: The unburned mixture turbulent RMS velocity of ULG at stoichiometric condition versus distance from flame for flame radius from 5 mm to 19 mm under engine speed of 750 RPM and 1500 RPM.

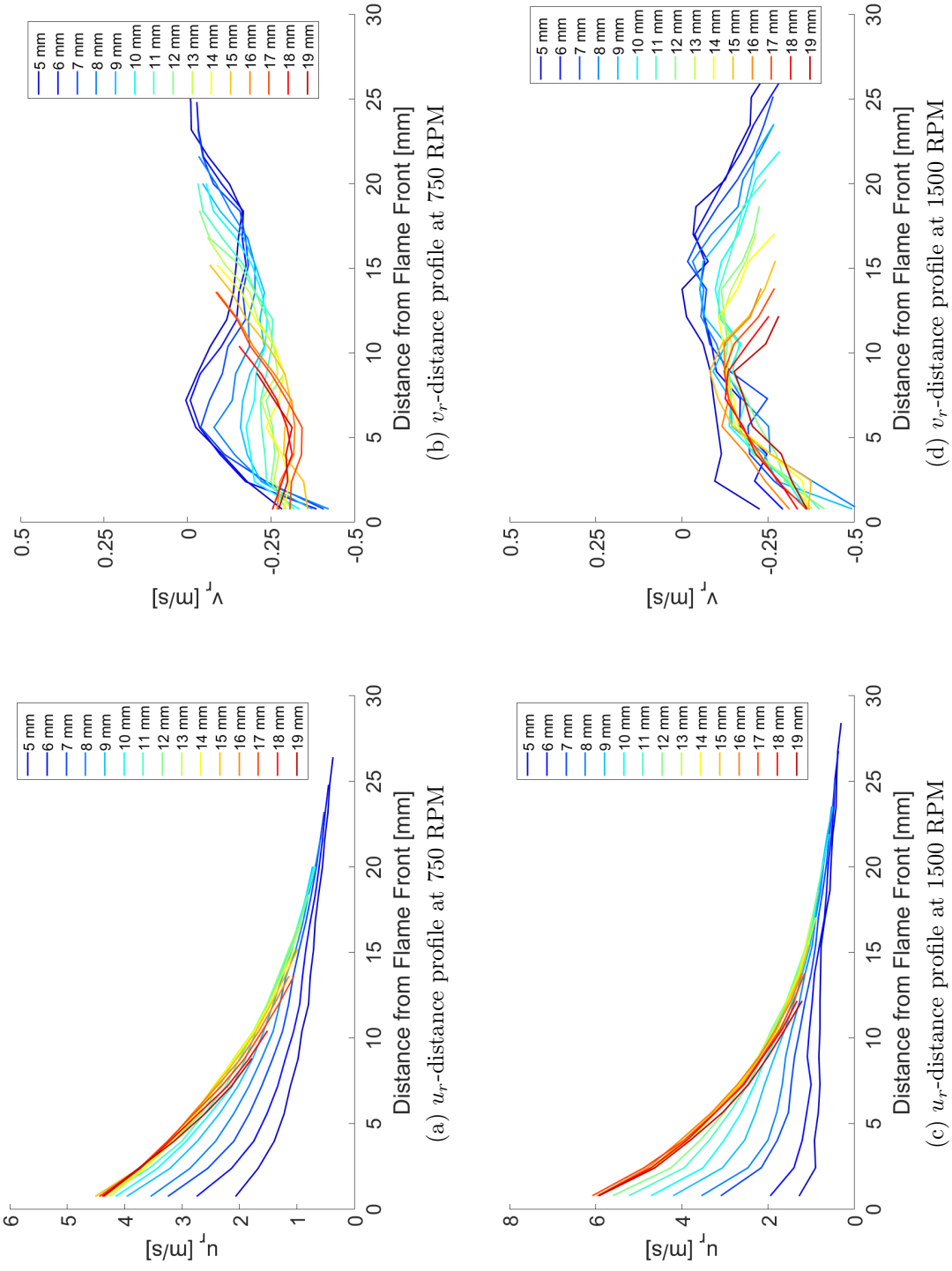

(a) u_r-distance profile at 750 RPM

(b) v_r-distance profile at 750 RPM

(c) u_r-distance profile at 1500 RPM

(d) v_r-distance profile at 1500 RPM

Figure 7.33: The unburned mixture flow velocity versus measured distance for flame radius from 5 mm to 19 mm at engine speed of 750 RPM and 1500 RPM for stoichiometric ULG.

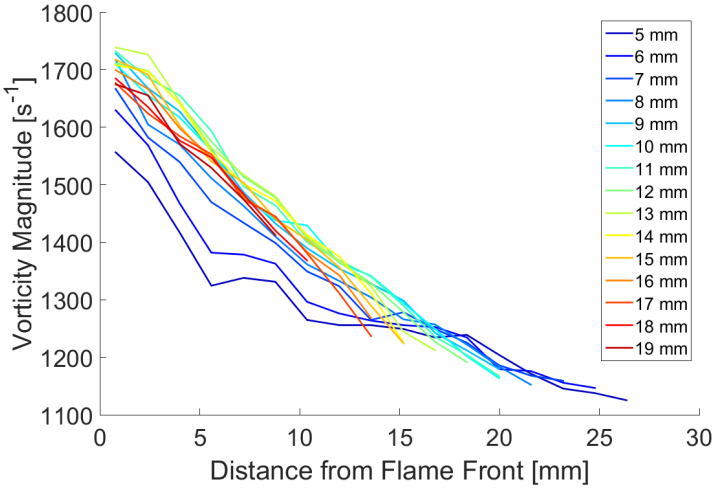

(a) Vorticity magnitude-distance profile at 750 RPM

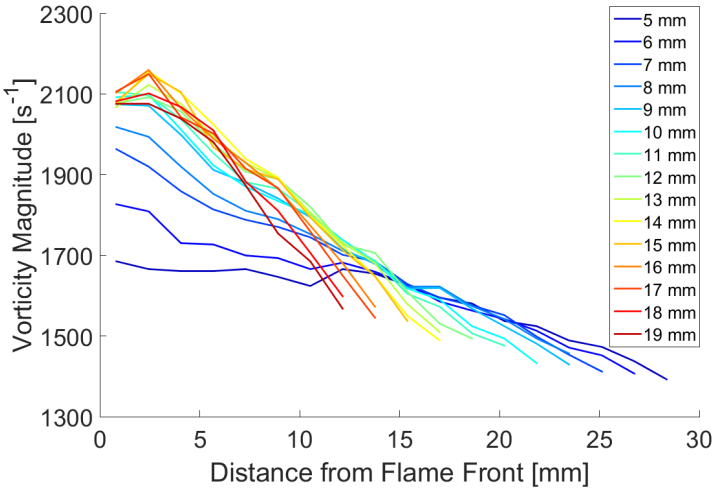

(b) Vorticity magnitude-distance profile at 1500 RPM

Figure 7.34: Unburned vorticity magnitude-distance profile for flame radius from 5 mm to 19 mm at engine speed of 750 RPM and 1500 RPM for ULG at stoichiometric condition.

7.3.3 Turbulence at Flame Surface

Figure 7.35 shows the relationship between the flame speed and the turbulent RMS velocity u' at flame surface at flame radius from 12 - 18 mm. According to the figure, those two different fuels, each fuel show the agreement of flame speed is proportional to their flame front u'_r, and there is little influence from the fuel difference. According to Figure 7.35(a), it seems that there is a linear relationship between the fully developed flame speed and u'_r next to the flame front. Furthermore, there is no clear observation of the effect of equivalence ratio on the relation between flame speed and u'_r at the flame surface. Considering the equivalence ratio may have influence on the turbulent flame speed – cold flow turbulence intensity correlation. However, a same fitting line satisfy all the conditions including the different equivalence ratio which potentially refers that the flame surface turbulence may not have impact on the flame speed as same as the cold flow turbulence. Since the equivalence ratio is not affect the $u'_r - S_t$ relations, it is possible that the u'_r at flame surface is not involved in combustion. The linear relationship between the u'_r at flame surface and the S_t indicates the u'_r is potentially generated by the burned gas expansion physically disturbs the fresh gas.

The v'_r at flame surface is shown in Figure 7.35(b), the v'_r - flame speed trace seems have a non-liner relationship. Furthermore, the effect of equivalence ratio on the relationship is not confirmed. However, the figures are confirmed that the flame front u' is not influenced by flame radius during the fully developed stage. Considering the u' in motoring cycle is not affected by the equivalence ratio, and there is a constant u' at same engine speed. However, the u' next to the flame front shows clear difference at the same engine speed with different flame speed. It seems that the u' next to flame front may not have direct connection with motoring cycle u'. Although the turbulent flame speed S_t is proportional to $u_l^{0.5} u'^{0.75}$ according to the Zimont turbulent burning velocity approach (Zimont et al. 1998). From the figure, there is no clear observation of $S_t \sim u'^{0.75}$ relationship in the data samples. Considering there is no clear evidence shows that the flame speed is totally dominated by the flame front u'. It seems that the mismatch of the u' from the motoring cycle is caused by flame fast expansion.

Figure 7.36 shows the flame speed as a function of the vorticity magnitude at flame surface at flame radius from 12 - 18 mm. There is no flame radius effect on the flame surface vorticity magnitude during the fully developed stage. Similar to the v'_r at flame surface, it seems that the ULG and iso-octane are shearing the same trend. There is also a non-liner relationship observed for the vorticity magnitude

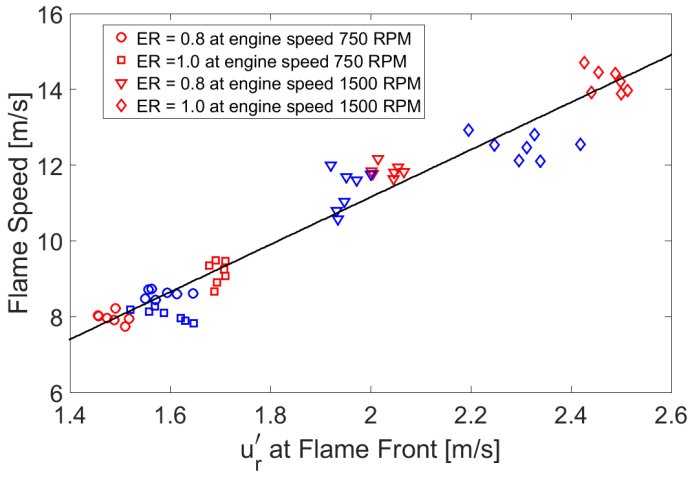

(a) Flame speed as a function of u'_r

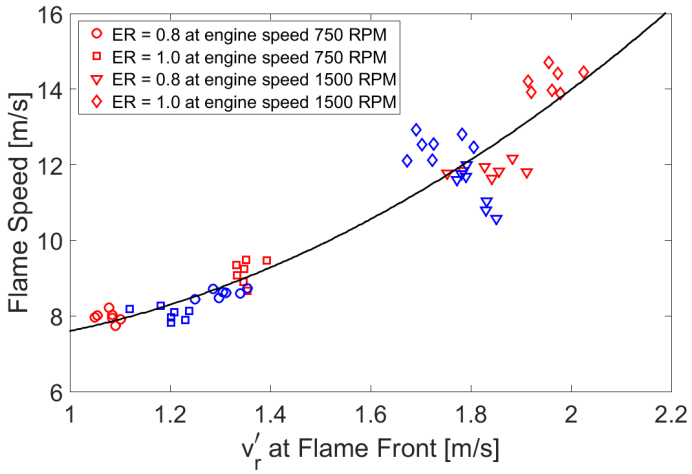

(b) Flame speed as a function of v'_r

Figure 7.35: Flame speed as a function of u'_r and v'_r next to the flame front, the red and blue makers refer ULG and iso-octane, respectively, sampling at fully developed flame stage with radius 12 - 18 mm with sample interval of 1 mm.

– flame speed trace. There is little influence from the equivalence ratio on the vorticity magnitude – flame speed relation. Comparing the vorticity magnitude at the motoring cycle, there is also an elevation of the magnitude for the vorticity once the flame propagation is involved.

Figure 7.37 shows the flame speed as a function of flame surface turbulent RMS velocity for the flame radius 6 - 12 mm during the flame acceleration stage. It clearly shows that the u' increases with the flame speed during the initial acceleration stage. The flame surface turbulent RMS velocities and flame speed stop increasing at the flame radius 7 - 8 mm at 750 RPM. The growth of the flame

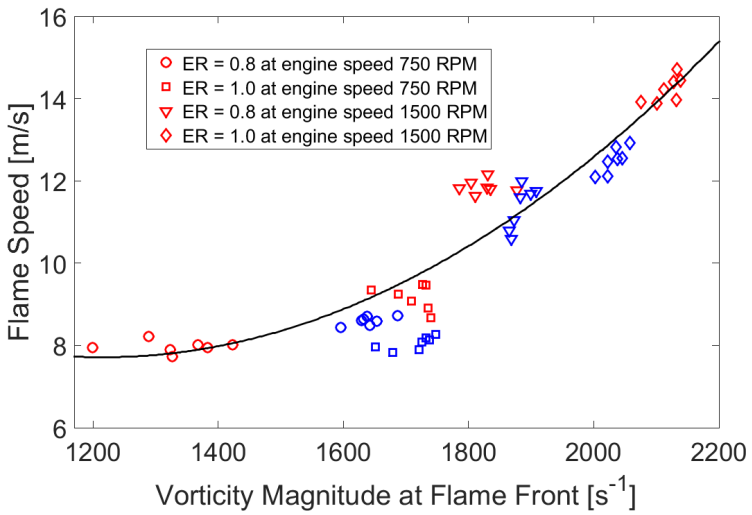

Figure 7.36: Flame speed as a function of flame surface vorticity magnitude, the red and blue makers refer ULG and iso-octane, respectively, sampling at flame radius 12 - 18 mm with sample interval 1 mm.

front RMS velocities at this engine speed is limited. However, there is a noticeable growth of the flame surface turbulent RMS velocities. Comparing the traces of the flame speed with respect of turbulent RMS velocities at 1500 RPM under different equivalence ratio, there is an elevation of the flame speed at the same turbulent RMS velocities for both fuels at stoichiometric condition. When the flame radius close to 12 mm, the effect of the flame surface turbulent RMS velocities on flame speed is decreasing. For the u'_r at flame surface during the initial acceleration stage, at the same level of u'_r, the flame speed is clearly higher than it is at the fully developed stage. For the v'_r - flame speed relation at the initial acceleration stage, it mostly agrees the trend at the fully developed stage.

Comparing these two turbulent RMS velocities, most of the u'_r is about 30% higher than the v'_r during the fully developed flame stage and the ratio maintain a constant during flame propagation, see Figure 7.38(a). For the initial flame acceleration stage, Figure 7.38(b) shows the ratio of u'_r over v'_r increases with flame propagation. Considering the direction of u_r is along the flame propagating direction and can be affected by the flame speed. On the other hand, v_r is not affected by the flame propagation. As a result, the u'_r is possibly increased by the growth of the u_r.

In terms of vorticity, Figure 7.39 shows the vorticity magnitude as a function of the flame speed during the initial flame acceleration stage. At the engine speed 750 RPM, vorticity magnitude - flame speed relation matches it is at the fully de-

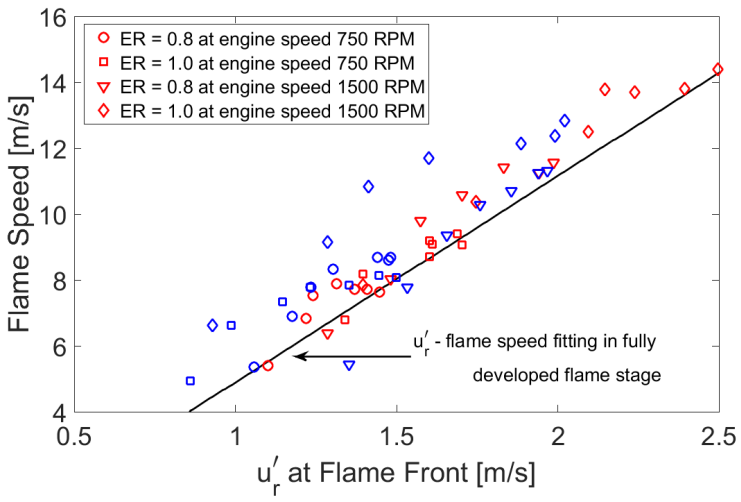

(a) Flame speed as a function of u'_r

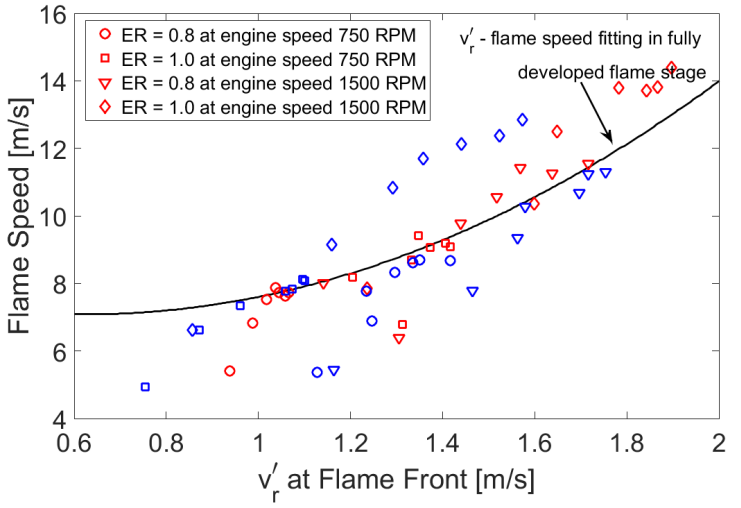

(b) Flame speed as a function of v'_r

Figure 7.37: Flame speed as a function of u'_r and v'_r next to the flame front, the red and blue makers refer ULG and iso-octane, respectively, sampling at initial flame acceleration stage with radius 5 - 11 mm with sample interval of 1 mm.

veloped flame stage mostly. However, at engine speed of 1500 RPM, the condition of $\phi = 0.8$ is failed to match the trend observed in fully developed flame stage for both fuels. On the other hand, for the stoichiometric condition, the vorticity magnitude - flame speed relation is comparable with the relation in the fully developed flame stage. For the condition of $\phi = 0.8$, there is a high level of vorticity magnitude but the flame speed is relatively low. It is possible that the vorticity magnitude makes contribution to flame acceleration in the initial flame accelera-

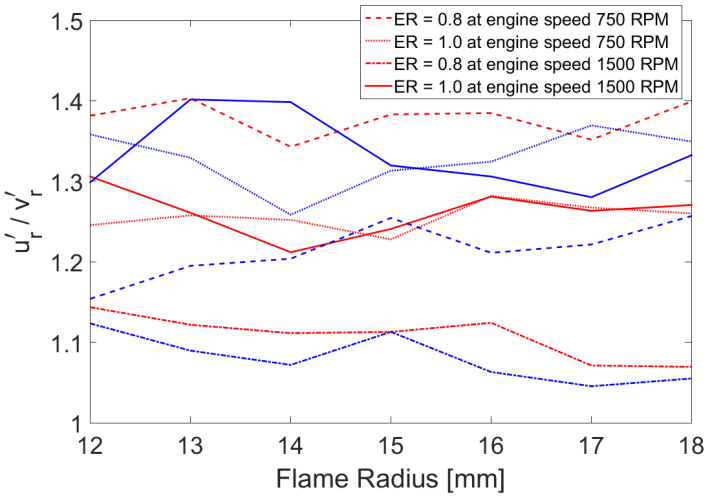

(a) u'_r over v'_r versus flame radius for the fully developed flame stage.

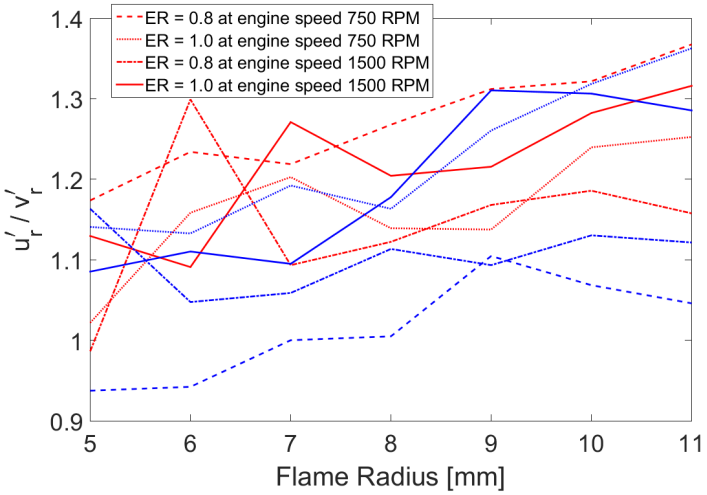

(b) u'_r over v'_r versus flame radius for the initial flame acceleration stage.

Figure 7.38: u'_r over v'_r ratio versus flame radius, the red and blue lines refer ULG and iso-octane, respectively.

tion stage. However, due to lack of images for small flame kernel development, it still need to be confirmed for other conditions. For the stoichiometric condition at engine speed of 1500 RPM, the vorticity magnitude - flame speed relation for both fuel show highly comparable to the fitting line derived from the fully developed flame stage.

Figure 7.40 shows the flame acceleration versus the flame radius during the initial flame acceleration stage. For the engine speed of 750 RPM, there is little difference between fuels and equivalence ratios. For the engine speed of 1500

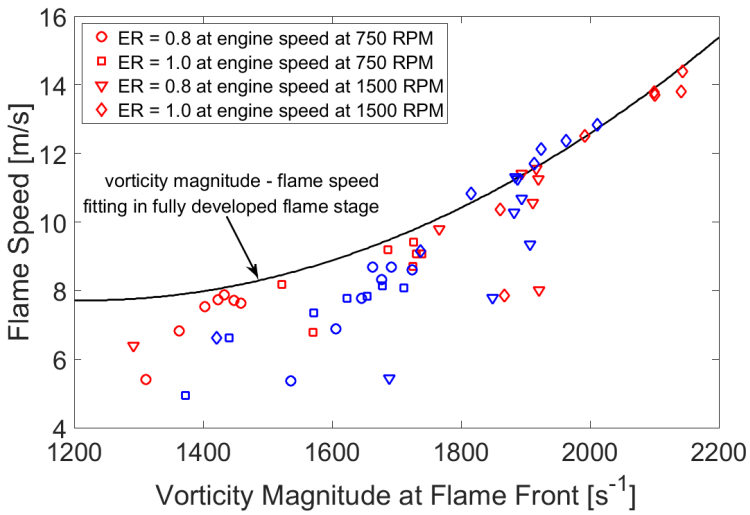

Figure 7.39: Flame speed as a function of flame surface vorticity magnitude, the red and blue makers refer ULG and iso-octane, respectively, sampling at flame radius 5 - 11 mm with sample interval of 1 mm.

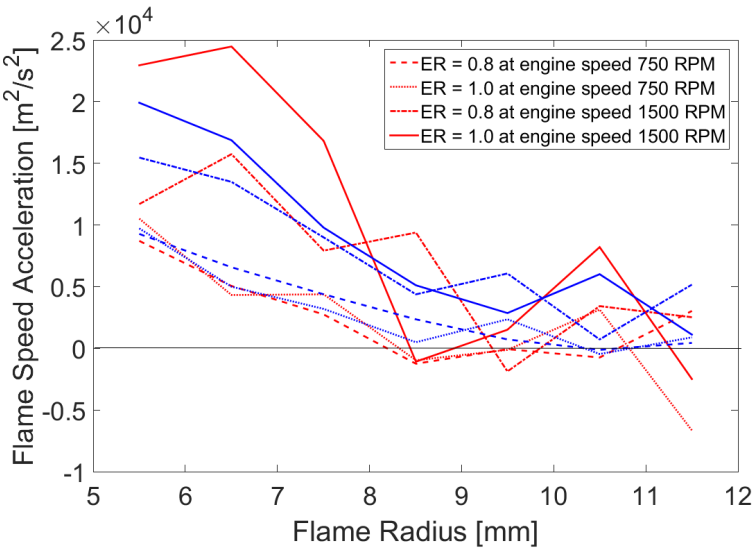

Figure 7.40: Flame acceleration as a function of flame radius, the red and blue lines refer ULG and iso-octane, respectively.

RPM, the flame acceleration is clearly higher than it is at 750 RPM. The fuel and equivalence ratio seems make great influence on the flame acceleration at engine speed. Figure 7.41 shows the u'_k development as a function of flame size. The experiment conditions in this study have little influence on the development of u'_k, at flame radius of 5 mm, the u'_k approximately reaches 50% of the u'. For the flame radius of 12 mm, the u'_k approximately over 70% of the u'. For the flame radius

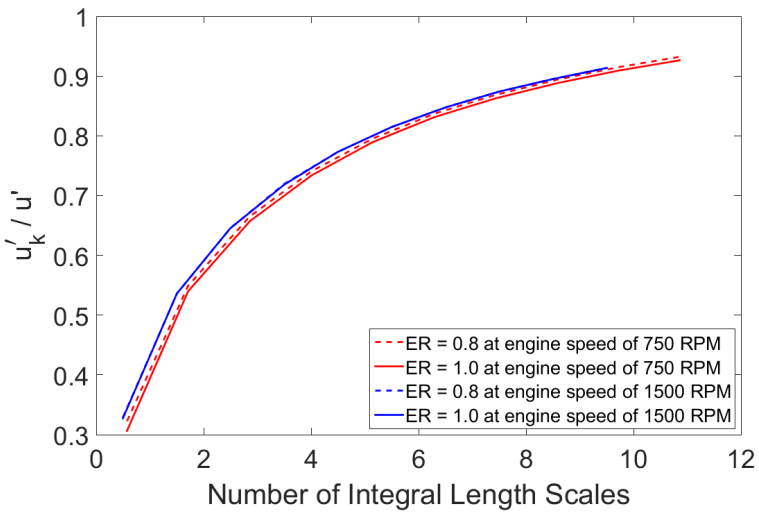

Figure 7.41: Variations of u'_k/u' with number of integral length scales at different experiment conditions

12 - 18 mm, the u'_k/u' is approximately between 0.7 and 0.8. Because of the u' at engine speed of 1500 RPM is higher compared with the u' at 750 RPM. It seems that the high flame speed acceleration in initial acceleration stage is supported by the u'_k development. In terms of the flame surface vorticity magnitude shown in Figure 7.39, the low flame speed corresponds to the high vorticity magnitude upon the flame radius is small. Based on the flame surface vorticity magnitude and flame speed correlation derived from fully developed flame, the difference of vorticity magnitude from the correlation is shown by Figure 7.42. Although there is overall trend showing that the vorticity magnitude difference is decreasing with the decrease of the flame speed acceleration, there are no obvious relations between them. For instance, the stoichiometric ULG-air mixture at engine speed of 1500 RPM shows the largest speed acceleration before flame radius of 8 mm, however, vorticity magnitude difference is not the largest. As a result, the flame speed acceleration may not relate to the flame surface flow. It is still unclear whether the flame surface turbulence could have influence on the flame propagation.

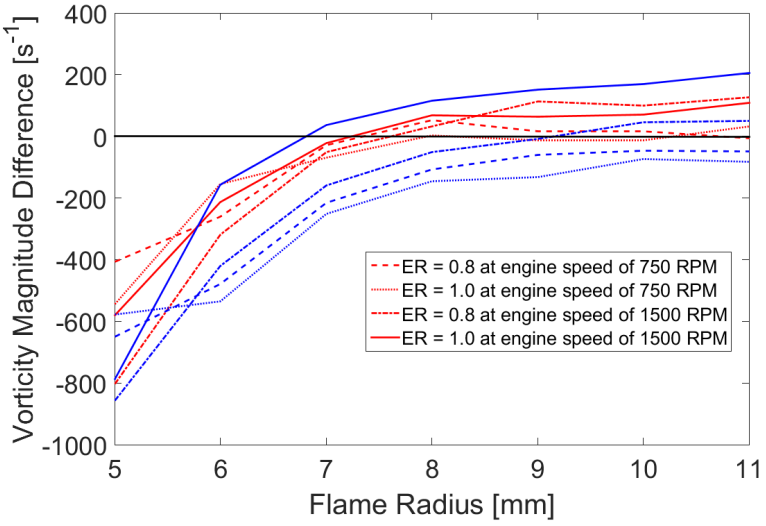

Figure 7.42: Difference of vorticity magnitude from the correlation as a function of flame radius, the red and blue lines refer ULG and iso-octane, respectively.

7.4 Burning Velocity

7.4.1 Unburned Mixtures Radial velocity at Flame Surface

The fresh gas radial velocity of ULG next to the flame surface is shown in Figure 7.43, where it was extrapolated by the continuity equation in 4.19. According to this figure, in the acceleration stage, the unburned gas radial velocity is growing with flame expansion. For the flame radius in the range of 12 - 18 mm, where the flame is upon the fully developed flame stage, at the equivalence ratio 0.8 and 1 under engine speed 750 RPM and 1500 RPM, the fresh gas radial velocities are nearly constant as 4.37 m/s, 5.19 m/s, 5.82 m/s and 7.18 m/s, respectively. The unburned gas radial velocity data samples show high levels of consistency, there is about ±1.5 m/s variation of unburned gas radial velocity and neither engine speed nor equivalence ratio has significant influence on the velocity variation. According to the flame speeds shown by Figure 7.14, the fresh gas radial velocities are about half of the flame speed with 55.0%, 56.7%, 48.6% and 50.6%, respectively. From the averaged flame speed and averaged radial unburned gas moving velocity, the burning velocity can be obtained at all the four conditions, 3.58 m/s, 3.96 m/s, 6.15 m/s, 7.00 m/s, respectively.

For iso-octane flame propagation, the unburned gas radial velocity at flame radius 12 - 18 mm in the fully developed flame stage is shown in Figure 7.44, the fresh gas radial velocity stays a constant 5.17 m/s, 4.19 m/s, 5.68 m/s and 5.74 m/s, at equivalence ratio 0.8 and 1 under engine speed 750 RPM and 1500 RPM, respectively. According to the flame speeds shown by Figure 7.15, the fresh gas radial velocity are about half of the flame speed with 60.3%, 52.0%, 50.6% and 46.1%, respectively. From the averaged flame speed and averaged radial unburned gas moving velocity, the burning velocity can be obtained at all the four conditions, 3.41 m/s, 3.87 m/s, 5.54 m/s, 7.01 m/s, respectively.

Comparing the unburned gas radial velocities between two fuels, they have very similar ratio of u_r over S_t and the burning velocity. At the engine speed of 750 RPM, the u_r over S_t ratio is higher than it is at 1500 RPM. For iso-octane at 750 RPM, although the flame speed at $\phi = 0.8$ is higher than $\phi = 1.0$, the burning velocity is shown reasonable lower than $\phi = 1.0$. The lower density ratio ρ_b / ρ_u at $\phi = 0.8$ is higher than $\phi = 1.0$ so that the flame speed is enhanced at $\phi = 0.8$ condition. At the condition of u' / u_l equals 1, Witze & Mendes-Lopes (1986) shows the u_r is about 57.6% of the flame speed, this is highly comparable to the results from this study. There is noticeable decrease of the u_r after flame radius of 25 mm. The reason may due to fresh gas is too close to the cylinder wall and

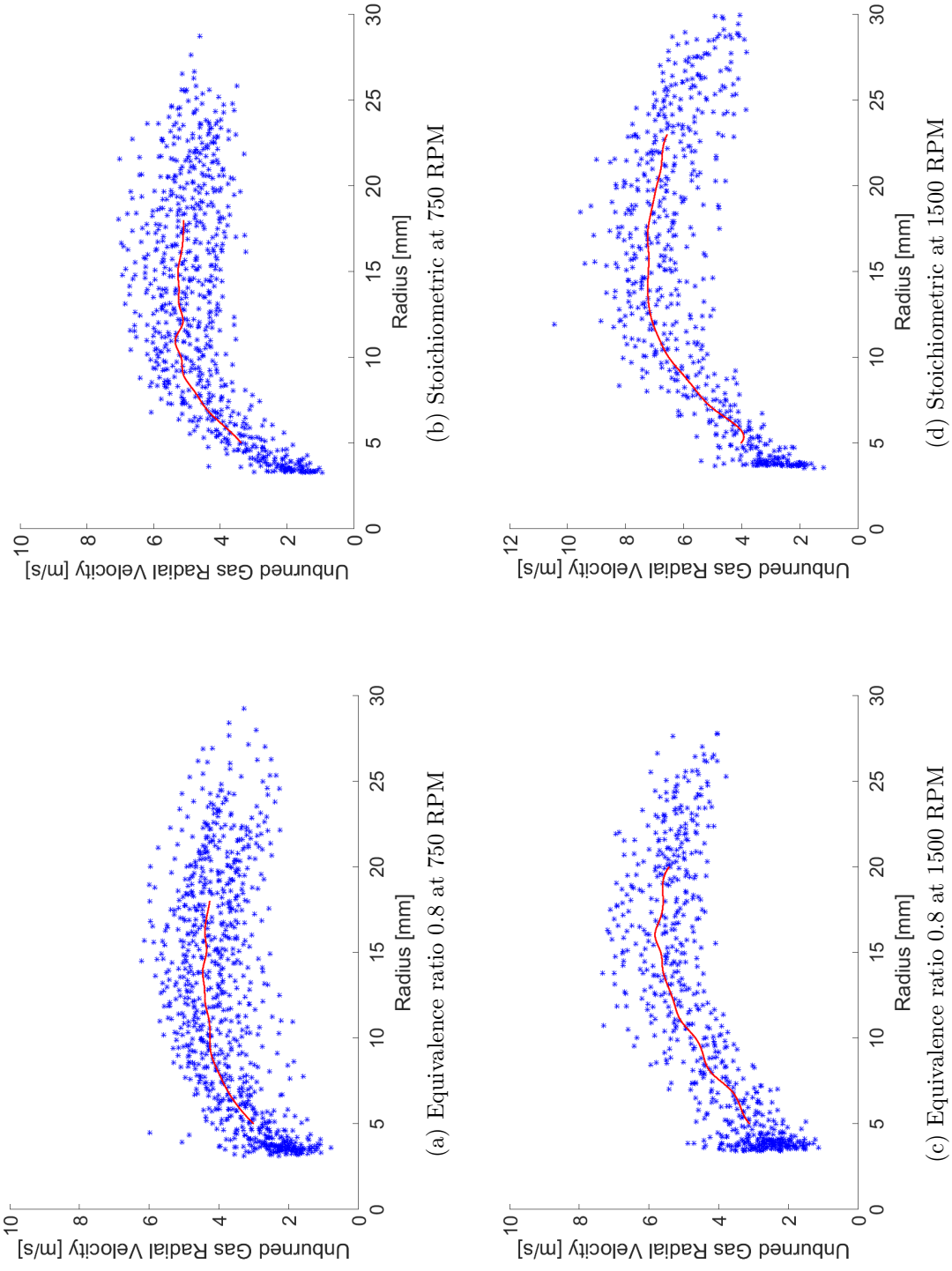

(a) Equivalence ratio 0.8 at 750 RPM

(b) Stoichiometric at 750 RPM

(c) Equivalence ratio 0.8 at 1500 RPM

(d) Stoichiometric at 1500 RPM

Figure 7.43: Extrapolated unburned gas radial velocity at flame surface versus flame radius for ULG, the averaged trace is shown in red.

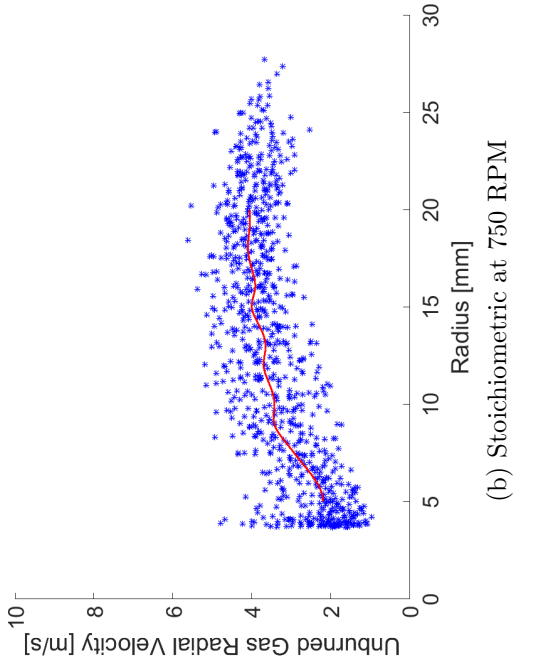

(a) Equivalence ratio 0.8 at 750 RPM

(b) Stoichiometric at 750 RPM

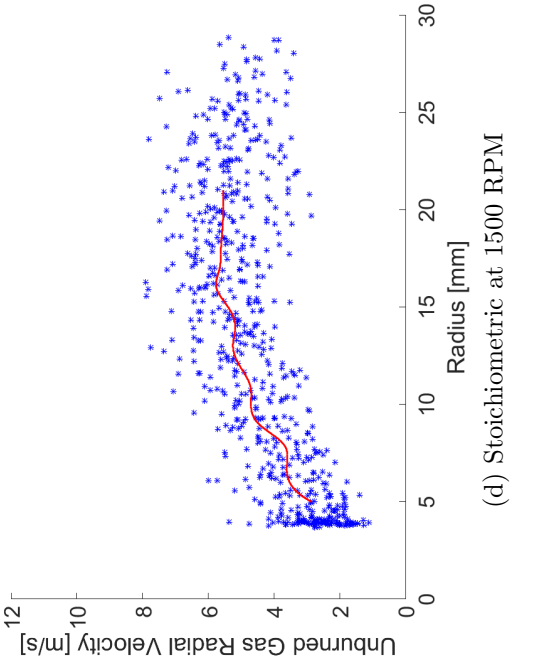

(c) Equivalence ratio 0.8 at 1500 RPM

(d) Stoichiometric at 1500 RPM

Figure 7.44: Extrapolated unburned gas radial velocity at flame surface versus flame radius for iso-octane, the averaged trace is shown in red.

the cylinder wall alters the fresh gas flow. The extrapolation of the flame surface unburned gas radial velocity is affected by the altered gas flow.

For the u_r derived from the zoomed-in case, Figure 7.45 shows the u_r at flame surface versus the flame radius. The u_r at the flame radius of 12 - 18 mm is 5.08 m/s, 4.73 m/s, 6.14 m/s and 7.38 m/s, at equivalence ratio 0.8 and 1 under engine speed 750 RPM and 1500 RPM, respectively. The fresh unburned gas velocity is 61.1%, 56.6%, 49.7% and 52.2% of the flame speed, respectively. Comparing with the non-zoomed in case, there is agreement on the ratio of S_t/u_r.

For the zoomed-in case at 750 RPM, the variation u_r at flame surface is similar to the non-zoomed in case. However, there is a wide spread of the u_r distribution for the zoomed-in 1500 RPM. This may caused by the large distance between the two flame front contours of a couple of PIV images.

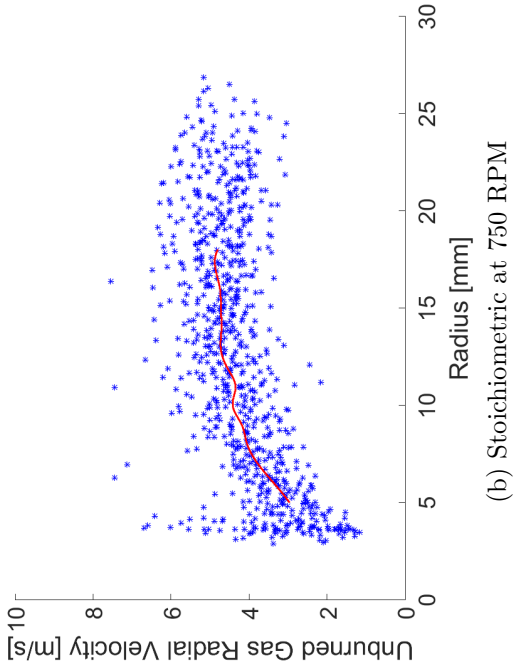

(a) Equivalence ratio 0.8 at 750 RPM

(b) Stoichiometric at 750 RPM

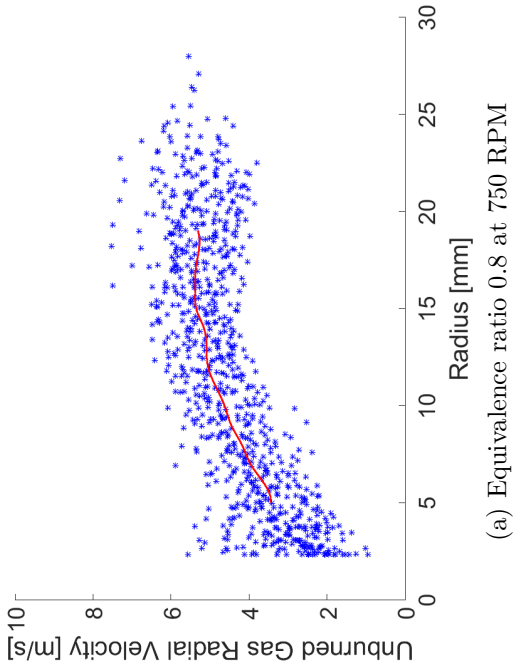

(c) Equivalence ratio 0.8 at 1500 RPM

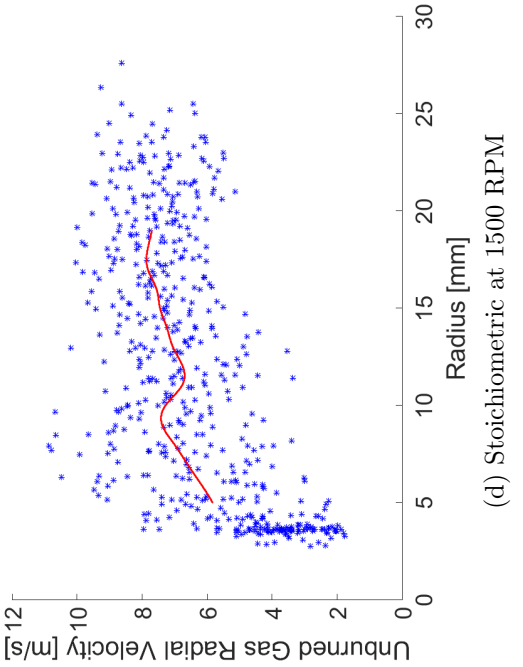

(d) Stoichiometric at 1500 RPM

Figure 7.45: Extrapolated unburned gas radial velocity at flame surface versus flame radius for iso-octane, the averaged trace is shown in red.

7.4.2 Burning Velocity in Engine Condition

The turbulent Burning velocity of ULG is shown in Figure 7.46. The burning velocity at flame radius 12-18 mm under engine speed 750 RPM is about 3.5 m/s at $\phi = 0.8$ and 4.0 m/s at $\phi = 1.0$; at engine speed of 1500 RPM is about 6.0 m/s at $\phi = 0.8$ and 7.1 m/s at $\phi = 1.0$. For the engine speed of 750 RPM cases, the turbulent burning velocity reduces 12.5% comparing $\phi = 0.8$ with stoichiometric mixtures. In high turbulence conditions, 1500 RPM, the turbulent burning velocity reduces 15.5% comparing $\phi = 0.8$ with stoichiometric mixtures. For the effect of engine speed on the burning velocity, there are 71.4% and 77.5% of increase for increasing the engine from 750 RPM to 1500 RPM at $\phi = 0.8$ and $\phi = 1.0$, respectively.

The turbulent burning velocity of iso-octane is shown in Figure 7.47. The burning velocity at flame radius 12-18 mm under engine speed 750 RPM is about 3.5 m/s at $\phi = 0.8$ and 3.8 m/s at $\phi = 1.0$; at engine speed of 1500 RPM is about 5.7 m/s at $\phi = 0.8$ and 6.7 m/s at $\phi = 1.0$. For the engine speed of 750 RPM cases, the turbulent burning velocity reduces 7.9% comparing $\phi = 0.8$ with stoichiometric mixtures. In high turbulence conditions, 1500 RPM, the turbulent burning velocity reduces 14.9% comparing $\phi = 0.8$ with stoichiometric mixtures. For the effect of engine speed on the burning velocity, there are 62.9% and 76.3% of increase for increasing the engine from 750 RPM to 1500 RPM at $\phi = 0.8$ and $\phi = 1.0$, respectively.

Figure 7.48 shows the comparison of standard deviation σ between S_t and u_t at stoichiometric condition. In general, the burning velocity σ follows the trend of the flame speed σ. Therefore, the large spread of the u_t shows on Figure 7.46 and 7.47 comes from the uncertainty of the flame speed. Moreover, the burning velocity σ lower than the flame speed σ indicates the flow velocity measured by PIV potentially have high levels of certainty.There is no outlier showing on the unburned gas velocity, although several outliers were observed on the flame speed samples. There is little effect of flame speed outlier on radial gas velocity. Therefore, the outliers on the burning velocity are mostly due to the measurement of flame speed.

For both fuels, they have comparable burning velocity at the engine speed of 750 RPM. Furthermore, there is limited effect of equivalence ratio on burning velocity for both fuels. The direct measured flame speed from the laser sheet image is also confirmed there is similar burning velocity at this engine speed. For the engine speed of 1500 RPM, The burning velocity between different equivalence ratios is clearly observed comparing it is at 750 RPM. The burning velocity difference is also found between ULG and iso-octane. Considering the Zimont turbulent

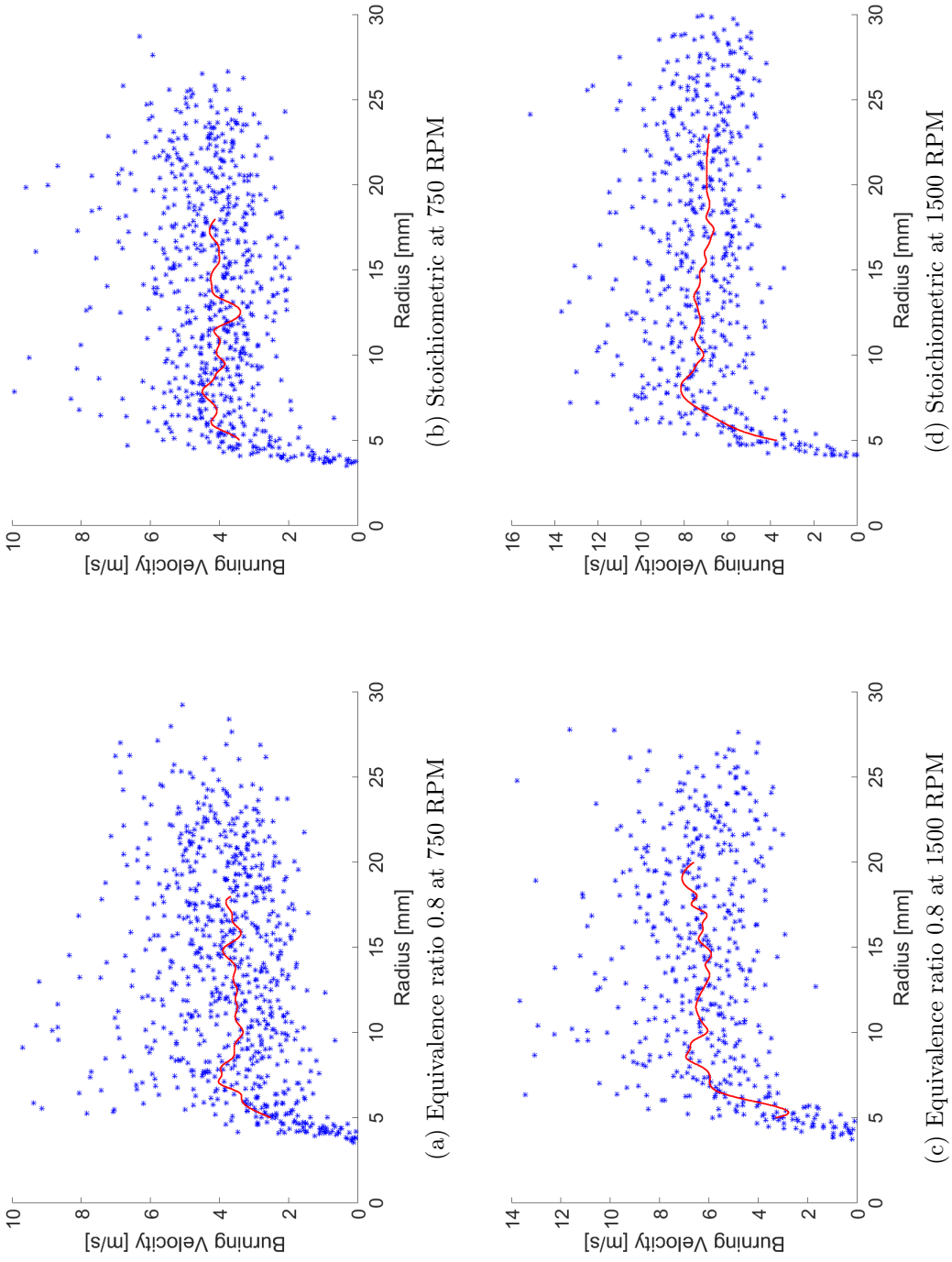

(a) Equivalence ratio 0.8 at 750 RPM

(b) Stoichiometric at 750 RPM

(c) Equivalence ratio 0.8 at 1500 RPM

(d) Stoichiometric at 1500 RPM

Figure 7.46: The burning velocity of ULG versus flame radius derived from sector flame speed S_{ti} and flame surface unburned gas radial velocity u_{ri} in the sector, the averaged trace is shown in red.

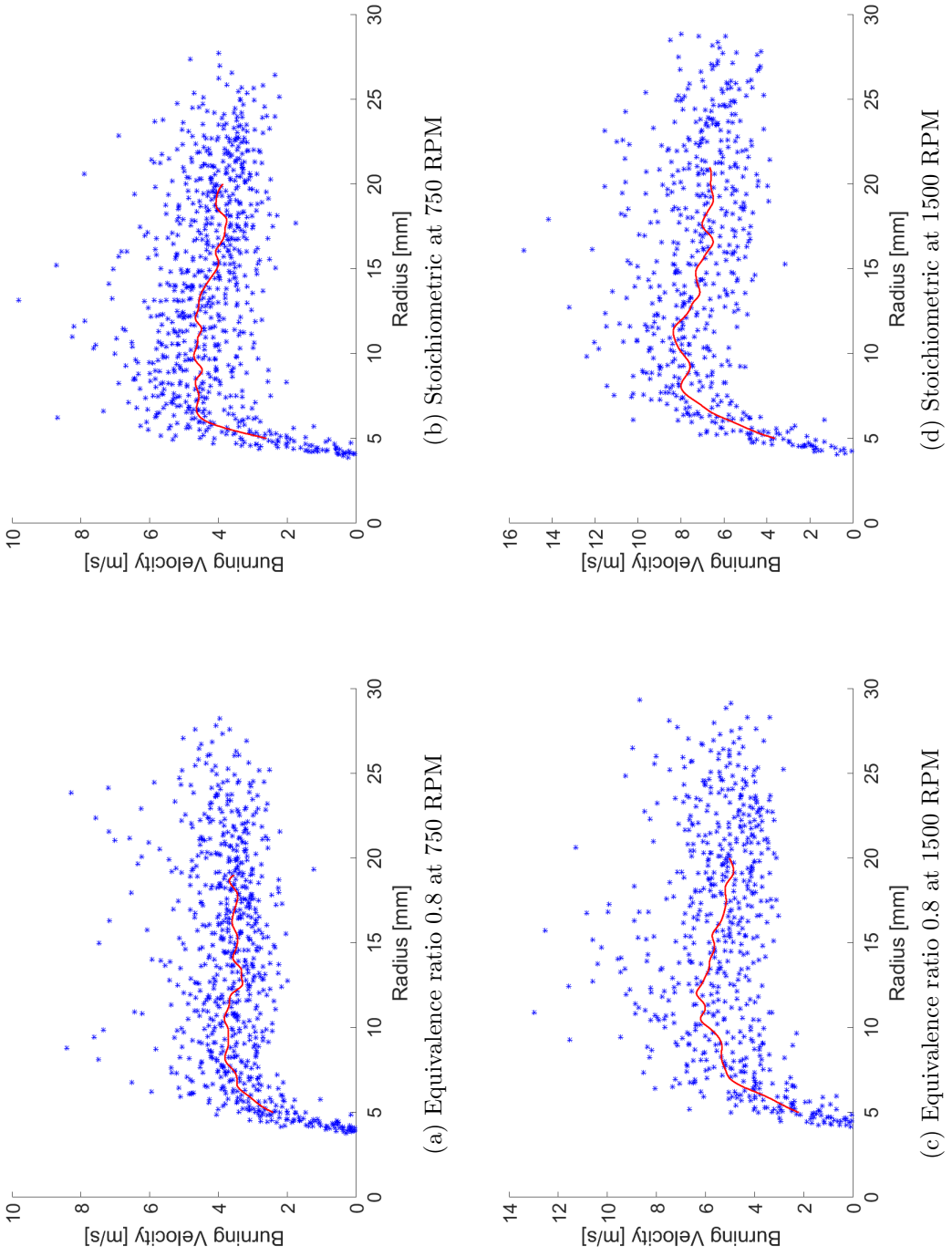

(a) Equivalence ratio 0.8 at 750 RPM

(b) Stoichiometric at 750 RPM

(c) Equivalence ratio 0.8 at 1500 RPM

(d) Stoichiometric at 1500 RPM

Figure 7.47: The burning velocity of iso-octane versus flame radius derived from sector flame speed S_{ti} and flame surface unburned gas radial velocity u_{ri} in the sector, the averaged trace is shown in red.

burning velocity correlation (Zimont et al. 1998), the relation between turbulent burning velocity and laminar burning velocity is $u_t \sim u_l^{0.5}$, theoretically, there are about 15% reduction on turbulent burning velocity comparing $\phi = 0.8$ with $\phi = 1.0$. However, both fuels show the burning velocity reduction is lower than the theoretical value at the engine speed 750 RPM. The results suggested that the lean mixtures turbulent burning velocity at 750 RPM is enhanced.

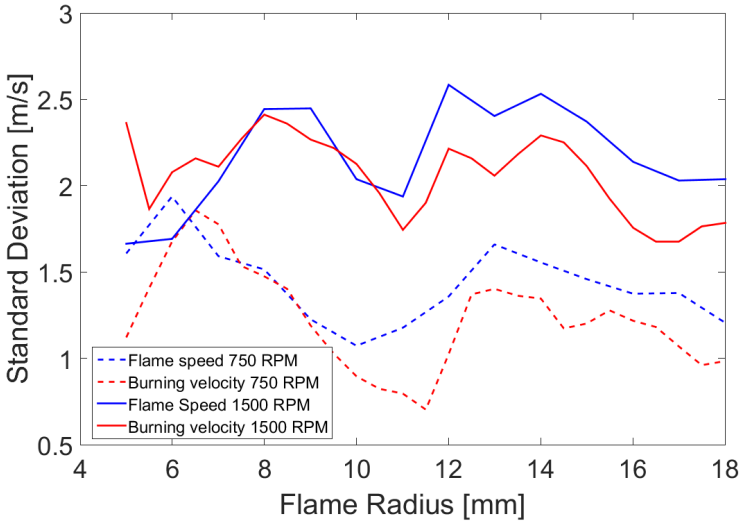

(a) ULG

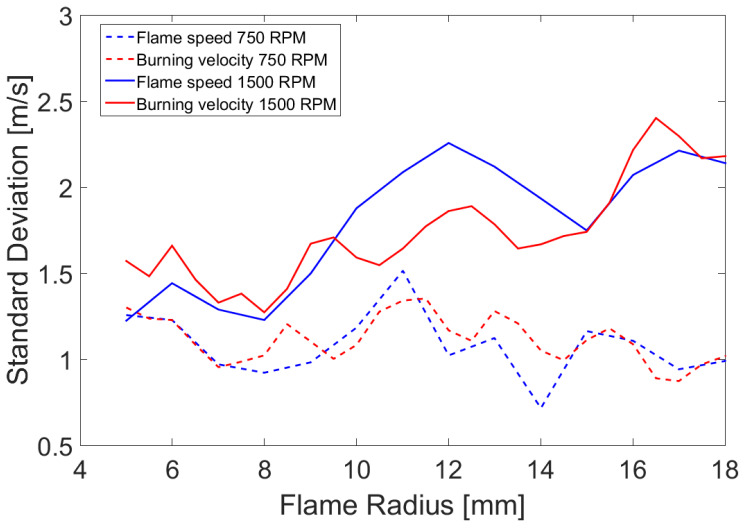

(b) Iso-octane

Figure 7.48: Comparison of standard deviation between S_t and u_t at stoichiometric condition.

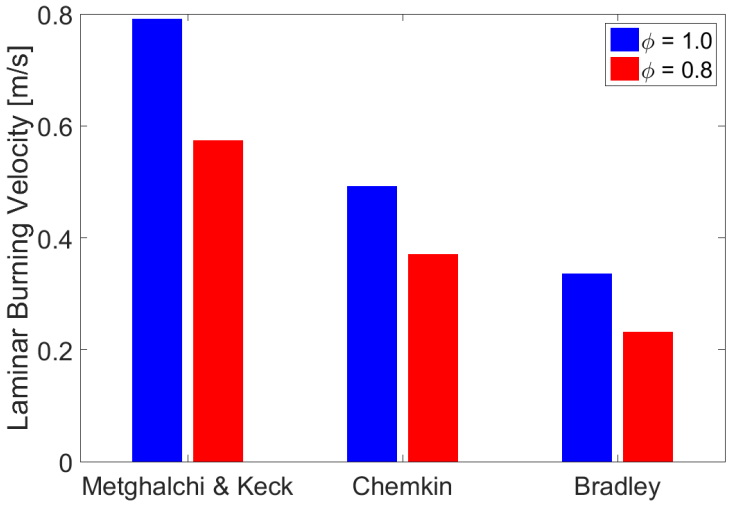

Figure 7.49: Laminar burning velocity at the experiment condition derived from Metghalchi & Keck (1982), Chemkin simulation, Bradley et al. (1998), respectively.

7.4.3 Comparison of Burning Velocity Results

Figure 7.49 shows the u_l in the experiment conditions. Considering the experiment conditions in Borghi diagram, the ratio of u_l/u_t is theoretically as same as the sphericity. The u_t derived from the sphericity and the Metghalchi & Keck laminar burning velocity is present in Figure 7.50. The u_t is close to it is derived from the PIV method. According to the theoretical model for deriving the laminar burning velocity (Metghalchi & Keck 1982), the potential cellular flame appears in high pressure was ignored. As a result, the Metghalchi & Keck u_l is more like the non-turbulent cellular flame burning velocity. Considering the experiment condition in this study, the laminar flame is unable to exist in such condition, it seems the non-turbulent cellular flame burning velocity is potentially applicable for the experiment condition in this study. However, this only be applicable when the flame cell size due to flame cellularity is smaller than the smallest eddy size.

In order to obtained the laminar burning velocity, a proprietary software tool Chemkin was used to solve the complex chemical kinetics in calculating laminar burning velocity. For the laminar burning velocity from Chemkin simulation and the laminar burning velocity correlation derived from experiment (Bradley et al. 1998), the turbulent burning velocity derived from the sphericity is shown in Figure 7.51 and Figure 7.52. Both two derived u_t is clearly lower than the u_t derived from PIV method.

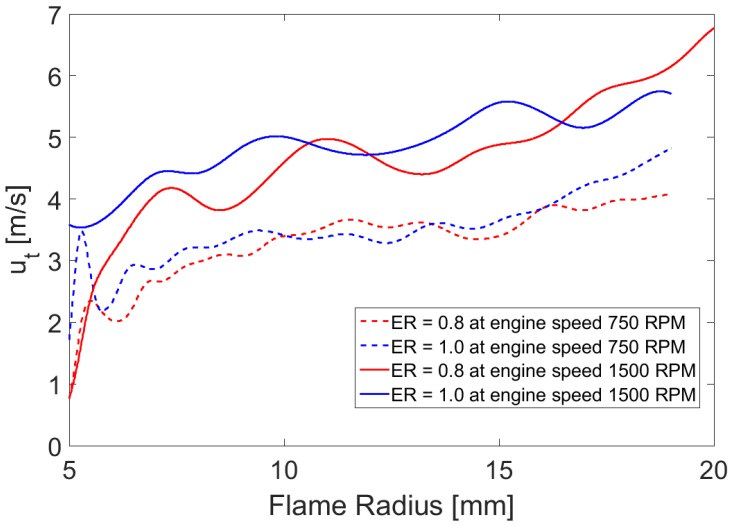

Figure 7.50: Turbulent burning velocity derived from the sphericity and the Metghalchi & Keck laminar burning velocity.

For all the sphericity derived u_t, the effect of equivalence ratio on the u_t is not obvious. Considering the camera resolution in zoomed-in case still not capable to capture the small wrinkles generated by the turbulence. The sphericity of the flame may potentially smaller than those obtained in this study. As a result, There is an underestimate of u_t derived from the sphericity. For the PSD of the flame wrinkling in the zoomed-in case, see Figure 7.29, the spectrum is mainly following the turbulent energy spectrum. There is no observation of 'wrinkling energy' brought by the flame instability. As a result, it is highly possible that the characteristic instability scale is too small to capture, thus, the flame wrinkles due flame instability may not contribute in calculating the flame sphericity.

For the effect of engine speed on the sphericity derived u_t, there are less than 50% of u_t increase with engine speed increases from 750 RPM to 1500 RPM. However, the u_t derived from PIV method is more than 60% increase for engine speed increases from 750 RPM to 1500 RPM. Considering the Kolmogorov length scale at engine speed of 750 and 1500 RPM, the smallest turbulent eddy at 1500 RPM is approximately 40% smaller than it is at 750 RPM. Therefore, the flame sphericity may have further underestimation at engine speed on 1500 RPM. Considering the stoichiometric flame shows instability at relatively lower pressure compared with the lean flame, the characteristic instability scale may for the stoichiometric flame may smaller than the lean flame. Similarly with the small turbulent scale size in flame wrinkles, it is possible that there is an underestimation the sphericity due to the smaller instability scale for the stoichiometric flame result in the comparable

u_t between stoichiometric condition and $\phi = 0.8$.

For the u_t derived from density ratio method, the density ratio of unburned over burned gas ρ_u/ρ_b as calculated by Gaseq is almost constant during flame expansion: 3.73 in $/phi = 0.8$ condition and 4.19 in stoichiometric condition. The iso-octane turbulent burning velocity is calculated by the non-zoomed in case flame speed divided by density ratio at the engine speed 750 RPM: 2.3 m/s, 1.9 m/s, at the engine speed 1500 RPM: 3.0 m/ and 2.97 m/s, respectively. For the zoomed-in case, the u_t at the engine speed 750 RPM: 2.2 m/s, 2.0 m/s, at the engine speed 1500 RPM: 3.3 m/ and 3.4 m/s, respectively. Comparing with the u_t obtained by PIV method, there is huge disagreement on the u_t derived by density ratio method. Furthermore, according to the turbulent burning velocity obtained by direct method, the burning velocity for $\phi = 0.8$ case is higher than stoichiometric case. Considering the turbulent eddy not able to penetrate the reaction zone and the flame is at the corrugated flamelets for all four condition. The sphericity is lower at $\phi = 0.8$ which enhances the u_t at $\phi = 0.8$. However, the unrealistic burning velocity is not only against the PIV method results but also the common sense. Figure 7.53 shows the ratio of S_t/u_t for non-zoomed in case. Theoretically the density ratio ρ_u/ρ_b equals S_t/u_t. However, the ratio of S_t/u_t for all conditions is smaller than the density ratio 3.73 and 4.19. In two zone case, which whole space is divided into unburned and burned region, the S_t/u_t smaller than ρ_u/ρ_b means there is an overestimation of ρ_u/ρ_b. Comparing the ratio S_t/u_t at different equivalence ratio at the same engine speed, the ratio of S_t/u_t at $\phi = 0.8$ is clearly higher than the stoichiometric condition. Therefore, the ratio of S_t/u_t $\phi = 0.8$ is closer to the theoretical density ratio than the stoichiometric condition. Furthermore, the higher engine speed will result in the ratio of S_t/u_t away from the density ratio.

Figure 7.54 shows the ratio of S_t/u_t versus the flame radius for ULG. From the S_t/u_t ratio, the u_t derived from the density ratio method will far less than the u_t derived from the PIV method. The effect of engine speed on the ratio of S_t/u_t is also found in ULG turbulent flames. Similar to the iso-octane, both higher equivalence ratio and engine speed will result in the ratio of S_t/u_t away from the density ratio.

The most obvious problems in density ratio method are the uniform density distribution in the burned and unburned region. The preheat zone will potentially attribute underestimation of the density ratio. Heat transfer to the preheat zone from the reaction zone is potentially under the influence of the turbulence intensity and the equivalence ratio. The experiment from Buschmann et al. (1996) and

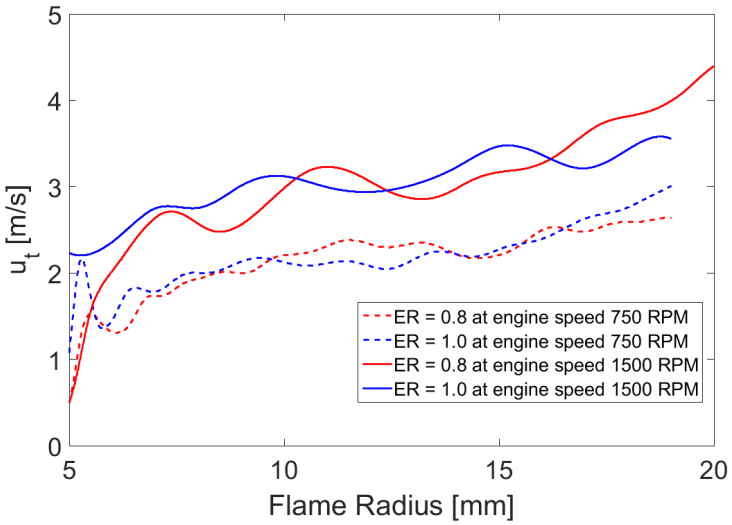

Figure 7.51: Turbulent burning velocity derived from the sphericity and the laminar burning velocity from Chemkin simulation.

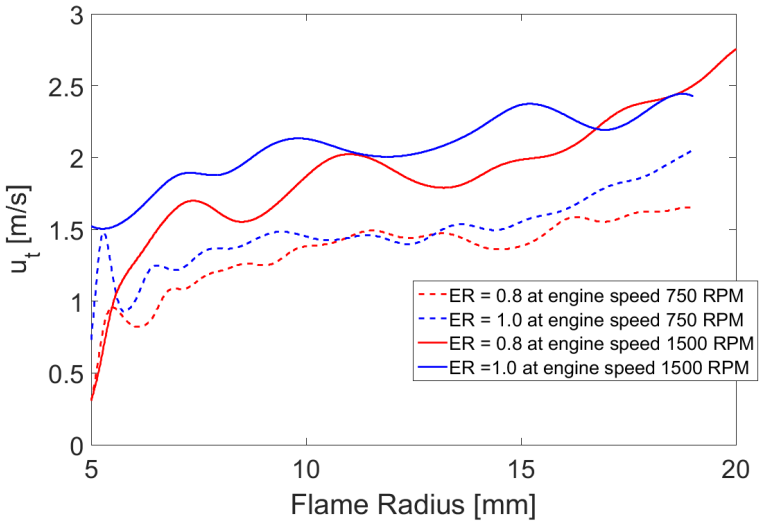

Figure 7.52: Turbulent burning velocity derived from the sphericity and the Bradley laminar burning velocity.

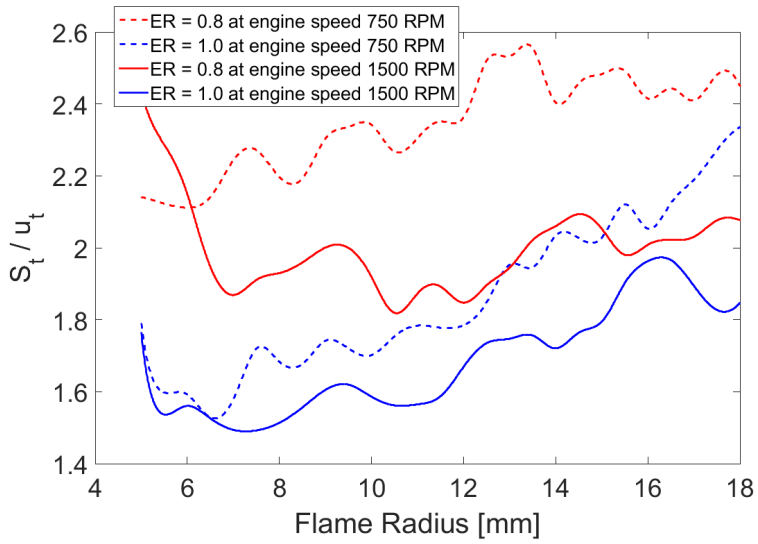

Figure 7.53: The ratio of the turbulent flame speed over the turbulent burning velocity derived from PIV method versus the flame radius for iso-octane

Kortschik et al. (2004) for investigation of flame structure and temperature distributions is suggested that there are a few millimetre in between the fresh charge temperature and the adiabatic flame temperature. And the distance increases with the increasing of the turbulence intensity. Considering the flame radius in this study is relatively small, therefore, the non-uniform temperature distribution may potentially have significant underestimation of the density ratio. For increasing the engine speed, there is further underestimation of the density ratio.

Due to the seeds for PIV measurement used in this study can be easily vaporised in the flame preheat zone. Considering the burned and unburned region was defined by the image brightness in this study. The preheat zone is potentially defined as the part of the burned region. Therefore, for the u_r measurement, value may not exactly be measured as the velocity at the reaction zone surface. There is potentially an underestimation of the u_r at the flame surface, especially when the flame size is relatively small. The u_t derived from the PIV method may be higher than the actual value. The u_t shows in Figure 7.46 and 7.47 at flame radius about 8 - 12 mm is higher than the u_t at other flame radius. This may due to insufficient flame size for observing the actual u_r. Furthermore, according to Figure 7.53 and 7.54, there is an increase of S_t/u_t ratio with the increase of flame radius. Therefore, the flame size for this study may significant to the PIV measurement results.

For comparison, the burning velocity calculated by Zimont turbulent flame

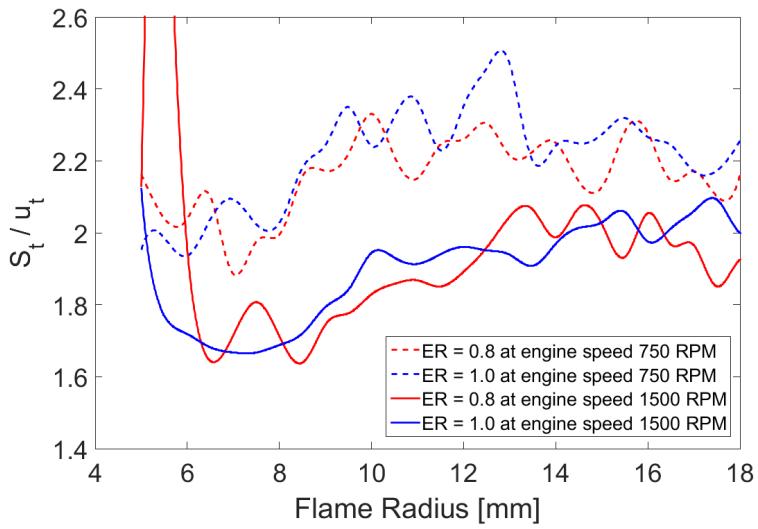

Figure 7.54: The ratio of the turbulent flame speed over the turbulent burning velocity derived from PIV method versus the flame radius for ULG

speed closure model (Zimont et al. 1998):

$$u_t = Au'^{0.75} u_l^{0.5} \alpha^{-0.25} L^{0.25} \tag{7.2}$$

where A is 0.52, unburned thermal diffusivity α is given by Gaseq 2.14x10^{-6} m^2/s for stoichiometric mixtures, u_l uses the correlation from Metghalchi & Keck (1982). The Zimont model shows at 750 RPM, about 1.9 m/s at $\phi = 0.8$ and 2.3 m/s at stoichiometric condition; For engine speed of 1500 RPM is about 2.8 m/s at $\phi = 0.8$ and 3.4 m/s at stoichiometric condition. Although the derived u_t is comparable to the u_t derived from density ratio method, the zimont approximation shows a reasonable equivalence ratio effect on turbulent burning velocity. By applying the u'_r at the flame surface from Figure 7.35 with an integral length scale of 3.5 mm. The correspondent turbulent burning velocity is 3.5 m/s, 4.2 m/s, 4.2 m/s, and 5.5 m/s, respectively. There is highly comparable u_t between Zimont approximation uses flame surface u'_r and the PIV method at the engine speed of 750 RPM. However, the u_t at engine speed 1500 RPM shows lower than the PIV method. The possibility of the PIV method overestimates the u_t cannot be ruled out. The flame speed S_t is not exactly proportional to the $u'^{0.75}_r$ and their is no evidence showing that the flame flame surface turbulence have the same effectiveness as cold flow turbulence on the flame propagation.

For other turbulent flame speed approximation which take the flame instability

into consideration, such as a empirical expression from Bray (1990):

$$u_t/u_l = 0.875Ka^{-0.392}u'/u_l \tag{7.3}$$

where Ka is Karlovitz number followed by expression (Bradley et al. 2011),

$$Ka = 0.25(u'/u_l)^2(Re)^{-0.5} \tag{7.4}$$

Table 7.1 shows the u_t/u_l derived from PIV method and the empirical expression. From the table, the estimated u_t/u_l from the empirical expression shows within a reasonable range. However, there is minor mismatch between the empirical expression correlation and the PIV method. Based on different engine speed, there is lack of the consistency of effect of u' on the u_t/u_l ratio. This may come from the accuracy of u_t derived from PIV method, as previous mentioned, there is potentially underestimate the u_r at the flame surface, the engine speed may have effect on the accuracy of the u_t derived from PIV method. Moreover, the flame propagation in engine may be influenced by some other factor. Considering the flame in the laser sheet is less than 4 mm away from the engine head and it is possibly under the influence of the engine head. On the other hand, the prediction seems to underestimate the effect of u' on the u_t, from the results derived from the correlation, there is only about 22% of u_r increases with an increasing of 60% in u' under stoichiometric condition. For the correlation, the $u_t \sim u_t^{0.412}$ provide an underestimation of the effect of turbulence on the u_t considering the u_t and S_t under different engine speed.

According to Abdel-Gayed et al. (1987), the ratio of u_t/u_l for Lewis Number lower than 1.3 shows highly comparable to the PIV method. at the condition of $Re = 1382$, the ratio of u_t/u_l at $\phi = 0.8$ is approximately 10, at $\phi = 1.0$ is approximately 9. at the condition of $Re = 2211$, the ratio of u_t/u_l at $\phi = 0.8$ is approximately between 12 to 13, at $\phi = 1.0$ is approximately 12. Similar with the correlation from Bray (1990), there is a mismatch of the effect of turbulence on the u_t considering the derived burning velocity results. However, the correlation show that for a small Ka (less than 0.1), the ratio of u_t/u_l is very sensitive to the u'/u_l especially when the ratio of u'/u_l is small. As a result, Any potentially error in estimating the ratio u'/u_l could result in huge disagreement in u_t/u_l ratio.

In conclusion, it has been shown that the S_t derived from the laser sheet image and it is highly comparable to the S_t derived from LUSIEDA. From the PIV measurement, it is confirmed that there is an increase of flame front turbulent intensity during the flame propagation. However, this enhancement of the turbulent

Table 7.1: Results of Reynolds number Re, Karlovitz number Ka, u_t/u_l from empirical expression and PIV method, the u_l is from Chemkin simulation.

Condition	Re	Ka	$0.875Ka^{-0.392}u'/u_l$	u_t/u_l (PIV method)
$\phi = 0.8$ 750RPM	1382	0.0276	7.2	9.5
$\phi = 1.0$ 750RPM	1382	0.0156	6.8	7.7
$\phi = 0.8$ 1500RPM	2211	0.0559	8.8	15.4
$\phi = 1.0$ 1500RPM	2211	0.0316	8.3	13.6

intensity is only confirmed when flame speed is higher enough. Turbulent burning velocity of ULG and iso-octane derived from PIV method was obtained, however, there is an argument between turbulent combustion models and the experiment results.

Chapter 8

Conclusions and Recommendations

8.1 Conclusions of PIV Measurement on Motoring Cycle

This section summarizes the main finds from the PIV measured cold flow parameter in engine. motoring cycles with fuel-air mixture in stoichiometric condition with engine speeds of 750 RPM and 1500 RPM were studied and the firm conclusions have been drawn as below..

- The turbulent RMS velocity measured from cold flow based on spacial averaging is about 0.75 m/s at the engine speed of 750 RPM and 1.20 m/s at the engine speed of 1500 RPM for the period that fully developed flame occurs. The turbulent RMS velocity measured in annulus shows it is nearly a uniform distribution along the radial direction.

- The turbulent RMS velocity in x-axis direction and y-axis direction as well as in radial and tangential direction are identical. The mean gas velocity at TDC is low, which indicates there is not big motion of turbulent flow in the engine. For the turbulent integral length scale measured in engine at different engine speeds, the results show highly comparable between 750 RPM and 1500 RPM. An integral length scale of 3.5 mm was observed for the period that fully developed flame occurs.

8.2 Conclusions of Characterisation of Combustion in LUPOE2-D

This section summarizes the main finds from the LUSIEDA derived combustion characterisation based on combustion pressure data. ULG and its TRF surrogate were studies in this study. Two renewable bio-energy sources were applied as fuel additives to investigate their anti-knock performance in a strongly charged engine. The experiment was preformed at an engine speed of 750 RPM with a constant air flow rate at the intake. An intake temperature of 323 K was applied in this experiment to mimic the condition of an strongly changed engine. The present study provides an insight into the anti-knock performance in engine which takes the unburned gas temperature history into consideration, the introduction of TRF as base fuel was seen to provide representation of gasoline in simulations. Moreover, the cycle-to-cycle to variation study in strongly charged engine in present work potentially suggested that an improvement of engine performance by optimising engine combustion chamber design.

- turbulent flame speed in strongly charged engine study was preformed, For ULG as base fuel, the n-butanol and 2,5-DMF as additives show no major impact on the turbulent flame speed in the engine. And the pressure traces for those blends are identical to the ULG.

- The n-butanol perform as additive for TRF has minor impact on the flame speed at a relatively retarded spark timing. For an advanced spark timing, n-butanol improves the flame speed and the pressure growth rate. For the 2,5-DMF, it slows the flame speed in the engine. In retarded spark timing, the blends shows a slow growth rate of pressure trace until an advanced spark timing, at high temperature and pressure region the blends are comparable to TRF.

- The duration of initial flame acceleration stage shows great impact on the peak pressure and cycle-to-cycle variations. TRF does not show a good representative of ULG small flame kernel behaviour. There is little impact on the initial flame propagation for n-butanol perform as additive. For 2,5-DMF as additive, a longer duration of flame initial acceleration stage was observed for both ULG and TRF.

- The mass fraction burned shows significant impact on the knock intensity, there may be exemptions that the knock onset at low mass fraction burned

may not always result in a strong knock. At high levels of mass fraction burned, the knock was unlikely to onset and it always result in a mild knock.

- TRF shows very good representative for ULG relative ignition delay in a relatively high temperature region. However, this does not necessarily mean the TRF perform the same anti-knock property as ULG in a strongly charged engine. The mismatch of ignition delay at low temperature may influence the anti-knock performance in the engine. The difference between flame speed and initial stage flame kernel propagation can affect the temperature history. The anti-knock performance in engine is under the influence of the temperature history.

- For ULG as base fuel, there is limit improvement on the anti-knock performance in the engine for n-butonal as additive. For 2,5-DMF as additives, there is great improvement on the anti-knock performance in the engine.

- For TRF as base fuel, both n-butanol and 2,5-DMF as additive improves the anti-knock performance of blends in the engine. The anti-knock performance in engine for n-butanol is highly comparable to the 2,5-DMF in this study.

- For the additives anti-knock performance in a strongly charged engine, the additives have different impact on the ULG and TRF. Because of the complexity of ULG, TRF and the additive may not fully represent the anti-knock performance of the blends in the engine.

8.3 Conclusions of Turbulent Flame Propagation in Engine

This section summarizes the main finds from the laser tomographic flame image study and PIV study. This study focused on the effect of engine speed and equivalence ratio on the flame propagation in the fully developed flame stage. The experiment has achieved nearly constant temperature and pressure during the flame radius from 12 - 19 mm. This study is to provide insight into the effect of thermal expansion on the flame front turbulent. Current research may provide some views on self-accelerating flame. Moreover, it suggested that correlations my not applicable for some extreme conditions (i.e. high temperature with low cold flow turbulence). Those extreme conditions usually result in flame front turbulence higher than cold flow.

- The turbulent flame propagation derived from the laser tomographic image is highly comparable to the LUSIEDA result. The flame speed at flame radius 12 - 19 mm is nearly constant. For the ULG, the averaged flame speed is 7.95 m/s for equivalence ratio 0.8 mixture, 9.15 m/s for stoichiometric mixture at 750 RPM, 11.97 m/s for equivalence ratio 0.8 mixture and 14.18 m/s for stoichiometric mixture at 1500 RPM. For the iso-octane, the averaged flame speed is 8.58 m/s for equivalence ratio 0.8 mixture, 8.06 m/s for stoichiometric mixture at 750 RPM, 11.22 m/s for equivalence ratio 0.8 mixture and 12.46 m/s for stoichiometric mixture at 1500 RPM. The results also show the zoom-in laser tomographic image is similar with non-zoomed-in cases.

- The turbulent flame speed of ULG and iso-octane are enhanced at $\phi = 0.8$. At lower engine speed, the effect of equivalence ratio on the turbulent flame speed is not as strong as it is at higher engine speed.

- The flame sphericity in different condition was investigated. Because of the small wrinkling scale in the flame, not only non-zoomed in case but also the zoomed in case are failed to resolve the flame wrinkling. The flame sphericity is possibly lower than 0.25 in this study. Higher engine speed or lower equivalence ratio may lower the sphericity.

- The flame wrinkling amplitude RMS and integral length scale of the wrinkling were investigated. Those parameters increase with increasing of the flame radius. The equivalence ratio and engine speed also influence those parameters.

- Power spectral density was derived from each condition. It seems the flame size has no influence on the energy contained in the wrinkles with same scale during the fully developed flame stage. Engine speed or equivalence ratio may potentially influence the power spectral density.

- A slope of-2.7 of the power spectral density was obtained for large wrinkles. For small winkles, the slope approximately obtained as -1.67. It shows highly agreement on the turbulence energy spectrum. However, the limited camera pixel size in this study suggested that there is no clear observation of the flame instability involved in providing the 'wrinkling energy'.

- The turbulent flow RMS velocity ahead of flame is larger than it is measured at cold flow when the flame speed is high. The magnitude of turbulent RMS velocity in front of the flame decreases with the distance away from the flame, the magnitude of the turbulent RMS velocity is same as cold flow until the measured region is 15 - 20 mm away from the flame.

- The turbulent flame speed keeps constant during flame radius 12 - 19 mm, meanwhile, turbulent flow RMS velocity at flame flame surface is nearly a constant. Although the flame speed has strong relations to the turbulent RMS velocity at the flame surface, there is no firm agreement on the relationship between cold flow RMS velocity and the flame speed. However, the effect of the turbulent RMS velocity at flame surface on flame speed is unclear, the correlations applied in this study could not satisfy the relationship between the turbulent RMS velocity at flame surface and the flame speed.

- The turbulent burning velocity of ULG and iso-octane were obtained by PIV method and the results are highly comparable. The effect of equivalence ratio on the turbulent burning velocity at low engine speed is weaker compared to the high engine speed. This might be due to lower sphericity in a lean condition so that enhances the turbulent burning velocity.

- A series of turbulent burning velocity correlations were compared with PIV method. The results show some of the correlations no longer match the experiment results under the experiment conditions in this study. Among those correlations, Abdel-Gayed et al. (1987) provides the closest match to the PIV method in this study.

8.4 Recommendations for Future Work

This section provides the recommendations for the future work. It is involved some areas related this study are unsorted.

- The engine temperature applied in this study was calculated by using reverse thermodynamic models, this may be affected by the input parameters such as mixture specific heat capacity, heat transfer model, intake pressure. A hot wire temperature measurement or laser-induced temperature gradients could achieve the temperature distribution in the engine. Furthermore, planar laser-induced fluorescence would help to define the reaction zone. Combining with the temperature distribution, an accurate flame burned region can be defined.

- Because pressure history has a great influence on a fuel anti-knock performance in engine. The effect of engine intake pressure, temperature, equivalence ratio as well as engine speed on the anti-knock performance in a strongly charged engine worth investigating. A knock boundary map and knock intensity may be helpful for investigating the anti-knock performance in a engine.

- For a further study on effect of initial acceleration stage on the cycle-to-cycle variation. A different spark intensity can be introduced for investigating the effect of initial flame kernel on the cycle-to-cycle variation.

- The fuelling system potentially needs further improvement. For a rich condition, the fuel potentially does not fully vaporise due to large fuel flow rate. The undesired self-ignition after the firing cycle suggested that the retard fuel valve reaction and its downstream fuel line need to be redesigned. A high supply pressure for the fuel line with an atomizing nozzle is suggested.

- In this study, a single cavity cooper vapour laser with repetition rate of 10 KHz was used in this study. As a result, a 0.1 ms time interval is used for deriving the flow velocity. Considering the velocity magnitude of flow is large, a short time interval between two images would improve the accuracy of the flow field. It is suggested that a dual cavity laser would help to obtain a better result for the future study.

- In this study, due to a limited resolution for the high speed camera at 10 KHz frame speed was failed to obtained the detailed flame contour in the

engine condition. It is suggested that a higher resolution image would help to obtain the characteristic length scale of flame wrinkling due to flame instability.

Bibliography

Abdel-Gayed, R., Bradley, D., Hamid, M. & Lawes, M. (1985), Lewis number effects on turbulent burning velocity, *in* 'Symposium (international) on combustion', Vol. 20, Elsevier, pp. 505–512.

Abdel-Gayed, R., Bradley, D. & Lawes, M. (1987), 'Turbulent burning velocities: a general correlation in terms of straining rates', *Proc. R. Soc. Lond. A* **414**(1847), 389–413.

Abdel-Gayed, R., Bradley, D. & Lung, F.-K. (1989), 'Combustion regimes and the straining of turbulent premixed flames', *Combustion and Flame* **76**(2), 213–218.

Abdi Aghdam, E. (2003), Improvement and validation of a thermodynamic SI engine simulation code, PhD thesis.

Adrian, R. J. (1991), 'Particle-imaging techniques for experimental fluid mechanics', *Annual review of fluid mechanics* **23**(1), 261–304.

Agbro, E., Tomlin, A. S., Lawes, M., Park, S. & Sarathy, S. M. (2017), 'The influence of n-butanol blending on the ignition delay times of gasoline and its surrogate at high pressures', *Fuel* **187**, 211–219.

Atashkari, K., Lawes, M., Sheppard, C. & Woolley, R. (1999), 'Towards a general correlation of turbulent premixed flame wrinkling', *Engineering turbulence modelling and experiments 4* pp. 805–814.

Attard, W. P., Toulson, E., Watson, H. & Hamori, F. (2010), Abnormal combustion including mega knock in a 60% downsized highly turbocharged pfi engine, Technical report, SAE Technical Paper.

Ayala, F. A. & Heywood, J. B. (2007), Lean si engines: the role of combustion variability in defining lean limits, Technical report, SAE Technical Paper.

Ballal, D. R. & Lefebvre, A. H. (1975), The influence of flow parameters on minimum ignition energy and quenching distance, *in* 'Symposium (International) on Combustion', Vol. 15, Elsevier, pp. 1473–1481.

Balusamy, S., Cessou, A. & Lecordier, B. (2011), 'Direct measurement of local instantaneous laminar burning velocity by a new piv algorithm', *Experiments in fluids* **50**(4), 1109–1121.

Bardin, M., El-Dein Hussin, A., Gushchin, P., Vinokurov, V. & Burluka, A. (2014), 'Technical aspects of ethyl tert-butyl ether (etbe) for large-scale use as gasoline improver', *Energy Technology* **2**(2), 194–204.

Bellenoue, M., Kageyama, T., Labuda, S. & Sotton, J. (2003), 'Direct measurement of laminar flame quenching distance in a closed vessel', *Experimental thermal and fluid science* **27**(3), 323–331.

Bhattacharya, S., Charonko, J. J. & Vlachos, P. P. (2018), 'Particle image velocimetry (piv) uncertainty quantification using moment of correlation (mc) plane', *arXiv preprint arXiv:1804.10854* .

Boxx, I., Slabaugh, C., Kutne, P., Lucht, R. & Meier, W. (2015), '3khz piv/oh-plif measurements in a gas turbine combustor at elevated pressure', *Proceedings of the Combustion Institute* **35**(3), 3793–3802.

Boyer, L. (1980), 'Laser tomographic method for flame front movement studies', *Combustion and Flame* **39**(3), 321–323.

Bradley, D., Hicks, R., Lawes, M., Sheppard, C. & Woolley, R. (1998), 'The measurement of laminar burning velocities and markstein numbers for iso-octane–air and iso-octane–n-heptane–air mixtures at elevated temperatures and pressures in an explosion bomb', *Combustion and flame* **115**(1-2), 126–144.

Bradley, D., Lau, A., Lawes, M. & Smith, F. (1992), 'Flame stretch rate as a determinant of turbulent burning velocity', *Phil. Trans. R. Soc. Lond. A* **338**(1650), 359–387.

Bradley, D., Lawes, M., Liu, K. & Mansour, M. S. (2013), 'Measurements and correlations of turbulent burning velocities over wide ranges of fuels and elevated pressures', *Proceedings of the Combustion Institute* **34**(1), 1519–1526.

Bradley, D., Lawes, M. & Mansour, M. (2011), 'Correlation of turbulent burning velocities of ethanol–air, measured in a fan-stirred bomb up to 1.2 mpa', *Combustion and Flame* **158**(1), 123–138.

Bray, K. N. C. (1990), 'Studies of the turbulent burning velocity', *Proc. R. Soc. Lond. A* **431**(1882), 315–335.

Buschmann, A., Dinkelacker, F., Schäfer, T., Schäfer, M. & Wolfrum, J. (1996), Measurement of the instantaneous detailed flame structure in turbulent premixed combustion, *in* 'Symposium (International) on Combustion', Vol. 26, Elsevier, pp. 437–445.

Caris, D. & Nelson, E. (1959), 'A new look at high compression engines', *Sae Transactions* pp. 112–124.

Clenci, A., Descombes, G., Podevin, P. & Hara, V. (2007), 'Some aspects concerning the combination of downsizing with turbocharging, variable compression ratio, and variable intake valve lift', *Proceedings of the Institution of Mechanical Engineers, Part D: Journal of Automobile Engineering* **221**(10), 1287–1294.

Cooney, C., Wallner, T., McConnell, S., Gillen, J. C., Abell, C., Miers, S. A. & Naber, J. D. (2009), Effects of blending gasoline with ethanol and butanol on engine efficiency and emissions using a direct-injection, spark-ignition engine, *in* 'ASME 2009 Internal Combustion Engine Division Spring Technical Conference', American Society of Mechanical Engineers, pp. 157–165.

Damköhler, G. (1947), 'The effect of turbulence on the flame velocity in gas mixtures'.

Desoky, A. (1981), An experiental and theoretical study of the combustion process in a divided chamber spark ignition engine, PhD thesis.

Dreizler, A. & Böhm, B. (2015), 'Advanced laser diagnostics for an improved understanding of premixed flame-wall interactions', *Proceedings of the Combustion Institute* **35**(1), 37–64.

EBRAHIM, A. A. (2003), Improvement and validation of a thermodynamic S.I. engine simulation code. Doctor of Philosophy, PhD thesis.

Fristrom, R. & Westenberg, A. (1961), Experimental chemical kinetics from methane-oxygen laminar flame structure, *in* 'Symposium (International) on Combustion', Vol. 8, Elsevier, pp. 438–448.

Fristrom, R. & Westenberg, A. (n.d.), 'Flame structure,(1965)', *E, McGraw-HilI* .

Gaydon, A. (1974), *The spectroscopy of flames (Second Edition)*, Chapman and Hall.

Gillespie, L., Lawes, M., Sheppard, C. & Woolley, R. (2000), 'Aspects of laminar and turbulent burning velocity relevant to si engines', *SAE transactions* pp. 13–33.

Glassman, I. & Yetter, R. A. (2008), *Combustion (Fourth Edition)*, Academic Press.

Hadded, O. & Denbratt, I. (1991), 'Turbulence characteristics of tumbling air motion in four-valve si engines and their correlation with combustion parameters', *SAE transactions* pp. 741–759.

Hanabusa, H., Kondo, T., Hashimoto, K., Sono, H. & Furutani, M. (2013), Study on homogeneous lean charge spark ignition combustion, Technical report, SAE Technical Paper.

Hattrell, T. (2007), A Computational and Experimental Study of Spark Ignition Combustion, PhD thesis.

Heywood, J. B. et al. (1988), 'Internal combustion engine fundamentals'.

Hirano, T. (2000), 'Generation of flame front turbulence', *Combustion science and technology* **158**(1), 35–51.

Hynes, J. (1986), A Computational and Experimental Study of Spark Ignition Combustion, PhD thesis.

Inoue, T., Nakanishi, K., Noguchi, H. & Iguchi, S. (1980), 'The role of swirl and squish in combustion of the si engine', *VDI-Berichte* **370**, 181.

Jomaas, G., Law, C. & Bechtold, J. (2007), 'On transition to cellularity in expanding spherical flames', *Journal of fluid mechanics* **583**, 1–26.

Kalghatgi, G. T. (2005), Auto-ignition quality of practical fuels and implications for fuel requirements of future si and hcci engines, Technical report, SAE Technical Paper.

Keane, R. D. & Adrian, R. J. (1990), 'Optimization of particle image velocimeters. i. double pulsed systems', *Measurement science and technology* **1**(11), 1202.

Kobayashi, H., Kawabata, Y. & Maruta, K. (1998), Experimental study on general correlation of turbulent burning velocity at high pressure, *in* 'Symposium (International) on Combustion', Vol. 27, Elsevier, pp. 941–948.

Kobayashi, H., Seyama, K., Hagiwara, H. & Ogami, Y. (2005), 'Burning velocity correlation of methane/air turbulent premixed flames at high pressure and high temperature', *Proceedings of the Combustion Institute* **30**(1), 827–834.

Kortschik, C., Plessing, T. & Peters, N. (2004), 'Laser optical investigation of turbulent transport of temperature ahead of the preheat zone in a premixed flame', *Combustion and Flame* **136**(1-2), 43–50.

Kyriakides, S. & Glover, A. (1989), 'A study of the correlation between in-cylinder air motion and combustion in gasoline engines', *Proceedings of the Institution of Mechanical Engineers, Part D: Journal of Automobile Engineering* **203**(3), 185–192.

Lawes, M., Ormsby, M. P., Sheppard, C. G. & Woolley, R. (2012), 'The turbulent burning velocity of iso-octane/air mixtures', *Combustion and Flame* **159**(5), 1949–1959.

Ling, Z. (2014), Flame propagation and autoignition in a high pressure optical engine, PhD thesis.

Ling, Z., Burluka, A. & Azimov, U. (2014), Knock properties of oxygenated blends in strongly charged and variable compression ratio engines, Technical report, SAE Technical Paper.

Lipatnikov, A. (2012), *Fundamentals of premixed turbulent combustion*, CRC Press.

Liu, K., Burluka, A. & Sheppard, C. (2013), 'Turbulent flame and mass burning rate in a spark ignition engine', *Fuel* **107**, 202–208.

Lourenco, L. & Krothapalli, A. (1995), 'On the accuracy of velocity and vorticity measurements with piv', *Experiments in fluids* **18**(6), 421–428.

Lumley, J. L. (1999), *Engines: an introduction*, Cambridge University Press.

Lumsden, G., Eddleston, D. & Sykes, R. (1997), Comparing lean burn and egr, Technical report, SAE Technical Paper.

Mallard, E. & Le Chatelier, H. (1883), Thermal model for flame propagation, *in* 'Annales des mines', Vol. 4, pp. 379–568.

Metghalchi, M. & Keck, J. C. (1982), 'Burning velocities of mixtures of air with methanol, isooctane, and indolene at high pressure and temperature', *Combustion and Flame* **48**, 191 – 210.

Morley, C. (2005), *Gaseq: a chemical equilibrium program for windows*, http://www.gaseq.co.uk.

Nau, P., Krüger, J., Lackner, A., Letzgus, M. & Brockhinke, A. (2012), 'On the quantification of oh*, ch*, and c 2* chemiluminescence in flames', *Applied Physics B* **107**(3), 551–559.

Nobach, H. & Honkanen, M. (2005), 'Two-dimensional gaussian regression for subpixel displacement estimation in particle image velocimetry or particle position estimation in particle tracking velocimetry', *Experiments in fluids* **38**(4), 511–515.

Otsu, N. (1979), 'A threshold selection method from gray-level histograms', *IEEE transactions on systems, man, and cybernetics* **9**(1), 62–66.

Pan, J. & Sheppard, C. (1994), 'A theoretical and experimental study of the modes of end gas autoignition leading to knock in si engines', *SAE transactions* pp. 1925–1947.

Pera, C. & Knop, V. (2012), 'Methodology to define gasoline surrogates dedicated to auto-ignition in engines', *Fuel* **96**, 59–69.

Peters, N. (1999), 'The turbulent burning velocity for large-scale and small-scale turbulence', *Journal of Fluid mechanics* **384**, 107–132.

Quader, A. A. (1974), Lean combustion and the misfire limit in spark ignition engines, Technical report, SAE Technical Paper.

Raffel, M., Willert, C. & Kompenhans, J. (n.d.), 'Particle image velocimetry: a practical guide. 1998', *l46* p. 134.

Rallis, C. J. & Garforth, A. M. (1980), 'The determination of laminar burning velocity', *Progress in Energy and Combustion Science* **6**(4), 303–329.

Rösgen, T. (2003), 'Optimal subpixel interpolation in particle image velocimetry', *Experiments in Fluids* **35**(3), 252–256.

Rothamer, D. A. & Jennings, J. H. (2012), 'Study of the knocking propensity of 2, 5-dimethylfuran–gasoline and ethanol–gasoline blends', *Fuel* **98**, 203–212.

Russ, J. C. (2016), *The image processing handbook*, CRC press.

Schwarz, H. (1979), Ignition systems for lean burn engines, *in* 'Fuel Economy and Emissions of Lean Burn Engines, Inst. Mech. Eng. Conf. Pub', Vol. 9.

Scott, M, J. (1992), Distributions of strain rate and temperature in turbulent combustion, PhD thesis.

Stone, R. (1999), 'Introduction to internal combustion engines'.

Tabaczynski, R. J. (1979), Turbulence and turbulent combustion in spark-ignition engines, *in* 'Energy and Combustion Science', Elsevier, pp. 259–281.

Tennekes, H., Lumley, J. L., Lumley, J. et al. (1972), *A first course in turbulence*, MIT press.

Thielicke, W. & Stamhuis, E. J. (2014), 'Pivlab-towards user-friendly, affordable and accurate digital particle image velocimetry in matlab', *Journal of Open Research Software* **2**.

Vancoillie, J., Sharpe, G., Lawes, M. & Verhelst, S. (2014), 'The turbulent burning velocity of methanol–air mixtures', *Fuel* **130**, 76–91.

Vermorel, O., Richard, S., Colin, O., Angelberger, C., Benkenida, A. & Veynante, D. (2009), 'Towards the understanding of cyclic variability in a spark ignited engine using multi-cycle les', *Combustion and Flame* **156**(8), 1525–1541.

Veynante, D. & Vervisch, L. (2002), 'Turbulent combustion modeling', *Progress in energy and combustion science* **28**(3), 193–266.

Witze, P. . & Vilchis, F. R. (1981), 'Stroboscopic laser shadowgraph study of the effect of swirl on homogeneous combustion in a spark-ignition engine', *SAE Transactions* pp. 979–991.

Witze, P. O. & Mendes-Lopes, J. M. (1986), Direct measurement of the turbulent burning velocity in a homogeneous-charge engine, Technical report, SAE Technical Paper.

Zimont, V. (1979), 'Theory of turbulent combustion of a homogeneous fuel mixture at high reynolds numbers', *Combustion, Explosion and Shock Waves* **15**(3), 305–311.

Zimont, V., Polifke, W., Bettelini, M. & Weisenstein, W. (1998), 'An efficient computational model for premixed turbulent combustion at high reynolds numbers based on a turbulent flame speed closure', **120**.